

MEASURING THE CONTRIBUTION OF LOW BJORKEN-X GLUONS TO THE  
PROTON SPIN WITH POLARIZED PROTON-PROTON COLLISIONS

BY

SCOTT JUSTIN WOLIN

DISSERTATION

Submitted in partial fulfillment of the requirements  
for the degree of Doctor of Philosophy in Physics  
in the Graduate College of the  
University of Illinois at Urbana-Champaign, 2013

Urbana, Illinois

Doctoral Committee:

Professor Jen-Chieh Peng, Chair  
Professor Matthias Große Perdekamp, Director of Research  
Professor James N. Eckstein  
Professor John D. Stack

# Abstract

The PHENIX experiment is one of two detectors located at the Relativistic Heavy Ion Collider (RHIC) at Brookhaven National Laboratory in Upton, NY. Understanding the spin structure of the proton is a central goal at RHIC, the only polarized proton-on-proton collider in existence. The PHENIX spin program has two primary objectives. The first is to improve the constraints on the polarized parton distributions of the anti-u and anti-d quarks within the proton. The second objective is to improve the constraint on the gluon spin contribution to the proton spin,  $\Delta G$ . The focus of this thesis is the second objective.

The motivation to study  $\Delta G$  originates with polarized Deep Inelastic Scattering (DIS) experiments, in which a polarized lepton is scattered off of a polarized proton. Polarized DIS scattering experiments have found that the quark polarization is significantly less than expected and too small to account for the proton spin of  $\frac{1}{2}\hbar$ . This result was published first in 1989 by the European Muon Collaboration. After it was further confirmed through DIS experiments at SLAC, CERN and DESY, it was natural to try measuring  $\Delta G$ , as a non-zero value would imply that the missing quark spin was due to gluon spin. Polarized DIS experiments are able to indirectly access gluons, however, the kinematic reach has so far been insufficient to put a strong constraint on  $\Delta G$ . Even extreme scenarios for the gluon polarization could not be excluded by these experiments. At a polarized proton-on-proton collider, one gains direct access to gluons and more powerful constraints to the gluon polarization become possible with relatively small data samples.

The PHENIX experiment has been successful at providing the first meaningful constraints on  $\Delta G$ , along with STAR, the other detector located at RHIC. These constraints have, in fact, eliminated the extreme scenarios for gluon polarization through measurements of the double spin asymmetry,  $A_{LL}$ , between the cross section of like and unlike sign helicity  $pp$  interactions.  $A_{LL}$  measurements can be performed with a variety of final states at PHENIX. Until 2009, these final states were only measured for pseudo-rapidities of  $|\eta| < 0.35$ . This range of  $\eta$  is referred to as mid-rapidity. These mid-rapidity measurements, like the polarized DIS measurements, suffer from a limited kinematic reach.

Final states containing a measured particle with  $p_T \gtrsim 1\text{ GeV}/c$  are considered to have occurred in the hard scattering domain where the  $pp$  interaction is well approximated as an interaction of a quark or gluon in one proton and a quark or gluon in the second proton. Each of these interacting particles has a momen-

tum fraction,  $x$ , of its parent proton's momentum. The gluon polarization is dependent on the momentum fraction and the net gluon polarization can be written as the integral of the momentum fraction dependent polarization:  $\Delta G = \int_0^1 \Delta g(x) dx$ .

The momentum fractions of the two interacting particles give information about the final state jets. Likewise, one can work backwards. By measuring the kinematics of final state hadrons or jets, information about quark and gluon momentum fractions can be learned. It turns out that mid-rapidity measurements of  $A_{LL}$  are primarily sensitive to  $pp$  collisions in which the gluon momentum fraction was in the range  $0.05 < x < 0.2$ . Therefore, mid-rapidity measurements are capable of constraining  $\Delta g(x)$  only within this range and the polarization of gluons having a momentum fraction outside this range do not play a significant role in the observed  $A_{LL}$ . This leaves a large gap in understanding as the gluon number density at low- $x$ ,  $x < 0.05$ , grows rapidly. It is, therefore, precisely the region not constrained by mid-rapidity  $A_{LL}$  measurements that is the most interesting place to look for a potentially large gluon polarization.

This provides the motivation to build a new calorimeter for PHENIX that is able to measure final states of  $pp$  interactions in which a low- $x$  gluon was a participant. Like a fast moving car crashing into a slow moving car and the debris ending up mostly along the line of motion of the fast moving car, the debris of a high- $x$  quark interacting with a low- $x$  gluon will result in debris at forward rapidity at small angles to the initial quark momentum. The Muon Piston Calorimeter (MPC) was installed in 2006 and 2007 at forward rapidity,  $3.1 < |\eta| < 3.9$ , with the intention of giving PHENIX the ability to constrain  $\Delta g(x)$  for  $x < 0.05$ . In this thesis, the first two measurements of  $A_{LL}$  using the MPC to measure a single hadron in the final state will be presented.

Following this, an electronics upgrade to the MPC will be described which enables the selection of events with two hadrons detected in the MPC. This requirement favors gluons at even lower  $x$  than the single hadron event selection. The di-hadron measurement that this upgrade makes possible will allow PHENIX to produce an  $A_{LL}$  measurement that constrains  $\Delta g(x)$  in the range of  $5 \times 10^{-4} < x < 0.01$ .

Finally, we discuss the most important systematic uncertainty common to all  $A_{LL}$  measurements which arises from the determination of the relative luminosity. A precision  $A_{LL}$  measurement requires measuring the final state yield from the portions of the proton beams that collide like and unlike sign helicity protons separately. It also requires understanding the ratio of the collision rates of these two portions of the beam

exquisitely well. This is a long standing problem and, until recently, had threatened to severely restrict the ability of PHENIX to utilize the large data sets that have been acquired in the last two years to improve the constraints on  $\Delta G$ . We will conclude this thesis with a comprehensive overview of the relative luminosity systematic uncertainty and present a new framework within which this uncertainty can be determined. It will be demonstrated that not only were very large effects previously overlooked, but that by accounting for these effects the systematic uncertainty is reduced by an order of magnitude, from  $O(10^{-3})$  to  $O(10^{-4})$ . This improvement has consequences for all high statistics measurements at PHENIX which were previously limited by their systematic uncertainty.

The measurement of the gluon contribution to the proton spin at the PHENIX experiment is a multi-faceted problem which requires a multi-faceted solution. This thesis describes several aspects of the solution as the single- and di-hadron measurements from MPC data are likely to provide the best constraints to  $\Delta G$  at low- $x$  for the next decade. Eventually, an Electron-Ion Collider (EIC) will be designed and commissioned that will further extend the kinematic reach of the polarized DIS experiments that motivated the spin program at RHIC. In the meantime, the goal of PHENIX in general, and the MPC in particular, is to glean as much information about the gluon polarization as possible before the EIC era arrives.

# Acknowledgements

To the best of my recollection, I was fascinated by physics as early as middle school. I recall spending hours at Barnes and Noble reading whatever I could get my hands on. I even recall purchasing *Gravitation* by Misner, Thorne and Wheeler knowing that I would have to return it because it was too expensive. Never mind that I was no match for that book at the time, it was too intimidating to not at least try to conquer. Nevertheless, come holiday time, I always requested some new physics books and my parents, Ken and Sandy, always obliged. They have always encouraged my education and made every possible effort to support my interest in science.

I would also like to thank my advisor, Matthias Perdekamp, and to congratulate him on his recent and well-deserved promotion to Professor of Physics. He is extraordinarily ambitious in his work and manages to maintain active involvement in numerous collaborations on a global scale while simultaneously staying actively engaged in the day-to-day work of each of his graduate students, myself included. His support has been invaluable.

Mickey Chiu has been a close collaborator and his support on my analyses, his leadership of the MPC electronics upgrade project and his overall dedication to PHENIX have provided me with a great example of the type of physicist one should strive to be. His mental horsepower is matched by few.

I would also like to thank John Koster for spending hours explaining the basics of PHENIX to me when I first joined and also Beau Meredith and Cameron McKinney for their help.

I would also like to thank Steve Boose and Sal Polizzo for their support in designing and producing the transition boards for the MPC upgrade, and Cheng-Yi Chi for programming the necessary electronics. John Haggerty, Frank Toldo, and James LaBounty were also instrumental, along with numerous other technicians who provided support in this project. I want to thank Emily Zarndt for her help in understanding the performance of the new trigger and Pedro Montuenga for his continuing hard work to optimize our understanding of the data.

Finally, my fiancée, Megan, has provided me with a constant bedrock of support even as she deals with the high stress of medical school herself. I am unbelievably lucky to have her constant support and any amount of success I might experience in my own endeavors would likely not be possible without her.

# Table of Contents

<b>Chapter 1 Introduction . . . . .</b>	<b>1</b>
<b>Chapter 2 Nucleon Structure Functions and the Gluon Polarization . . . . .</b>	<b>6</b>
2.1 Deep Inelastic Scattering: $ep \rightarrow eX$ . . . . .	7
2.2 Bjorken Scaling . . . . .	9
2.3 Quark Parton Model . . . . .	11
2.4 Evolution of PDF's . . . . .	12
2.5 Polarized Parton Distribution Functions . . . . .	14
2.6 The Spin Puzzle . . . . .	17
2.7 The Gluon Contribution to the Proton Spin . . . . .	20
2.8 Kinematic Definitions for Proton-Proton Interactions . . . . .	22
2.9 Accessing $\Delta g(x)$ . . . . .	23
2.10 Global Analysis Results for $\Delta G$ . . . . .	25
<b>Chapter 3 Experimental Apparatus . . . . .</b>	<b>30</b>
3.1 Production, Acceleration, and Storage of Polarized Protons at RHIC . . . . .	30
3.2 Detector Overview . . . . .	32
3.3 Beam Beam Counter . . . . .	34
3.4 Zero Degree Calorimeter . . . . .	35
3.5 Data Acquisition System . . . . .	38
<b>Chapter 4 Muon Piston Calorimeter . . . . .</b>	<b>39</b>
4.1 Description of MPC . . . . .	39
4.2 MPC Trigger and Readout . . . . .	40
4.3 Measuring $A_{LL}$ from Single and Di-Hadrons in the MPC . . . . .	41
4.4 Summary . . . . .	44
<b>Chapter 5 Measurement of Forward Cluster <math>A_{LL}</math> at <math>\sqrt{s} = 200\text{ GeV}</math> . . . . .</b>	<b>46</b>
5.1 Why EM Clusters are Measured . . . . .	46
5.2 Definition of $A_{LL}$ . . . . .	48
5.3 Detector Calibration . . . . .	49
5.3.1 ADC and TDC Overflows . . . . .	49
5.3.2 Energy Scale Determination . . . . .	51
5.3.3 Warnmap: List of Excluded Towers . . . . .	53
5.3.4 $\pi^0$ Reconstructed Mass Dependence on Pair Energy . . . . .	57
5.3.5 $\pi^0$ Stability . . . . .	58
5.3.6 $\eta$ Meson Reconstruction . . . . .	59
5.4 Detector Quality Assurance . . . . .	60
5.5 MPC Triggers and Trigger Performance . . . . .	61
5.5.1 Reduced Bit Inputs . . . . .	62
5.5.2 MPC Radiographs . . . . .	62
5.5.3 Vertex Distributions . . . . .	63

5.5.4	Cluster Energy and $p_T$ Spectra . . . . .	64
5.5.5	<i>MPC_2x2(PT)</i> Trigger Consistency Issue . . . . .	65
5.6	Relative Luminosity . . . . .	69
5.7	Analysis Cuts . . . . .	71
5.8	Binning For Asymmetry Calculation . . . . .	72
5.9	Asymmetry Results . . . . .	73
5.10	Bunch Shuffling . . . . .	73
5.11	Final $A_{LL}^{cluster}$ . . . . .	74
5.12	Check of Spin Pattern Consistency . . . . .	78
5.13	Check of Single Spin Asymmetry, $A_L^{cluster}$ . . . . .	79
<b>Chapter 6</b>	<b>Measurement of Forward Cluster <math>A_{LL}</math> at <math>\sqrt{s} = 500\text{ GeV}</math> . . . . .</b>	<b>81</b>
6.1	Cluster Decomposition . . . . .	81
6.2	Calibration of Data . . . . .	82
6.2.1	ADC Pedestals . . . . .	82
6.2.2	ADC and TDC Overflow Determination . . . . .	83
6.2.3	High-Low ADC ratio . . . . .	83
6.2.4	LED Analysis and Determination of ADC to Energy Conversion Factors . . . . .	83
6.2.5	Warnmap . . . . .	84
6.3	Single Tower Background . . . . .	87
6.4	$\pi^0$ Mass Reconstruction . . . . .	89
6.5	$\pi^0$ Counts Per Minimum Bias Trigger . . . . .	95
6.6	$\pi^0$ Mass Stability . . . . .	95
6.7	$\pi^0$ Width Stability . . . . .	96
6.8	$\pi^0$ Eta Mass Reconstruction and Stability . . . . .	99
6.9	Quality Assurance . . . . .	103
6.9.1	MPC QA . . . . .	103
6.9.2	Run QA . . . . .	103
6.9.3	Spin and Bunch Crossing QA . . . . .	103
6.9.4	Final List of Excluded Crossings and Runs . . . . .	103
6.10	Cluster $A_{LL}$ and Bunch Shuffling Results . . . . .	106
6.11	Final Result for $A_{LL}^{cluster}$ . . . . .	110
6.12	Spin Pattern Separated $A_{LL}$ Check . . . . .	112
6.13	Relative Luminosity . . . . .	113
6.14	$A_L^{cluster}$ Results . . . . .	113
6.15	Analysis of Ghost Clusters . . . . .	114
6.15.1	Definitions . . . . .	115
6.15.2	The Effect of Ghost Clusters on $A_{LL}$ . . . . .	116
6.15.3	Estimate of the Size of the Ghost Cluster Effect . . . . .	117
<b>Chapter 7</b>	<b>MPC Electronics and Trigger Upgrade . . . . .</b>	<b>119</b>
7.1	Motivation for an MPC Upgrade . . . . .	119
7.2	Scope of Changes to the MPC Electronics . . . . .	120
7.3	Transition Board . . . . .	121
7.4	HBD Front End Module ADC Board . . . . .	129
7.5	Test Stand Setup . . . . .	135
7.6	Trigger Algorithm . . . . .	138
7.7	MPC Trigger Emulation and Performance . . . . .	140
7.8	MPC Trigger Configuration Details . . . . .	143
7.9	DCM Readout Format . . . . .	145
7.10	Modifications to MPC Offline Code and Node Structure . . . . .	146
7.11	MPC Di-Hadron Trigger . . . . .	147
7.12	New Electronics Rack Installation within PHENIX . . . . .	148
7.13	List of Advantages Of New Electronics . . . . .	152

<b>Chapter 8 Relative Luminosity . . . . .</b>	<b>153</b>
8.1 Bunch Helicities and Spin Patterns . . . . .	153
8.2 Definition of Relative Luminosity . . . . .	154
8.3 Effect of an $A_{LL}$ in the Luminosity Monitor . . . . .	157
8.4 GL1P Scalers and Live Triggers . . . . .	158
8.5 STAR Scalers . . . . .	162
8.6 Estimating the Relative Luminosity Uncertainty via Width Corrections . . . . .	163
8.7 Pileup Corrections . . . . .	169
8.8 Determining $k_N$ and $k_S$ . . . . .	175
8.9 Using the Pileup Corrections . . . . .	178
8.10 Combined Width and Pileup Corrections . . . . .	179
8.11 Full BBC Simulations . . . . .	182
8.11.1 Description of Simulations . . . . .	184
8.11.2 Simulation Weighting . . . . .	185
8.11.3 Wall Current Monitor Data . . . . .	186
8.11.4 BBC and ZDC Trigger Emulation . . . . .	190
8.11.5 Method of ZDC Simulation . . . . .	192
8.11.6 Comparison of Data and Simulation . . . . .	194
8.11.7 Vertex Width Dependence on Beam Rate . . . . .	195
8.11.8 Determining the True Beam Rate . . . . .	196
8.12 Concluding Remarks on Relative Luminosity Status . . . . .	198
<b>Chapter 9 Residual Rate Correlation . . . . .</b>	<b>202</b>
9.1 Derivation of a Residual Rate Correlation in the Two Collision Approximation . . . . .	202
9.2 Observation of a Residual Rate Correlation in the Data . . . . .	208
9.3 Time Dependence of the Residual Rate Correlation Parameters . . . . .	211
9.4 Residual Rate Correction to the ZDC Luminosity . . . . .	213
9.5 Impact of Residual Rate Correction on $A_{LL}^{ZDC/BBC}$ . . . . .	216
9.6 The Spin Pattern Problem . . . . .	221
9.7 Replicating the Residual Rate Correlation in Simulations . . . . .	224
9.8 Effect of a Systematic Error of $k_{N,S}$ on the Residual Correlation . . . . .	226
9.9 Residual Rate Correlation in the Run09 $\sqrt{s} = 200$ GeV Data and Elsewhere . . . . .	232
9.10 Concluding Remarks on the Residual Rate Correlation and Correction . . . . .	233
<b>Chapter 10 Conclusion . . . . .</b>	<b>235</b>
<b>References . . . . .</b>	<b>239</b>

# Chapter 1

## Introduction

The contribution of Ph.D. research to the sum total of human knowledge is increasing either the breadth or depth of the “sphere of knowledge” originating from and surrounding some initial central discovery. This relation is shown schematically in Figure 1.1 ([1]). The central discovery, the blue region in Fig. 1.1, spawns perhaps an entire new field or fields of research. The subsequent outer layers in different colors represent the breadth and depth of knowledge that is developed over the course of time. For the case of the gluon

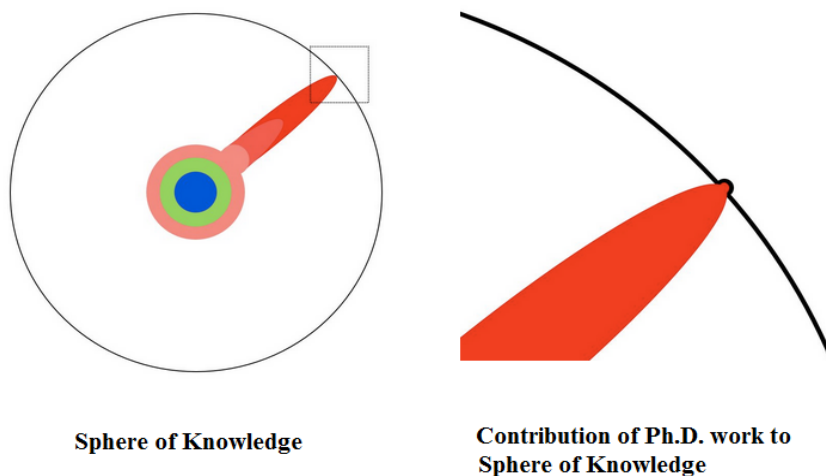


Figure 1.1: Left: A sphere of knowledge. The blue core represents an important foundational aspect of nature, such as the discovery of the proton. Additional layers of knowledge then get added over time, which include establishing the existence of a proton substructure and understanding that substructure both theoretically and experimentally increasingly well. Right: Thesis research increases either the precision or depth of already existing knowledge or it provides a first step into a new aspect of the foundational natural phenomena at the center of the Sphere of Knowledge.

spin contribution to the overall proton spin, the central discovery, the blue circle, would arguably be the discovery of a charged nucleus by Ernest Rutherford. Based on his famous gold foil experiment in which he and his team observed that alpha particles would occasionally ricochet at large angles after colliding with gold atoms, he effectively disproved J.J. Thomson’s plum pudding model of atomic structure ([2]). This result was published in 1911([3]), and although this showed that the electrons that Thomson had observed

14 years prior were not the only particles comprising the atom, it would take another 8 years, until 1919, for Rutherford to identify the proton as part of this core (the neutron would take an additional 13 years before discovery). The experiment that led Rutherford to observe the proton directly used alpha decays from a Radium source to collide with Nitrogen in a gas filled chamber, in what is considered to be the first observed nuclear interaction:



The next major shell would be the realization that the nucleon (referring to both protons and neutrons) itself is not a fundamental particle. The first piece of experimental evidence for this came from the measurement of the proton magnetic moment. In general the magnetic moment can be identified from Dirac theory as:

$$\mu_p = g \frac{e}{2m_p} S \quad (1.2)$$

where the terms are defined as follows:

- $\mu_p$  is the proton magnetic moment
- $g$  is the gyromagnetic ratio
- $e$  is the net proton charge equal to  $1.602 \times 10^{-19} \text{ C}$
- $m_p$  is the proton mass of  $1.672 \times 10^{-27} \text{ kg}$
- $S$  is the proton spin,  $\frac{1}{2}\hbar$

For a point particle having no internal structure,  $g = 2$  up to leading order Feynman diagrams. Higher order diagrams will cause slight deviations from this. However, for the proton it is found that  $g = 5.586$  and for the neutron,  $g = -3.826$ . Aside from their marked difference from 2, the fact that the neutron is electrically neutral and still interacts with magnetic fields definitively shows that there must be a dynamic internal structure of charge. The fact that such a wide variety of particles similar to the neutron and proton also exist is further evidence of internal structure, much the same way as the periodic table of elements hints strongly at a more fundamental atomic substructure.

The next shell outward is the detailed understanding of this internal structure of the nucleon. While some sort of plum pudding nucleon model could have been the case, as with the atomic structure this is not so. Just as in the gold foil experiment, in  $e + p$  collisions the electron is observed to undergo large angle

scattering. For the proton case, Bjorken scaling<sup>1</sup> shows that this occurs as a result of the underlying parton structure of a proton, where each parton, nominally a quark or gluon, is a point particle with spin  $\hbar/2$ . In Chapter 2 we will discuss this further.

Once the parton substructure has been established, along with its relationship to the proton structure functions, it is natural to investigate the number densities of the various partons inside the proton along with their momentum and polarizations. The question of parton polarization is particularly interesting because we know that the partons, along with their relative orbital angular momenta, must account for the full spin of the proton. This will be discussed in more detail in the next section. The topic of present concern, understanding the gluon contribution to the proton spin through its polarization, will be developed. While Semi-Inclusive Deep Inelastic Scattering (SIDIS) experiments have estimated the net polarization of the quarks, there remains much uncertainty in the gluon polarization. The reason for this in the case of SIDIS is that gluons have no electric charge, hence cannot interact directly with the virtual photon emitted by the electron. A gluon can only indirectly interact with the photon by first splitting into a quark-antiquark pair. One of the quarks may then interact with the virtual photon. We will see later that this splitting process,  $g \rightarrow q\bar{q}$ , amongst others, gives access to the gluon polarization, but only through its derivative in the momentum transfer. Without these processes Bjorken scaling would be preserved. However, because of it weak scaling violations do exist which allow limited sensitivity to the gluon polarization. At a polarized hadron-hadron accelerator, the Relativistic Heavy Ion Collider is presently the only polarized proton-proton collider in the world, direct access to gluon-gluon and quark-gluon vertices is possible. This significantly increases our ability to study the gluon polarization, but it comes at the cost of more complex kinematics. Whereas in DIS and SIDIS the kinematics of the struck quark are well determined, in  $p + p$  scattering there are two partons and it is not possible to precisely control the kinematics of either. Therefore when the gluon polarization is probed through the measurement of asymmetries between hadron yields from proton-proton collisions with different relative spin orientations, gluons are probed over a wide range of momenta inside the proton. Since the gluon polarization depends on the gluon momentum,  $p_g$ , relative to the proton momentum,  $p_p$ , the momentum dependent gluon spin distribution,  $\Delta g(x)$ , needs to be unfolded through a complex theoretical analysis from the observed asymmetries. Here we use  $x = \frac{p_g}{p_p}$  which is defined in an appropriate frame.

After a discussion of some of the theoretical aspects underlying the extraction of  $\Delta g(x)$  we will briefly

---

<sup>1</sup> The cross section for large momentum transfer between the electron and proton does not drop as steeply as expected. This implies the proton has internal structure. A cross section that scales with (is independent of) momentum transferred is consistent with the idea that the internal structure arises from point-like constituents.

describe the relevant aspects of the PHENIX experiment. The detectors at PHENIX are capable of observing a variety of final state particles including single  $\pi^0$ , charged pions,  $\eta$ , electrons, and electromagnetic clusters. In addition, di-hadron final state asymmetries are observed at both mid-rapidity (nearly perpendicular to the beam axis) and forward rapidity (small angle to the beam axis).

Next, we will describe the Muon Piston Calorimeter (MPC). The MPC was installed as an upgrade in 2006 and 2007 and sits at roughly  $3^\circ - 10^\circ$  from the beam line. It will be explained why this calorimeter extends the range of sensitivity to gluons with lower momentum fraction than the mid-rapidity detectors, which allows it to constrain the function  $\Delta g(x)$  in a range of  $x$  not previously accessed.

We will then describe the calibration and measurement of the double longitudinal helicity asymmetry,  $A_{LL}$ , in single electromagnetic clusters using the MPC from the first two sets of data it acquired in longitudinally polarized  $pp$  running. These sets of data were taken at center of mass collision energies of  $\sqrt{s} = 200\text{ GeV}$  and  $\sqrt{s} = 500\text{ GeV}$  and represent the first asymmetry measurements at the PHENIX experiment to have large sensitivity to gluons with momentum fraction  $x_g < 0.05$ .

The original MPC electronics were capable of triggering on only one hadron. To extend the sensitivity to even lower  $x_g$ , it was necessary to design and install an electronics and trigger upgrade capable of triggering on di-hadrons. This project to enable such a measurement was completed prior to the 2012 data taking run. We will describe in detail the technical aspects of this project.

Finally, we will extensively address the issue of the systematic uncertainty on the  $A_{LL}$  measurements. The dominating systematic uncertainty comes from how well we understand the relative intensities of the beams between different spin orientations. We will explain the necessary ideas and the current state of the uncertainty. Minimizing this uncertainty is critical in order for precision measurements at PHENIX to be able to constrain  $\Delta G$ . At the moment, however, this uncertainty remains the limiting factor. However, in this thesis, we describe a method to achieve unparalleled precision in the determination of the beam intensities. What we will find, however, is that to achieve this does not require a revolutionary new method, rather a clear understanding and application of existing methods. We will provide a thorough accounting of the two existing methods, width correlations and pileup corrections. Both of these are designed to systematically account for an incorrect determination of beam intensity and both are theoretically justified. We will investigate quantitatively how well these corrections improve the measurement of beam intensity but ultimately

realize there is a missing piece. Part of the missing piece is that these two methods are not independent of one another. In other words, the corrections do not “commute”. The result of applying one correction before the other is not the same as doing the reverse. Since only one answer can be correct, and it is not clear in which order to apply the two corrections, we are left with a serious conceptual problem. Further, we will show how various experimental details, not previously considered, cause the intensity corrections to fail. We will introduce a new framework to account for all of these effects together and show that its predictions agree quantitatively with the data. We will then study this new correction in a simplified form and demonstrate the marked improvement this provides in our understanding of the beam intensity. We will also demonstrate why this simplified form can and should be improved. We lay the groundwork for a fully correct application to be implemented. This framework is intrinsically applicable at any beam intensity, including the intensities seen in years 2009, 2011, 2012 and 2013. We propose that by using this framework, our understanding of beam intensities is improved by an order of magnitude, as is the corresponding systematic uncertainty. The implication for this is that the constraint on  $\Delta G$  is now limited by the statistical uncertainty, not the systematic uncertainty. A non-zero  $\Delta G$  is expected to produce  $A_{LL} \sim O(10^{-4})$ , and with the large sets of data accumulated, particularly in 2012 and 2013, PHENIX may now be sensitive at this level. As an electron-ion collider (EIC) will not be operational for several years, at a minimum, maximizing the impact of  $\Delta G$  measurements now is critical.

## Chapter 2

# Nucleon Structure Functions and the Gluon Polarization

We begin by showing how the nucleon (proton and neutron) structure functions arise when calculating the  $ep$  cross section at leading order in the strong coupling constant  $\alpha_S$ . These non-perturbative but universal functions describe, or parameterize, the internal structure of the nucleon, which cannot be determined from first principles in Quantum Chromodynamics (QCD). We will then show that the nucleon can be considered as comprised of independent partons (quarks and gluons) based on the observation of Bjorken scaling. These partons can be related to the structure functions by defining parton distribution functions (PDF). While at low momentum transfer, the nucleon has a structure that is difficult to interpret in terms of partons, at high momentum transfer, it behaves as a loosely bound collection of partons with non-overlapping wavefunctions. At this scale, the virtual photon emitted by the electron can be well approximated as interacting with just one parton, which on the time scales of the interaction is a free particle. This interpretation is what allows us to clearly talk about the number of quarks or the net polarization of gluons inside of a nucleon. The gluon polarization,  $\Delta g(x, Q^2)$ , is one of several polarized parton distribution functions. DIS and semi-inclusive DIS experiments have resulted in strong constraints on the quark PDF's ([13]) and polarized PDF's ([44], [45]). However, because the virtual photon emitted from the electron cannot directly interact with the gluons within the proton, only indirect constraints can be put on the gluon polarization through Bjorken scaling violations in the (negative of) momentum transfer squared,  $Q^2$ . To get direct access to  $\Delta G$  requires a polarized proton-proton collider. The kinematics of proton-proton collisions can not be known as precisely as in the (SI)DIS case on a collision-by-collision basis. However, by constraining or specifying the final state kinematics of  $pp$  collisions, one can deduce a range of kinematic conditions that would have produced it. One of the biggest mysteries of the nucleon spin structure is “how polarized are the gluons?”. There are a lot of gluons at low- $x$  and the gluon PDF,  $g(x)$ , is a rapidly increasing function of  $\ln(\frac{1}{x_g})$ . Therefore, even a slight imbalance of gluons with positive versus negative helicity can produce a significant net spin contribution. Even at moderate values of gluon momentum fraction where constraints already exist, there is a tendency toward positive gluon spin with  $\Delta G^{[0.05,0.2]} = 0.10_{-0.07}^{+0.06}$  (Ref [53]). It is interesting to muse how this means it is quite possible that a common procedure such as Magnetic Resonance Imaging (MRI),

often used to detect cancer and make other diagnoses, owes much of its effectiveness, quite literally, to the fundamental force carrying particle of Quantum Chromodynamics. As of 2013, a large amount of data has also been accumulated with the upgraded MPC fully functional in the PHENIX detector. These data will be used to constrain  $\Delta g(x)$  in the region  $x < 0.05$ . At high-x,  $x > 0.2$ , the gluon number density is very small, and is constrained by longitudinal data taken at  $\sqrt{s} = 62.4$  GeV and by the constraint that  $|\Delta g(x)| < g(x)$ .

## 2.1 Deep Inelastic Scattering: $ep \rightarrow eX$

The first attempts to probe the internal structure of the nucleon used electron scattering ([5],[6]). Electrons, like all leptons, are fundamental particles. Currently, there is no experimental evidence that leptons have internal structure. Therefore, the electron can be cleanly used to probe the complicated internal structure of the proton. In Figure 2.1 we show the leading order Feynman diagram for deeply inelastic scattering (DIS). By leading order we mean the diagram which contributes to the overall scattering amplitude at lowest order in the electromagnetic coupling constant,  $\alpha_{EM}$ . Electromagnetic radiative contributions also contribute higher orders of  $\alpha_{EM}$ , while additional QCD diagrams lead to  $\alpha_S$  terms. A lepton with initial 4-momentum  $k$  scatters off of a proton with 4-momentum  $p$  via the exchange of a virtual photon. After the interaction the lepton is observed to have 4-momentum  $k'$ . The exchanged virtual photon therefore has 4-momentum  $q = k - k'$ . Since  $q^2 < 0$ , the quantity  $Q^2 \equiv -q^2 > 0$  is more commonly used.  $\alpha_S(Q^2)$  is a decreasing function of the momentum transfer, a phenomenon called asymptotic freedom that, along with confinement, gives the theory of Quantum Chromodynamics so much of its richness. While we will not digress into this, we note that for large momentum transfers, higher order corrections from diagrams with multiple intermediate particles are suppressed. At low  $Q^2$  where particles with the color degree of freedom interact most strongly, multi-particle interactions cannot be ignored. In fact, it is precisely this regime where the dynamics of bound states of quarks (mesons and baryons, collectively referred to as hadrons) as well as jet fragmentation cannot be ignored ([4]). The typical energy scale separating the strongly coupled and asymptotically free regimes is  $E \sim 1$  GeV, similar to the radius of the proton of  $r_p = 0.81$  GeV obtained from measurements of its charge and magnetic moment distributions.

In Figure 2.1, where it is assumed we are safely in the asymptotically free region, there are four commonly defined relativistically invariant variables:

$$Q^2 \equiv -q^2 > 0 \quad (2.1)$$

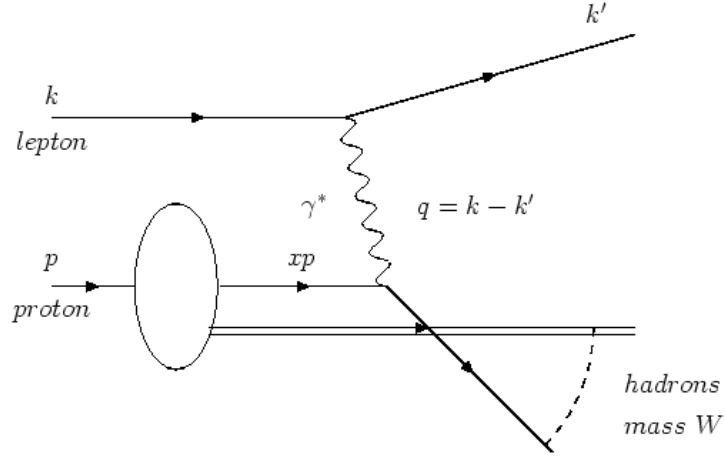


Figure 2.1: The leading order diagram for  $e + p \rightarrow e + X$  scattering. In this diagram the electron emits a virtual photon which, at high enough momentum, has a wavelength small enough such that it interacts with just a single proton constituent of momentum  $xp$ .  $x = \frac{p_i}{p}$  is the fraction of the proton's total momentum,  $p$ , carried by the constituent in question having momentum  $p_i$ .

$$y \equiv \frac{p \cdot q}{p \cdot k} \quad (2.2)$$

$$\nu \equiv \frac{p \cdot q}{M_p} \quad (2.3)$$

$$x \equiv \frac{Q^2}{2p \cdot q} = \frac{Q^2}{2M_p \nu} \quad (2.4)$$

It can be shown that  $0 < x < 1$  and  $0 < y < 1$ . In the lab frame, it can be shown that  $y$  is the fractional energy loss of the electron and  $\nu$  is the energy carried by the virtual photon. The limit  $x = 1$  occurs for an elastic collision. In the Breit frame, where the virtual photon momentum is purely space-like,  $x$  may be interpreted as the parton momentum fraction:  $x = \frac{p_{parton}}{p_{proton}}$ .

The DIS cross section in the lab frame is:

$$\frac{d^2\sigma}{dE'd\Omega} = \frac{\alpha_{EM}^2}{4E^2 \sin^4 \frac{\theta}{2}} (W_2(\nu, q^2) \cos^2 \frac{\theta}{2} + 2W_1(\nu, q^2) \sin^2 \frac{\theta}{2}) \quad (2.5)$$

Where:

- $E$  = the energy of the electron in the initial state.

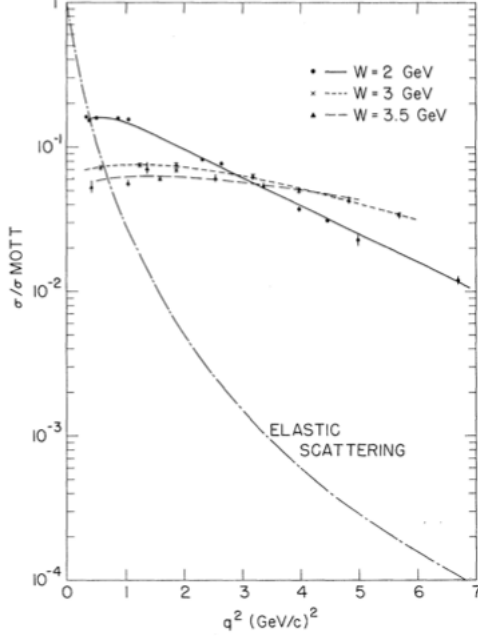


Figure 2.2: The double differential cross section for elastic and inelastic scattering is shown. For the inelastic case where  $e + p \rightarrow e + X$ , three curves are shown corresponding to the invariant mass,  $W$  of the final state  $X$ . The notable feature is the very weak dependence of these inelastic cross section curves on  $q^2$  ([6]).

- $E'$  = the energy of the electron in the final state.
- $d\Omega$  = a unit of solid angle.
- $\alpha_{EM}$  = the electromagnetic coupling constant.  $\alpha_{EM} \approx \frac{1}{137}$ .
- $\theta$  = the scattering angle between the beam axis and the 3-momentum of the final state electron.

The functions  $W_1(\nu, q^2)$  and  $W_2(\nu, q^2)$  are called the inelastic form factors. During elastic scattering, where the proton survives intact, elastic form factors  $G_E(q^2)$  and  $G_M(q^2)$  appear instead and are functions only of the resolving power  $q^2$ .

## 2.2 Bjorken Scaling

The inelastic form factors parametrize one's ignorance of the internal structure of a proton. So, in effect, by measuring the differential cross section  $\frac{d\sigma}{dE'd\Omega}$ , one can deduce  $W_1$  and  $W_2$ . Figure 2.2 shows the first such cross section measurement [6]. Here, the ratio  $\frac{d\sigma}{dE'd\Omega}/\sigma_{MOTT}$  is plotted in order to remove the  $Q^2$

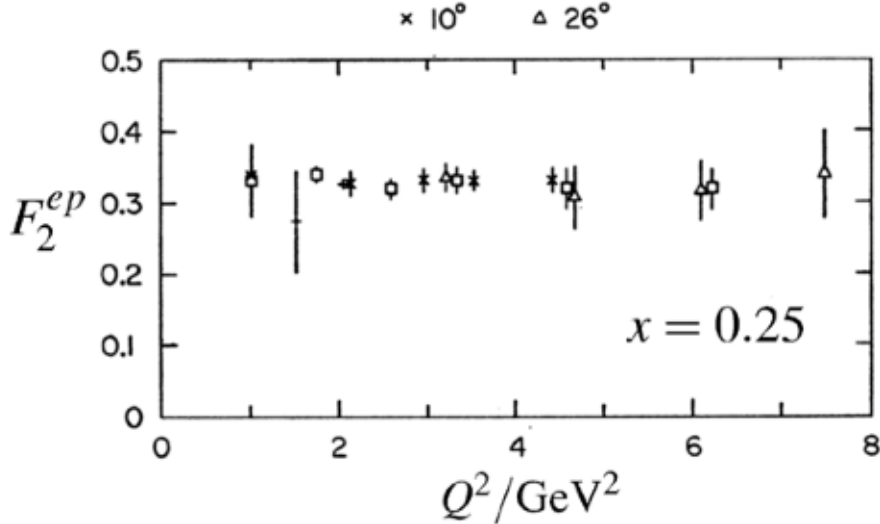


Figure 2.3: The scaling function  $F_2$  is shown as a function of  $Q^2$  at constant Bjorken- $x = 0.25$ . The fact that  $F_2$  satisfies Bjorken scaling, as predicted, is strong evidence in favor of the parton view of the proton structure.

dependence of the cross section due to the photon propagator and

$$\sigma_{MOTT} = \frac{e^4}{4E^2} \frac{\cos^2 \frac{1}{2}\theta}{\sin^4 \frac{1}{2}\theta} \quad (2.6)$$

is the reference cross section for a structureless target. The elastic scattering cross section can be seen to decrease rapidly with  $q^2$ . This is expected. The higher the energy of the virtual photon, the less likely the proton is to stay intact. However, the fact that the dependence of  $\sigma/\sigma_{MOTT}$  on  $q^2$  gets weaker and weaker as the final state invariant mass,  $W$ , increases implies that the nature of the scattering is qualitatively starting to look more and more like scattering of point-like partons. This limit is often called the DIS limit and may be considered to have been reached when the final hadronic state invariant mass,  $W$ , and momentum transfer squared,  $Q^2$ , are sufficiently large. A typical boundary is  $W > 2 \text{ GeV}$  and  $Q^2 > 1 \text{ GeV}^2$ . In fact, Bjorken showed ([7]) that if point-like partonic scattering was occurring in this limit, then scaling functions  $F_1(x)$  and  $F_2(x)$  could be defined that depend only on the ratio  $x = \frac{Q^2}{2M_p\nu}$  using the identifications:

$$M_p W_1(\nu, Q^2) \rightarrow F_1(x) \quad (2.7)$$

$$\nu W_2(\nu, Q^2) \rightarrow F_2(x) \quad (2.8)$$

In this limit, the information about the proton structure, which had been contained in  $W_1$  and  $W_2$ , is now contained in the scaling functions  $F_1(x)$  and  $F_2(x)$ . In terms of these Bjorken scaling functions it can be shown that the Lorentz invariant double differential cross section for inelastic scattering via an exchanged virtual photon is:

$$\frac{d^2\sigma^{e^-+p \rightarrow e^-+X}}{dx dQ^2} = \frac{4\pi\alpha_{EM}^2}{Q^4} [(1-y - \frac{M_p^2 y^2}{Q^2}) \frac{F_2(x, Q^2)}{x} + y^2 F_1(x, Q^2)] \quad (2.9)$$

Early experimental evidence, as shown in Figure 2.3, suggested that Bjorken scaling holds. If the proton is a composite object of point-like particles, partons, then momentum probability distributions,  $f_i(x)$ , can be defined that represent the probability for a parton  $i$  to carry a momentum fraction  $x$  of the proton's total momentum.

## 2.3 Quark Parton Model

The Quark Parton Model (QPM), as introduced by Richard Feynman in 1972 ([10],[11]) naturally follows once Bjorken scaling is established. This model studies the proton in the so-called “infinite momentum frame” in which the proton momentum is chosen to be very large. In this frame the proton structure can be approximated as follows:

- The proton constituents, partons, have momentum parallel to its parent proton. Transverse momentum components are negligible.
- An incoming photon interacts instantaneously with a parton due to time dilation within the proton.  
As a result, the struck parton may be approximated as free and non-interacting.
- Each constituent has charge  $e_i$  and its momentum distribution is described by the momentum probability distribution  $f_i(x)$ .

In the QPM, Bjorken's scaling variable  $x$ , a quantity experimentally derived solely from the kinematics of the initial and final state electron momentum, can be identified with the fraction of the proton momentum carried by the parton itself. In this way the kinematics of the electron, the parton, and the exchange photon are linked. In the QPM it can be shown that the structure function  $F_2(x)$  is directly related to the parton momentum distribution functions via:

$$F_2(x) = \sum_{i=partons} e_i^2 x f_i(x) \quad (2.10)$$

where  $e_i$  is the charge of each parton. In this model the Callan-Gross relationship between the structure functions can be shown to hold, as expected for spin  $\frac{1}{2}$  constituents:

$$2xF_1(x) = F_2(x) \quad (2.11)$$

Therefore a measurement of the cross section in Eq. 2.9 makes it possible to determine information with regards to parton distribution functions. The QPM solidifies the connection between  $F_1(x)$ ,  $F_2(x)$ , and  $f_i(x)$  and experimentally, the Callan-Gross relationship has been found to hold. Comparing the cross section for  $e + \mu \rightarrow e + \mu$  with Eq. 2.5 shows that the spin  $\frac{1}{2}$  structure functions are constant, consistent with the picture that is emerging. More discussion of this can be found in [25]. It is well established that the partons in this model are to be identified with the quarks and gluons of QCD. Gluons have spin 1, but their interaction with quarks (and each other) is what causes the scaling violations that are observed. If gluons did not interact with quarks, scaling would be preserved and gluons could not be even indirectly observed in DIS. (Of course, if gluons were not present there would be no protons to begin with.)

## 2.4 Evolution of PDF's

Bjorken scaling holds true only for a limited kinematic range in  $x$  and  $Q^2$ . Later measurements over a wider kinematic range reveal a departure from the scaling behavior found in the early experiments at SLAC. The most recent data from the HERA accelerator at DESY in Hamburg are shown in Figure 2.4a ([14], [15], [16], [17]). This shows the same dependence of  $F_2$  on  $Q^2$  as Figure 2.3, but over a wider range of  $x$  now. In this case, for large  $x$ ,  $F_2(Q^2)$  has a small negative slope while for small  $x$ , it has a positive slope. This scaling violation arises from the fact that partons in fact are spin  $\frac{1}{2}$  quarks that radiate gluons to interact with other quarks inside the proton. These gluons can also split into  $q\bar{q}$  pairs. Both the radiated gluon in the first case and the  $q\bar{q}$  pair in the second have lower momentum than the initial parton. As a result, when probing the proton with an increased  $Q^2$ , and increased spatial resolution, what appears to be a bare quark or gluon can start to be resolved as a cloud of lower momentum quarks and gluons. The probabilities for a gluon to split into a quark-anti-quark pair and the probability for a quark to radiate a gluon are described quantitatively by splitting functions  $P_{ij}(\frac{y}{x})$ . Splitting functions give the probability that a parton  $j$  with momentum  $y$  results from a radiative event of its parent parton  $i$  with momentum  $x$ . The splitting functions can be calculated with perturbative techniques in QCD. ([20], [21], [22], [23],[24]). Because a parton at high Bjorken- $x$  can split into partons of lower Bjorken- $x$ , we should find higher parton densities as we look further down in  $x$ . Note that to explain these scaling violations we have to invoke vertices that

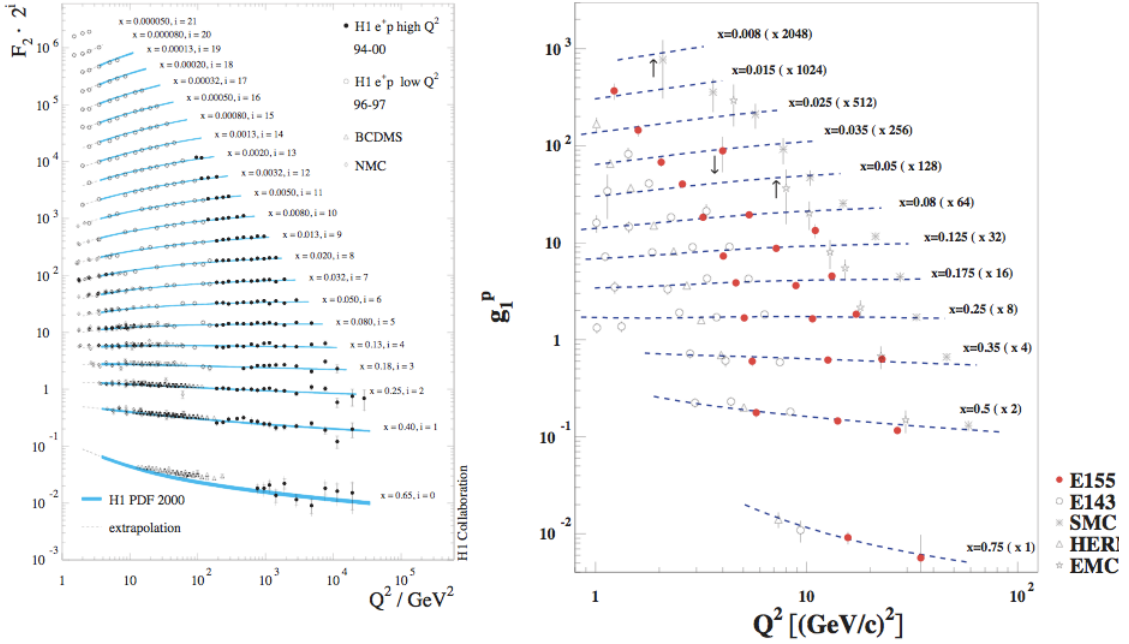


Figure 2.4: Left (a): Data from a variety of experiments showing that scaling violations in the structure function  $F_2(x, Q^2)$  are observed due to the  $Q^2$  dependence. This scaling violation can be used to determine the gluon momentum distribution  $G(x)$ . Right (b): Data showing the spin dependent structure function  $g_1^p(x, Q^2)$ . This allows access to the spin dependent quark distribution functions. And, due to the scaling violation observed in  $g_1^p$ , the spin dependent gluon momentum distribution,  $\Delta G$ , can be constrained. ([14], [15], [16], [17], [18], [19])

explicitly require the QCD Lagrangian and so we must regard scaling as a “quark and gluon” property, not a “parton” property. Detailed calculations show that the scaling violation of structure functions and distribution functions is in fact a dependence of these on  $\log Q^2$  as described analytically by the DGLAP (Dokshitzer,Gribov,Lipatov,Altarelli,Parisi) evolution equations ([20], [21], [22]):

$$\frac{d}{d \log Q^2} q(x, Q^2) = \frac{\alpha_S}{2\pi} \int_x^1 \frac{dy}{y} \left( q(y, Q^2) P_{qq} \left( \frac{x}{y} \right) + g(y, Q^2) P_{qg} \left( \frac{x}{y} \right) \right) \quad (2.12)$$

$$\frac{d}{d \log Q^2} g(x, Q^2) = \frac{\alpha_S}{2\pi} \int_x^1 \frac{dy}{y} \left( \sum_i q_i(y, Q^2) P_{gq} \left( \frac{x}{y} \right) + g(y, Q^2) P_{gg} \left( \frac{x}{y} \right) \right) \quad (2.13)$$

The ability to describe the  $Q^2$  dependence of the structure functions and distribution functions from first principles is of great importance for the extraction of quark and gluon distributions from data taken in experiments at different  $Q^2$ . The DGLAP equations make it possible to evolve cross sections, for example,

calculated from a set of quark and gluon distributions specified at a certain  $Q^2$  to a new scale  $Q'^2$  and to compare the calculation results to experimental cross section data taken at  $Q'^2$ . This technique is used in so-called global QCD analyses of DIS data sets that allow one to determine the best possible parametrization of quark and gluon distributions from the sum of all available data sets. The technique can be extended to include data sets from DIS, semi-inclusive DIS and  $p - p$  scattering. A very interesting example of this, from the MSTW collaboration <sup>1</sup>, is shown in Figure 2.5 ([13]). The quark and gluon PDF's are shown at two very different energy scales,  $Q^2 = 10 \text{ GeV}^2$  and  $Q^2 = 10^4 \text{ GeV}^2$ . In the latter case the density of each constituent is much larger at low- $x$ , especially so for the gluons. But if one looks only in the “valence” region, roughly  $x > 0.1$ , the view of the proton is less different between the two scales than in the “sea” region. Instead of

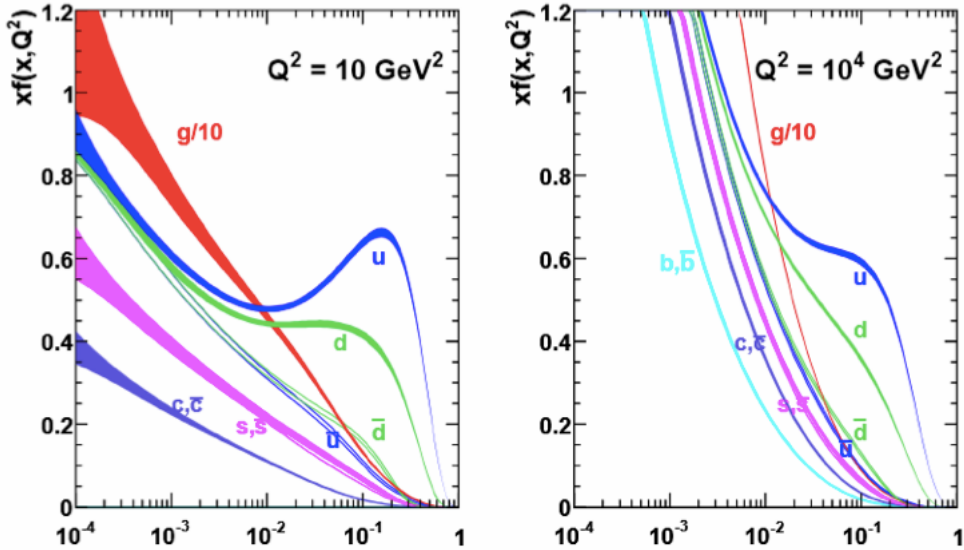


Figure 2.5: Result from the MSTW collaboration from 2008 showing the evolution of parton distribution functions between  $Q^2 = 10 \text{ GeV}^2$  (left) and  $Q^2 = 10^4 \text{ GeV}^2$  (right). ([13])

plotting  $f(x, Q^2)$  vs.  $x$ ,  $xf(x, Q^2)$  vs.  $\log x$  is plotted. This has the obvious advantage of making it easier to see what is going on in the deep sea region. At the same time it also preserves the integral of the PDF when integrating over some  $x$  range:  $\int_a^b f(x, Q^2) dx = \int_{\log a}^{\log b} xf(x, Q^2) d \log x$ .

## 2.5 Polarized Parton Distribution Functions

So far in the DIS framework we have considered unpolarized PDF's. A very large amount of knowledge has been generated on these functions over the last 40 years and the resulting precise knowledge of the unpolarized PDF's has wide ranging applications in the fields of nuclear and high energy physics. This

---

<sup>1</sup>Martin, Stirling, Thorne, Watt

includes the precise calculations of  $W$ ,  $Z$  and Higgs cross sections in  $pp$  collisions at the LHC as well has the calculation of  $pp$  reference cross sections for various final state particles for the interpretation of final states in heavy ion collisions at RHIC and at the LHC. To understand the spin structure of the proton, the polarized PDF's must also be understood. To account for polarization, we use the momentum axis (nominally the  $z$ , or beam axis) as the quantization axis, and assign every parton either a positive helicity, denoted by a  $(+)$ , or a negative helicity, denoted by a  $(-)$ . Therefore we make the definitions:

$$f_i(x) \equiv f_i^+(x) + f_i^-(x) \quad (2.14)$$

$$\Delta f_i(x) \equiv f_i^+(x) - f_i^-(x) \quad (2.15)$$

where  $\Delta f_i(x)$  is the longitudinally polarized PDF. Using the relations from Eq. 2.10 and Eq. 2.11, we have  $F_1(x) = \frac{1}{2} \sum_i e_i^2 f_i(x)$  where the summation is over quarks, antiquarks and gluons. Analogous to  $F_1(x)$ , the unpolarized structure function, the polarized structure function for the proton is defined as:

$$g_1(x) = \frac{1}{2} \sum_i e_i^2 \Delta f_i(x) \quad (2.16)$$

where the  $Q^2$  dependence from scaling violation is not shown explicitly. When averaging over spin states for beam and target for the unpolarized cross section, the symmetric components of the cross section are projected out.  $F_1$  and  $F_2$  parameterize this. If instead, the difference of the cross sections for different relative spin states between beam and target are taken then the symmetric components cancel and the antisymmetric components are projected out. In this case, the difference in cross sections is parameterized through the spin dependent structure functions  $g_1$  and  $g_2$  (Ref. [25]). From [26] it is found that

$$\frac{d^2\sigma^{\uparrow\downarrow}}{dx dQ^2} - \frac{d^2\sigma^{\uparrow\uparrow}}{dx dQ^2} = a g_1(x, Q^2) + b g_2(x, Q^2) \quad (2.17)$$

where  $a$  and  $b$  result from the kinematics of the electron vertex.  $g_2$ , unlike  $g_1$ , does not have a clear partonic interpretation. Experimentally in DIS, the virtual photon asymmetry,  $A_1$ , is obtained from the cross section difference:

$$A_1 = \frac{\sigma_{1/2} - \sigma_{3/2}}{\sigma_{1/2} + \sigma_{3/2}} \quad (2.18)$$

where  $\sigma_{1/2}$  is the  $ep$  cross section when the photon-proton total angular momentum is  $J_z = \frac{1}{2}$ .  $\sigma_{3/2}$  is for the case that the photon-proton angular total angular momentum is  $J_z = \frac{3}{2}$ . Since the polarization of the electron is experimentally controlled, the polarization of the photon is determined by angular momentum

conservation since we can only have  $e_{1/2} \rightarrow e_{-1/2} + \gamma_1$  or  $e_{-1/2} \rightarrow e_{1/2} + \gamma_{-1}$  where the subscript indicates the  $J_z$  quantum number of the electron and photon. In the parton model, it is found that  $A_1$  and  $g_1$  are related simply by:

$$A_1(x, Q^2) = \frac{g_1(x, Q^2)}{F_1(x, Q^2)} \quad (2.19)$$

Figure 2.4b shows data taken from several experiments to measure  $g_1$  and, similar to  $F_2$ , scaling behavior is observed up to a logarithmic dependence on the scale  $Q^2$ . One departs from the measurement of inclusive cross sections to the measurement of semi-inclusive cross sections where, in addition to detecting the scattered final state electron, a final state hadron is also detected. The detection of the hadron in Semi-Inclusive DIS (SIDIS) gives additional sensitivity for understanding and separating the flavor dependence of the quark polarizations. This allows the individual quark and antiquark spin-dependent distributions,  $\Delta q(x)$  and  $\Delta \bar{q}(x)$  of the proton to be constrained.

In the preceding discussion it was shown how DIS and SIDIS map out the momentum and spin structure of the partons inside the proton that carry electrical charge, namely the quark momentum distributions  $q(x)$  and spin distributions  $\Delta q(x)$ . Unfortunately, DIS and SIDIS processes cannot probe directly the corresponding gluon distributions functions  $g(x)$  and  $\Delta g(x)$ . Some sensitivity for the gluon distributions does, however, remain through the logarithmic  $Q^2$  dependence of the measured quark distributions. The precise data in the spin averaged case are used to determine  $g(x)$  from the scaling violation present in the data for  $F_2$  using the DGLAP equations (Eq. 2.12 and 2.13). The situation is different for the spin-dependent case. Compared to the  $F_2$  data, the  $g_1$  data, shown in Figure 2.4b, are sparse and cover a significantly smaller range in  $Q^2$ . As a result no strong constraint of  $\Delta g(x)$  has been obtained from the DIS and SIDIS data. Nevertheless, a number of global analyses have been performed on the polarized DIS data (AAC[35], BB[36], GRSV[37]). Figure 2.6 from the AAC03 extraction of  $\Delta G$  at  $Q^2 = 1\text{GeV}^2$  gives  $\Delta G = 0.499 \pm 1.266$ .

It has been shown that DIS and SIDIS data can constrain the spin-dependent quark structure of the proton. However, it also has been shown that the limited kinematic range over which  $g_1$  has been measured is the limiting factor in our ability to determine  $\Delta g(x)$  based on its scale dependence. A high energy and high luminosity electron-ion collider (EIC) is currently being proposed to extend the kinematic reach of  $g_1$  beyond that of the existing world data on polarized  $ep$  scattering. In Figure 2.7 we show the projected kinematic reach of an EIC (Ref. [39]) compared with the kinematics that have been sampled to date. In the current era, before such an EIC is constructed and operational, one is motivated to consider polarized proton-proton collisions as a probe for gluon spin distributions in the proton.

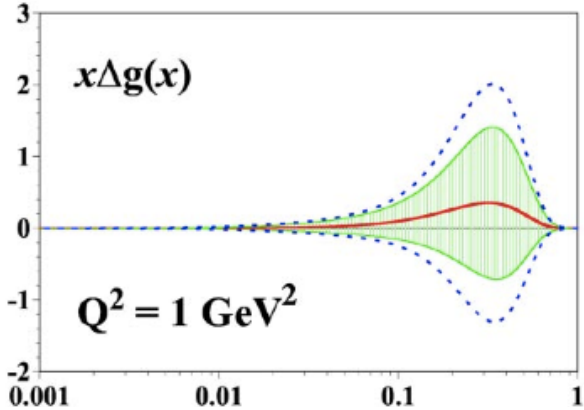


Figure 2.6: The  $\Delta G$  extraction from the AAC collaboration based on polarized DIS data. (Ref. [35])

## 2.6 The Spin Puzzle

One of the surprising and unexpected properties of the proton, and there are many, is that the gluons carry about half of the proton's total momentum, despite the proton being nominally comprised of only three valence quarks according to the QPM. In models that include gluons and quark-gluon interactions this is less surprising but is still a strong hint that there are intricate dynamics within the proton. Similarly, it was assumed these valence quarks would account for most, if not all, of the proton's total spin, depending on which model one chose to believe. R. Jaffe wrote an interesting summary (Ref. [27]) of the rich history, both technically and sociologically, that went into this assumption and its eventual demise.

The Proton Helicity Sum Rule reads:

$$\frac{1}{2} = \frac{1}{2} \Delta\Sigma(Q^2) + \Delta G(Q^2) + L_{q,g}(Q^2) \quad (2.20)$$

where, ignoring the  $Q^2$  dependence,

$$\Delta\Sigma = \int_0^1 \Delta u(x) + \Delta \bar{u}(x) + \Delta d(x) + \Delta \bar{d}(x) + \Delta s(x) + \Delta \bar{s}(x) dx \quad (2.21)$$

$$\Delta G = \int_0^1 \Delta g(x) dx \quad (2.22)$$

$\Delta\Sigma$  is the overall polarization from quarks of all flavors and momentum fractions and therefore represents the total quark contribution to the proton spin.  $\Delta g(x)$  is the gluon polarization as a function of  $x$ , and

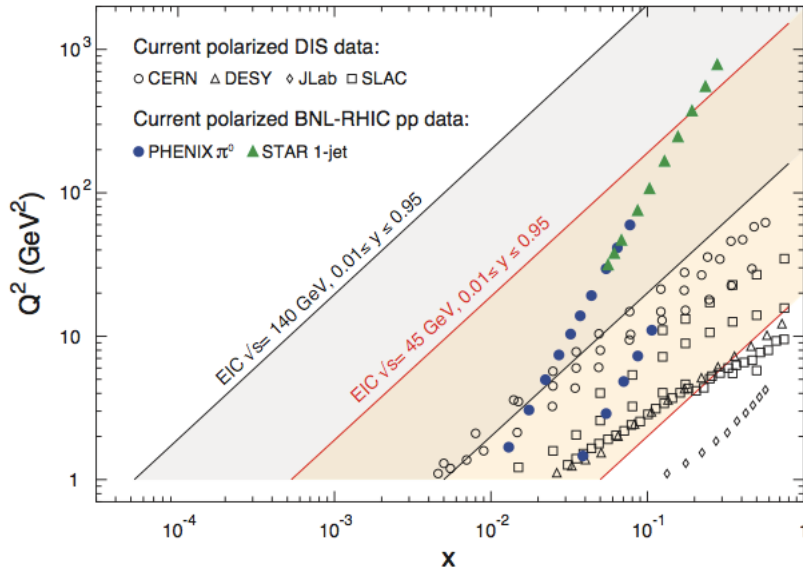


Figure 2.7: A comparison of the projected kinematic reach of an EIC operating at  $\sqrt{s} = 45 \text{ GeV}$  and  $\sqrt{s} = 140 \text{ GeV}$  with the existing polarized DIS and  $pp$  data. (Ref. [39])

its integral,  $\Delta G$ , is the total gluon contribution to the proton spin. In addition to their spin contributions, quarks and gluons can also contribute with orbital angular momentum (OAM),  $L_{q,g}$ , to the proton spin. There are few constraints on the value of  $L_{q,g}$  as of 2013. For a discussion of the description of OAM in QCD and, in particular, the choice of related operators see the work by Jaffe-Manohar in Ref. [28], and by Ji in Ref. [29]. Additionally, a summary of different model calculations is given in Ref. [30]. Experimental methods to measure OAM are also developing.

Measurements in the early 1980's (E80, [32],[33] and E130, [34]) at the Stanford Linear Accelerator (SLAC), using electron beams, determined  $\Delta\Sigma$  from measurements of  $A_1(x)$  for large  $x$ ,  $x > 0.1$ . The measured  $A_1(x)$  was extrapolated to zero based on a fit to the data. From this, a total quark spin contribution of  $\Delta\Sigma \approx 0.6$  was found, in agreement with expectations from relativistic quark models. The first measurement of  $\Delta\Sigma$  including low- $x$  ( $x < 0.1$ ) data was published by the European Muon Collaboration (EMC) in 1989 ([38]). The EMC data are shown in Figure 2.8 along with the Quark-Parton Model prediction of  $A_1(x)$  ([40],[41],[42]). The EMC and SLAC measurements of  $A_1$  for the proton agree well with each other in their region of overlap,  $x > 0.1$ . However, the EMC data at  $x < 0.1$  fall systematically below the extrapolation from the SLAC  $A_1(x)$  data. This resulted in a violation of the Ellis-Jaffe Sum Rule ([43]) and implied a

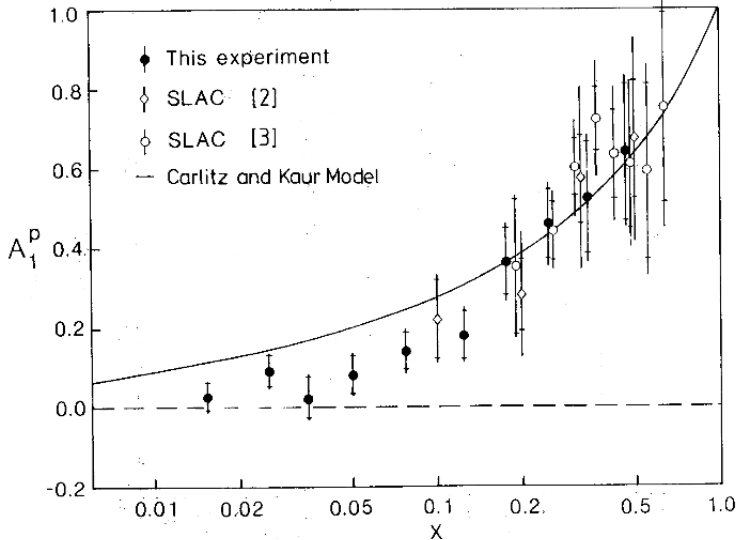


Figure 2.8:  $A_1$  measurements for polarized electron and muon scattering off proton targets. Data shown comes from SLAC and EMC. The EMC had some overlap in  $x$  with SLAC, and also extended to smaller  $x$  where a clear disagreement with the model extrapolation can be seen. This is the origin of the spin crisis.

deficit of quark spin in the sea region. The original estimate from the EMC was ([38]):

$$\Delta\Sigma = 0.098 \pm 0.076(\text{stat.}) \pm 0.113(\text{syst.}) \quad (2.23)$$

In other words, the quark polarization within the proton was consistent with zero, though with large uncertainties. This apparent shortfall of the quark contribution to the proton spin was coined the "Spin Crisis" by Elliott Leader and Mauro Anselmino in 1988. The spin crisis triggered further measurements at SLAC, CERN and DESY and extensive theoretical studies. A more modern constraint from the HERMES experiment ([31]) gives a result of:

$$\Delta\Sigma = 0.330 \pm 0.011(\text{theo.}) \pm 0.025(\text{exp.}) \pm 0.028(\text{evol.}) \quad (2.24)$$

The total uncertainty on this measurement is less than 5% of the proton spin, significantly smaller than the original EMC uncertainties. It has therefore been firmly established that  $\approx 67\%$  of the proton spin must originate from gluon spin or orbital angular momentum contributions. It is natural to search for gluon spin contributions first by measuring  $\Delta G$  and this is the second motivation to study the gluon polarization via hadron-hadron collisions.

## 2.7 The Gluon Contribution to the Proton Spin

At this point, although the quark polarization falls short of naïve expectations, it is clear that quarks and gluons are the constituents of the proton. The interpretations of  $f_i(x)$  and  $\Delta f_i(x)$  are well understood:  $f_i(x)$  is the probability distribution for parton  $i$  to be found with momentum fraction  $x$ , while  $\Delta f_i(x)$  is the difference in probability distributions for parton  $i$  to have a spin aligned versus anti-aligned with its parent proton's momentum. The unpolarized and polarized PDF's are non-perturbative. They describe long distance correlations at a low energy scale in the nucleon target where perturbative QCD cannot be applied. However, they are universal functions, so once they are measured in lepton-proton experiments, they can be used to predict observables for proton-proton experiments at high momentum transfer using perturbative techniques.

We also introduce another universal function, the fragmentation function (FF)  $D_f^h(z)$ . This is the probability for a parton  $f$ , that is struck in a high energy collision, to fragment into an observed final state hadron  $h$  having momentum fraction  $z$  of its parent parton ([4]). The PDF's represent the state of the proton prior to collision and are independent of the choice of probe. Likewise, the fragmentation functions empirically describe how quarks and gluons carrying a QCD color charge emerge at long distances as color neutral hadrons. How the final state quark or gluon was created is of no concern for  $D_f^h$  which makes it also a universal property.

Before PDFs and FFs can be used to calculate hard scattering cross sections for various collision systems it is necessary to describe the partonic scattering process that translates the initial state partons, described by their respective PDFs, into the final state quarks and partons whose fragmentation into final state hadrons is governed by the FFs. The cross section for the parton-parton scattering processes  $\hat{\sigma}^{f_a f_b \rightarrow f_c f_d}$  are analytically calculable from first principles using perturbative QCD and are typically calculated to Next-to-Leading Order (NLO). This procedure of breaking the proton-proton scattering process into three separate components is called factorization and is illustrated in Figure 2.9. This validity procedure has been demonstrated to work in the hard scattering limit. Using factorization, the cross section for  $pp \rightarrow h + X$  reads:

$$\sigma^{pp \rightarrow h + X} = \sum_{f_1, f_2, f} \int_0^1 \int_0^1 \int_0^1 dx_1 dx_2 dz f_1(x_1, \mu^2, Q^2) f_2(x_2, \mu^2, Q^2) \hat{\sigma}^{f_1 f_2 \rightarrow f X'}(x_1 p_1, x_2 p_2, p_h/z, \mu^2) D_f^h(z, Q^2) \quad (2.25)$$

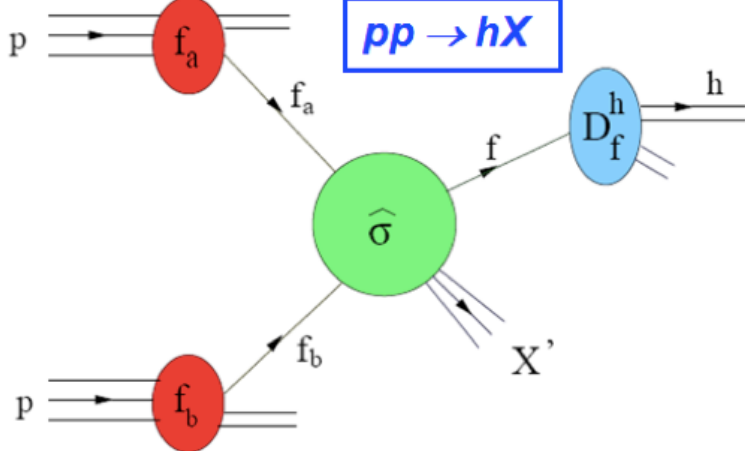


Figure 2.9:  $p + p \rightarrow h + X$  scattering can be factorized into a partonic initial state (the PDF's), a partonic interaction with cross section  $\hat{\sigma}$  and (if the final state contains a hadron) a fragmentation function.

Using factorization requires significant theoretical care to understand the uncertainties associated with the choice of  $\mu$ , the factorization scale<sup>2</sup> ([12]). Also, a consistent treatment at NLO not only requires NLO partonic cross sections but also appropriate scale evolution in  $Q^2$  of the PDF's ([44]) since precise control of  $Q^2$  is no longer possible. Eq. 2.25 is often written more concisely as:

$$\sigma^{pp \rightarrow h+X} = f_1 \otimes f_2 \otimes \hat{\sigma}^{f_1 f_2 \rightarrow f X'} \otimes D_f^h \quad (2.26)$$

The cross section can be divided into a cross section for same sign helicity protons, denoted  $(++)$  and opposite sign helicity protons, denoted  $(+-)$ :

$$\sigma = \sigma^{++} + \sigma^{+-} \quad (2.27)$$

Similarly, the difference in cross sections between these two spin configurations is defined as:

$$d\sigma \equiv \sigma^{++} - \sigma^{+-} \quad (2.28)$$

---

<sup>2</sup> This is a momentum transfer chosen in the calculation to separate "hard" processes that are treated perturbatively and "soft" processes that are parametrized by the PDFs. At sufficiently high  $Q^2$ , the cross section should become independent of the choice of  $\mu^2$  and factorization should work perfectly.

The polarized version of Eq. 2.25 can be written

$$d\sigma^{pp \rightarrow h+X} = \sum_{f_1, f_2, f} \int_0^1 \int_0^1 \int_0^1 dx_1 dx_2 dz \Delta f_1(x_1, \mu^2, Q^2) \Delta f_2(x_2, \mu^2, Q^2) d\hat{\sigma}^{f_1 f_2 \rightarrow f X'}(x_1 p_1, x_2 p_2, p_h/z, \mu^2) D_f^h(z, Q^2) \quad (2.29)$$

Since the proton helicity can be controlled in polarized  $pp$  collisions at RHIC, the double longitudinal helicity asymmetry is defined as:

$$A_{LL} \equiv \frac{d\sigma}{\sigma} = \frac{\sigma^{++} - \sigma^{+-}}{\sigma^{++} + \sigma^{+-}} \quad (2.30)$$

$A_{LL}$  can be measured experimentally for any observed final state. Depending on this state, information about different PDFs can be learned. For instance, if a  $\pi^+$  is observed in the final state, then sensitivity is much more significant to  $\Delta u$  than  $\Delta d$  since  $D_u^{\pi^+} > D_d^{\pi^+}$ . As another example, heavy mesons containing a charm or bottom quark are the dominant source of final state single electrons, and such mesons are produced mainly in gluon-gluon fusion interactions. Thus, the single electron channel provides sensitivity to  $(\Delta G)^2$ . The most complete information on spin dependent quark and gluon distributions from polarized  $pp$  scattering can be gained by the combined analysis of double spin asymmetries for a broad range of final state particles. As we will show next, the measurement of final state particles at different scattering angles provides sensitivity to the  $x$ -dependence of PDFs.

## 2.8 Kinematic Definitions for Proton-Proton Interactions

At PHENIX, a cylindrical coordinate system is used with the  $z$ -axis chosen to coincide with the beam axis. The “blue” beam moves to the north in PHENIX, in the  $+z$  direction, while the “yellow” beam moves south in PHENIX, in the  $-z$  direction.  $\phi$  is the azimuthal coordinate with a range of  $[0, 2\pi]$ .  $\theta$  is the angle of inclination with respect to the beam and has the range  $-180^\circ < \theta < 180^\circ$ . The pseudo-rapidity,  $\eta$ , is typically used instead of  $\theta$ :

$$\eta = -\ln \tan \theta/2 \quad (2.31)$$

The rapidity of particle,  $y$ , with 4-momentum  $p = (E, \vec{p})$  is defined in terms of its kinematics:

$$y = \frac{1}{2} \ln \frac{E + p_z}{E - p_z} \quad (2.32)$$

In the relativistic limit  $E \gg m$ ,  $y \rightarrow \eta$ .  $\eta$  is a convenient variable to use because it is a Lorentz invariant of the scattering angle which is easy to measure experimentally. The transverse momentum is defined as

$p_T \equiv |p| \sin\theta$ . Note that the measure  $d p_T |d\eta|$  often used for differential cross sections is related to the energy and angle differential because  $d p_T |d\eta| = dE \sin\theta \frac{d\theta}{\sin\theta} = dE d\theta$  which differs from the  $dE d\Omega$  seen in Eq. 2.5 by a factor of  $\sin\theta$  (there is also  $d\phi$  but in longitudinal running there is no preferred angle, so azimuthal asymmetry holds and the integration over  $\phi$  is trivial.)

Viewing a  $pp$  interaction at the partonic level we have the reaction  $f_1 + f_2 \rightarrow f_3 + f_4$  where  $f_{1,2}$  are combinations of quarks and gluons and  $f_{3,4}$  are combinations of quarks, gluons, photons or leptons as allowed by QED and QCD. In the Breit or infinite momentum frames where the parton model holds, we can assume the parton momentum is parallel to its parent proton. Ignoring mass terms, the 4-momenta in the lab frame are  $p_1 = (x_1 E_p, 0, 0, x_1 E_p)$  and  $p_2 = (x_2 E_p, 0, 0, -x_2 E_p)$  where  $E_p$  is the proton energy and taken to be the same in both beams. The center of mass collision energy for the protons is  $\sqrt{s} = 2E_p$  while the partonic center of mass collision energy,  $\sqrt{\hat{s}}$ , can be shown to be:

$$\sqrt{\hat{s}} = \sqrt{x_1 x_2 s} \quad (2.33)$$

The underlying parton kinematics can be determined by measuring the  $p_T$  and  $y$  of the the outgoing jets created from the fragmentation of partons  $f_{3,4}$ :

$$x_1 = \frac{p_T}{\sqrt{s}} (e^{y_3} + e^{y_4}) \quad (2.34)$$

$$x_2 = \frac{p_T}{\sqrt{s}} (e^{-y_3} + e^{-y_4}) \quad (2.35)$$

Finally, in the case that  $y_3 \approx y_4$ , we find:

$$y \approx \frac{1}{2} \ln \frac{x_1}{x_2} \quad (2.36)$$

which shows that jets at mid-rapidity tend to be formed by partons of roughly equal momenta while forward(large)-rapidity jets tend to be formed by the interaction of two partons with greatly different momentum fractions.

## 2.9 Accessing $\Delta g(x)$

In DIS, the parton  $x$  and momentum transfer  $Q^2$  can be determined for each event from the measured lepton momentum and scattering angle. This allowed the global analyses to determine the PDFs and polarized

PDFs as a function of  $x$ . Using reconstructed jets in  $pp$  scattering, it would be possible to measure the  $x$ -dependence of  $\Delta g(x)$  in a similar way. However, due to the non-hermetic acceptance of PHENIX, jets are difficult to reconstruct. Instead, PHENIX measures cross sections and spin asymmetries for hadrons with high transverse momentum which carry only a fraction of the jet energy. This means applying Eqs. 2.34 and 2.35 does not yield a precise result about the underlying parton kinematics. These relationships are still very useful, however, as estimates for the underlying parton kinematics. Given an angle, a  $p_T$ , and a center-of-mass collision energy, an approximate range of  $x$  sensitivity can be found.

There is also a tradeoff that should be mentioned. In Eqs. 2.34 and 2.35, the assumption is that both jets are measured. At PHENIX this would be implemented by measuring two final state particles, with assurances they come from separate jets (ignoring details such as where one jet exactly ends and another begins). While this does constrain the partonic kinematics better, requiring a second particle to be measured comes at the heavy cost of statistics due to the very limited PHENIX acceptance. The statistics can be recovered by requiring just a single particle. This leaves one of the final state parton rapidities unconstrained. The conclusion is, therefore, that single particle measurements offer higher statistics at the expense of poor resolution for the kinematics of the underlying parton-parton reaction.

A number of results from PHENIX including Refs. [48], [49], [50], and [51] have been published by measuring one final state particle at mid-rapidity where  $|\eta| < 0.35$  and  $\sqrt{s} = 200$  GeV. The range of  $x$  that these measurements are sensitive to for different  $p_T$  bins is shown in Figure 2.10. These distributions come from NLO pQCD simulations at mid-rapidity ([122]). The typically quoted range of sensitivity is  $0.05 < x < 0.2$ . Therefore, to the extent that  $\Delta g(x)$  is accessed, only the truncated integral  $\int_{0.05}^{0.2} \Delta g(x) dx$  can be constrained. This can be confirmed very easily also using estimations from Eqs. 2.34 and 2.35 with  $\eta \sim 0$ . We find  $x_1 \sim x_2 \sim \frac{p_T}{50}$ , which for  $5 \text{ GeV} < p_T < 10 \text{ GeV}$ , gives a similar range.

While the rapidity of the measurement is now understood to have a large impact on what range of  $\Delta g(x)$  is sampled, it, along with the final state measured, also impacts what fraction of events come from quark-quark, quark-gluon, or gluon-gluon scattering. In Figure 2.11, the process fractions are shown for a reconstructed  $\pi^0$  at mid-rapidity as a function of  $p_{T,\pi^0}$ . Understanding this is important for two reasons. First, the process fractions determine which PDF's contribute to an observed  $A_{LL}$ . Second, each partonic scattering process has its own intrinsic asymmetry, called its analyzing power, which determines how much a given process can

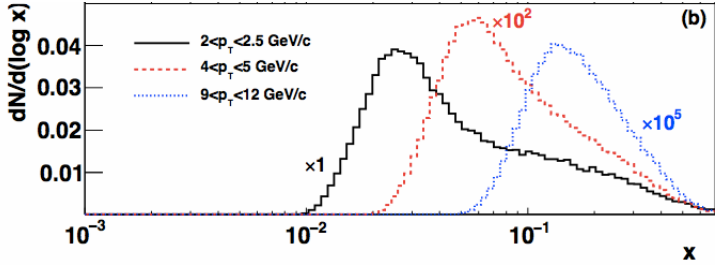


Figure 2.10: The distribution of parton  $x$  sampled for events in which a  $\pi^0$  at  $|\eta| < 0.35$  is found for the bins  $2 \text{ GeV} < p_T < 2.5 \text{ GeV}$ ,  $4 \text{ GeV} < p_T < 5 \text{ GeV}$ , and  $9 \text{ GeV} < p_T < 12 \text{ GeV}$ . As expected, higher  $p_T$  bins have higher mean  $x$ .

contribute to an observed asymmetry. The analyzing power is defined as:

$$\hat{a}_{LL} = \frac{\Delta\hat{\sigma}}{\hat{\sigma}}, \quad -1 \leq \hat{a}_{LL} \leq 1 \quad (2.37)$$

and is shown as a function of  $\theta$ , the scattering angle in the partonic center of mass frame, in Fig. 2.12. See Ref. [47] for further details. Inspired by Eqs. 2.25, 2.29 and 2.30 we can write down a heuristic proportionality to illustrate the relationship between the PDF's and  $A_{LL}$ :

$$A_{LL} \propto a \frac{\Delta q}{q} \frac{\Delta g}{g} \hat{a}_{LL}^{qq} + b \frac{\Delta g^2}{g^2} \hat{a}_{LL}^{gg} + c \frac{\Delta q^2}{q^2} \hat{a}_{LL}^{qg} \quad (2.38)$$

For mid-rapidity at low- $p_T$  the first two terms dominate while at high- $p_T$  the first and third terms dominate. Figure 2.13 shows the process fractions at forward rapidity,  $\eta = 3.3$ . At low  $p_T$   $qg$  processes are the majority of all processes and this fraction increases with  $p_T$ . This is why the measurement of  $A_{LL}$  at forward-rapidity constrains the sign of  $\Delta G$ . In Chapter 4 the  $x$ -sensitivity for forward hadron and di-hadron measurements will be shown.

## 2.10 Global Analysis Results for $\Delta G$

The most recent and complete global analysis for extracting the polarized PDFs from DIS, SIDIS and RHIC measurements has been carried out by De Florian, Sassot, Stratmann and Vogelsang (DSSV08) ([44],[45]). Recently, with the inclusion of a 2009 measurement of  $A_{LL}^{jet}$  from the STAR collaboration, the DSSV authors have provided an improved extraction of  $\Delta g(x)$ , DSSV++ ([53]), shown in Figure 2.14. Figure 2.14a shows the DSSV08  $\Delta G$  uncertainty band in yellow and the DSSV++ uncertainty band in red. The DSSV++

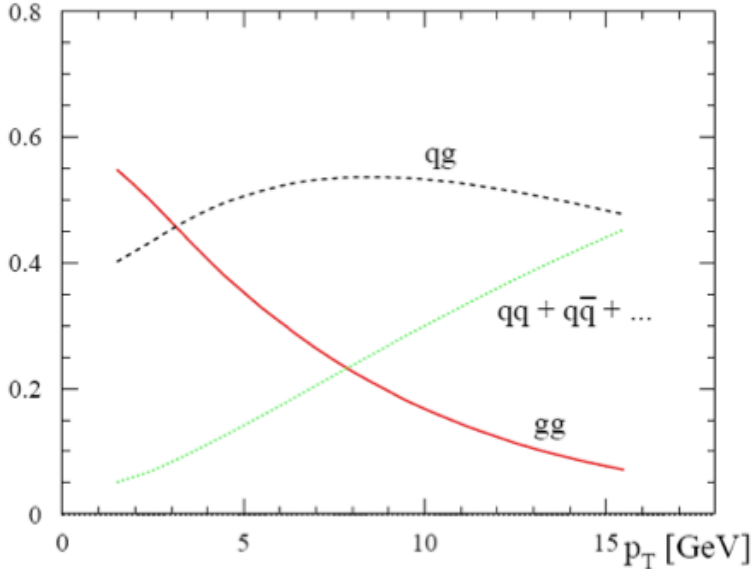


Figure 2.11: Underlying partonic process fractions for events in which a mid-rapidity  $\pi^0$  is produced vs.  $p_T$ .

analysis presently exists as a conference result but still awaits a complete treatment of all systematic errors and publication. As a consequence, the inclusion of the experimental systematic errors is not exactly correct. Nevertheless, it serves to underscore the point that recent experimental evidence has tended to favor scenarios where  $\Delta g(x)$  is modestly larger than previous analyses had found. The upward shift yields a new estimate for the truncated integral:

$$\int_{0.05}^{0.2} \Delta g(x, Q^2 = 10 \text{ GeV}^2) dx = 0.10^{+0.06}_{-0.07} \quad (2.39)$$

This estimate is based on the  $\chi^2$  profile for the value of the integral from the DSSV++ analysis shown in Figure 2.15. It is important that the  $Q^2$  be specified as  $\Delta G$  experiences scaling violations. To LO,  $\Delta G(Q^2) \propto \frac{1}{\alpha_s(Q^2)}$ . So with large uncertainty, based on  $\sqrt{s} = 200$  GeV data, the gluon polarization might account for around 20% of the proton's spin. The region  $x > 0.2$  is also well constrained both from data at 62.4 GeV data and also naturally because  $G(x)$  itself is very small when  $x > 0.2$ . Since  $|\Delta G(x)| < G(x)$ , these gluons cannot contribute very much spin. The major uncertainty in  $\Delta G$  therefore comes from low- $x$  where  $G(x)$  is very large and where, until recently, there has been no data. This is nicely illustrated by Figure 2.14b, which estimates the integral  $\int_{x_{min}}^1 \Delta g(x) dx$ . As expected, when  $x_{min} < 0.05$  the uncertainty grows rapidly.

Other collaborations of theorists have extracted polarized PDFs from polarized data as well. In particular, a fairly recent development using Neural Network techniques has emerged from the NNPDF collaboration

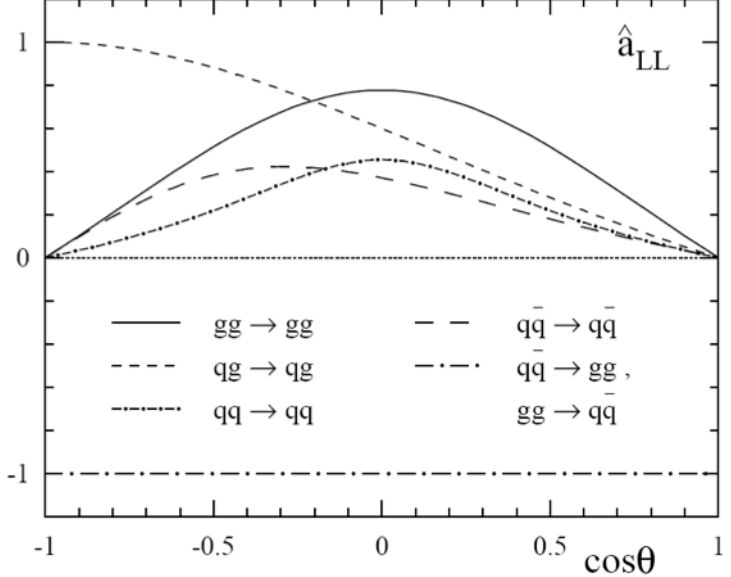


Figure 2.12: The differential analyzing power from each possible subprocess is shown as a function of scattering angle in the parton center of mass frame. (Ref [47])

(Ref.[52]). The results from their extraction are shown in Figure 2.16 and is compared with DSSV08. The neural network approach avoids the issue of unquantifiable systematic uncertainties arising from the use of specific functional forms for the different polarized PDFs in global analyses based on  $\chi^2$  minimization.

From Eq. 2.36 we see that a low- $x$  gluon interacting with a valence, or high- $x$ , quark will produce large rapidity jets, so a forward detector will be needed to reduce the large uncertainties in  $\Delta g(x)$  at small  $x$ . Before 2006-2007 when the Muon Piston Calorimeter (MPC) was installed, such a detector did not exist. The data sample collected with the MPC over the 2009, 2011, 2012 and 2013 runs will reduce the large uncertainties in  $\Delta g(x)$  at low- $x$ .

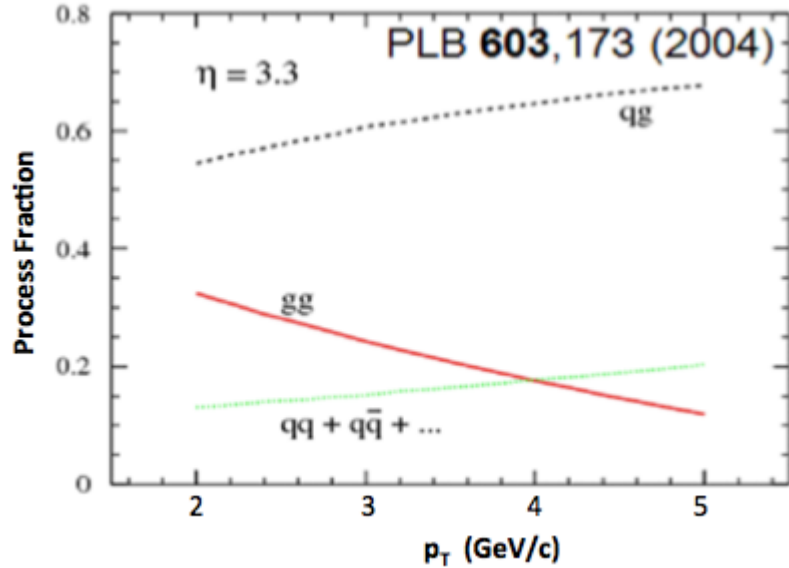


Figure 2.13: Process fractions for  $\eta = 3.3$  and  $p_T = 2 - 5 \text{ GeV}/c$ .

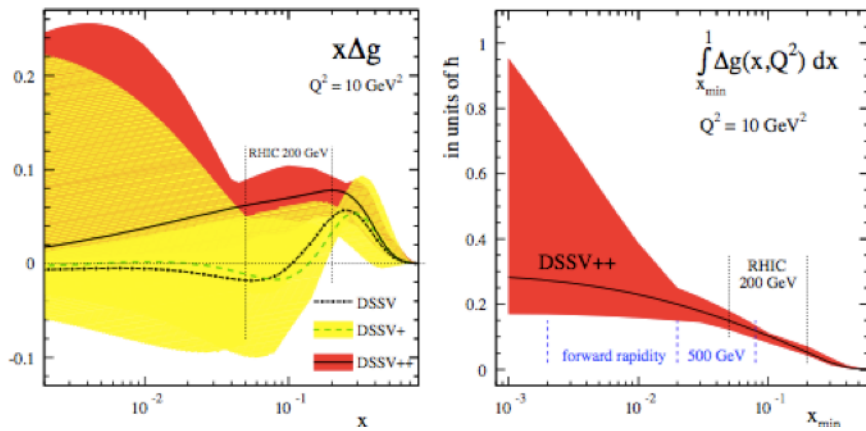


Figure 2.14: (Left)a The yellow band is the DSSV08 extraction for  $\Delta G$ . The red band is the extraction including RHIC measurements from 2009 data (DSSV++). A clear upward shift is seen between DSSV08 and DSSV++. (Right)b An estimate of  $\int_{x_{\min}}^1 \Delta g(x) dx$  is shown. (Ref [53])

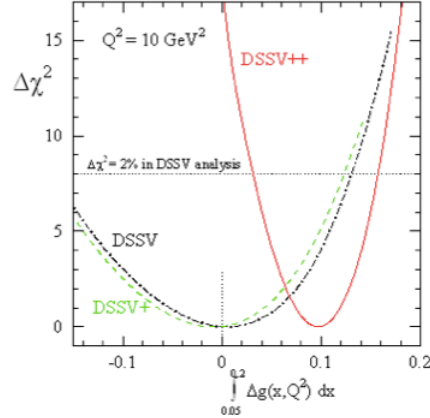


Figure 2.15: The  $\chi^2$  profile for the truncated integral corresponding to Figure 2.14 shows a minimum at 0.10. The asymmetric error bars reflect the fact that this profile is not exactly symmetric. The error bars are estimated by taking  $\Delta\chi^2 = 8$  on either side. This is just a reasonable approximation, there is nothing inherent in the DSSV++ procedure that fixes this.

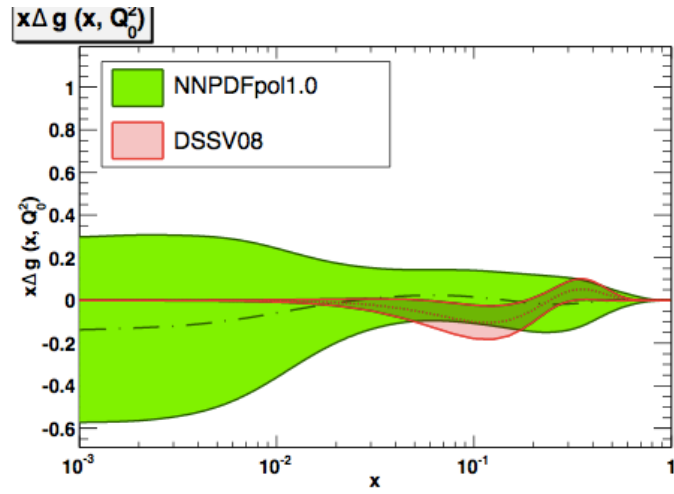


Figure 2.16: Neural Network extraction of  $\Delta G$  with uncertainty bands. A comparison with DSSV08 is also shown. (Ref.[52])

# Chapter 3

# Experimental Apparatus

The purpose of this chapter is to transition from the previous discussion on the theoretical and motivational aspects of measuring  $\Delta G$  to the experimental details of RHIC, the world's only polarized  $pp$  collider. We will briefly discuss the RHIC/AGS (Relativistic Heavy Ion Collider/Alternating Gradient Synchrotron) accelerator complex and the PHENIX (Pioneering High Energy Nuclear Interaction Experiment) detectors. However, each aspect will be discussed only to the extent that it is relevant for understanding the methods, reasoning and analysis contained in future chapters. The PHENIX apparatus is a  $\approx \$100M$  experiment and any attempt at a comprehensive description would lead us far astray and well beyond the scope of what is necessary to understand the subsequent chapters. References are, however, provided to the reader who becomes interested to learn more about a particular component of the PHENIX detector.

RHIC is a highly versatile collider and has demonstrated the ability to accelerate high current proton beams to energies of  $100\text{ GeV}$  and  $250\text{ GeV}$  with polarizations exceeding 50%. RHIC also has accelerated and stored a wide variety of heavy ion species to study the properties of the Quark-Gluon Plasma, a primordial form of quark gluon matter present in the first instants of the universe and possibly at the core of neutron stars.

## 3.1 Production, Acceleration, and Storage of Polarized Protons at RHIC

Figure 3.1 shows the general layout of the primary instrumentation used to produce, accelerate and store polarized protons within the RHIC/AGS complex. The source of polarized protons at RHIC is the Optically-Pumped Polarized H<sup>-</sup> Ion Source (OPPIS). It produces a maximum of  $40 \times 10^{11}$  polarized H<sup>-</sup> ions/pulse with a polarization of 85 – 90% and energy of  $35\text{ keV}$ . More information on OPPIS can be found in Refs. [9], [54], and [55]. From here, the pulse is directed into the Linear Accelerator (LINAC) where each proton is accelerated to  $200\text{ MeV}$ . At this stage the polarization remains near 85% and about  $5 \times 10^{11}$  protons remain in the pulse. The next stage is transfer to the Booster where the protons are accelerated up to  $2.3\text{ GeV}$ .

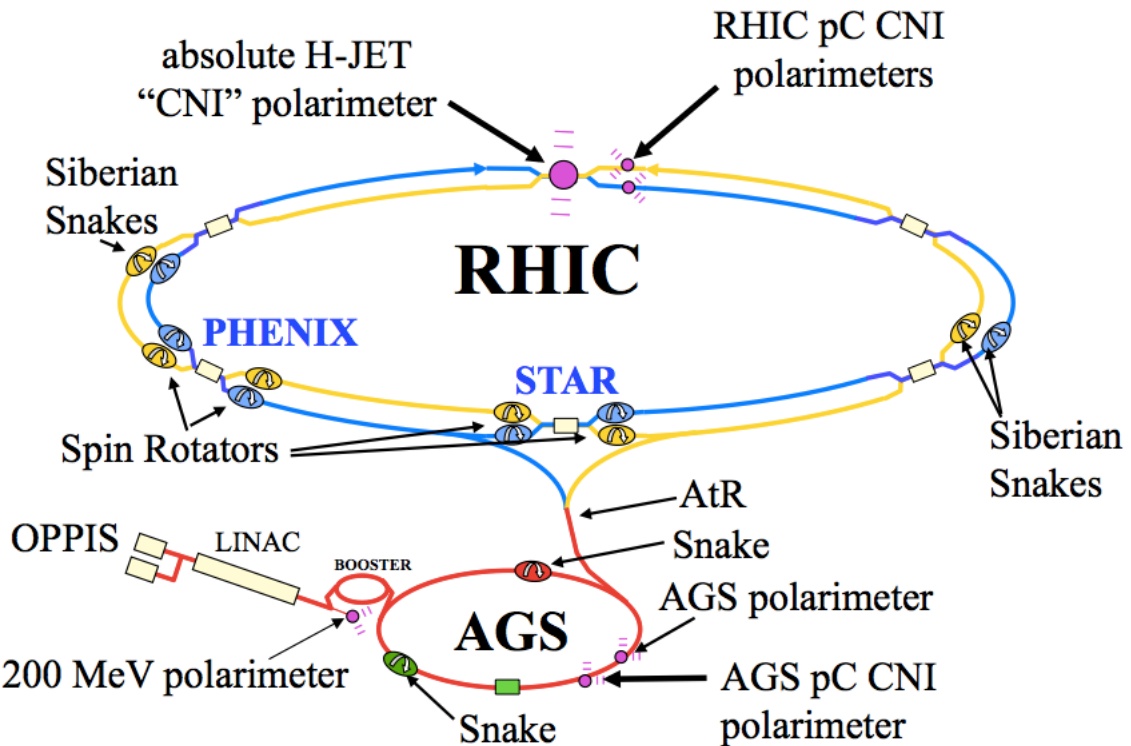


Figure 3.1: A diagram of the path of polarized protons from production to storage and maintenance in the RHIC ring is shown. Each of the components shown in this diagram is defined and its purpose stated within the text.

with an intensity drop to  $2 \times 10^{11}$  protons. The polarization is not affected at this stage. From here the protons are injected into the AGS where they are accelerated to  $24.3\text{ GeV}$ . The polarization by this point drops to 65 – 70% and the intensity is now  $1.5 – 1.7 \times 10^{11}$  protons. The AGS-to-RHIC (AtR) transfer line then injects these bunches into the blue and yellow rings. The LINAC, Booster and AGS systems are described further in Ref.[9]. A broad overview of the RHIC/AGS accelerator complex is also given in Ref. [56].

In addition to maximizing the delivered luminosity, a principle goal at the RHIC/AGS complex is to maximize the beam polarization. The natural direction of polarization is vertical, however, a number of effects tend to decrease the polarization over time. These effects are overcome by an ingenious invention called the Siberian Snake (Ref. [57]). Two sets of Siberian Snakes exist within RHIC and partial snakes are used in the AGS as well. Their function is to flip the proton spin by  $180^\circ$ . If a proton enters with polarization up it is flipped to down, and vice versa. This procedure greatly increases the stability of the beam polarization. To measure the polarization two polarimeters are used. The Hydrogen Jet Polarimeter ([58]) measures

the absolute scale of the polarization but requires long measurement intervals. The pC Polarimeter ([59]) provides a very fast measurement but is not calibrated to the absolute polarization scale. A final analysis which combines the data from both measurements is performed to produce final polarization values which can achieve 5% accuracy. The location of both of these polarimeters can be seen in Fig. 3.1. The last main aspect of the spin is the direction of the polarization. While the Siberian Snakes flip the spins between vertically up or down states, the proton spins need to be aligned (positive helicity) or anti-aligned (negative helicity) with the proton beam momentum for longitudinal running. This requires the use of Spin Rotators ([60]) placed locally on either side of each experimental hall. A proton bunch polarized vertically up is rotated to a positive helicity state before intersecting the other beam and is then rotated back to vertically up after intersecting with the other beam. It is possible for one experiment to turn their rotators on while the other leaves theirs off. This allows one experiment to take data for transverse physics interests while simultaneously the other experiment takes data for longitudinal spin physics interests.

The magnet system at RHIC/AGS is used to steer, focus, and dump the beam as necessary. A description of the magnet system is found in Refs. [61],[117]. Quadrupole magnets on either side of each experimental hall are used to focus the beams to a small transverse size to maximize the number of collisions. Typically, the transverse beam size at the nominal collision point is  $300\ \mu m - 400\ \mu m$ . The beam focusing creates an hourglass effect which helps to maximize the fraction of collisions that happen within some distance of the nominal interaction point, typically  $30\ cm$ . The longitudinal width of a beam bunch is typically  $\approx 50\ cm$ .

RHIC/AGS is a massively complex network of instrumentation. It requires a complex automated system to interface with all accelerator components needed for beam control and spin manipulation to keep the beam in a stable condition (Ref. [62]).

A number of other beam characteristics are constantly being monitored, such as its position and the bunch by bunch beam current. The latter will be relevant to the discussion in Chapter 8 when we are interested to understand the precise longitudinal structure of each bunch. More information can be found in Ref. [63].

## 3.2 Detector Overview

In Figure 3.2 a beam-line and side view of PHENIX are shown. Very generally, PHENIX can be divided into three sets of detectors: Central Arm Detectors which sit in the pseudo-rapidity range  $|\eta| < 0.35$ , Muon Arm

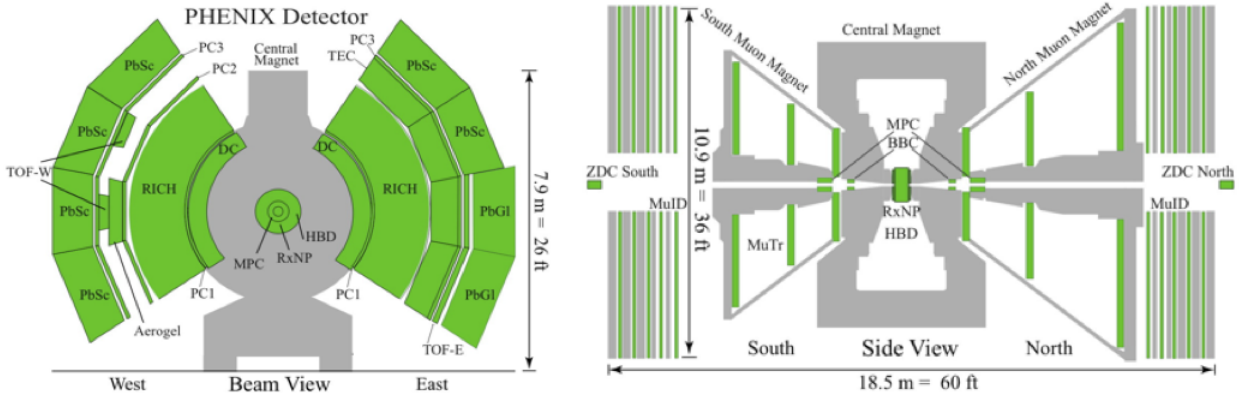


Figure 3.2: Left: Beam-line view of PHENIX showing a cross section of the central arm detectors. Right: A side view of PHENIX showing a cross section of the muon arm detectors.

Detectors which sit in the pseudo-rapidity range  $1.2 < |\eta| < 2.4$  and the Forward Detectors which sit in the pseudo-rapidity range  $|\eta| > 3.0$ . Ref. [64] provides a summary of many of these detectors. The central arm detectors can be more specifically divided into three classes: tracking ([65]), particle identification ([66]), and calorimetry ([67]). The muon arms focus on tracking the flight path of muons, with a recent upgrade to trigger on high momentum muons based on these tracks. ([68],[69]). The author contributed significantly to the construction of the Resistive Plate Chambers (RPCs) needed for this upgrade, transporting the metal detector casing for the RPCs between the University of Illinois at Urbana-Champaign and Brookhaven National Laboratory (BNL), and further assembly and testing at BNL. The central and muon arm detectors are not used for the data analysis in this thesis and will not be discussed further with the exception of the Forward Vertex Detector (Ref. [70]). This detector has proven its potential to act as a new luminosity monitor. For the data analysis in this thesis, the three main detectors we will utilize are the Beam Beam Counter (BBC), the Zero Degree Calorimeter (ZDC) and the Muon Piston Calorimeter (MPC). The BBC and ZDC are the two standard luminosity monitors and will be discussed now. The MPC will be discussed in the next chapter.

Locations within PHENIX are typically described by a cylindrical coordinate system  $(z, \theta, \phi)$ . The  $z$ -axis is chosen to coincide with the beam axis, with the north arm of PHENIX corresponding to  $z > 0$ . The point  $z = 0, \theta = 0$  is defined as the center of PHENIX and corresponds to the nominal interaction point. Here,  $\theta$  is the angle of inclination of a point with respect to the positive  $z$ -axis.  $\phi$  is the azimuthal angle. The pseudo-rapidity and  $\theta$  are related by  $\eta = -\ln \tan \frac{\theta}{2}$ .

### 3.3 Beam Beam Counter

The BBC is a two arm detector. The north and south arms are located at  $z = \pm 144\text{ cm}$ . Both arms of the detector have full azimuthal coverage in the pseudo-rapidity range  $3.1 < |\eta| < 3.9$ , corresponding to an inner radius of  $10\text{ cm}$  from the beam-line and an outer radius of  $30\text{ cm}$ . The BBC serves numerous functions. The subset of these functions that will be utilized here includes:

1. Vertex and  $t_0$  determination. The vertex gives the  $z$  coordinate of the collision vertex and  $t_0$  is the time of the collision, with respect to a predefined start time.
2. Luminosity monitor.
3. Minimum Bias trigger. It triggers on a sample of events with the only requirement that a coincidence hit in both arms of the detector is found.

Each arm is comprised of 64 quartz-based Cherenkov radiators with a transverse dimension of  $2.54\text{ cm}$  and a depth of  $3\text{ cm}$ . The Cherenkov light from each quartz radiator is collected by a mesh-dynode photomultiplier tube (PMT). The Cherenkov threshold in quartz is  $\beta_{ch} = 0.7$ . The most abundant charged hadrons are  $\pi^\pm$  and  $K^\pm$ . For these particles, this threshold corresponds to  $E_\pi > 195\text{ MeV}$  and  $E_K > 690\text{ MeV}$ . In Figure 3.3 a picture of the full assembly of one BBC channel is shown. The intrinsic timing resolution of a

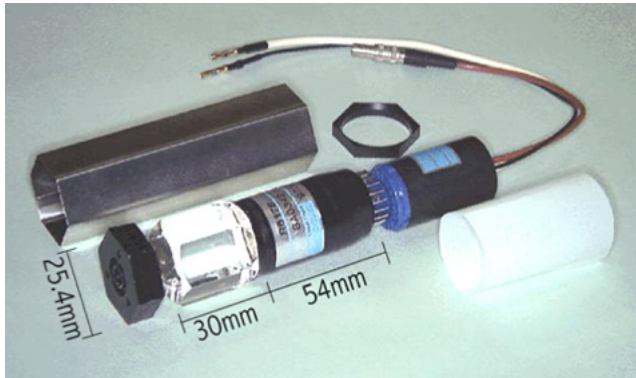


Figure 3.3: A BBC channel is shown. An incident charged particle enters from the left and, if above the Cherenkov threshold, radiates photons while traversing the quartz. These photons then interface to the photocathode of the PMT which converts the photons into electrons which the dynodes then amplify. On the right are the high voltage pins for each dynode as well as the signal readout.

single PMT is  $O(60\text{ ps})$ . In reality, it is slightly higher than this due to secondary hits. Figure 3.4 shows the full set of 64 channels assembled together. The timing resolution of an entire arm depends on the average occupancy. For heavy ion collisions, where the occupancy is very large, especially when the colliding ions

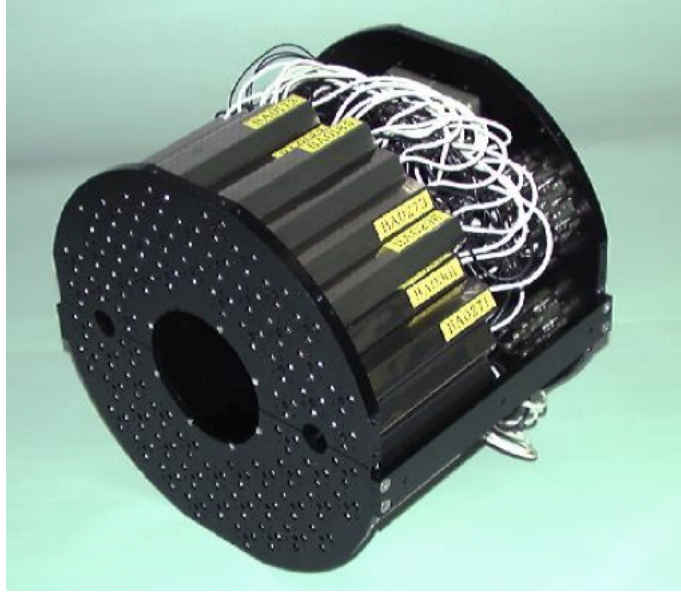


Figure 3.4: Full arrays of channels stacked together form the BBC north and south arms. Each quartz crystal and casing is hexagonally shaped which allows them to form a tessellation.

have a large spatial overlap, many PMT's are hit. The hit time is normally determined based on the average of all occupied channels and so will be more precise when the average is taken over many channels. For  $pp$  collisions the occupancy is much lower. The online trigger vertex resolution for the BBC (used for the trigger decision) is  $\sigma_{BBC,online} \approx 5\text{ cm}$ . The offline resolution (used in data analysis) has been recently found to be as good as  $\sigma_{BBC,offline} \approx 1\text{ cm}$ . This larger online resolution is partially due to the trigger calculation removing bits of information from the timing values. The signal from each PMT is digitized and stored in a buffer in the BBC Front End Module (FEM). The signal is digitized to both an ADC (Analog-to-Digital Conversion) and two TDC's (Time-to-Digital-Conversion). Each TDC has a dynamic range of about  $20\text{ ns}$ . A hit occurring after this will register as a TDC timeout and will not play a role in the time determination for that BBC arm or in the vertex determination. The ADC measurement is proportional to the PMT charge.

This completes the BBC “crash course”. The reader is referred to Ref. [71] for more details.

### 3.4 Zero Degree Calorimeter

While the BBC detects charged particles from inelastic  $pp$  collisions, the Zero Degree Calorimeter is designed to detect neutral particles, mainly neutrons and photons with very low transverse momenta, arising from

diffractive  $pp$  collisions.<sup>1</sup> The ZDC is also a two arm detector with a south arm and a north arm. The detector in each arm has transverse dimensions of about  $10\text{ cm} \times 15\text{ cm}$ . It is located  $18\text{ m}$  from the center of PHENIX. It therefore has an angular coverage of  $-2.8\text{ mrad} < \theta < 2.8\text{ mrad}$ . Identical detectors were created and used for each RHIC experiment to provide a common luminosity measurement based on the coincidence of the south and north arms for the Collider-Accelerator Department. Additionally, like the BBC, it can serve as a minimum bias trigger with low beam background and also serves a number of purposes that are not peripherally<sup>2</sup> related to this document. A diagram of the ZDC is shown in Figure 3.5 .

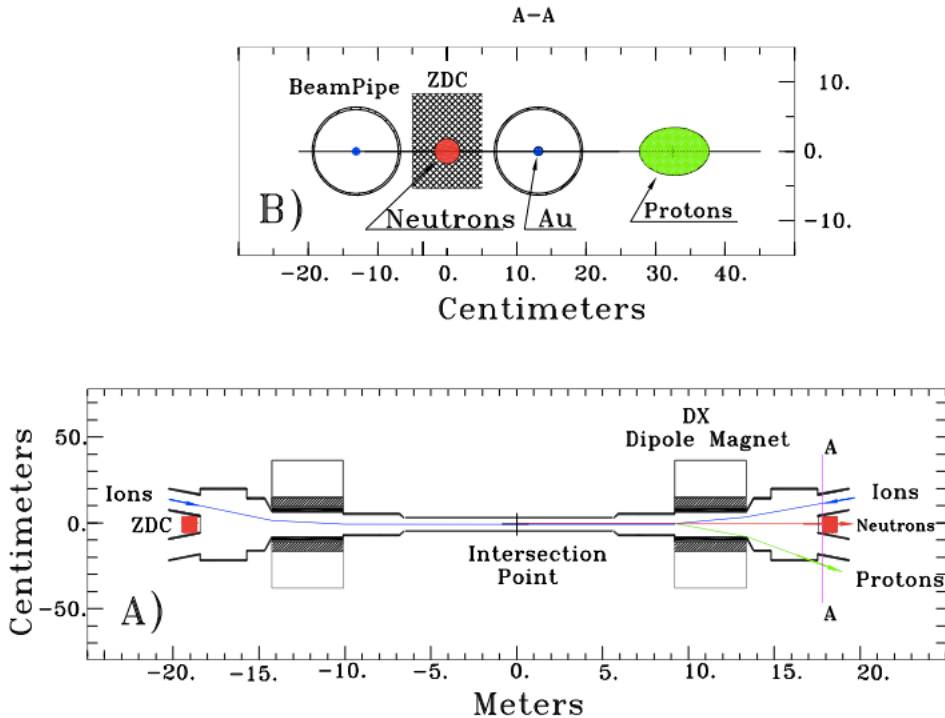


Figure 3.5: Top: View of the ZDC from the beam-line. The ZDC is located between the beam pipes of the yellow and blue beams (after they separate) past the bending DX magnets which are used to guide the beams out of the PHENIX IR and back around the ring. These DX magnets also serve to sweep away charged particles providing a relatively clean sample of neutral particles for the ZDC. Bottom: Birds eye view of the beam line and the ZDC. Protons and other ions can be seen to be swept to the left or right of each ZDC.

<sup>1</sup>Diffractive collisions are typically characterized by a very low momentum exchange between the two protons. Single diffractive events refer to the case where one of the protons remains intact while double diffractive events indicate both protons stayed intact. Diffractive collisions result in extremely low transverse momentum remnants, often staying within the confines of the beam pipe. Resonances, or excited states of the proton, can be produced which decay back to a proton and additional particles. One example is  $\pi^0$  production via  $pp \rightarrow pp\pi^0$ . The subsequent decay  $\pi^0 \rightarrow \gamma\gamma$  produces two photons with very small transverse momentum photons that can be detected by the ZDC. An example of a single diffractive event is  $pp \rightarrow pn\pi^+$ . In this case, the neutron does not get swept away by the beam magnets and can shower in the ZDC.

<sup>2</sup>Heavy ion collision pun intended.

The ZDC detectors are sampling hadronic calorimeters. This means that there are alternating layers of absorber material, used to generate the showering process, and sampling material, used to measure the energy deposited from the shower. For the ZDC the absorbing material used is Tungsten which has a nuclear interaction length of  $9.9\text{ cm}$ . The sampling is done via carbon-based fiber. Each ZDC detector module consists of 27 0.5 cm thick Tungsten plates stacked together with alternating layers of readout fibers. The ZDC detector in each arm consists of three modules, each with a separate readout. Figure 3.6 shows a diagram of the setup. The hit signal from each ZDC module is digitized by its FEM to create an ADC and

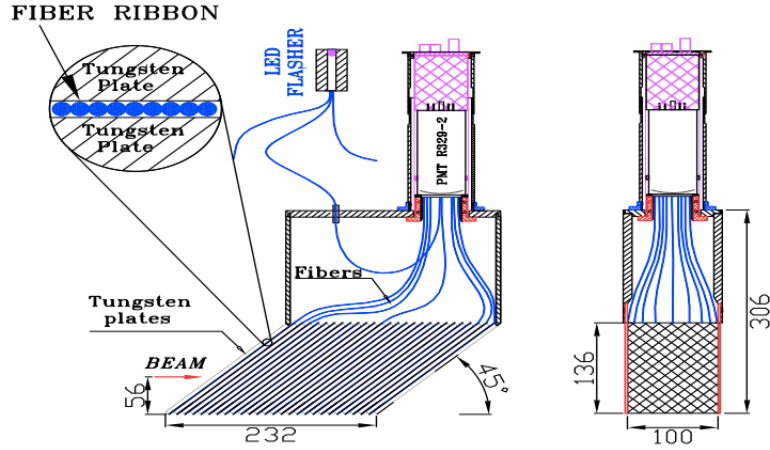


Figure 3.6: Mechanical design of the Tungsten Modules. Left: A side view of the sampling fibers, absorber plates and LED pulser. Right: A top view of the ZDC.

two TDC values. The ZDC trigger is digitally based, like the BBC, and operates on the analog sum of the signals from the three individual modules. This amounts to an earliest time trigger algorithm in the ZDC, as compared to the mean time trigger algorithm used in the BBC. The timing resolution of the ZDC is significantly higher than for the BBC, typically about  $200\text{ ps}$  for a module. This is due partly to the spread in transit time of light emitted in the fibers as it propagates from different vertical positions based on the shower location. The ZDC is observed to have both an online trigger and offline vertex resolution of about  $30\text{ cm}$ .

For more information on the ZDC the reader is referred to Ref. [72], [73] and [127].

### 3.5 Data Acquisition System

The data acquisition (DAQ) system at PHENIX produces one of the fastest readout chains in the world. It has a capacity to read out  $> 7000$  events per second corresponding to a data volume rate of around  $700\text{MB}/\text{s}$ . A thorough explanation of the DAQ is given in Ref. [74]. The essential idea is modularization of data flow starting with a Front End Module (FEM), or set of FEMs, for each modularized detector subsystem. Each FEM receives instructions to send its data to a Data Collection Module (DCM) from its Granule Timing Module (GTM). From here, the data is sent to Sub-Event Buffers (SEB) and then to Assembly and Trigger Processors (ATPs). The ATPs assemble all packet information from a specified crossing and write it to disk. The MPC upgrade (Chapter 7) involved changing the MPC FEM. This resulted in a change to the raw data format output by the DCM.

# Chapter 4

## Muon Piston Calorimeter

An extensive list of double helicity spin asymmetry,  $A_{LL}$ , measurements has been produced by the PHENIX Spin Collaboration using the central arm detectors. The  $\pi^0$   $A_{LL}$  has been measured and published using data taken over several years (Refs. [75], [76], [77], and [78]). Additionally, the charged hadron  $A_{LL}$  has been analyzed and published (Ref. [79]) as has the single electron  $A_{LL}$  (Ref. [80]). Additionally, numerous analyses are currently being worked on and several publications are in progress as of this writing. Each of the measurements contained in these publications provides a unique insight into  $\Delta G$  either kinematically or by isolating the coupling of specific quark PDFs with  $\Delta G$ . The details of this are explained in the references provided. The main limitation that all of the central arm ( $|\eta| < 0.35$ ) measurements suffer from is that they are not sensitive to gluons with  $x < 0.05$ .

The MPC was designed with the intent of extending the sensitivity of longitudinal double spin asymmetries to gluons with  $x < 0.05$ . A detailed writeup of the procedure used for installing and commissioning the MPC is given in Ref. [8]. Here we discuss aspects of the MPC that directly apply to understanding the MPC data, performing an analysis of this data and using the results.

### 4.1 Description of MPC

Figure 4.1 shows a cross section of the MPC as seen from the center of PHENIX. Each scintillating lead tungstate crystal,  $PbWO_4$ , is  $18\text{ cm}$  deep and  $2.2\text{ cm} \times 2.2\text{ cm}$  laterally. They are stacked together as shown with 196 crystals in the south MPC and 220 in the north. The Molière radius<sup>1</sup> of lead tungstate is  $2\text{ cm}$ . A fraction of the scintillation light produced in each crystal is read out by an Avalanche Photodiode (APD), which is used instead of a PMT readout due to its insensitivity to the magnetic fields that are present as well as space limitations. The APDs cover the front face of each crystal (shown in green, their actual color, in Fig. 4.1). The APDs convert the scintillation light into photoelectrons which are accelerated to form

---

<sup>1</sup>The radius within which 90% of the energy from an EM shower is contained.

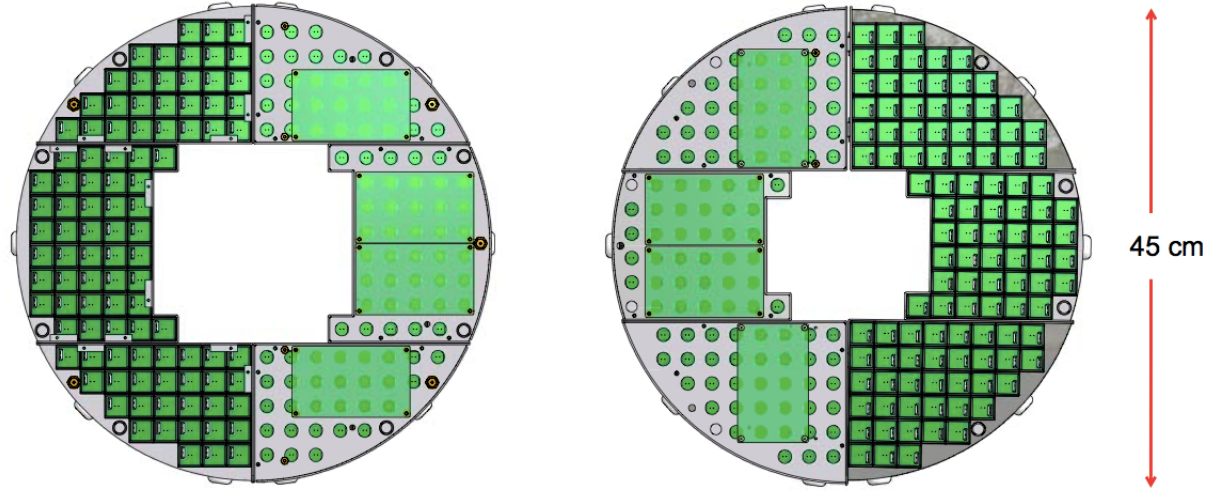


Figure 4.1: A diagram of the MPC. Relevant details are contained in the text. A complete description of the MPC layout and construction may be found in Ref. [8].

avalanches when a high voltage (HV) bias is applied. The driver boards, the larger green rectangles seen in Fig. 4.1, act as interfaces between the crystal+APDs and the FEMs. They supply HV to the APDs and also carry the signal from each APD up to the electronics rack. Each arm uses 10 driver boards, each of which interface with  $\approx 20$  APDs. A driver board channel has a small potentiometer that can be used to tweak the relative gain of each APD.

## 4.2 MPC Trigger and Readout

The MPC electronics are taken from spare parts of the Central Arm Electromagnetic Calorimeter.<sup>2</sup> The electronics are well understood, and it provided a fast and inexpensive solution. The signals sent up from the driver board are stored in a memory buffer of 64 Analog Memory Units (AMU) for each channel. As the name implies, these signals have not been digitized yet. The AMUs are part of the MPC FEMs. Each MPC arm is allotted 2 FEMs, with each FEM having a maximum of 144 inputs. The mapping of FEM to crystal is done, very roughly, by separating “inner” crystals, crystals closer to the beam-pipe, from “outer” crystals that are farther from the beam-pipe. The exact mapping may be found in Figure 4.2. The trigger calculation is then done within each FEM on the analog information by forming sums of signals from groups of  $2 \times 2$  or  $4 \times 4$  tower arrays and comparing the signal sum to a set threshold. When the MPC trigger, or some other trigger, fires, and the PHENIX Global Level 1 (GL1) accepts the trigger for data taking, the FEM

---

<sup>2</sup>The EMCal electronics were used for 2006-2011 and upgraded in time for the 2012 data taking.

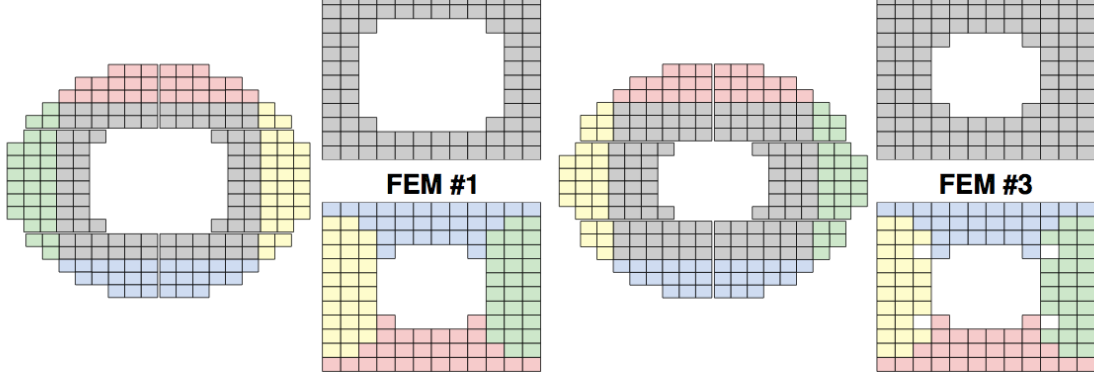


Figure 4.2: The Front End Module (FEM) mapping to crystals is shown for the south(left) and north(right) MPC. Ref. [8]

will, only at this point, digitize the signal. A TDC is readout, along with a “pre” and “post” ADC value<sup>3</sup>. The pre-ADC is taken from the AMU corresponding to 4 beam ticks back and the post-ADC is taken from the crossing of interest. Both the pre- and post-ADC are read out in a low and high gain form for larger dynamic range in the former case and higher energy resolution in the latter case. The conversion factor between the low gain and high gain ADCs is typically close to 16. More information about the hardware and operations can be found in Ref [91].

### 4.3 Measuring $A_{LL}$ from Single and Di-Hadrons in the MPC

Figure 4.3 effectively illustrates the scenario in which two  $\pi^0$ 's, each from a separate jet, decay into two photons that shower in the MPC. Until 2012, the MPC was only capable of triggering on a single large energy deposit. In this case, one of the two jets is not directly measured in the trigger. Some MPC di-jet events are triggered based on the energy of a single hadron, but the presence of a second hadron is not considered. This represents a very small fraction of the data. An effective di-jet trigger would require separate energy deposits in a single MPC arm, where the threshold of each hadron is substantially lower than the threshold in a single hadron trigger. The di-jet threshold might be  $p_T \gtrsim 1.0 \text{ GeV}/c$  for each hadron while the single jet threshold might be set at  $p_T \gtrsim 3.0 \text{ GeV}/c$ .

The difference between a single hadron and a di-hadron measurement is in the distribution of the underlying parton kinematics that is sampled. For a single hadron data set, one can perform a higher statistics measurement, but not having information regarding the kinematics of the second jet means it could have

---

<sup>3</sup>The pre-ADC reading reads the ADC charge before the signal arrives and the post-ADC reads the charge after the signal has been integrated.

been pointed anywhere. This can be seen from Eqs. 2.34-2.36. If the rapidity of both jets,  $y_{3,4}$ , are known, then  $x_{1,2}$  of the original partons can be constrained. However, if the rapidity of one jet is not known, then a range of kinematic conditions could have resulted in production of the jet that does have a rapidity within the MPC acceptance. In the di-hadron case, the rapidities of both jets (technically the  $\pi^0$ 's are jet proxies, which introduces additional kinematic smearing) are constrained. When both jets are constrained to be within the MPC acceptance, the underlying event kinematics are constrained and are dominated by the case of a high momentum, valence quark interacting with a low momentum gluon. Figure 4.3 illustrates this.

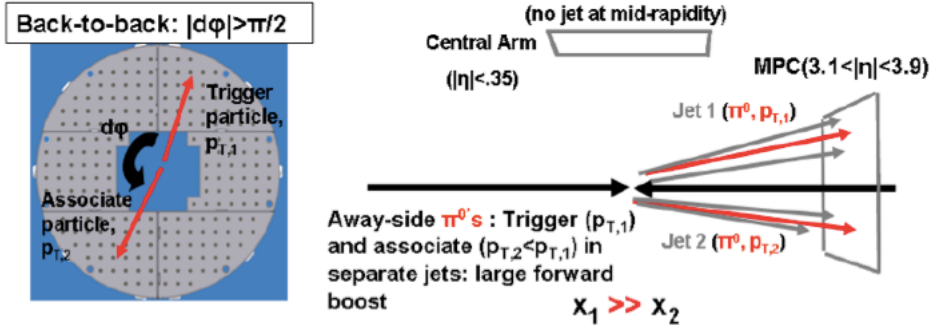


Figure 4.3: A typical di-jet event, with a boosted center of mass, is shown. A  $\pi^0$  within each jet decays into two photons and showers in the MPC. If both pions can be triggered on separately then a di-hadron trigger can be constructed in which the two hadrons are required to have some minimal azimuthal separation to ensure they came from separate jets. This upgrade has been done and is discussed in Chapter 7. Prior to the upgrade, the MPC had the capability to trigger on one of these jets (using the  $\pi^0$  as a standard proxy) which provides a high statistics measurement with a broad range of underlying parton kinematics sampled.

trates, qualitatively, the collision kinematics the MPC can access in the case of di-hadrons. The center of mass is heavily boosted in the forward (or backward) direction. A detailed study of the parton- $x$  range that is accessed in MPC single- and di-hadron triggers has been performed (Ref. [81]) to allow a quantitative understanding of the kinematics sampled by the MPC. This study used PYTHIAv6.4 (Ref. [122]) in TuneA with PYTHIA processes 11,12,13,28,53,68, and 96 turned on. The simulation was also configured using the inputs shown in Table 4.1. Fig. 4.4 shows the resulting distributions of the momenta fractions

Table 4.1: Pythia Configuration for events generated at  $\sqrt{s} = 500 \text{ GeV}$ .

Setting	Value
MSTP	91 1
PARP	91 1.5
MSTP	33 1
PARP	31 2.5
CKIN	3 1.0

of the two partons. The single  $\pi^0$  case shows a maximal sensitivity to partons with  $x \sim 0.02$ , but also

with significant sensitivity in the  $10^{-3} < x < 10^{-1}$  range as well. The leading parton, typically a quark, is seen to usually be in the valence region at high momentum fraction. In the di-hadron case, we see the expected skewing of the leading parton  $x$  even further into the valence region and the lower  $x$  parton further into the sea region. Much of the statistics generated with these kinematics is seen to come from partons with a momentum fraction in the range  $0.5 \times 10^{-3} < x < 10^{-2}$ . As the gluon PDF is dominant at low- $x$  while the (u and d) quark PDFs dominate at large  $x$  (Ref. 2.5), quark-gluon scattering is confirmed to be the dominant process we are interested in. This conclusion is also consistent with what was seen in Fig. 2.13.

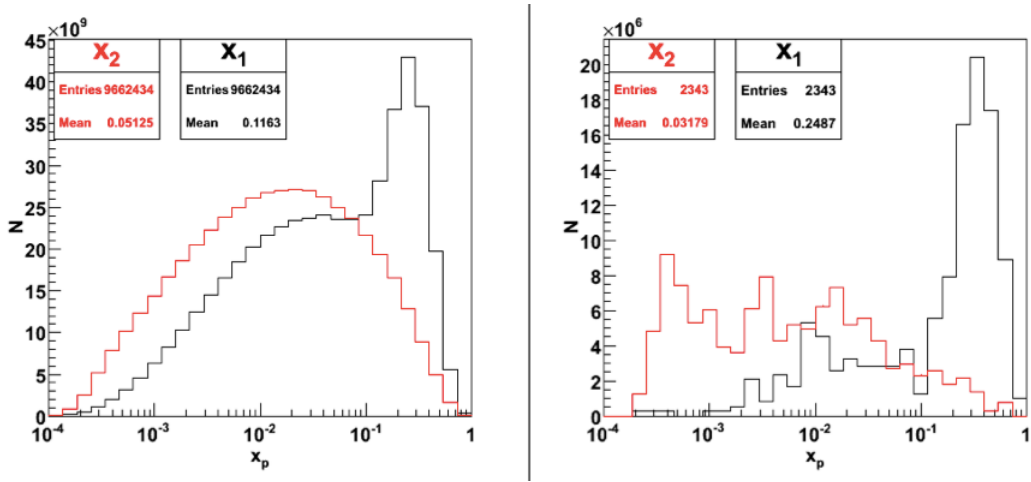


Figure 4.4: Left (a): In black is the leading parton  $x$  and in red is the trailing parton  $x$  for a PYTHIA simulation of events that produce a single  $\pi^0$  with  $3.1 < |\eta| < 3.9$ , the acceptance of the MPC. Right (b) The same distribution of momenta fractions is shown for PYTHIA events that produce two  $\pi^0$ 's into the MPC acceptance, each with  $p_T > 1.0 \text{ GeV}/c$ . (Ref. [81])

The second important issue to address is the order of magnitude of the size of the double longitudinal helicity asymmetries one expects to measure in the MPC. This can be estimated by combining the most up-to-date understanding of the functional form of  $\Delta g(x)$  (and the other PDFs and pPDFs) using the DSSV framework([44],[45]) with Next-to-Leading Order (NLO) calculations of partonic cross sections and asymmetries (see Fig. 2.12) to generate the predicted total polarized production cross sections and asymmetries for neutral pions. For  $\sqrt{s} = 500 \text{ GeV}$ , using an input distribution of  $x$  the results are shown for  $A_{LL}$  for the single  $\pi^0$  case in Figure 4.5 and the di-hadron case in Figure 4.6. In these figures the assumed integrated luminosities are  $180 \text{ pb}^{-1}$  and  $416 \text{ pb}^{-1}$  respectively<sup>4</sup>.

<sup>4</sup>This number is determined by counting BBC coincidences. Often, a vertex cut on the BBC coincidence is used in determining the luminosity which has an efficiency of around 60%. The number quoted here is an estimate without using a vertex cut.

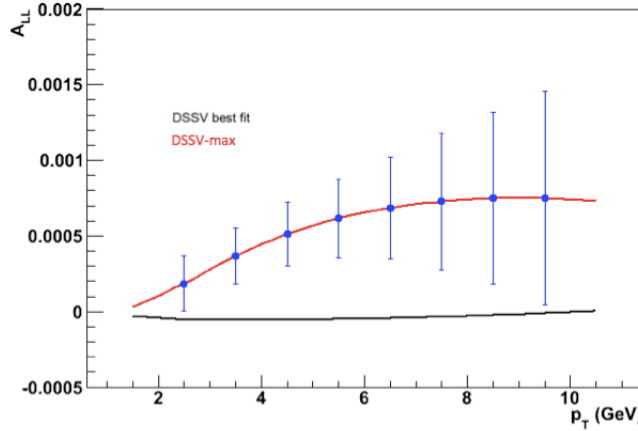


Figure 4.5: The projected asymmetry vs.  $p_T$  using  $\Delta G$  from the DSSV best fit and DSSV-max. These are defined in Refs. [44] and [45]. The statistical error bars assume an integrated luminosity of  $180 \text{ pb}^{-1}$ . Recent jet  $A_{LL}$  measurements have modified these DSSV fits to be more consistent with what is here referred to as DSSV-max. We therefore expect to measure asymmetries at the level of  $O(10^{-4})$ . Having acquired a total of around  $300 \text{ pb}^{-1}$  we expect to have the necessary statistics to resolve an asymmetry this small.

## 4.4 Summary

In Chapter 2 we summarized the theory underlying  $\Delta G$  and motivated its measurement at a  $pp$  collider. In Chapter 3 we summarized some key aspects of the RHIC accelerator, the PHENIX detector, and focused on necessary details of the BBC and ZDC detectors which are used for the luminosity measurement. In this brief chapter we have described the MPC and shown that it is capable of extending the sensitivity of  $\Delta G$  measurements to lower  $x$  and that the asymmetries it is predicted to generate are large enough to be able to be measured with the statistics available. Table 4.2 summarizes this information. In each year in which

Year	$\sqrt{s}$ (GeV)	$L_{30\text{cm}}(\text{pb}^{-1})$	Polarization	FoM ( $P^4 L$ )	MPC Installation Status	MPC Trigger
2005	200	2.5	50%	0.15	Not installed	N/A
2006	200	7.5	57%	0.79	South Arm	Analog
2006	62.4	0.08	48%	0.0042	South Arm	Analog
<b>2009</b>	<b>200</b>	<b>14</b>	<b>57%</b>	<b>1.5</b>	<b>Both Arms</b>	<b>Analog</b>
<b>2009</b>	<b>500</b>	<b>10</b>	<b>40%</b>	<b>0.26</b>	<b>Both Arms</b>	<b>Analog</b>
2011	500	17	52%	1.4	Both Arms	Analog
2012	510	32	56%	3.1	Both Arms	Digital
2013	510	150	55%	14	Both Arms	Digital

Table 4.2: Summary of longitudinal data acquired by PHENIX and the status of the MPC installation and trigger. In the next two chapters the analysis of the 2009 data will be explained.

the protons were longitudinally polarized, the integrated luminosity within  $30 \text{ cm}$  is shown, along with the average beam polarization for that year, the Figure of Merit (FoM) which is inversely proportional to the expected statistical uncertainties, the status of which arms of the MPC detectors were installed, and the

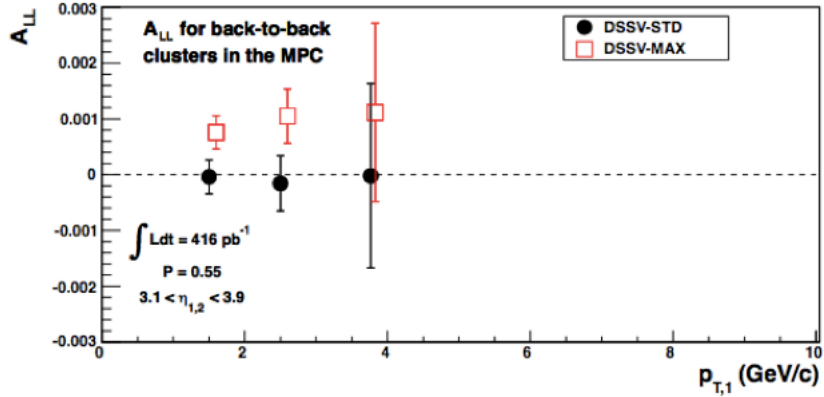


Figure 4.6: The projected  $A_{LL}$  for back-to-back di-hadrons is shown assuming  $416 \text{ pb}^{-1}$ . In this case the projected asymmetries are also shown using the DSSV-std and DSSV-max scenarios for  $\Delta G$ . For the DSSV-max scenario, which recently has shown to be quite plausible, we can reasonably expect to see asymmetries different from zero at the  $1 - 1.5\sigma$  level in the first three  $p_T$  bins. The axis in this case is taken to be the  $p_T$  of the leading  $\pi^0$ .

status of the trigger. Next, in Chapters 5 and 6, we will discuss the analysis of merged clusters<sup>5</sup>, using the 2009 longitudinally polarized  $pp$  data taken with the MPC. The two measurements represent the first such measurements that extend the sensitivity of  $\Delta G$  to low- $x$ . Chapter 7 is dedicated to explaining an electronics and trigger upgrade that vastly extends the capabilities of the MPC, including the addition of a di-hadron trigger to gain sensitivity to even lower momentum gluons. Finally, we will discuss (quite extensively) the dominant systematic uncertainty from relative luminosity that is common to all measurements of  $A_{LL}$ . This uncertainty points to fundamental issues that were not previously understood. A summary of the current understanding is explained in Chapter 8. Chapter 9 is then dedicated to the development of a comprehensive new approach and understanding of the luminosity measurements. It will be demonstrated that, fortunately, the performance of the BBC and ZDC and the quality of the data are all adequate. However, a large number of the unexplained features contained in the data that will be uncovered in Chapter 8 turn out to have elegant explanations based on the theory that will be developed in Chapter 9. The result of this is that by simply analyzing the existing data through a new lens allows the relative luminosity uncertainty to be shrunk to the  $10^{-4}$  level needed to observe an  $A_{LL}$  at the same scale. At this juncture, the reader has now been presented the necessary background information and we proceed to measurement of the single hadron  $A_{LL}$ .

---

<sup>5</sup>What is meant by merged will be made clear in the next chapter.

# Chapter 5

## Measurement of Forward Cluster $A_{LL}$ at $\sqrt{s} = 200\text{ GeV}$

In this chapter, we describe the  $A_{LL}$  analysis of electromagnetic (EM) clusters in the MPC from the 2009 data at  $\sqrt{s} = 200\text{ GeV}$  (Ref.[83]). 2009 was the first year of longitudinal running with the MPC fully installed. This analysis represents the first MPC measurement that will contribute to constraining  $\Delta G$ . In the process, it will extend the sensitivity of the  $A_{LL}$  measurements at PHENIX to gluons with  $x < 0.05$ .

### 5.1 Why EM Clusters are Measured

The optimal particle to measure with a forward electromagnetic calorimeter such as the Muon Piston Calorimeter (MPC) is the  $\pi^0$ . It is the lightest meson, copious quantities are produced (i.e. large cross section) and it decays electromagnetically into two photons via  $\pi^0 \rightarrow \gamma\gamma$  with a mean decay time of  $\tau \sim 8.4 \times 10^{-17}\text{s}$ . The kinematics of a two-body decay such as this are fairly routine to calculate ([82]). A particularly relevant relationship that can be derived in the lab frame is:

$$m_{\gamma\gamma}^2 = \frac{1}{2}E_{pair}^2 (1 - \gamma^2) (1 - \cos \theta) \quad (5.1)$$

where  $m_{\gamma\gamma}$  is the invariant mass of the photons (typically close to the  $\pi^0$  mass),  $E_{pair} \equiv E_{\gamma_1} + E_{\gamma_2}$  is the photon pair energy,  $\gamma \equiv \left| \frac{E_{\gamma_1} - E_{\gamma_2}}{E_{\gamma_1} + E_{\gamma_2}} \right|$  is their energy asymmetry and  $\theta$  is the angle, in the lab frame, between the two decay photons. While the charged pions have a very long decay length ( $O(10^2 m)$ ), even an extremely relativistic neutral pion with  $E = 100\text{ GeV}$  has a decay length of just  $d = \frac{E c \tau}{m} \sim 2.2\mu\text{m}$ . Therefore, one is always relegated to reconstructing the invariant photon mass in order to measure an identified  $\pi^0$ . When the photon enters the MPC matter, it begins a complicated and stochastic showering process. This must be understood well from simulations in order to reconstruct the photon kinematics and, ultimately, the  $\pi^0$  kinematics. It has been studied and written up in Ref. [84].

The MPC crystals are located at  $z_{MPC} = \pm 220\text{ cm}$  from the nominal interaction point. Each  $PbWO_4$  crystal has a transverse size (the area as seen by an incoming photon) of  $2.2\text{ cm} \times 2.2\text{ cm}$ . In order to distin-

guish the two photons in practice, they must be separated by at least the dimension of two crystals. It can be seen from Eq. 5.1 that at increasing energies the angular separation between the photons decreases. This means there is an upper limit on the pion energy beyond which its decay photons will shower into roughly the same set of crystals. Figure 5.1 shows a pictorial example of how this occurs. When this happens, the two

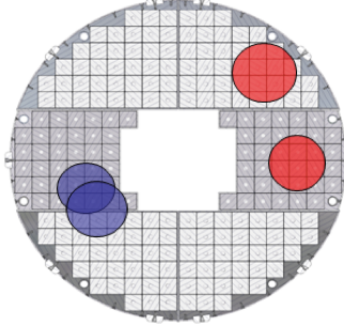


Figure 5.1: Red: Two showers produced by decay photons of a low energy  $\pi^0$ . The showers do not overlap to any appreciable extent and the MPC clustering algorithm ([86]) can distinguish two distinct clusters on energy deposits in the crystals. Blue: The showers produced by decay photons of a high energy  $\pi^0$  have less separation and the MPC clustering algorithm cannot distinguish the two clusters.

separate EM clusters cannot be discerned in order to determine an invariant mass. We can estimate that this happens when the separation between the two photons is two crystal lengths,  $d$ , apart. This corresponds to  $\theta_{min} \approx \frac{2d}{z_{MPC}} \approx \frac{4.4\text{ cm}}{220\text{ cm}} \approx 0.02$ . For a pion decaying into two photons of equal energy this yields a maximum pion energy,  $E_{\pi^0,max}$ , of  $E_{\pi^0,max} \approx \frac{2m_{\gamma\gamma}}{\theta_{min}} \approx 14\text{ GeV}$ . The typical radial distance of an MPC crystal from the beam-line is  $15\text{ cm}$ . Therefore, the typical angle of a  $\pi^0$  decaying into photons incident on the MPC is  $\theta \approx \frac{15\text{ cm}}{220\text{ cm}} \approx 0.07$ . So the maximum pion  $p_T$  that can be reconstructed is  $p_{T,max} \approx E_{max}\sin\theta \approx 1\text{ GeV}$ . Beyond roughly this point, the two clusters merge into a single cluster and the efficiency for  $\pi^0$  reconstruction drops rapidly. This happens to roughly coincide with the transition region from non-perturbative QCD to perturbative QCD. Of course, plenty of photons from pions with higher  $p_T$  still enter the MPC, but their showers merge and the  $\pi^0$  is only observed as an electromagnetic cluster. No invariant mass can be reconstructed in this case.

The result of all this is that to access the perturbative region of QCD, where strong evidence exists that factorization holds, we have to rely on merged clusters instead of reconstructed  $\pi^0$ 's. This comes at the cost of additional background due to not being able to distinguish merged clusters from photons from other sources. This has been studied from a set of full simulations ([85]) where it is found that merged clusters from  $\pi^0$ 's are the dominant source of clusters. Other sources of clusters contribute 20 – 30% depending on

$p_T$ . The result is shown in Figure 5.2.

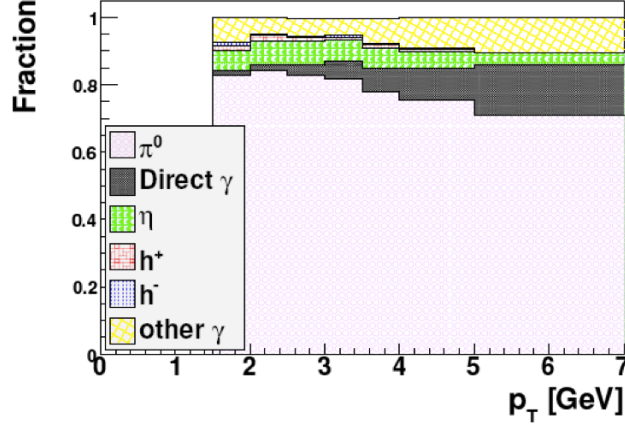


Figure 5.2: Cluster decomposition is shown. As a function of cluster  $p_T$ , the fraction of clusters that are actually merged clusters from a  $\pi^0$  decay is shown and compared with other sources of electromagnetic clusters. At low  $p_T$  roughly 80% of clusters are merged clusters while at high  $p_T$  this drops to about 70%.

## 5.2 Definition of $A_{LL}$

The definition of the double longitudinal helicity asymmetry,  $A_{LL}$  was given in Eq. 2.30. Written out fully, it is:

$$A_{LL} = \frac{\sigma^{++} + \sigma^{--} - \sigma^{+-} - \sigma^{-+}}{\sigma^{++} + \sigma^{--} + \sigma^{+-} + \sigma^{-+}} \quad (5.2)$$

Experimentally, we measure the asymmetry as a function of the cluster transverse momentum,  $p_T^{clus}$ , via:

$$A_{LL} = \frac{1}{P_B P_Y} \frac{N^{++} - RN^{+-}}{N^{++} + RN^{+-}} \quad (5.3)$$

which follows from Eq. 5.2 using parity conservation, and with the assumption of spin independent efficiencies.  $N$  represents the cluster yield in the MPC from same or opposite sign helicity crossings in a given  $p_T$  bin.  $P_{B,Y}$  are the beam polarizations and act as a scaling factor in the asymmetry and its uncertainties. The definition of relative luminosity,  $R$ , is given here by:

$$R = \frac{L^{++}}{L^{+-}} \quad (5.4)$$

which is the ratio of the luminosity measured in same sign versus opposite sign crossings. The statistical error on  $A_{LL}$  is found from propagation of errors

$$\delta A_{LL} = \frac{1}{P_B P_Y} \frac{2RN^{++}N^{+-}}{(N^{++} + N^{+-})^2} \sqrt{\left(\frac{\Delta N^{++}}{N^{++}}\right)^2 + \left(\frac{\Delta N^{+-}}{N^{+-}}\right)^2 + \left(\frac{\Delta R}{R}\right)^2} \quad (5.5)$$

The statistical contribution of relative luminosity to the overall statistical uncertainty is essentially negligible. Additionally, the sources of systematic uncertainty that arise are:

- Polarization uncertainty which acts as an overall scale uncertainty.
- Relative luminosity. We will discuss this, very briefly, in this chapter before spending two chapters and about 80 pages dedicated to the matter.
- Other systematic uncertainties resulting from internal consistency checks.

## 5.3 Detector Calibration

The calibration of the MPC is necessary to turn the raw Analog-To-Digital Converted (ADC) and Time-To-Digital Converted (TDC) data into physics deliverables. We are primarily concerned with getting the right conversion from ADC to energy on a channel by channel basis. Complete documentation for the calibration procedure has been written up in [82]. Here we show the implementation of the methods described in that note on the Run09  $\sqrt{s} = 200 \text{ GeV}$  data. The following sections will also provide some examples of how the data is handled, and to be perfectly imprecise, how it “feels”.

### 5.3.1 ADC and TDC Overflows

When a given event is to be written to disk, a digitized time, the TDC and a digitized pulse integral, the ADC are produced from a buffer of analog signals stored in Analog Memory Units (AMU’s) located on the MPC Front End Module (FEM). More details regarding the AMU’s and FEM can be found in Ref. [8]. Both a high gain ADC and a low gain ADC are written out. Both ADC’s are 12-bit values and typically the high gain is amplified by a factor of  $\approx 16$  from the low gain ADC. The high ADC has better energy resolution at low energy but reaches its dynamic limit ( $2^{12} - 1 = 4095$ ) at a low energy corresponding typically to  $E \approx 6 \text{ GeV}$ . This corresponds to an energy resolution of 1 ADC count  $\approx 0.7 \text{ MeV}$ . The low gain ADC is typically set to reach the end of its dynamic range at around  $90 \text{ GeV}$ . However, both ADC’s overflow at some value below this, typically around 3000. When the high gain ADC has not overflowed,

we prefer to use that value due to its better resolution. When it is overflowed the low gain ADC is used for energy determination. For very large energy deposits even the low gain ADC can overflow. In this case a reliable energy determination cannot be made. Figure 5.3 shows a sample low gain ADC spectrum for

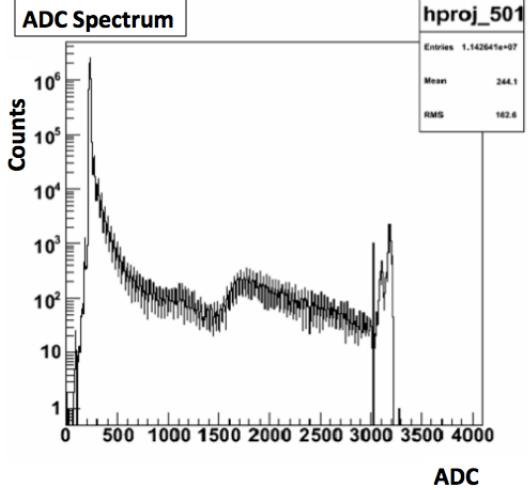


Figure 5.3: Sample low gain ADC Spectrum from one MPC channel. The black vertical line indicates where the overflow value is found to be.

one channel. A fairly simple algorithm can be implemented to scan through this spectrum and extract a reasonable overflow value, indicated by the black vertical line in the figure. When this simple algorithm is run over the spectrum for all MPC channels, the result is Figure 5.4. Although the TDC spectrum is not

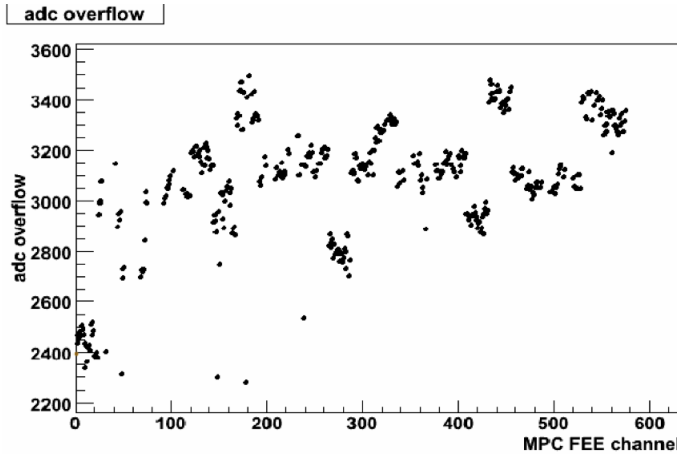


Figure 5.4: The low gain ADC overflow value is shown channel by channel. Channels with Front End Electronics (FEE) value less than 288 are in the south MPC. Otherwise they are in the north MPC.

calibrated directly for Time-of-Flight, its overflow values can be used to help eliminate stray hits in the MPC

that are out of time with the collision remnants. A TDC overflow cut will remove hits that occurred outside the crossing of interest and the following crossing. Figure 5.5 shows the channel by channel TDC overflow values as determined using the same simple algorithm as for the ADCs.

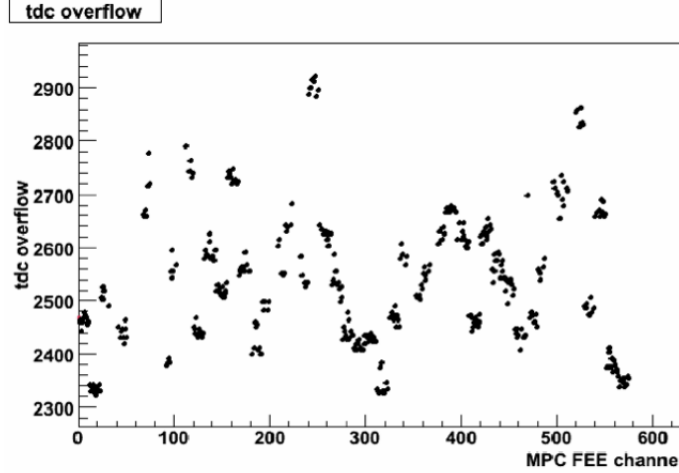


Figure 5.5: TDC overflow values are shown channel by channel.

### 5.3.2 Energy Scale Determination

Three steps are used to determine the energy scale in the Run09 data. They are the LED calibration, MIP calibration and  $\pi^0$  iterative calibration. A complete description of all of these may be found in Ref. [82].

#### LED Calibration

Each MPC crystal has an LED that fires a light pulse of nearly constant intensity into the crystal. By looking at the ADC response to this constant input over time, we can monitor the how the relative response scale of each crystal is changing due to a variety of external factors and well as crystal degradation itself. This relative scale is then used to normalize all ADC outputs to a constant scale over time.

#### Minimum Ionizing Particles

To determine the absolute energy scale of each crystal we use Minimum Ionizing Particles (MIPs) which are based on the Bethe-Bloch description of charged particle passage through matter ([87]). The idea is that MIPs will deposit a known, fixed quantity of energy (with some spread) as they pass through the full length of the MPC crystal. This has been studied in simulations and via beam tests at Fermi National Accelerator

Laboratory. ([82],[89], [90]). The result is that a MIP is expected to deposit  $234\text{ MeV}$ , which gives the absolute scale.

Two cuts are made to isolate MIPs:

- A hit is required in the BBC where the MIP was expected to have passed through.
- No surrounding MPC towers are allowed to have hits in them. This serves to eliminate electromagnetic showers which MIPs cannot initiate.

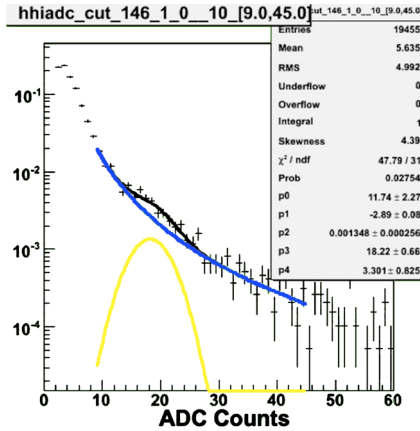


Figure 5.6: ADC spectrum for one MPC crystal is shown. The yellow curve is a Gaussian fit to the MIP peak. The center of the gaussian is taken as the MIP value. The blue curve is a power law fit to the background shape. The black curve is the sum of the MIP signal and the background. From this example, one finds a MIP energy deposit corresponds to 18 ADC counts.

Figure 5.6 shows a sample ADC spectrum from one crystal after making these cuts. The absolute energy scale is then defined by the gain,  $G$ , of the crystal where:

$$E_{mip} = 0.234\text{ GeV} = G \times ADC_{mip} \quad (5.6)$$

At  $\sqrt{s} = 200\text{ GeV}$  the high voltage applied to the crystal APD's was such that one photoelectron was converted into 50 avalanche electrons. This has been found to be the optimal setting for the MPC ([90]). However, at higher energies where more dynamic range is needed, the  $M = 50$  high voltage setting was lowered. As can be seen in Fig. 5.6, when the MIP peak is decreased, it begins to run into a very large background that swamps the MIP peak making its detection very difficult or impossible. In Figure 5.7a we show the time dependence of the MIP peak. Figure 5.7b demonstrates that the LED's are capable of tracking the MPC gain over time and can be used as a normalization.

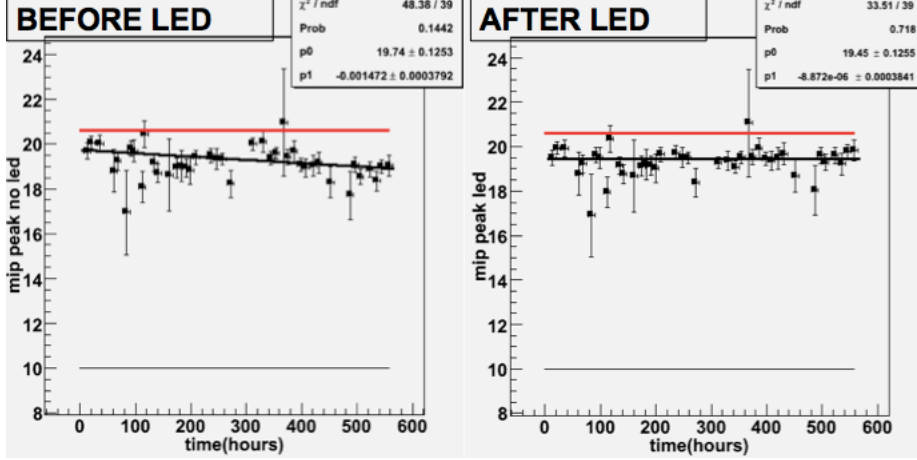


Figure 5.7: Left (a): Time dependence of the MIP peak shows that the crystal response decreases over the course of the run. Right (b): However, the LED can account for this. Once the absolute scale is determined the relative scale from the LED removes the time dependence of the MIP.

### Iterative $\pi^0$ Calibration

To confirm the energy scale and make modifications to the crystal gains as necessary, an iterative process is employed. The idea is to use an input set of gains, which are determined by the MIP peaks, to determine the tower energies in each event. Then the MPC clustering algorithm ([86]) is used to identify electromagnetic clusters of energy deposits in groups of adjacent crystals. Then, a di-photon invariant mass distribution is formed from all pairs of clusters with minimal cuts applied at the cluster level (energy, shower shape, dispersion) and the cluster pair level (pair energy, energy asymmetry, separation). The resulting peak is used to determine the  $\pi^0$  mass. A reconstructed  $\pi^0$  is determined for each tower and is compared with the expected mass from simulations. Based on this comparison, the gain is increased or decreased. Finally, this new set of gains is used as input for the next iteration. In the next iteration, the cluster center of gravity is recalculated according to the current iteration of gains. Once the gains are correct for each tower, the extracted masses are expected to reproduce the simulation masses and produce a stable result in the following iteration. Figure 5.8a shows the distribution of  $\pi^0$  peak positions and widths before the iterative calibration is applied. Figure 5.8b shows the same after the calibration has been done.

#### 5.3.3 Warnmap: List of Excluded Towers

The warnmap is the set of MPC channels that are excluded from analysis for one reason or another. The list develops through the calibrations process. For example, in this dataset one driver board (about 20 channels) did not have a functional LED, so these channels cannot be corrected for relative gain changes.

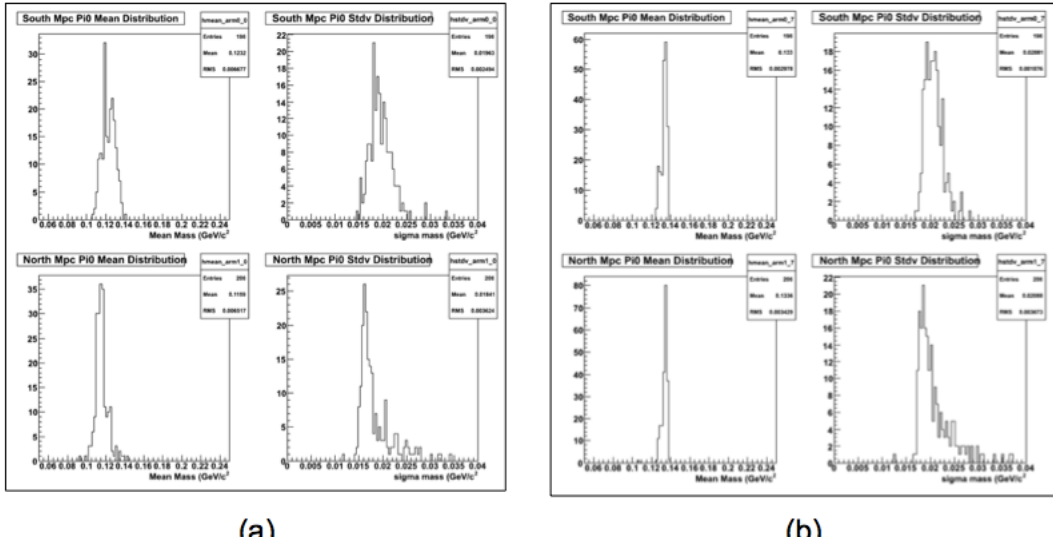


Figure 5.8: (a) Top Left: Distribution of  $\pi^0$  masses for channels in the south MPC. Top Right: Distribution of  $\pi^0$  widths for channels in the south MPC. Bottom Left: Distribution of  $\pi^0$  masses for channels in the north MPC. Bottom Right: Distribution of  $\pi^0$  widths for channels in the north MPC. (b) The same plots as in (a) showing how the iterative technique is able to narrow the distribution of  $\pi^0$  masses. 7 iterations are used.

In some cases, the FEM has a stuck bit for a given readout channel. This will cause the ADC spectrum to have a large ringing, or oscillation, in it. This typically makes it impossible to extract a reasonable gain. Also, we check for hot and dead channels that count hits either too often and too little. This can be due to a noisy driver board, a bad value for the ADC gain, or, in the case of some channels in the north MPC, being geometrically blocked by a beampipe support structure. Experimentally, it is found that  $\log \frac{N_{\text{count}}}{N_{\text{trig}}}$  linearly decreases with tower radius <sup>1</sup>, as shown in Figure 5.9. We then define hot towers and dead towers as those with counts too far above or below the expectation. A constant warnmap is preferred to a run dependent warnmap, so if a tower is hot or dead in  $> 10\%$  of runs, it is used in the warnmap for the entire dataset. Figure 5.10 shows the results of a run by run study of hot and dead towers via the counts per trigger method. In addition, sometimes control of the beam is lost causing an unexpected abort. It can happen that this deflects the beam into the MPC which overloads some APD transistors with too much current thereby blowing out their fuses. Afterwards, these APD's cannot function and the associated channels are dead until a repair can be performed. An example of this is shown in Figure 5.11 where this occurred to four channels. This example is from a different dataset and this did not happen in Run09.

<sup>1</sup>By radius we mean radial distance from the beam axis.

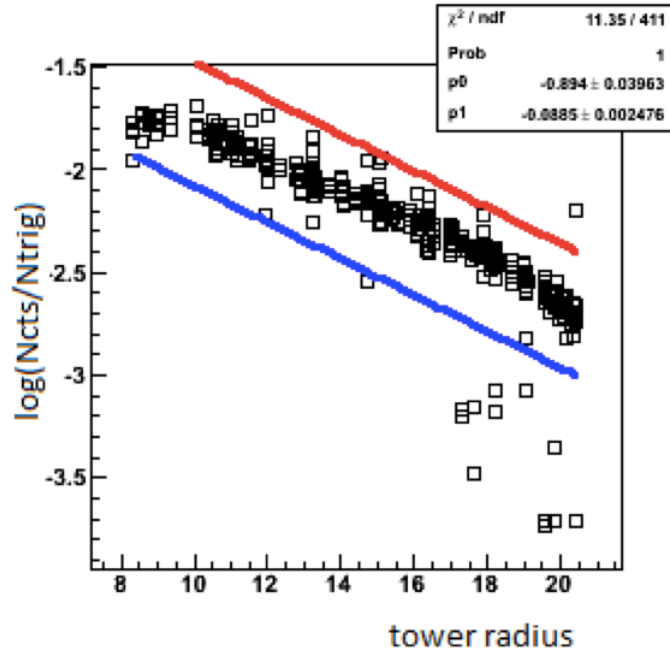


Figure 5.9: For each channel we determine the fraction of minimum bias (BBC) triggers in which the crystal registers a hit in the range of  $3 - 20\text{ GeV}$ . Channels lying above the red line are considered hot while channels lying below the blue line are considered dead. These lines are set (by convention) at  $\pm 3.5\sigma$  offset from the central fit.

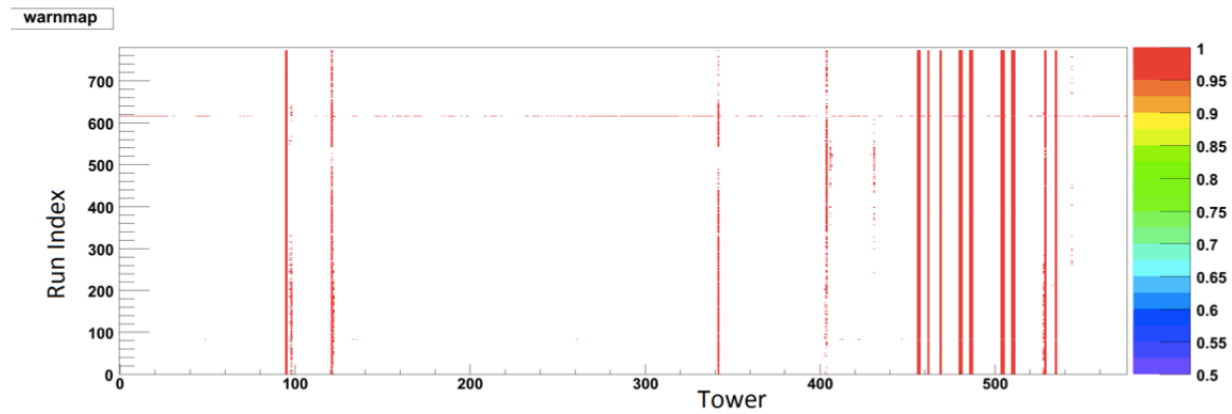


Figure 5.10: Each of the 416 channels (with indices ranging from 0 – 575) is shown on the  $x$ -axis. The  $y$ -axis is a run index, covering the full range of Run09. If a given tower in a given run is hot or dead, that coordinate is shown in red.

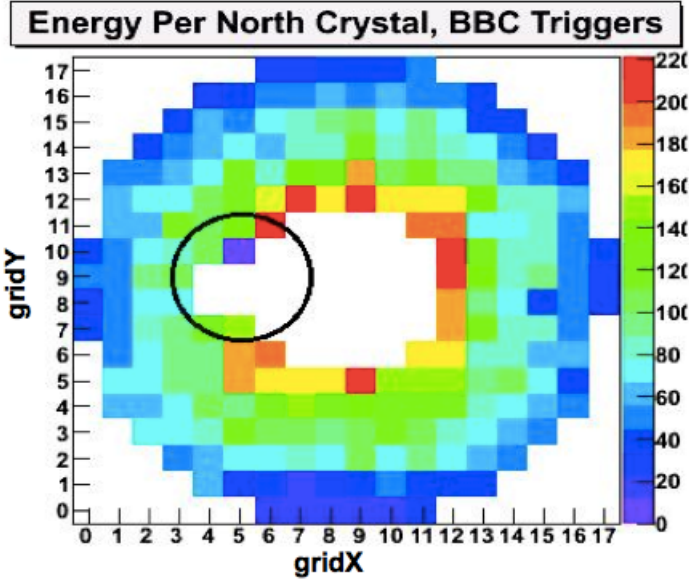


Figure 5.11: An example of the damage an uncontrolled beam dump can do to the MPC. The MPC is particularly susceptible to damage from such events due to its physical proximity to the nominal beam axis. In this example, it appears the beam was dumped into four channels near on the inner region of the MPC.

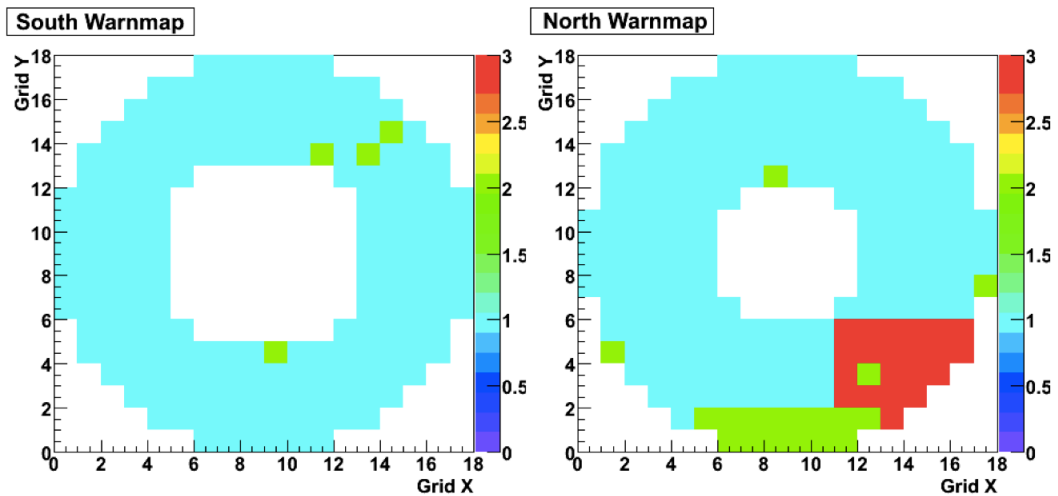


Figure 5.12: The final warnmap used for the Run09 MPC analysis is shown. The crystal map in the south MPC is on the left, while the right is the north MPC map. Channels in blue are used. Channels in red are excluded due to a noisy driver board. Channels in green are excluded due to being hot or dead.

### 5.3.4 $\pi^0$ Reconstructed Mass Dependence on Pair Energy

For higher cluster energies, the minimum reconstructable mass increases. This can be seen from Eq. 5.1. A constant minimum angle between clusters is required in order to resolve both and avoid a single merged cluster. What remains is a proportionality between the reconstructed mass and the pair energy. Figure 5.13

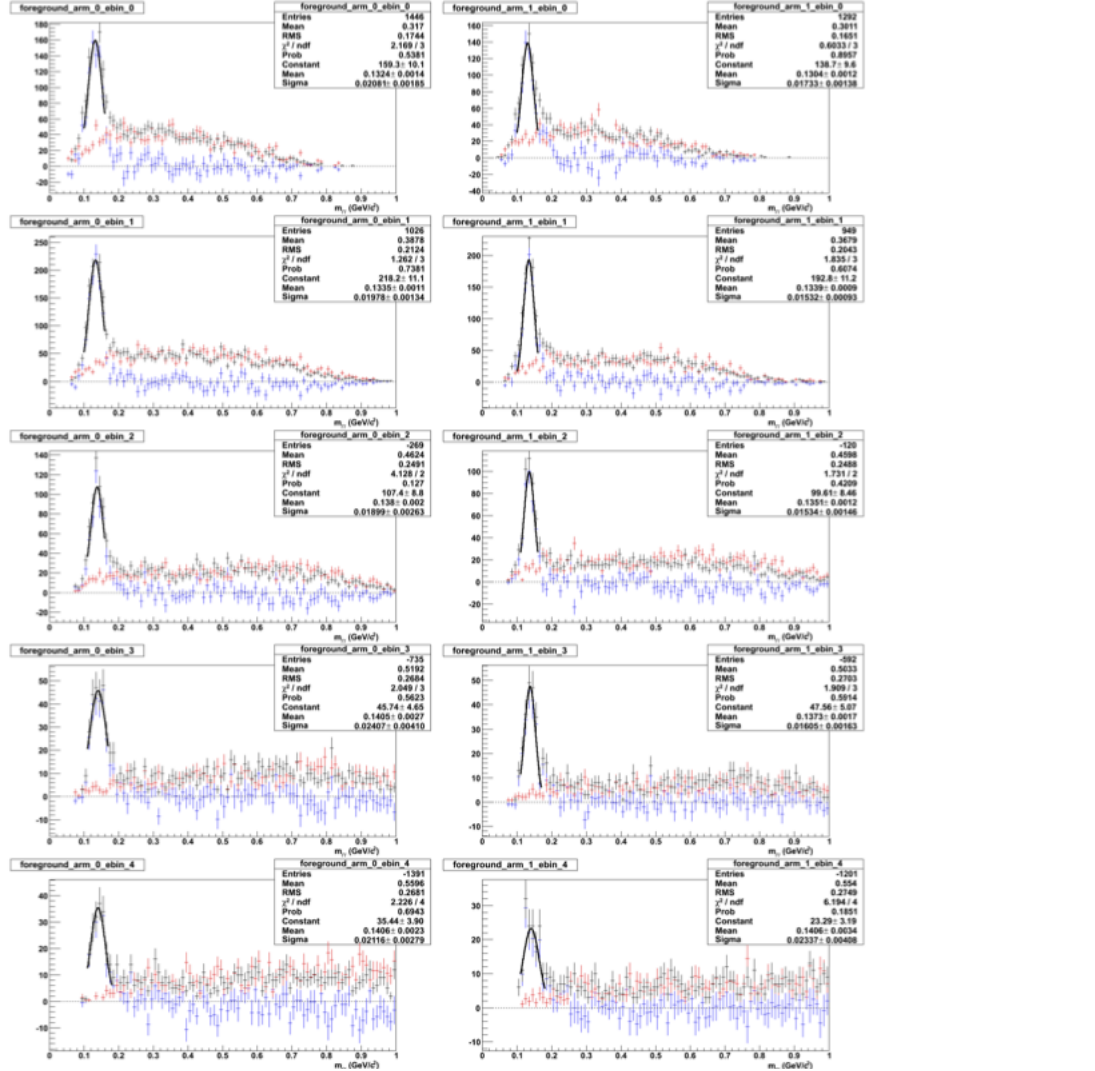


Figure 5.13:  $\pi^0$  peaks for a single fill. The left column is for the south arm, the right column is for the north arm. Going down the peaks are shown in increasing energy bins. Here, we show the signal+background in black. The mixed event background is shown in red. The red blue is the difference.

shows the cluster pair invariant mass spectra for the south and north arms separately in energy bins [10 – 11]  $GeV$ , [11 – 13]  $GeV$ , [13 – 15]  $GeV$ , [15 – 17]  $GeV$ , and [17 – 30]  $GeV$ . These spectra come from one fill, using a minimum bias data with a 30 cm vertex cut. The results are summarized in Figure 5.14 and the

mass dependency on energy can be seen. The cluster cuts used are:

- TDC overflow cut
- $E_{cluster} > 2 \text{ GeV}$
- $\text{chi2core} < 2.5$ . This quantity describes how well the cluster energy distribution across crystals fits the expected electromagnetic shower shape.
- Dispersion  $< 4 \text{ cm}^2$ . This parameter quantifies the lateral spread of energy.

The cluster pairs cuts are:

- Same MPC arm
- Energy asymmetry  $< 0.6$
- $dR > 2.6 \text{ cm}$  where  $dR$  is the distance between the center of gravities of the two clusters.
- Central towers of the two clusters are not adjacent.
- $p_T > 0.5 \text{ GeV}$

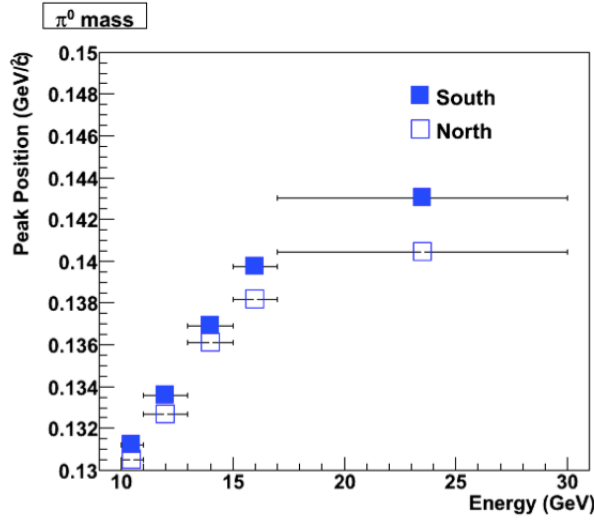


Figure 5.14: Reconstructed  $\pi^0$  mass versus cluster pair energy for the north and south MPC arms.

### 5.3.5 $\pi^0$ Stability

It is expected that the LED's stabilize the detector performance as we saw for the MIPs. For additional confirmation that the LED's track the channel gains and maintain stable detector performance throughout

the run, we check that the location of the  $\pi^0$  mass peak stays constant throughout over time. This check is shown in Figure 5.15.

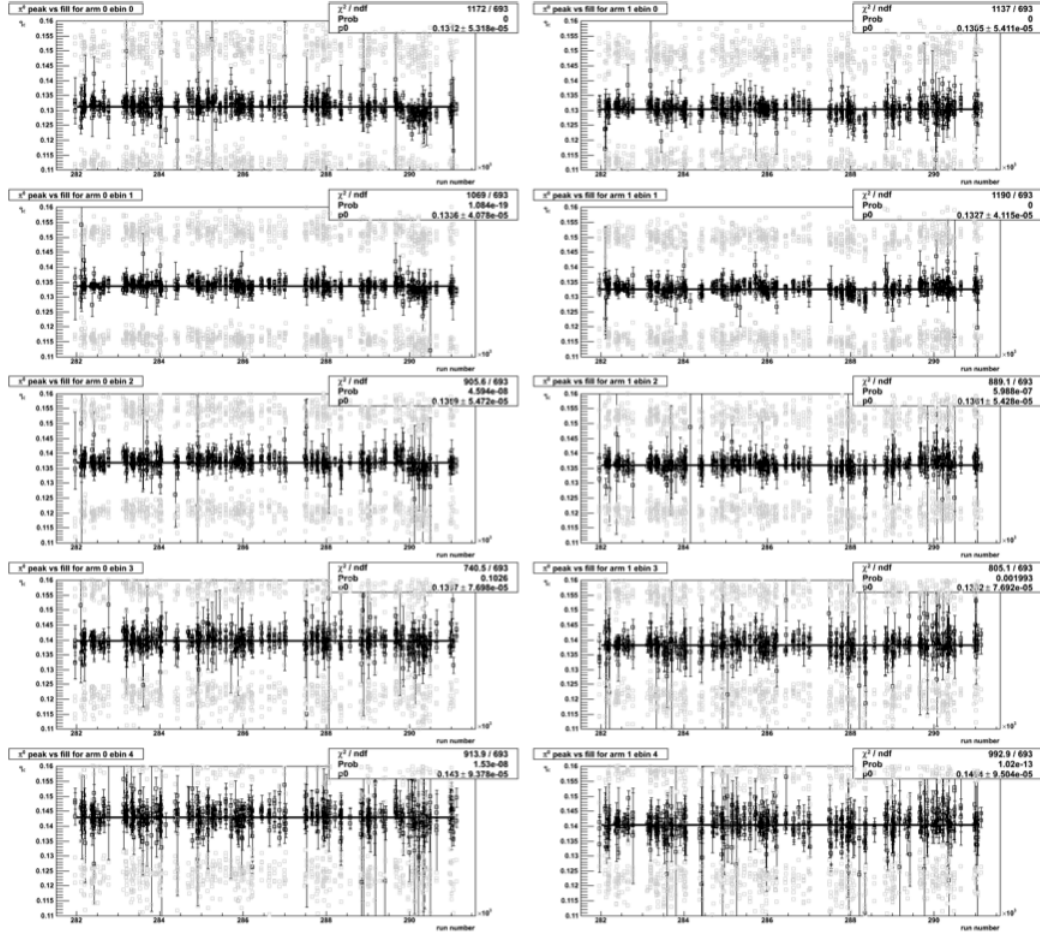


Figure 5.15: The stability of the  $\pi^0$  mass peak is shown for each energy bin for the south(left) and north(right) arms. The grey values indicate the width of the  $\pi^0$  mass peak in each run. The values are stable over the course of the run in all energy bins.

### 5.3.6 $\eta$ Meson Reconstruction

The  $\eta \rightarrow \gamma\gamma$  decay occurs about 39% of the time. Its heavier mass of  $547 \text{ MeV}/c^2$  makes it much less susceptible to merged clusters than the  $\pi^0$  decay. It also lies far above the minimum reconstructible mass so the peak invariant mass measured in the MPC is expected to be more insensitive to the cluster pair energy than the  $\pi^0$ . Therefore it should represent a reliable handle on the overall scaling error in the calibration gains. In Figure 5.16 we show the invariant cluster mass spectra for the south and north MPC with the same cuts as for the  $\pi^0$  but with a higher cluster energy pair requirement. These energy bins are  $[20 - 25] \text{ GeV}$ ,

[25 – 30]  $GeV$ , [20 – 25]  $GeV$ , [30 – 35]  $GeV$ , [35 – 40]  $GeV$  and [40 – 60]  $GeV$ . The cross section is much lower for the  $\eta$  than the  $\pi^0$ , so we use triggered data to recoup the necessary statistics. There is not enough data to do a run by run  $\eta$  stability analysis. Figure 5.17 shows the  $\eta$  mass as a function of energy. Up to

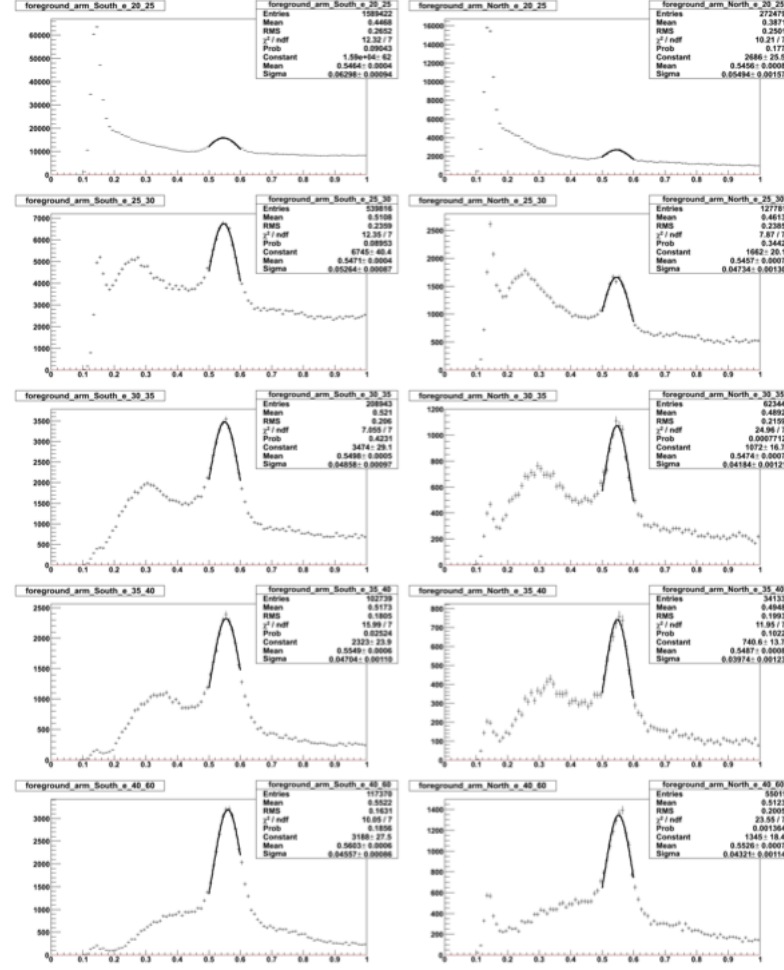


Figure 5.16:  $\eta$  invariant mass spectra using the full MPC triggered dataset. The left column is for the south arm, the right column is for the north arm. Going down the peaks are shown in increasing energy bins.

$E_{pair} = 35 GeV$  the calibration scale is correct to less than 1%. The upward drift in mass is limited to 2.5% and 1.1% for the south and north MPC, respectively.

## 5.4 Detector Quality Assurance

During Run09  $\sqrt{s} = 200 GeV$  running, there were 907 runs taken labeled 'PHYSICS'. Of these, 52 runs are excluded due to having a fillnumber of '0', having problems that were documented by the shift crew, or other miscellaneous reasons. 6 runs removed due to low trigger livetimes and possible DAQ problems. 1

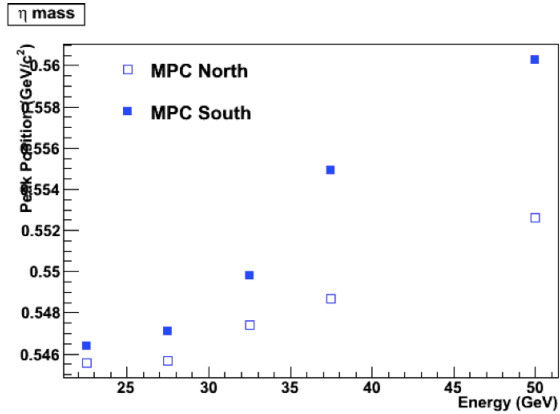


Figure 5.17: Reconstructed  $\eta$  mass versus cluster pair energy for the south and north MPC.

run was taken with the magnets turned off. 3 runs were excluded due to the MPC triggers being excluded. 50 runs are excluded due to not having polarization or helicity information available. 6 runs are excluded due to a spin flip of the bunches in the middle of a fill. 11 runs are excluded because the PHENIX analysis framework did not process them. 23 runs are excluded due to MPC checks, including  $\pi^0$  peak position and number of bad towers. 60 runs are excluded because they do not have physics events. This leaves 695 runs spanning 115 RHIC fills that can be used for the MPC  $A_{LL}$  analysis. Full details regarding the run QA checks for this analysis are available in Ref. [83].

## 5.5 MPC Triggers and Trigger Performance

Two dedicated MPC triggers are available from the Run09 data, the *MPC\_4x4A* and *MPC\_2x2(PT)*. The *MPC\_4x4A* trigger computes analog sums of crystals in 4x4 squares. The *MPC\_2x2(PT)* computes analog sums in 2x2 squares of crystals, and each crystal is weighted in the sum according to its radius in an effort to convert an energy based trigger into an effectively  $p_T$  based trigger. The sum in both cases is then compared to a predetermined threshold. Because the trigger operates on analog signals, not their digitized values, it cannot be precisely emulated offline.

To study the trigger performance we will look at the distribution of cluster centers within the MPC. This shows whether and/or where there is a position dependent trigger efficiency. Next we look at the vertex distributions in MPC triggered events. We will also look at the cluster energy and  $p_T$  spectra along with the trigger efficiency as a function of energy. Finally, we will show an apparent discrepancy in the trigger

logic. Additional information can be found in Ref. [8] and the references therein as well as Ref. [91].

### 5.5.1 Reduced Bit Inputs

The PHENIX GL1 can accommodate a set of 32 trigger inputs at a time. The Reduced Bit Input Board (RBIB) feeds into the GL1 but has trigger inputs (Reduced Bits, or RBITS) that are not used or combined with other inputs before being sent to GL1. However, the RBIB inputs are read out for each event. The MPC is allocated some of these inputs, which allows one to know slightly more information about the event. The

RBIT	Trigger
67	<i>MPC_4x4A</i>
68	<i>MPC_4x4C</i> North
69	<i>MPC_4x4C</i> South
70	<i>MPC_2x2(PT)</i> North
85	<i>MPC_2x2(PT)</i> South

Table 5.1: Summary of RBIT Inputs used for the Run09 analysis.

details of the RBIT inputs to the RBIB in Run09 are shown in Table 5.1. Information on the RBIB inputs in other years are documented in the PHENIX offline wiki at [offline/wikioff/index.php/MPC\\_TRIGGER](http://offline/wikioff/index.php/MPC_TRIGGER). The only difference between the *MPC\_4x4C* trigger seen in this table and the *MPC\_4x4A* trigger is the threshold against which the analog channel sum is compared. RBIT 67 is passed directly into GL1, but RBITS 70 and 85 are OR’ed. Therefore if the GL1 triggers on *MPC\_2x2(PT)* the RBIT lookup can distinguish between arms. The *MPC\_4x4A* was OR’ed between the north and south upstream of the RBIB. Therefore, information on which arm triggered is not directly available in this case. To distinguish between the arms in data we use the highest energy cluster in the event. RBITS 68 and 69 were AND’ed with central arm triggers and are available but are not used in this analysis due to their low threshold.

### 5.5.2 MPC Radiographs

The radiograph is a graph of the centers of clusters, integrated over a large number of events with a minimum energy of  $E_{cluster} > 15 \text{ GeV}$ . Figures 5.18(a,b) show a radiograph of both MPC arms for minimum bias events. In minimum bias events, we expect to see a nearly azimuthally symmetric distribution and no large abnormalities, conditional upon the quality of the calibrations. This is seen to be the case, and the position resolution is sufficient to even see some of the mechanical structure of the MPC frame. The only abnormality is seen in the bottom towers in the north MPC. This is expected since these are the towers blocked by the beam-pipe stand. Figures 5.18(c,d) show the radiograph in both MPC arms when the MPC triggers. A clear abnormality is seen in the south which means that the trigger efficiency is position dependent. In

Figure 5.18c, for example, many of the outer channels appear very hot in the triggered data, but normal in the minbias data. Other channels appear very cold in the triggered data but normal in the minbias data. The north arm also sees some position dependence. Based on the FEM-to-crystal channel mapping ([8]) the dependence of the trigger efficiency on position occurs in both FEM's.

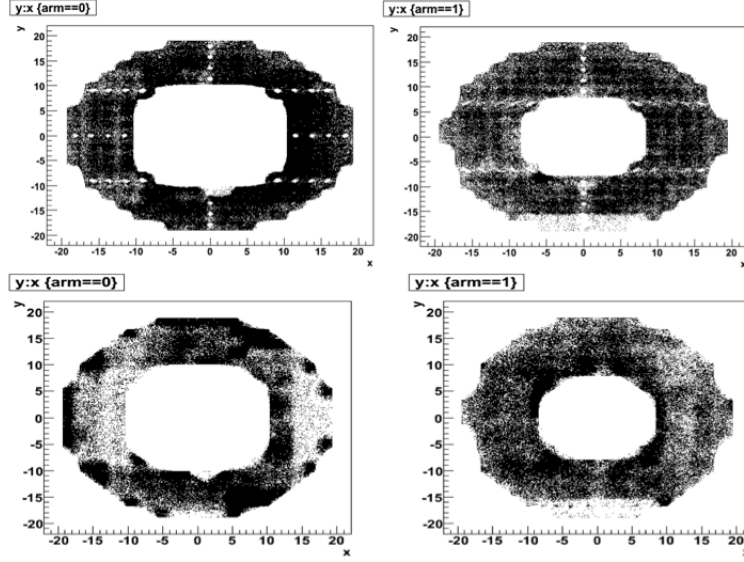


Figure 5.18: Top Left (a): Radiograph of south MPC clusters from minbias triggered events. Top Right (b): Radiograph of north MPC clusters in minbias triggered events. Bottom Left (c): Radiograph of south MPC clusters in MPC triggered events. Bottom Right (d): Radiograph of north MPC clusters in MPC triggered events.

### 5.5.3 Vertex Distributions

The standard vertex determination in PHENIX comes from the BBC. If the BBC measures one or more hits in each arm, the  $z$  position of the collision can be determined via  $z = \frac{c}{2}(t_S - t_N)$ . Figure 5.19 shows the vertex distribution for *MPC\_4x4A* triggered events. This is compared with the vertex distribution from minimum bias events taken from the *BBCLL1(noVertexCut)*. While the true collision distribution is seen to be nearly symmetric about  $z = 0$ , the north trigger has a bias towards events with  $z < 0$  while the south trigger has a bias towards  $z > 0$ . These biases can be understood in terms of the MPC acceptance. For example, for an event with  $z < 0$ , the MPC north acceptance is shifted from its nominal  $3.1 < |\eta_{nominal}| < 3.8$  to  $3.1 + \delta < |\eta_{effective}| < 3.8 + \delta$  where  $\delta > 0$ . This creates a bias in favor of events producing jets at higher rapidity in which the forward boost is greater and the energies, as measured in the lab frame, are larger. The opposite effect is true in the north for  $z > 0$ . The south bias towards events with  $z > 0$  is explained similarly.

The south trigger also has less statistics than the north. This is the same effect we saw in Figs. 5.18(c,d).

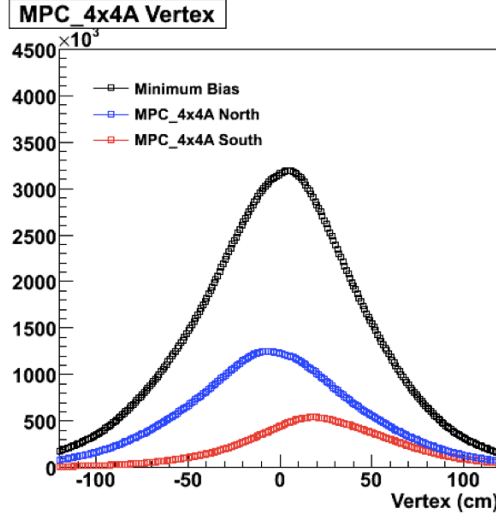


Figure 5.19: Vertex distributions are shown for the north and south *MPC\_4x4A* triggers. A comparison with the minimum bias vertex trigger shows each MPC arm is biased towards events occurring farther away from it.

Figure 5.20 shows the vertex distributions for the *MPC\_2x2(PT)* trigger. In this case the vertex bias is not so clear, but once again the south has many fewer trigger than the north. The settings in this trigger may not have been as reliable as in the case of the *MPC\_4x4A*. It should also be noted that no MPC triggers are logically AND'ed with the BBC coincidence trigger. This is done so as not to introduce any additional trigger biases. As a result, not every MPC triggered event has a reconstructed vertex. An analysis of this shows that a reconstructed vertex is available in about 80% of MPC triggered events.

#### 5.5.4 Cluster Energy and $p_T$ Spectra

Figure 5.21 shows the cluster energy and  $p_T$  spectra for the *MPC\_4x4A* trigger. The trigger turn-on can be seen to occur at  $E_{clus} \approx 20\text{GeV}$  or  $p_{T,clus} \approx 1\text{GeV}/c$ . Because the trigger is an analog sum and the channels are not calibrated in the sum, the turn-on curve is fairly broad. The minbias spectra in each arm are very similar, but the triggered spectrum drops off much earlier in the south than the north. In Figure 5.22 we show the ratio of the two spectra as a function of  $p_{T,clus}$ . At high  $p_T$  the south spectrum is nearly an order of magnitude lower indicating a large inefficiency. Therefore, the measured  $A_{LL}$ , while combined between north and south, will be dominated by clusters in the north. For a given  $p_T$  bin, defining the  $p_T$  of the event

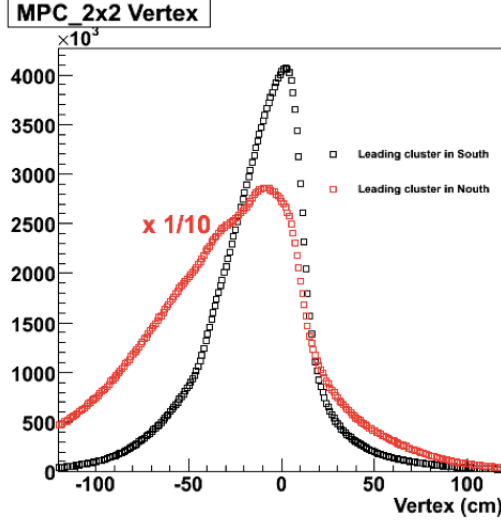


Figure 5.20: Vertex distributions are shown for the north and south  $MPC\_2x2(PT)$  triggers

as the highest cluster  $p_T$  in the event, we can calculate the trigger efficiency as:

$$\epsilon_{MPC} \equiv \frac{N^{MPC \wedge BBC}}{N^{BBC}} \quad (5.7)$$

To determine the efficiency, we simply loop over BBC triggered events and then determine the highest energy cluster and whether or not the MPC trigger fired for that event. The result is shown in Figure 5.23, which sums up what we have seen in the MPC radiographs, the vertex distributions, and the cluster spectra: the north trigger is highly efficient while the south is not. Specifically, the north reaches 50% efficiency for  $E_{clus} \approx 45\text{ GeV}$  and plateaus at 97% efficiency. The south plateaus at only 27% efficiency.

### 5.5.5 $MPC\_2x2(PT)$ Trigger Consistency Issue

As the RBIT inputs are available for the  $MPC\_2x2(PT)$  trigger we can check the consistency of the these bits with the trigger result. In Figure 5.24 we show each of the 8 combinations of the 2 RBITS and the trigger. The expectation is that the trigger fires if, and only if, the north or south RBITS fire. However, comparing the cases when just the south bit fires, it only results in a trigger 0.02% of the time. On the other hand, a trigger results with  $> 99.9\%$  probability if the north RBIT fires. In addition, about 10% of the trigger rate can be seen to have no associated RBIT hits. These two observations are consistent with a timing issue in the south trigger signal. This is separate from the low south efficiency as that was seen in the  $MPC\_4x4A$  trigger. We can learn more about this from Figure 5.25, where we show the vertex distributions when the  $MPC\_2x2(PT)$  fires. We separate the cases where neither RBIT fires, just the south(north) and

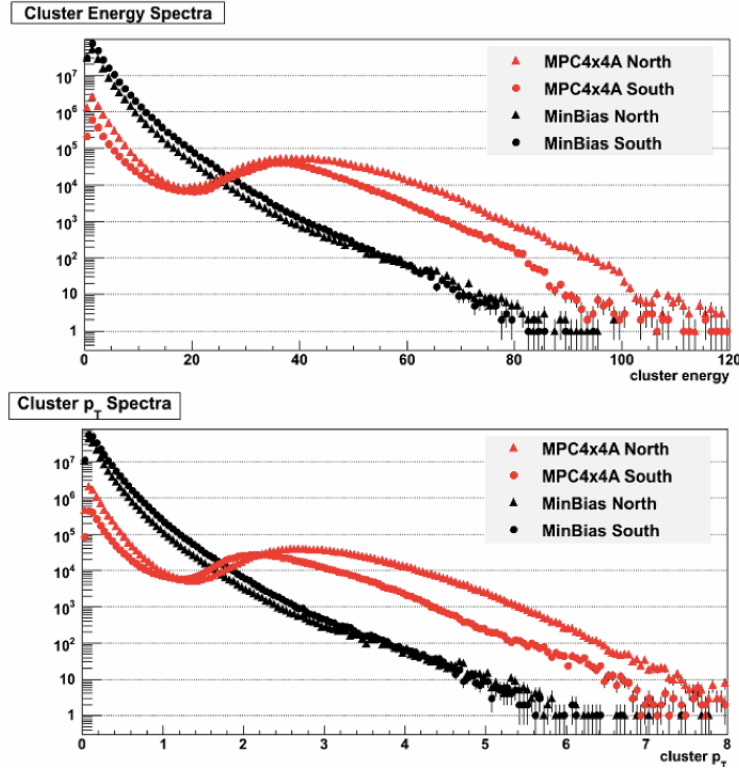


Figure 5.21: Top (a): Cluster energy spectra. Bottom (b): Cluster  $p_T$  spectra. The MPC triggered spectrum is shown for each arm and compared to the minimum bias spectrum.

both RBITs fire. When just the south fires, the vertex distribution looks like the minimum bias data. This is consistent with that trigger timing being matched to the phase of a different crossing. When the north fires, we see a vertex distribution consistent with a bias toward  $z < 0$ .

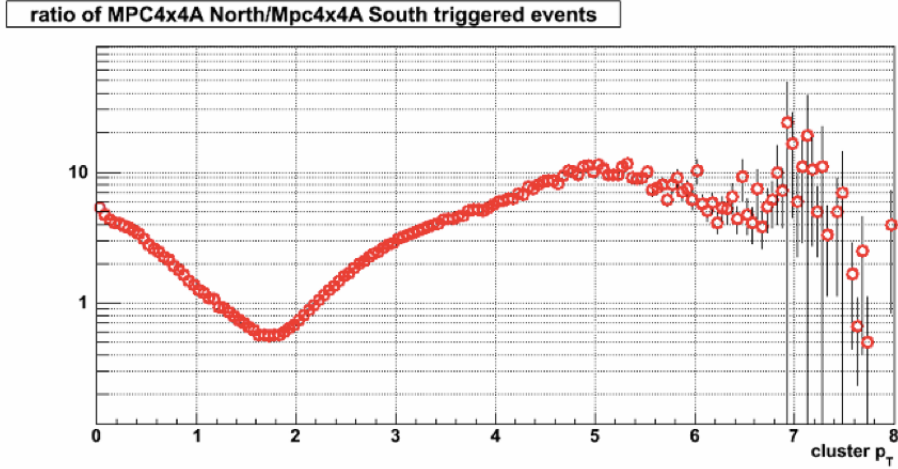


Figure 5.22: Ratio of the number of counts in the north arm versus south arm in *MPC\_4x4A* triggered events as a function of cluster  $p_T$ .

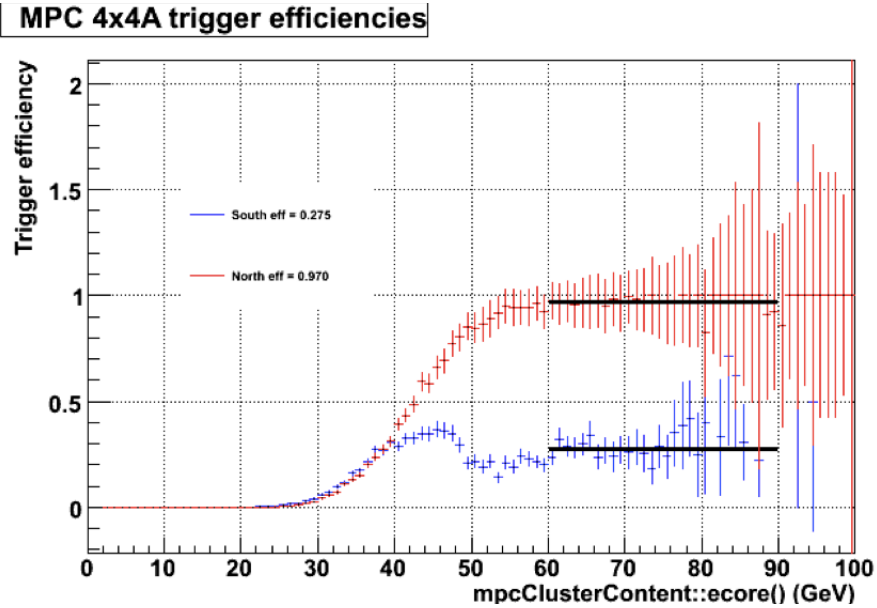


Figure 5.23: Efficiency of the *MPC\_4x4A* trigger versus energy. Both detectors can be seen to have the same threshold as the efficiency picks up near  $E_{clus} \approx 25 - 30$  GeV. However, the south is observed to plateau much earlier than intended. From Table 5.1, recall that we do not have information directly about which arm triggered. Therefore, as a proxy, as we loop through triggered events, we use the arm with the highest energy cluster as the triggered arm.

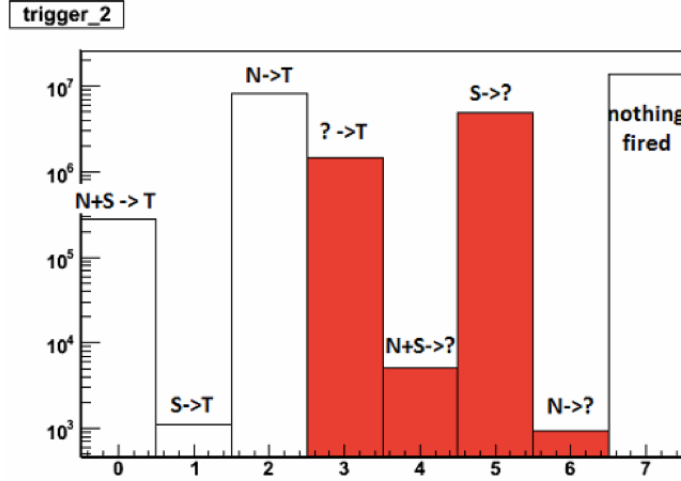


Figure 5.24: A plot checking the consistency of the  $MPC\_2x2(PT)$  trigger.  $N(S)$  means the north(south) RBIT fired, and  $T$  means the trigger fired. “?” means neither RBIT fired but the trigger did not, or that the trigger fired but the RBITs did not. “ $N+S \rightarrow T$ ” means the north and south RBITs fired and a trigger was found, while “ $S \rightarrow ?$ ” means the south RBIT fired but no trigger resulted.

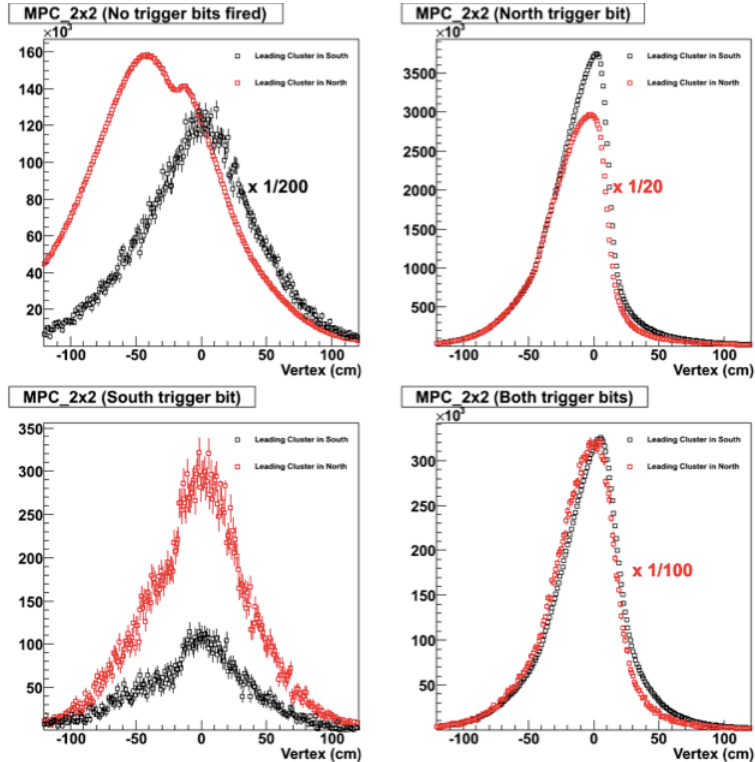


Figure 5.25: Top Left (a): No RBITs fired. Top Right (b): North RBIT only fired. Bottom Left (c): South RBIT only fired. Bottom Right (d): Both RBITs fired. In all cases the  $MPC\_2x2(PT)$  triggered and the north and south vertex distributions are separated based on which arm the leading cluster is found in.

## 5.6 Relative Luminosity

For this analysis we use the BBC as the relative luminosity detector, and the ZDC luminosity as a comparison.

For this analysis the relative luminosity is calculated as:

$$R = \frac{L_{BBCLL1}^{++}}{L_{BBCLL1}^{+-}} \quad (5.8)$$

For this analysis, no rate corrections applied to the BBC or ZDC luminosity scalers. The systematic uncertainty due to the relative luminosity is estimated in Ref. [110] via a width correction method to be:

$$\delta R = 1.407 \times 10^{-3} \quad (5.9)$$

As we will see in Chapters 8 and 9, recent developments have provided significant improvements in the level of control over this systematic error. The systematic error as determined in Ref. [110] does not yield a better agreement between the ZDC and BBC relative luminosities than making no corrections at all. Figure 5.26

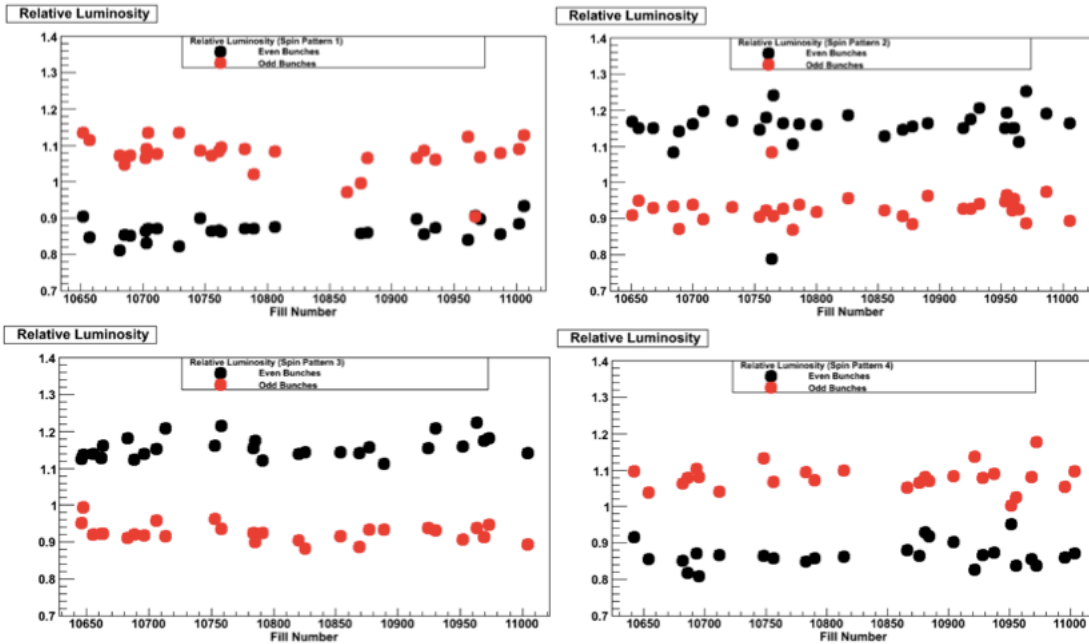


Figure 5.26: The relative luminosity is shown separately for each spin pattern (SP) vs. fill number. Top Left (a): SP1. Top Right (b): SP2. Bottom Left (c): SP3. Bottom Right (d) SP4. In each case even (black) and odd (red) bunches are shown separately.

shows the relative luminosities separated by spin pattern and by even or odd bunches. The definitions of the spin patterns used in this analysis are given in Ref. [83]. Typically, the relative luminosity between the

two helicity states is close to  $R \approx 0.9$  or  $R \approx 1.1$ . Figure 5.27 shows a comparison of the ZDC and BBC

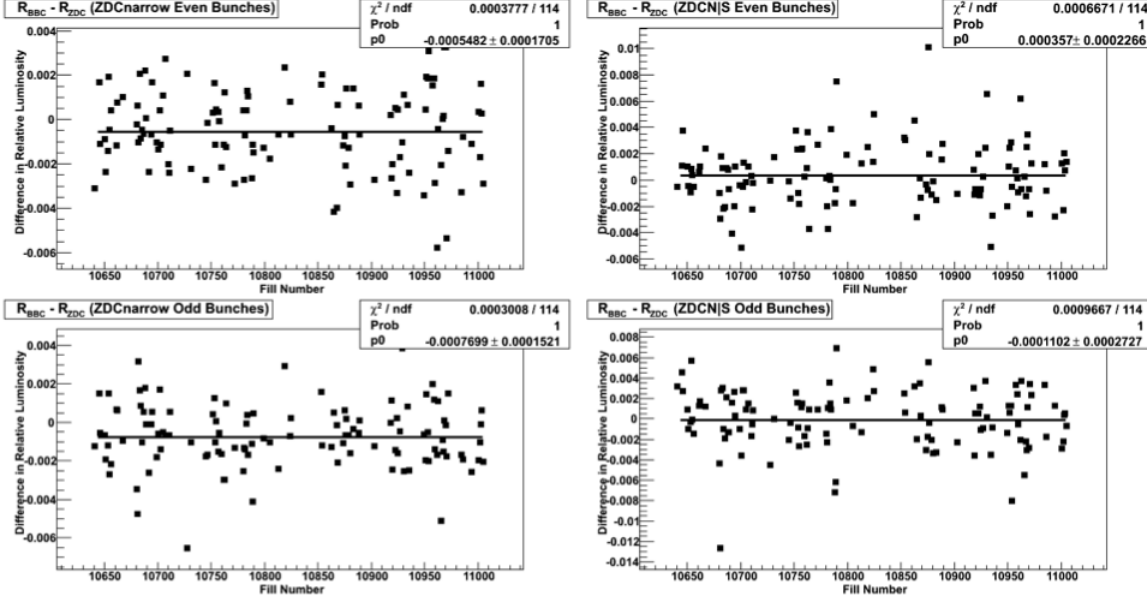


Figure 5.27: Top Left (a): Difference in relative luminosity vs fill using the  $BBCLL1$  and  $ZDCLL1$  narrow vertex triggers for even bunches only. Top Right (b): Same as (a), but using the single sided ZDC scaled trigger instead of the coincidence. Note the difference in sign of the average offset with (a). This shows that the two ZDC scalers are offset from one another. Bottom Left (c), and Bottom Right (d) show the same as (a) and (b) in the case of odd bunches. Again, an offset is seen between the ZDC and BBC as well as between the two ZDC scalers. The large fill- to-fill fluctuations at the level of  $O(10^{-3})$  are not understood yet or improved by the width correction.

relative luminosities using the uncorrected scalers. In Ref. [83] we also show this comparison separated by spin pattern, where additional systematic differences are seen. The results are summarized in Table ??.

The official determination of the relative luminosity uncertainty for this data set does not check or take into

Spin Pattern	Even/Odd	$\langle R_{BBC} - R_{ZDC} \rangle (\times 10^{-3})$
1	Even	-1.041
	Odd	-1.45
2	Even	0.258
	Odd	-0.458
3	Even	-0.145
	Odd	0.257
4	Even	-1.425
	Odd	-1.502

Table 5.2: Average difference in relative luminosity as measured in the BBC and the ZDC.

account these observations. It assumes the only effect that is present, on which the correction is based, is a ZDC resolution based miscounting of the luminosity.

## 5.7 Analysis Cuts

We use the *MPC4x4A* and *MPC\_2x2(PT)* triggered samples and require that a vertex was reconstructed for the event at  $|z| < 30\text{ cm}$ . The single cluster cuts are:

- $E_{clus} > 15\text{ GeV}$
- The center crystal of the cluster is not masked out by the warnmap.
- Cluster radius,  $r$ , from beam-line satisfies  $12\text{ cm} < r < 19\text{ cm}$ .
- ADC overflow is removed.
- TDC overflow is removed.

Note that no shower shape cut is applied. This is because we are expected to be looking at merged clusters. While each cluster alone would typically have an electromagnetic shower shape, the merged cluster is not expected to have a shape consistent with that of a single shower. In Figure 5.28 we show the efficiencies of these cuts as a function of cluster energy. The efficiency of each cut in MPC triggered events is defined as:

$$\epsilon_{cut} = \frac{\#(MPC \wedge cut)}{\#MPC} \quad (5.10)$$

where the numerator is the number of clusters in MPC triggered events passing the cut and the denominator is the number of MPC triggered events. For the case of the vertex cut, the numerator is the number of MPC triggered events with a vertex reconstructed within  $|z| < 30\text{ cm}$ . In this case the cluster with the highest energy is used. The efficiency of each cut is considered independently of the others. Figures 5.28a and 5.28c show the vertex and TDC cut efficiencies. These are largely independent of the cluster energy, or  $p_T$ . A slight dip is seen near the turn-on point in the south arm. Fig. 5.28b shows a significantly lower radius efficiency in the north than the south. This is due to the fact that the north arm has an inner ring of towers that the south arm does not have. These towers lie at a radius smaller than the radius cut so all clusters they see get cut. The efficiencies in both arms rise with  $p_T$ . This is due to higher energy, and higher  $p_T$ , clusters having a typically larger angle with respect to the beam-line. Fig. 5.28e shows that the ADC overflow cut removes 80 – 90% of clusters at high energy. The dynamic range of the crystals range from about  $40\text{ GeV}$  to  $60\text{ GeV}$ .

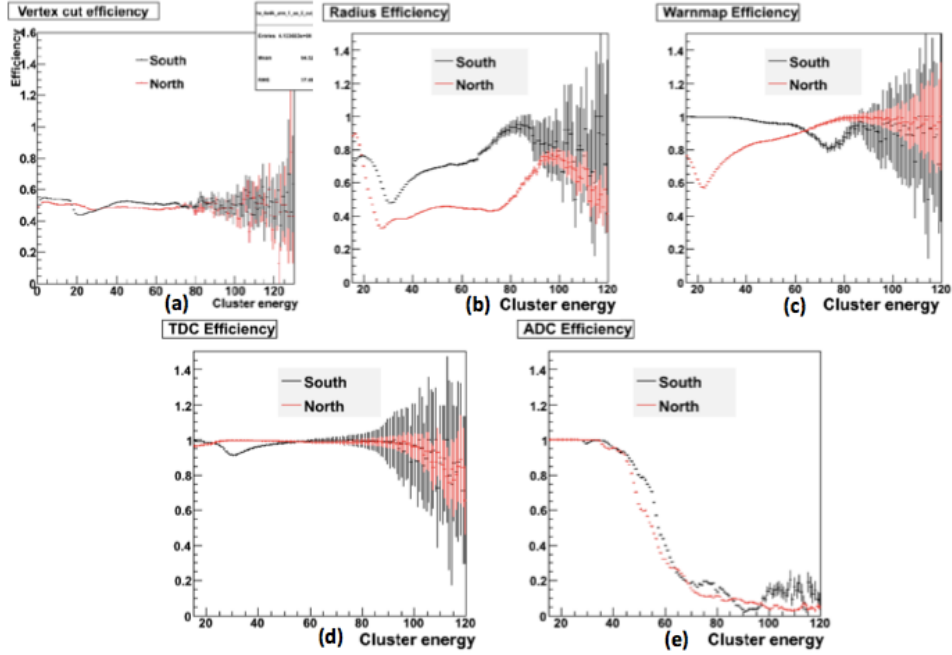


Figure 5.28: (a) Vertex cut efficiency. (b) Cluster radius cut efficiency. (c) Warnmap efficiency. (d) TDC overflow cut efficiency. (e) ADC overflow cut efficiency.

## 5.8 Binning For Asymmetry Calculation

Two trigger circuits alternate in the MPC trigger. To check whether this causes any systematic effects we perform the analysis separately on even and odd bunch crossings. Once the results are found to be statistically consistent with each other, they are combined. Additionally, asymmetries are calculated in the north and south arms separately, checked for consistency, then combined.

The kinematic binning is done in  $p_T$  and the bin ranges are as follows (all in units of  $(GeV/c)$ ): [1.0 – 1.5], [1.5 – 2.0], [2.0 – 2.5], [2.5 – 3.0], [3.0 – 4.0], [4.0 – 5.0], [5.0 – 10.0]. The asymmetry in each bin is plotted at the mean  $p_T$  for that bin.

## 5.9 Asymmetry Results

We calculate the  $A_{LL}$  for even and odd crossings and both arms, in a given  $p_T$  bin, for each fill independently. For odd(even) crossings the relative luminosity is calculated for the same crossings. The official polarizations for each fill are provided in Ref. [111]. Figure 5.29 shows the raw asymmetries for one bin. The asymmetry

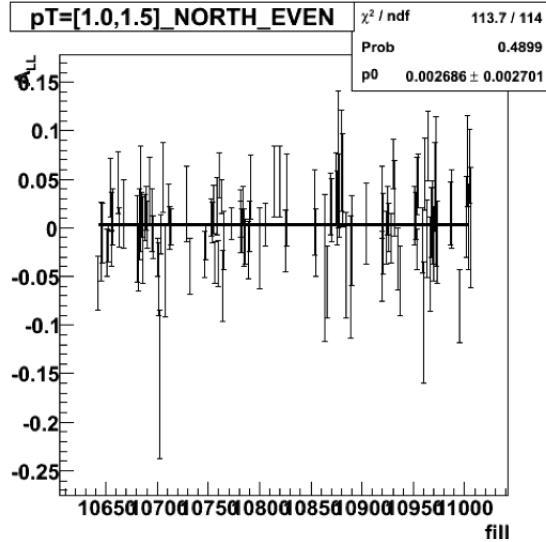


Figure 5.29: Sample fill by fill  $A_{LL}$  results. The final asymmetry for this bin is determined by taking the weighted average, or equivalently, fitting all the asymmetries to a constant value.

for that bin is determined from the weighted average of the fill by fill asymmetries. The complete numerical results are given in Table 5.3.

## 5.10 Bunch Shuffling

Bunch shuffling is a standard technique used to check the statistical uncertainties. After computing the physics asymmetry,  $A_{LL}^{phys} \pm \delta A_{LL}^{phys}$ , we shuffle, or randomize, all the spins and repeat the analysis 10,000 times, to get a set of shuffled asymmetries,  $A_{LL}^{shuf}$ . Then we plot  $A_{LL}^{shuf} / \delta A_{LL}^{phys}$ . With randomized spins, the mean of this distribution is expected to be 0 regardless of what the physics asymmetry is. Also, the width should be 1, indicating the uncertainty is correctly determined. Figure 5.30 shows an example of the results obtained in one bin from bunch shuffling. The bin by bin results of bunch shuffling are also shown in Table 5.3. An additional check that the  $\chi^2$  distribution of the bunch shuffled fits was consistent with that expected from the appropriate number of degrees of freedom was performed, with no anomalies found.

Table 5.3:  $A_{LL}$  results for electromagnetic clusters in the MPC at  $\sqrt{s} = 200$  GeV

$[p_T^{min}, p_T^{max}] (GeV/c)$	Arm	Crossings	$A_{LL}$	$\delta A_{LL}$	$\chi^2/NDF$	$\langle A_{LL}^{shuf}/\delta A_{LL}^{phys} \rangle$	$\sigma_{\langle A_{LL}^{shuf}/\delta A_{LL}^{phys} \rangle}$
[1.0, 1.5]	north	even	0.002686	0.002701	113.7/114	-0.0249±0.0104	1.0151
	north	odd	-0.001804	0.002627	117/114	-0.0039±0.0105	1.0278
	south	even	-0.00208	0.001459	108.5/114	0.0141±0.0104	1.0160
	south	odd	-0.000345	0.001425	106.3/114	-0.0039±0.0105	1.0278
[1.5, 2.0]	north	even	-0.0008083	0.001868	127.9/114	-0.0220±0.0109	1.0595
	north	odd	0.001071	0.001819	96.6/114	0.0012±0.0103	1.0109
	south	even	-0.001336	0.001408	130.8/114	-0.0145±0.0107	1.0454
	south	odd	0.001424	0.001371	143.4/114	0.0012±0.0103	1.0169
[2.0, 2.5]	north	even	0.000069	0.00181	102.9/114	0.0093±0.0106	1.0317
	north	odd	0.001117	0.001763	155.7/114	-0.0069±0.0105	1.0240
	south	even	-0.001802	0.002021	115.3/114	0.0047±0.0104	1.0168
	south	odd	0.000789	0.001963	124.2/114	-0.0069±0.0105	1.0240
[2.5, 3.0]	north	even	-0.001028	0.002006	115.4/114	0.0082±0.0101	0.9938
	north	odd	-0.001834	0.001955	138.2/114	0.0122±0.0103	1.0087
	south	even	-0.005428	0.002883	115.4/114	-0.0079±0.0101	0.9867
	south	odd	0.002448	0.002807	98.56/114	0.0122±0.0103	1.0087
[3.0, 4.0]	north	even	0.001285	0.002152	88.12/114	0.0084±0.00102	0.9995
	north	odd	0.004152	0.002094	115.8/114	0.0097±0.0102	0.9996
	south	even	0.002091	0.003326	101.9/114	0.0035±0.0100	0.9828
	south	odd	-0.004216	0.003237	111.8/114	0.0097±0.0102	0.9996
[4.0, 5.0]	north	even	-0.007069	0.005631	94.87/114	0.0191±0.0099	0.9740
	north	odd	0.001744	0.005484	130.1/114	0.0103±0.0102	1.0004
	south	even	0.005582	0.008668	125.9/114	0.0145±0.0103	1.0129
	south	odd	-0.008829	0.008402	99.67/114	0.0103±0.0102	1.0004
[5.0, 10.0]	north	even	-0.01593	0.01712	120.8/114	-0.0202±0.0103	1.0058
	north	odd	-0.002492	0.01678	117.3/114	0.0053±0.0105	1.0213
	south	even	-0.01709	0.01763	111.8/114	-0.0172±0.0105	1.0240
	south	odd	-0.02445	0.01715	111.6/114	0.0053±0.0105	1.0213

## 5.11 Final $A_{LL}^{cluster}$

The asymmetries in even vs odd crossings are found to be consistent with each other. They are statistically combined to yield a final asymmetry in the south and north arms separately. This result is shown in Figure 5.31. Due to the south MPC trigger inefficiency, the error bars in the north are much smaller. The south and north results are found to be statistically compatible and subsequently combined to yield the final MPC  $A_{LL}^{cluster}$  result in Figure 5.32. Table 5.4 contains the final asymmetries and statistical uncertainties by  $p_T$  bin. Aside from the relative luminosity error (the black bar), no internal consistency checks indicated the need for additional systematic uncertainties to be applied.

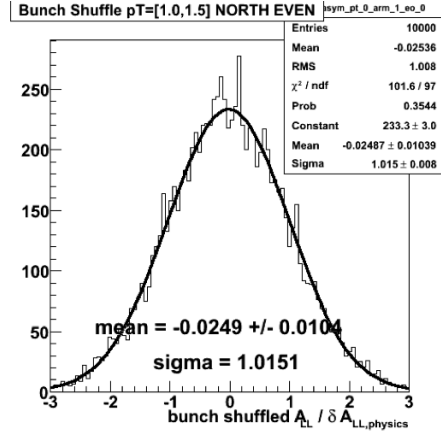


Figure 5.30: Example of the bunch shuffled analysis results. The distribution is a gaussian centered at 0 with a width close to 1, as expected.

Table 5.4:  $A_{LL}$  results for electromagnetic clusters in the MPC at  $\sqrt{s} = 200$  GeV

$p_T^{min}$	$p_T^{max}$	$\langle p_T \rangle$	$A_{LL}^{cluster}$	$\delta A_{LL}^{cluster,stat}$
1.0	1.5	1.29908	-0.000347715	0.000866202
1.5	2.0	1.71993	-0.00136702	0.000946358
2.0	2.5	2.22482	-0.000164827	0.00106187
2.5	3.0	2.71756	0.00172619	0.0012017
3.0	4.0	3.35776	-0.000423999	0.0012071
4.0	5.0	4.31682	0.00235937	0.00246881
5.0	10.0	5.55072	0.00271174	0.00568147

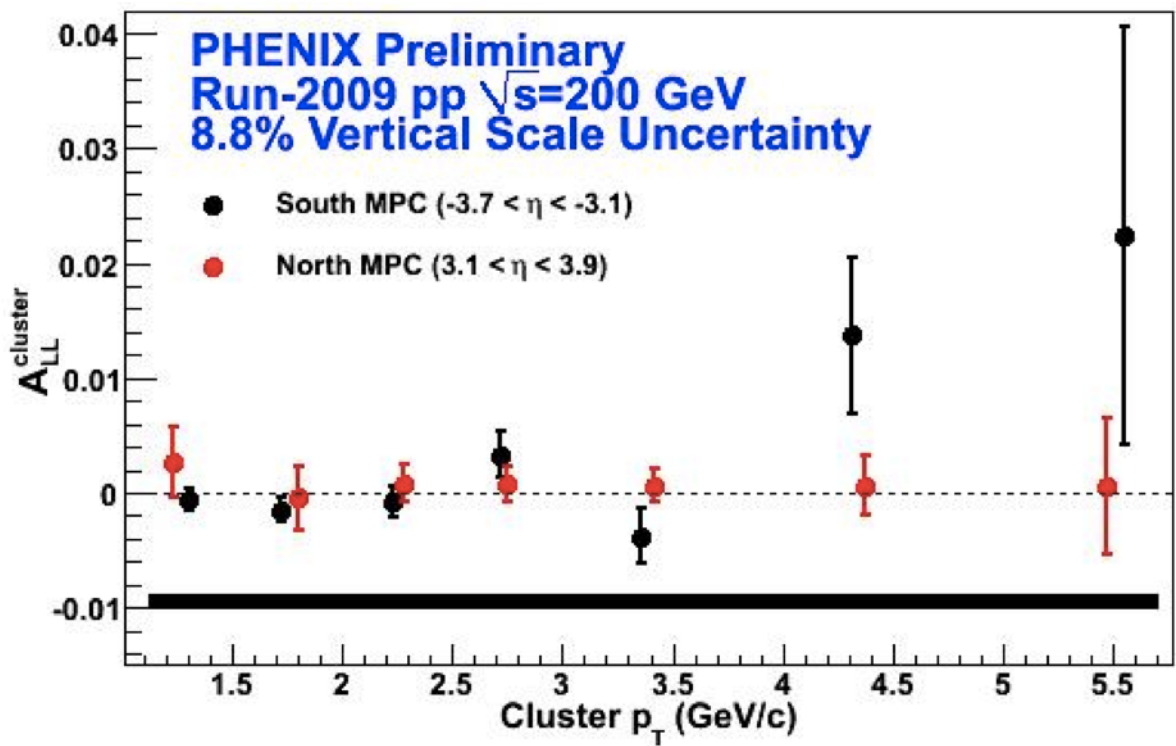


Figure 5.31: MPC  $A_{LL}^{cluster}$  result for the south and north arms separately.

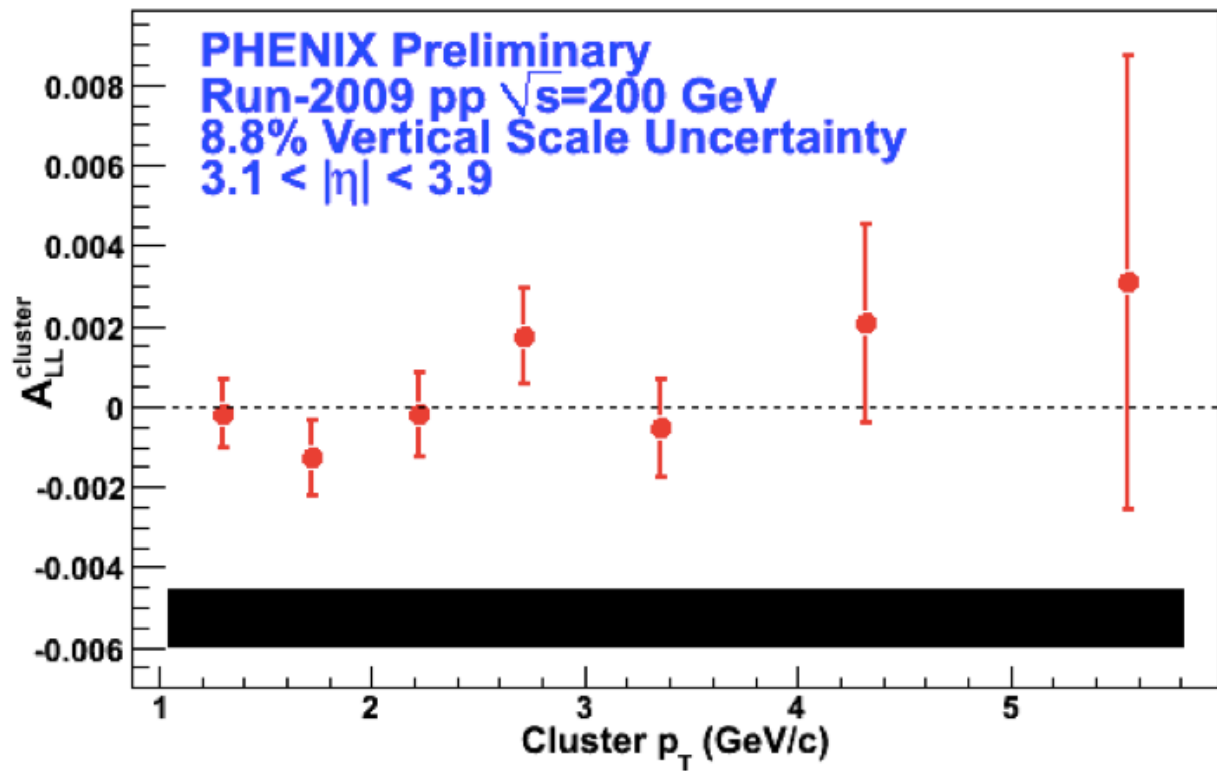


Figure 5.32: PHENIX preliminary result for  $A_{LL}^{cluster}$  in the MPC.

## 5.12 Check of Spin Pattern Consistency

An additional check is to compute the asymmetries separated by spin pattern, as systematic differences are liable to be found between them. The asymmetries for the south/north MPC using only even/odd bunches are shown in Figure 5.33, where the computation is done separately for all fills of each type of spin pattern. The T-test between two  $A_{LL}$ 's is defined by

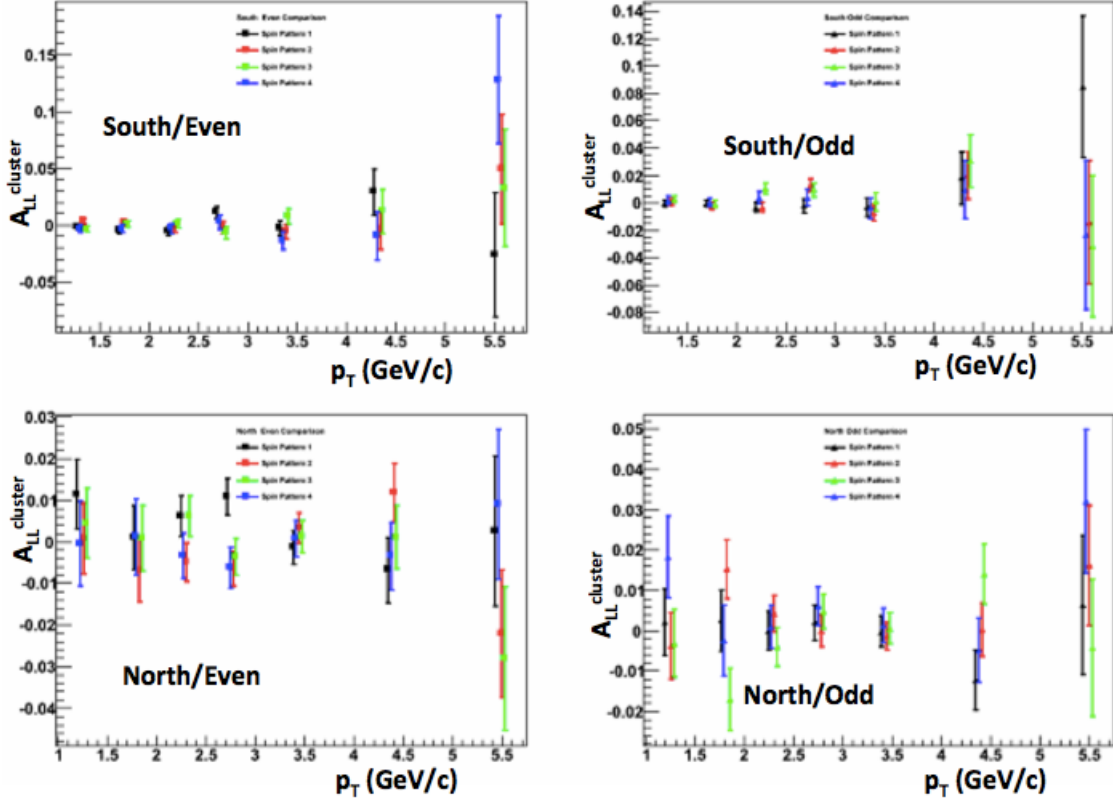


Figure 5.33:  $A_{LL}$  is computed in the south/north MPC for even/odd bunches. In each case the analysis is done for each spin pattern separately and the results are compared.

$$T\text{-score} = \frac{A_{LL,1} - A_{LL,2}}{\sqrt{\delta A_{LL,1}^2 + \delta A_{LL,2}^2}} \quad (5.11)$$

and the point by point T-score is shown between each pair of spin patterns in Figure 5.34. No systematic differences were found to exist between the different spin patterns.

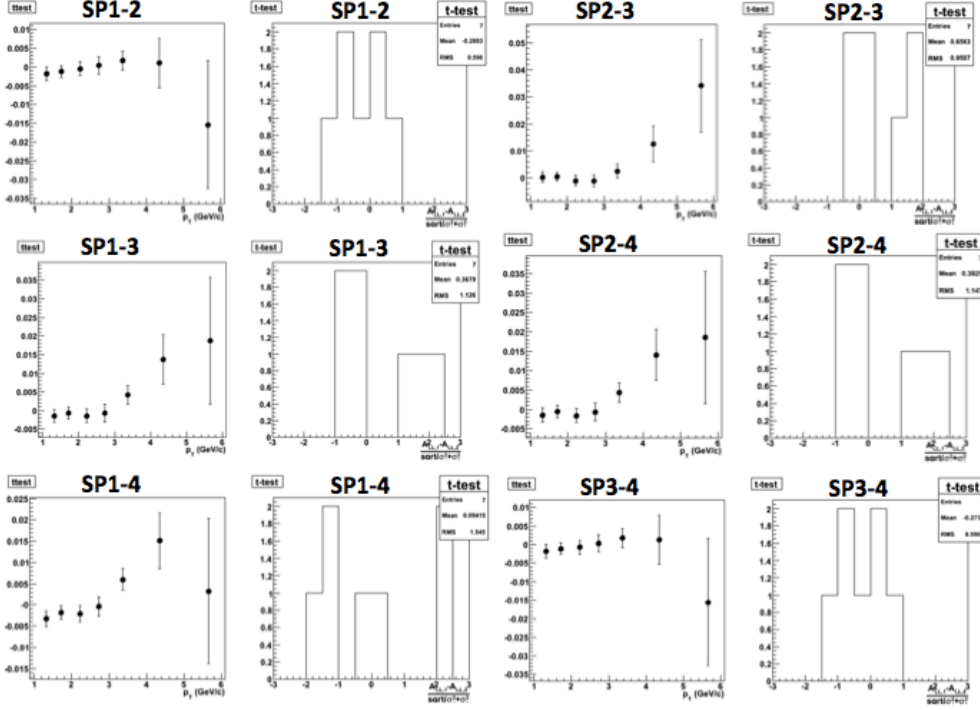


Figure 5.34: T-scores and their distributions are shown for each of the 6 possible pairings of spin patterns.

### 5.13 Check of Single Spin Asymmetry, $A_L^{cluster}$

The single spin asymmetry for each beam is defined by:

$$A_{L,beam} = -\frac{\sigma^+ - \sigma^-}{\sigma^+ + \sigma^-} = -\frac{1}{P_{beam}} \frac{N^+ - RN^-}{N^+ + RN^-} \quad R = \frac{L^+}{L^-} \quad (5.12)$$

where only the polarization of that beam is considered. The other beam is considered unpolarized by integrating over all of its bunches, not distinguishing between the two helicity states of its various bunches. As QCD interactions conserve parity, this check should yield a result of 0 for both beams in their forward direction. In the backward direction, the direction of the effectively unpolarized beam, the result is expected to be 0 automatically. The result is shown in Figure 5.35. The T-test comparison between each of the four sets of points are all consistent.

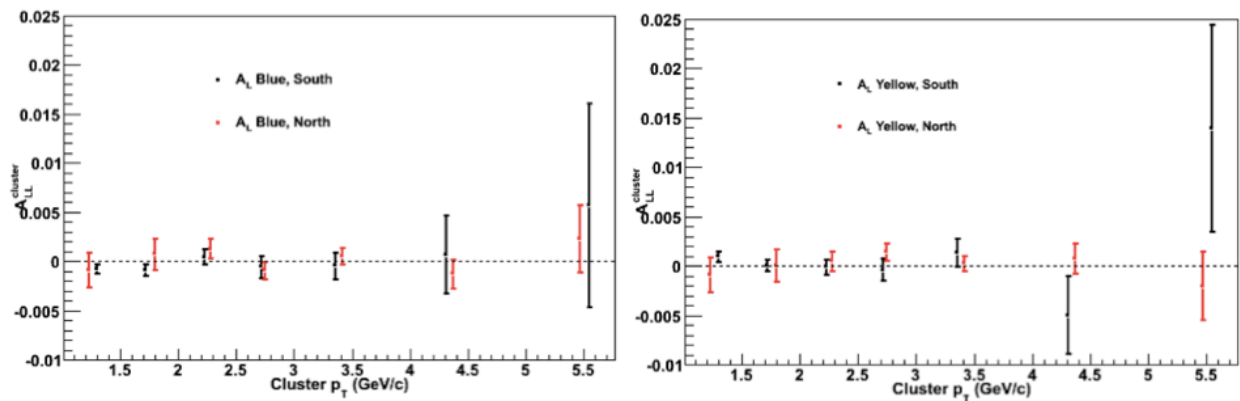


Figure 5.35: Left (a):  $A_{L,\text{blue}}$  in the forward and backward directions. Right (b):  $A_{L,\text{yellow}}$  in the forward and backward directions. All sets of points are statistically consistent with each other and with 0.

# Chapter 6

## Measurement of Forward Cluster $A_{LL}$ at $\sqrt{s} = 500 \text{ GeV}$

In this chapter, we present the details of the  $A_{LL}$  analysis of electromagnetic clusters in the MPC from the 2009 data at  $\sqrt{s} = 500 \text{ GeV}$  (Ref.[92]). The data used in this analysis was taken over a roughly one month period before the  $\sqrt{s} = 200 \text{ GeV}$  running. Many of the details in this analysis are similar.

### 6.1 Cluster Decomposition

In Fig. 5.2 we cited the results of a cluster decomposition analysis at  $\sqrt{s} = 200 \text{ GeV}$ . We performed a similar study at  $\sqrt{s} = 500 \text{ GeV}$  by generating a sample of 30 million PYTHIA ([122]) events that were reconstructed using the GEANT software package ([123],[124],[125]). The PYTHIA configuration details given in Table 6.1. The cluster decomposition for this energy is shown in Figure 6.1. The decomposition is

Table 6.1: PYTHIA configuration details for cluster decomposition study.

Parameter	Value
pytune	100
roots	500
proj	p
targ	p
frame	cms
msel	0
msub	11 1
msub	12 1
msub	13 1
msub	28 1
msub	53 1
msub	68 1
msub	96 1
ckin	3 2.0

overall fairly similar to the 200  $\text{GeV}$  case, but here the contribution from merged  $\pi^0$ 's looks to stay close to 80% out to the kinematic limit around  $p_{T,clus} \approx 10 \text{ GeV}$ .

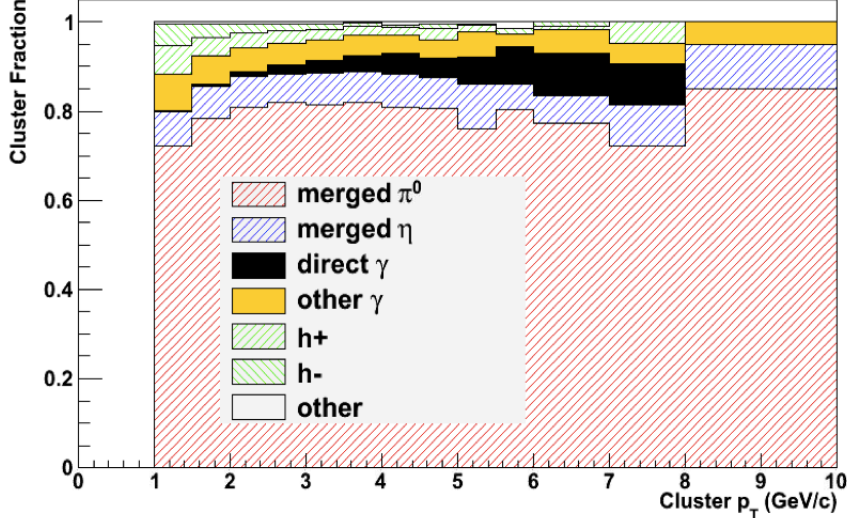


Figure 6.1: The fraction of clusters reconstructed in the MPC that arise from merged  $\pi^0$ 's,  $\eta$ 's, photons and hadrons at  $\sqrt{s} = 500 \text{ GeV}$ . Merged  $\pi^0$ 's are slightly more dominant here than at  $\sqrt{s} = 200 \text{ GeV}$ .

## 6.2 Calibration of Data

During production of the raw data, the uncalibrated raw ADC and TDC values are written out. The gains, overflow values and conversion factors need to be determined for each running period. A significant difference between the  $200 \text{ GeV}$  vs.  $500 \text{ GeV}$  period is that the silicon APD's were operated at a lower high voltage bias in the latter case. It was reduced from the  $M = 50$  to the  $M = 25$  setting so that each photoelectron produces, on average, 25 avalanche electrons. This increases the dynamic range so that the higher energy particles that are created can be measured. The cost of this is that it pushes the MIP peak too low to be able to be discerned from the noise, making the energy calibration somewhat more challenging, and also decreases the energy resolution.

### 6.2.1 ADC Pedestals

The energy deposited in crystal  $i$  is determined by:

$$E_i = \frac{G_i [(ADC_{i,post} - ADC_{i,pre}) - (ped_{i,post\_amu} - ped_{i,pre\_amu})]}{LED_i(t)} \quad (6.1)$$

where  $ped_{i,post(pre)_amu}$  are the pedestal values for crystal  $i$  in AMU cells  $post(pre)$  amu.  $LED_i(t)$  is the time dependent LED normalization factor and  $G_i$  is the ADC to energy conversion factor. All  $416 \times 64$  pedestals were determined but using them did not improve the energy spectra resolution. Therefore, for this analysis, as in the last, we do not use the pedestal values.

### 6.2.2 ADC and TDC Overflow Determination

This procedure used in the calibration of this data was not significantly different from the previous analysis.

### 6.2.3 High-Low ADC ratio

The conversion factor between the high gain and low gain ADC is determined for each channel in the same manner as the  $200\text{ GeV}$  data. Figure 6.2 shows an example of the consistency seen when scaling the high gain ADC down by the conversion factor. The effective overflow of the high gain ADC is seen and the transition to the low gain ADC is set to be at the vertical red line.

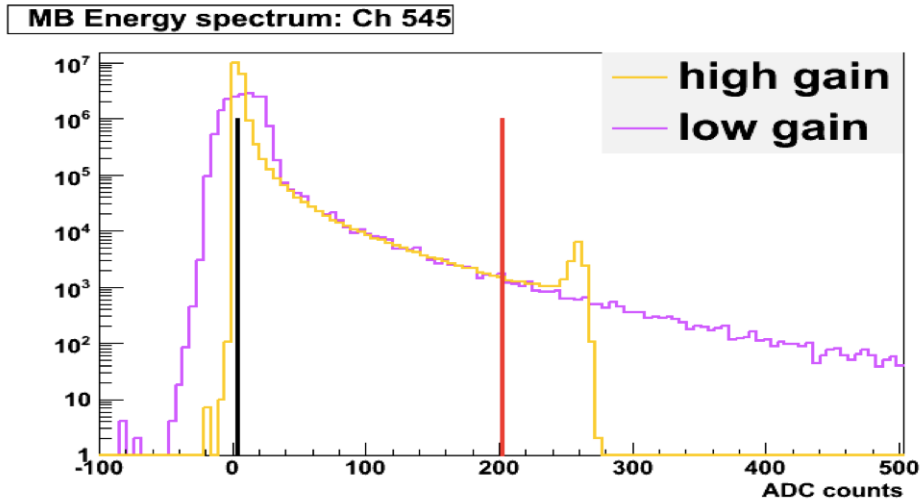


Figure 6.2: The high and low gain ADC spectra for a single crystal. The high gain values are normalized by the high-low ratio. From the pedestal peaks around 0, it can be seen that the high gain ADC provides much better energy resolution. However, its overflow is seen to occur at the low gain equivalent of about 250 ADC counts, corresponding to  $5 - 6\text{ GeV}$ .

### 6.2.4 LED Analysis and Determination of ADC to Energy Conversion Factors

For some channels, the PIN diode was not functional or other problems were found. In these cases, the LED response was taken to be that of its mirror image. Because MIP peaks cannot be found for this data, we need a different method to get a set of input gains that are reliable enough for input into the iterative  $\pi^0$  peak calibration ([82]). To do this, we bootstrap from the Run09  $\sqrt{s} = 200\text{ GeV}$  gains which we know are reliable. Further, we know that gain changes occur due to radiation degradation of the MPC crystals and also from changing the HV bias on the APD's. To account for how much the gains should change due to crystal degradation we assume the gains should be different by the ratio of the absolute values of the LED's

in the two periods in question. The LED reference runs used were 278640 and 283351 for the  $\sqrt{s} = 500\text{ GeV}$  and  $200\text{ GeV}$  periods, respectively. Based on changing the HV, we assume the gains should change by the ratio of the LED's before and after the change. Run 280911 measured the mean LED ADC in each channel at  $M = 25$  and 280912 did so at  $M = 50$  in run 280912. In Figure 6.3 we show this ratio. To summarize,

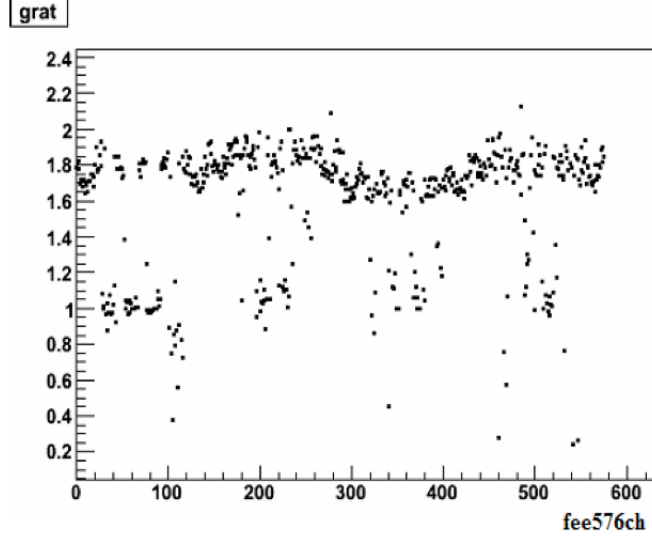


Figure 6.3: The ratio of the LED directly after the HV change to the LED right before the change. The  $x$ -axis is the channel number. Channels with ratios near 1 are either pin diode channels or other unused channels.

we expect that the channel gains at  $500\text{ GeV}$  and  $200\text{ GeV}$ ,  $G_{i,500(200)}$ , are related by:

$$G_{i,500} = G_{i,200} \times \frac{LED_{i,\text{ref},500}}{LED_{i,\text{ref},200}} \times \frac{LED_{i,M=25}}{LED_{i,M=50}} \quad (6.2)$$

### 6.2.5 Warnmap

With the gain inputs to the iterative  $\pi^0$  calibration determined based on the procedure above, the iterations yield convergence in most channels and reasonable results overall. As before, to see which channels are poorly calibrated or are hot or dead, we check the counts per minimum bias trigger in various energy ranges. This is shown in Figure 6.4. The channels in red are those deemed hot or red and can be seen to be essentially the same set of towers regardless of the chosen energy range. Another check is the time dependent channel by channel behavior. To study this, we pick an energy range and plot the counts per trigger in that range for a given channel over time. In Figure 6.5 we show an example of a well behaved tower that is stable and a misbehaved tower that seems to drop out for a few runs, but then recover later. In Figure 6.6 we show the final warnmap used for the  $500\text{ GeV}$  analysis. The only excluded towers are those blocked by the beam-pipe

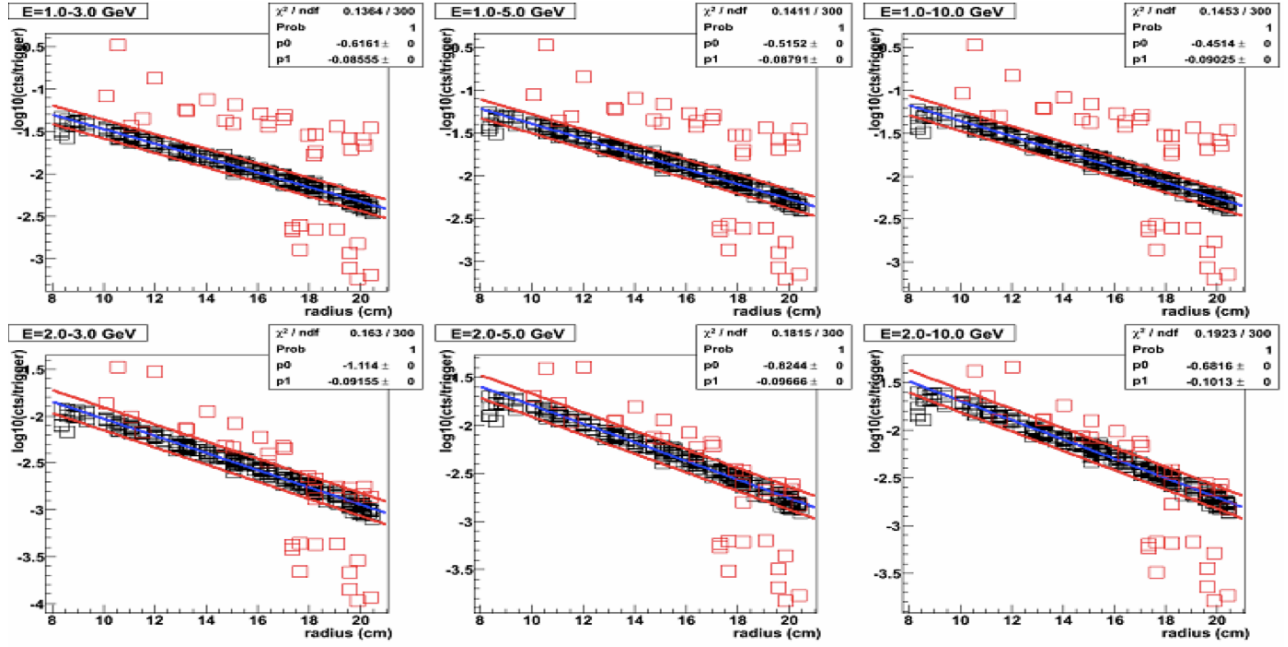


Figure 6.4: For 6 different energy ranges, we show the counts per minbias trigger. Each point is one channel. The majority of channels fall in a tight window and hot or dead channels can be identified as being more than  $3\sigma$  away from the expected value.

support in the north with low counts, one driver board in the north that the  $\pi^0$  calibration was unable to stabilize and three additional dead or hot channels.

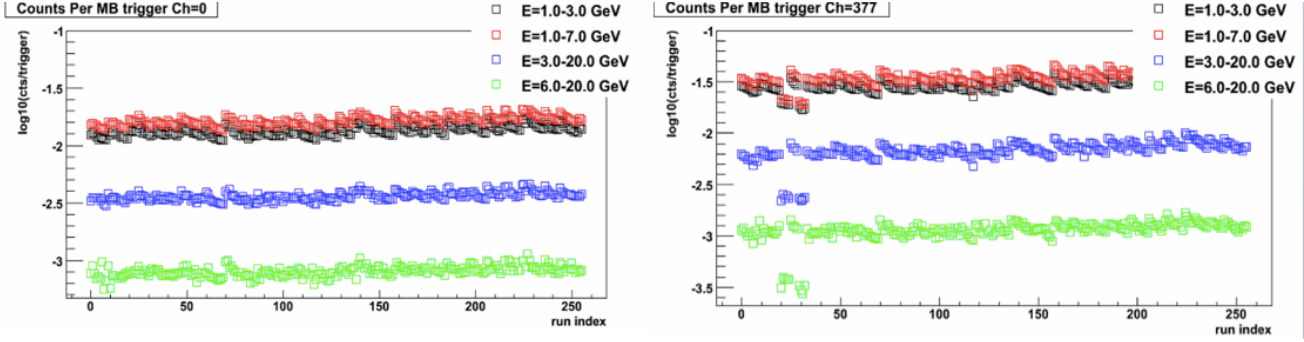


Figure 6.5: Top (a): An example of a channel that is stable throughout the entire running period. Bottom (b): An example where a given tower seems to drop out for one or two fills before recovering again. Four energy ranges are checked per channel.

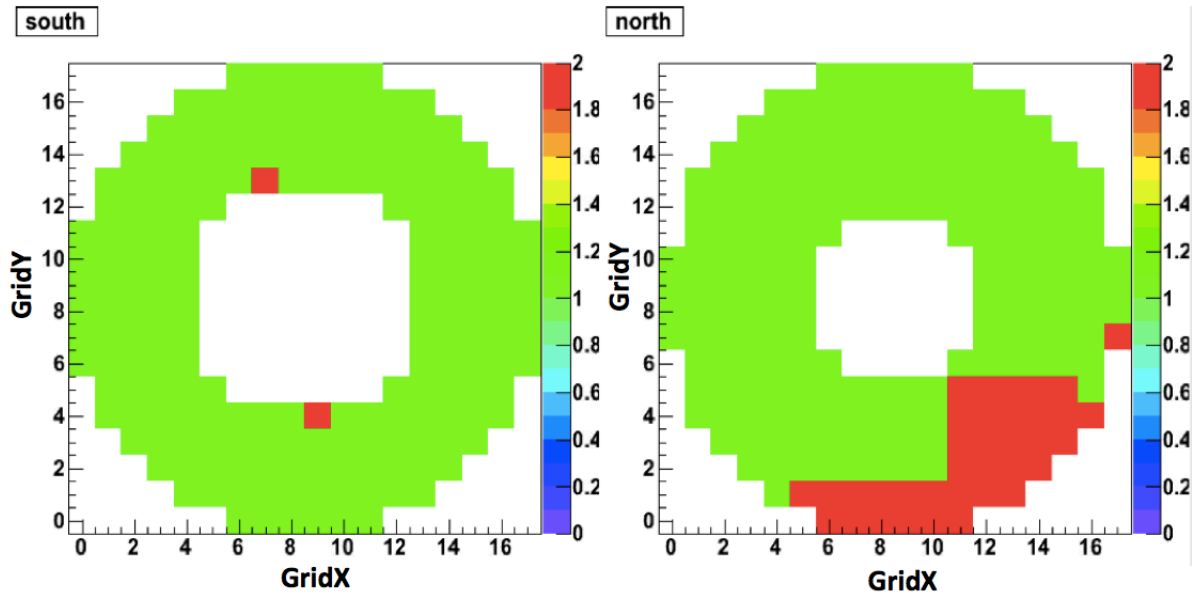


Figure 6.6: The set of excluded channels is shown in red. In the south MPC, two channels are excluded due to unstable LED's and being hot. In the north MPC, we exclude one full driver board due to high levels of noise as well as the bottom two row blocked by a beam-pipe support.

### 6.3 Single Tower Background

A significant fraction of triggers taken by the MPC were found to not contain a high energy electromagnetic cluster, or even a merged cluster, but rather a single tower with a very large energy deposit, which fired the trigger on its own. The clusters from these single tower triggers are inconsistent with the shower shape, or profile, that would be created by a photon. The shower from a photon is expected to develop transversely across a number of crystals. In the instances of single tower trigger, however, there is no evidence that the showering process has occurred in surrounding crystals. Figure 6.7 illustrates this point. In Fig. 6.7a each crystal is shown in a color representative of the energy it measured. There is a very high energy deposit seen in the central towers,  $E_{central} \approx 100\text{ GeV}$ , and in the surrounding towers measure of combine energy of only  $E_{surround} \approx 1\text{ GeV}$ . Much of this surrounding energy is likely just noise. By contrast, Fig. 6.7b shows an example of a normal electromagnetic shower. The energy is deposited into a central tower and also spreads out transversely.

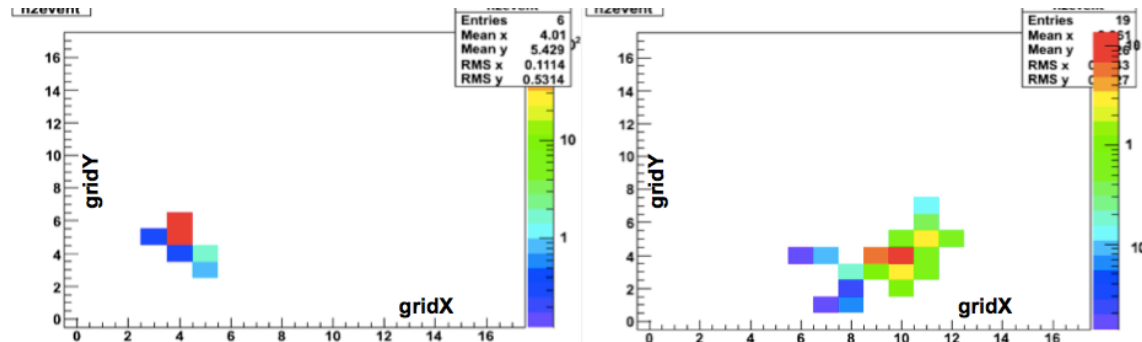


Figure 6.7: Left (a): An example of a single tower cluster. Right (b): An example of an electromagnetic cluster. In each case the energy deposited into a crystal is represented by its color. When a photon showers several towers ( $O(10)$ ) absorb the shower energy. However, in these non-photonic events just one or two channels get a very large energy deposit, while no other towers receive an amount of energy clearly discernible from noise.

The observation of this effect raises two issues. The first is that the purity of the trigger is decreased due to this effect. That is, the fraction of triggers recorded that contain high energy electromagnetic clusters is lower than if single tower events could be rejected by the trigger. Unfortunately, the trigger is designed to fire only when a large energy deposit is detected by computing sums over  $2 \times 2$  or  $4 \times 4$  squares. No check is done regarding the distribution of energy within that sum. In Chapter 7, we will describe an upgrade to the MPC electronics and trigger that does allow for these single tower events to be rejected. The new trigger upgrade is fully digitally based and can require that more than one channel is above some threshold before firing. This upgrade allows for more flexibility in configuring the trigger parameters and was exploited in the 2012 and

2013 data. The second issue is to understand the nature of these single tower hits. Figure 6.8 shows a finely

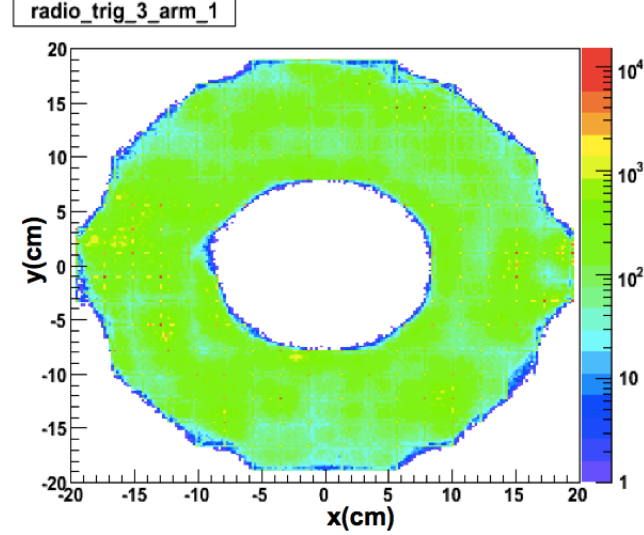


Figure 6.8: A radiograph of the centers of reconstructed clusters. The hit distribution looks mostly uniform, except for a grid of highly occupied bins due single tower clusters.

binned radiograph of reconstructed clusters in the MPC. This radiograph looks mostly uniform. However, upon close inspection, a grid of single bins corresponding to the geometric center of each crystal is found to have an unusually high occupancy (the yellow and red bins). The clusters in these bins all look like the example from Fig. 6.7a. In these cases, since the cluster is made up of just one tower, or perhaps one high energy tower and a very low energy tower, the center of gravity of the cluster is found to be at the tower center.

It is thought that single tower hits come from spallation neutrons interacting with the silicon APD itself. One way this might occur is a spallation neutron knocking out a proton, creating a negatively charged hole, resulting in an avalanche in a similar manner as a photoelectron. Another possible cause is from the decay of an excited spallation daughter nucleus. It is unlikely for this effect to be caused by thermal neutron capture because the timescale for this is too long. Fortunately, these single tower clusters can be identified with high efficiency offline and removed due to their unique nature. A commonly used cut to identify such clusters if by requiring that  $\frac{E_8}{E_{cent}} > 0.03$ , where  $E_{cent}$  is the energy measured by the central crystal in the cluster and  $E_8$  is the total energy of the eight surrounding crystals. Slight variants of this cut are also commonly used. Using this cut, we can study the energy spectrum of reconstructed clusters separated into those that pass this cut and those that do not. The result is shown in Figure 6.9. At high energy it is found that the spectrum is totally dominated by single towers. It is interesting to note that the single tower energy spectrum is nearly flat, consistent with the idea that the source is not a real energy deposition in the

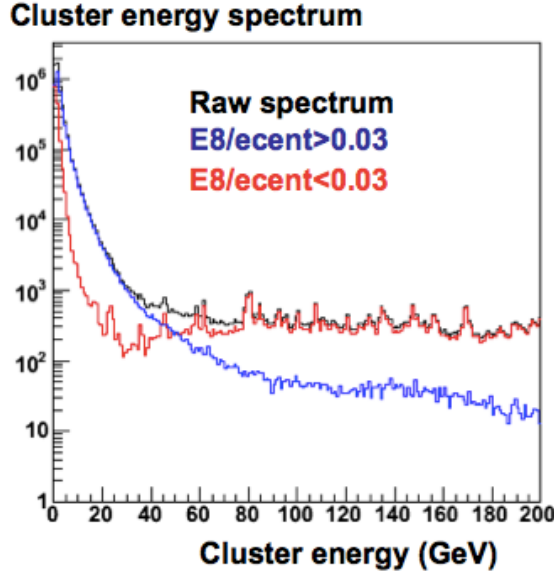


Figure 6.9: Cluster spectrum from *MPC\_4x4B* triggered events. The full spectrum is in black, the single tower cluster spectrum is in red and the remaining spectrum is in blue.

crystal itself. Additionally, this nearly flat spectrum means that triggers with a higher threshold will have less purity than those with lower threshold. This is because at lower energies,  $E < \sim 40\text{ GeV}$ , EM clusters are more abundant than single tower clusters. However, single towers are more and more dominant as one looks to higher energy. Therefore, the clusters sampled by the highest threshold “B” trigger are dominated to the largest extent of any trigger by single towers. We should also note that the physics spectrum falls faster than the blue plot of Fig. 6.9. This means this simple cut we have applied is not quite enough to eliminate such events. One instance that can be difficult is the situation where an EM cluster and a single tower cluster happen to overlap. In such a case, some contamination of the final spectrum is inevitable.

## 6.4 $\pi^0$ Mass Reconstruction

We now check the quality of the calibrations by looking at the reconstructed  $\pi^0$  mass from *BBC(novertex)* events with a vertex of  $|z| < 50\text{ cm}$ . For each cluster we make the following cuts:

- $E_{clus} > 2\text{ GeV}$
- Central tower of cluster must not be in the warnmap
- $\text{chi2core} < 3$ . The shower shape parameter must be reasonably consistent with an EM shower.

- $disp_x < 4 \text{ cm}^2$ ,  $disp_y < 4 \text{ cm}^2$ . The lateral dispersion of the cluster in each direction must not be too large.
- $11 \text{ cm} < r < 19 \text{ cm}$  where  $r$  is the cluster radius.
- ADC overflow veto
- TDC overflow veto
- The number of towers in the cluster, its multiplicity, must be  $> 2$ .
- $disp_x > 0.005 \text{ cm}^2$ ,  $disp_y > 0.005 \text{ cm}^2$ .
- Energy deposited in central tower  $< 95\%$  of cluster energy.

The last three cuts are in place to remove single tower clusters. The cluster pair cuts are:

- Energy asymmetry:  $\gamma < 0.6$
- $\Delta r = \sqrt{\Delta x^2 + \Delta y^2} > 4 \text{ cm}$
- $p_{T,pair} > 0.5 \text{ GeV}/c$
- same arm

In Figures 6.10, and 6.11 we show the resulting invariant mass spectra from minimum bias and MPC triggered events, respectively, in the cluster pair energy range of  $9 \text{ GeV} < E_{pair} < 11 \text{ GeV}$ . In each figure, the south and north arm spectra are shown separately. Figures 6.12, and 6.13 show the invariant mass spectra for  $11 \text{ GeV} < E_{pair} < 13 \text{ GeV}$ . Figures 6.14, and 6.15 show the invariant mass spectra for  $13 \text{ GeV} < E_{pair} < 15 \text{ GeV}$ . Figures 6.16, and 6.17 show the invariant mass spectra for  $15 \text{ GeV} < E_{pair} < 17 \text{ GeV}$ . In each of these figures the reconstructed mass spectrum is shown in black. A background mass spectrum is produced by pairing totally uncorrelated clusters from different events with each other and is shown in red. The blue histogram is the difference between these two and contains the  $\pi^0$  reconstructed pairs as well as any correlated backgrounds that may be present. In the highest energy bin a small peak near the  $\eta$  mass can also be seen. It should be noted that the MPC trigger threshold is generally higher than the threshold for cluster merging. Therefore, the clusters pairs found in triggered data that form an invariant mass in the  $\pi^0$  region are due to random benefit. This means they are clusters that do not cause a trigger, but are still written to disk because they are found in an event with a high energy cluster. Figure 6.18 shows a summary of the information including the  $\pi^0$  mass and width as a function of pair energy. This is shown for both minimum bias and MPC triggered data and is separated by arm.

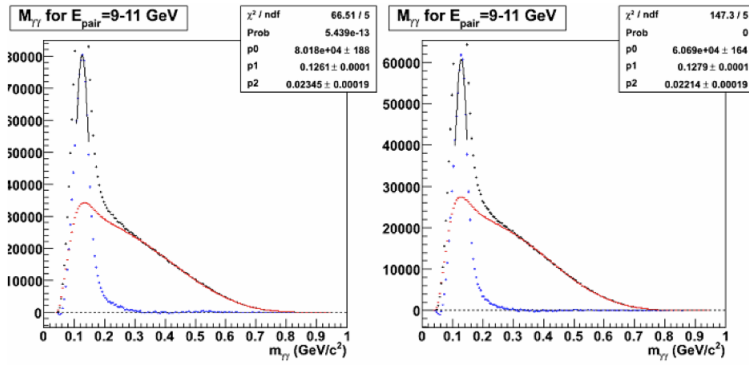


Figure 6.10: Invariant mass spectrum in minimum bias events for MPC south(left) and north(right) for  $E_{pair} = 9 - 11 \text{ GeV}$ .

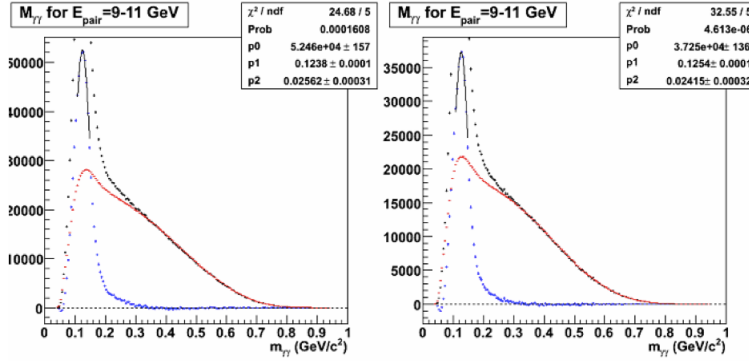


Figure 6.11: Invariant mass spectrum in MPC triggered events for MPC south(left) and north(right) for  $E_{pair} = 9 - 11 \text{ GeV}$ .

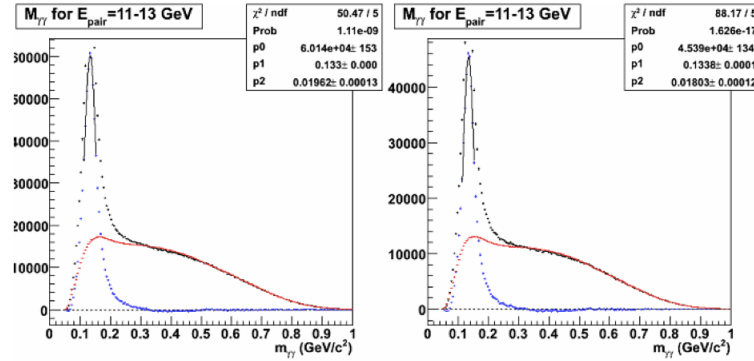


Figure 6.12: Invariant mass spectrum in minimum bias events for MPC south(left) and north(right) for  $E_{pair} = 11 - 13 \text{ GeV}$ .

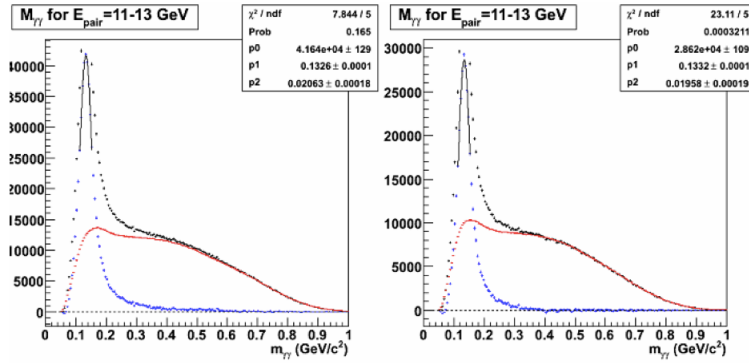


Figure 6.13: Invariant mass spectrum in MPC triggered events for MPC south(left) and north(right) for  $E_{pair} = 11 - 13 \text{ GeV}$ .

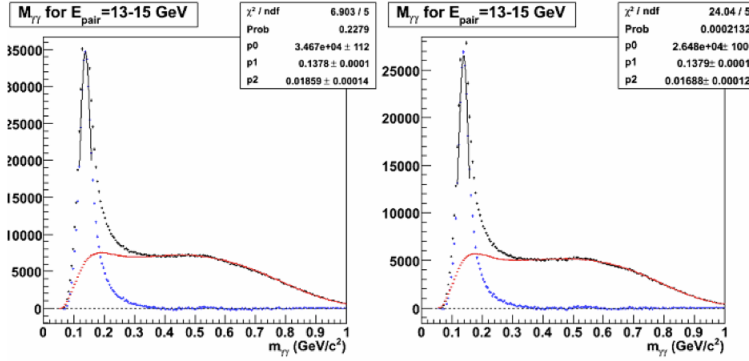


Figure 6.14: Invariant mass spectrum in minimum bias events for MPC south(left) and north(right) for  $E_{pair} = 13 - 15 \text{ GeV}$ .

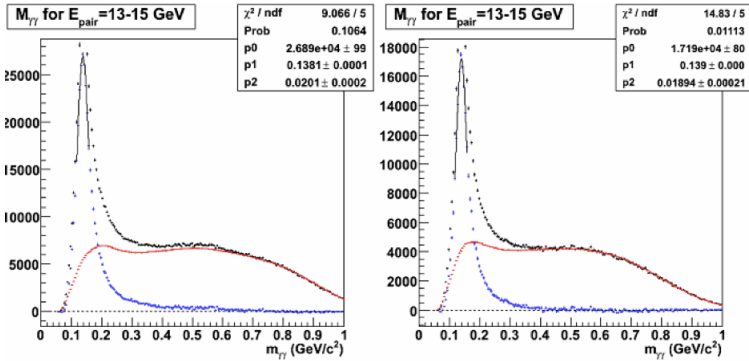


Figure 6.15: Invariant mass spectrum in MPC triggered events for MPC south(left) and north(right) for  $E_{pair} = 13 - 15 \text{ GeV}$ .

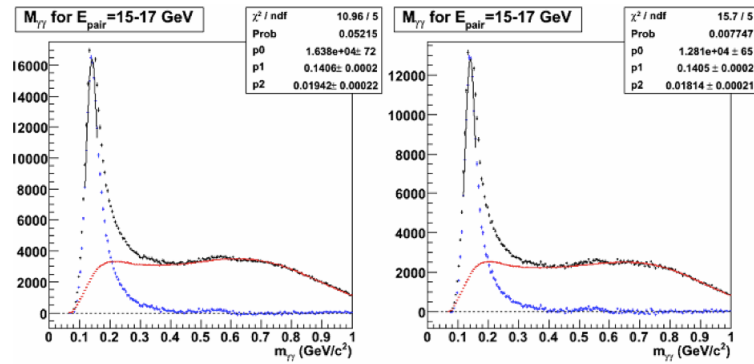


Figure 6.16: Invariant mass spectrum in minimum bias events for MPC south(left) and north(right) for  $E_{pair} = 15 - 17 \text{ GeV}$ .

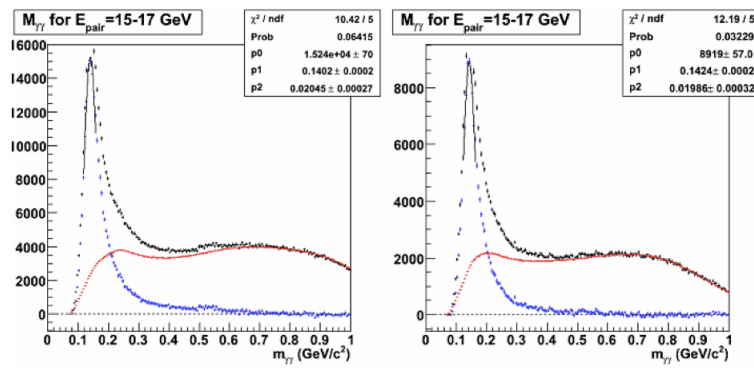


Figure 6.17: Invariant mass spectrum in MPC triggered events for MPC south(left) and north(right) for  $E_{pair} = 15 - 17 \text{ GeV}$ .

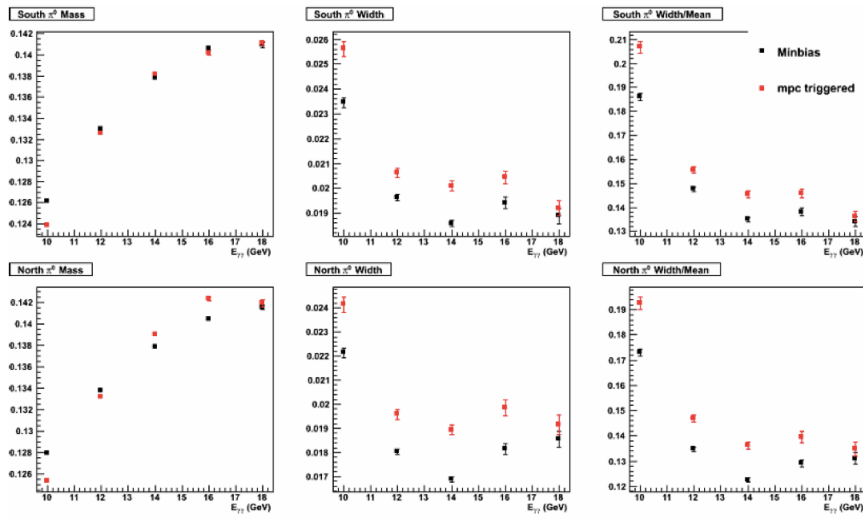


Figure 6.18: Summary of all  $\pi^0$  reconstruction information. The left, middle and right columns show the  $\pi^0$  mass,  $\pi^0$  width and  $\pi^0$  width/mass as a function of pair energy. The top row shows the quantities for the south MPC while the bottom row shows the north. In each plot, the results from minimum bias (black) and MPC triggered (red) data are compared.

## 6.5 $\pi^0$ Counts Per Minimum Bias Trigger

Figure 6.19 shows the number of cluster pairs per minimum bias trigger with an invariant mass close to the  $\pi^0$  mass in each arm and as a function of run number. In determining these counts we do not subtract uncorrelated background from mixed events. The overall level between fills (clusters of points with close run numbers) is seen to be nearly stable. However, within a fill the ratio of counts per trigger is seen to decrease. This is largely due to the decreasing beam rate. At the beginning of a fill, where the rate is the highest, multiple collisions have the largest effect. When more than one collision occurs the MPC sees the superposition of all of them which causes a larger uncorrelated background near the  $\pi^0$  mass. As the rate decreases, multiple collisions in one crossing occur less frequently, and this source of uncorrelated background decreases.

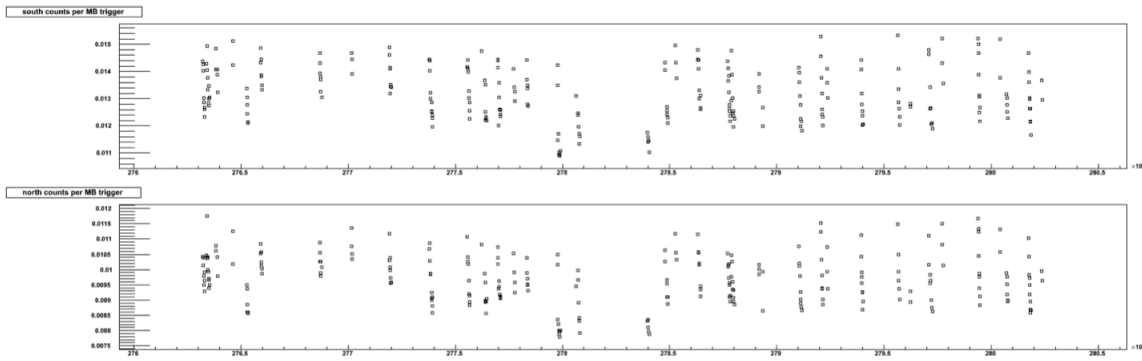


Figure 6.19: Number of reconstructed pair counts near the  $\pi^0$  mass as a function of run number for the south (top) and north (bottom) MPC.

## 6.6 $\pi^0$ Mass Stability

The LED monitoring system is expected to correct for the decreased response of the MPC crystals and APD over the course of the run. The LED corrections are embedded in the cluster reconstruction so we expect the mass and width of the  $\pi^0$  to hold steady. We can check this by examining the location of the  $\pi^0$  mass peak as a function of time. This is shown in Figures 6.20, 6.21, 6.22, and 6.23 for the same energy bins that were defined in Section 6.4. In the lowest energy bin, decreases of about 1% and 3% in the  $\pi^0$  mass are observed in the south and north MPC, respectively. A smaller decrease can be found for  $E_{pair} = 11 - 13 \text{ GeV}$  in both arms and for the  $13 - 15 \text{ GeV}$  and  $15 - 17 \text{ GeV}$  bins the mass remains constant.

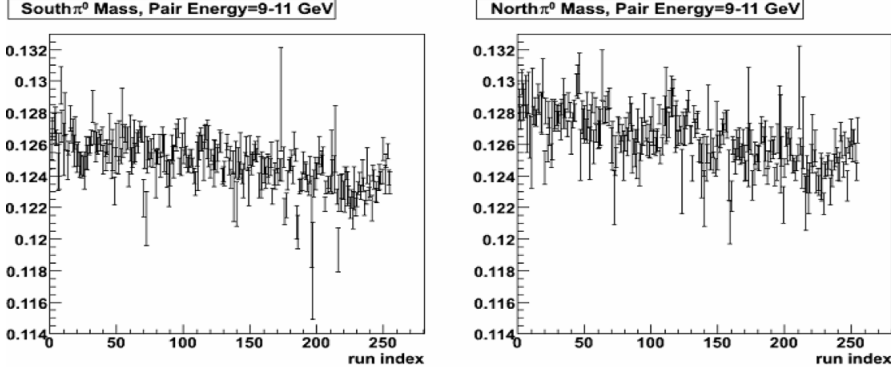


Figure 6.20:  $\pi^0$  invariant mass peak from minimum bias events for MPC south(left) and north(right) for  $E_{pair} = 9 - 11 \text{ GeV}$ .

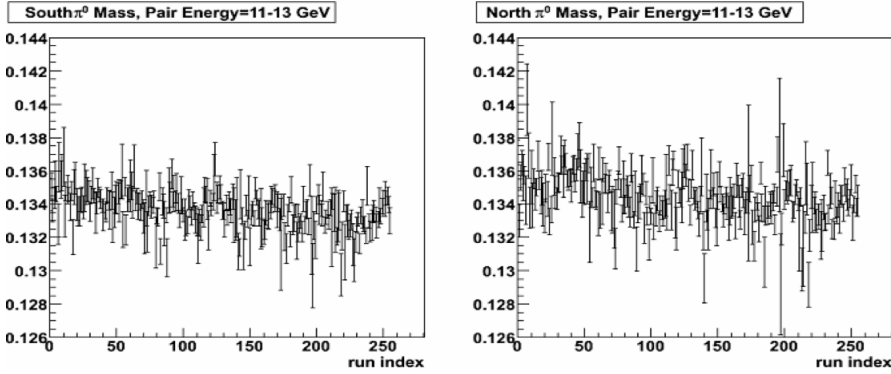


Figure 6.21:  $\pi^0$  invariant mass peak from minimum bias events for MPC south(left) and north(right) for  $E_{pair} = 11 - 13 \text{ GeV}$ .

## 6.7 $\pi^0$ Width Stability

In addition to the mass stability figures, we show the stability of the width of the reconstructed  $\pi^0$  peak by looking at its time dependence. This is shown in Figures 6.24, 6.25, and 6.26. This width is a combination of the intrinsic  $\pi^0$  width, intrinsic detector resolution, and any smearing associated with miscalibrated towers or other detector effects not taken into account. Small increases over time can be found in the peak resolution. In the  $E_{pair} = 9 - 11 \text{ GeV}$  bin an increase from  $\sigma_{\pi^0} \approx 24(23) \text{ MeV}$  to  $\sigma_{\pi^0} \approx 25(24) \text{ MeV}$  in the south(north) is seen. In the  $E_{pair} = 11 - 13 \text{ GeV}$  bin there is an increase from  $\sigma_{\pi^0} \approx 22(20) \text{ MeV}$  to  $\sigma_{\pi^0} \approx 23(22) \text{ MeV}$  for the south(north) MPC. For the bin with  $E_{pair} = 13 - 15 \text{ GeV}$  the width of the south MPC does not have quite a linear dependence on time, and does not appear to drift upward or downward. The south MPC measures a width near  $\sigma_{\pi^0} \approx 23 \text{ MeV}$ . For the north MPC the width does increase slightly from  $\sigma_{\pi^0} \approx 21 \text{ MeV}$  to  $\sigma_{\pi^0} \approx 22 \text{ MeV}$ .

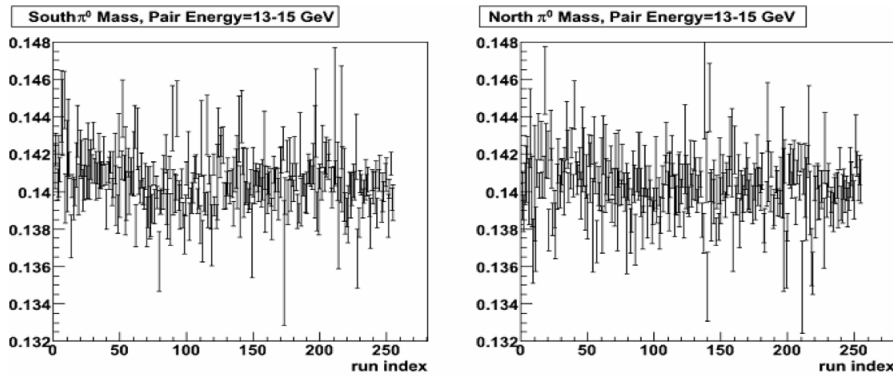


Figure 6.22:  $\pi^0$  invariant mass peak from minimum bias events for MPC south(left) and north(right) for  $E_{pair} = 13 - 15 \text{ GeV}$ .

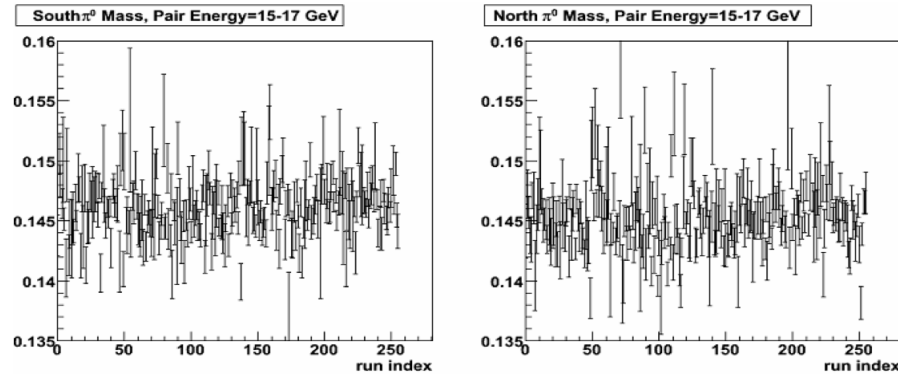


Figure 6.23:  $\pi^0$  invariant mass peak from minimum bias events for MPC south(left) and north(right) for  $E_{pair} = 15 - 17 \text{ GeV}$ .

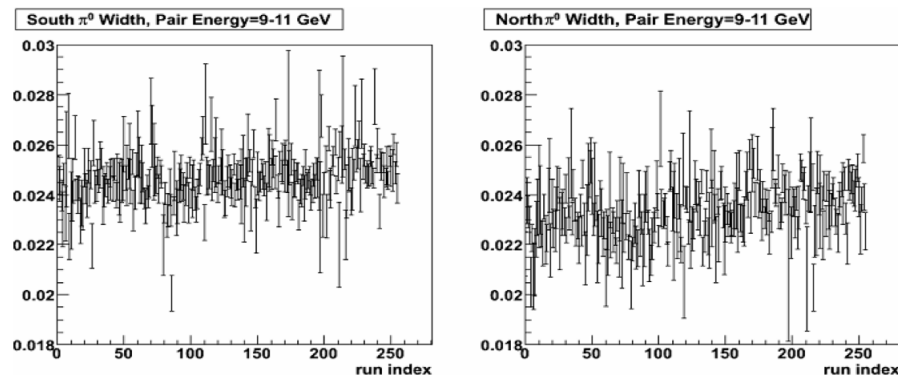


Figure 6.24: Width of  $\pi^0$  invariant mass peak from minimum bias events for MPC south(left) and north(right) for  $E_{pair} = 9 - 11 \text{ GeV}$ .

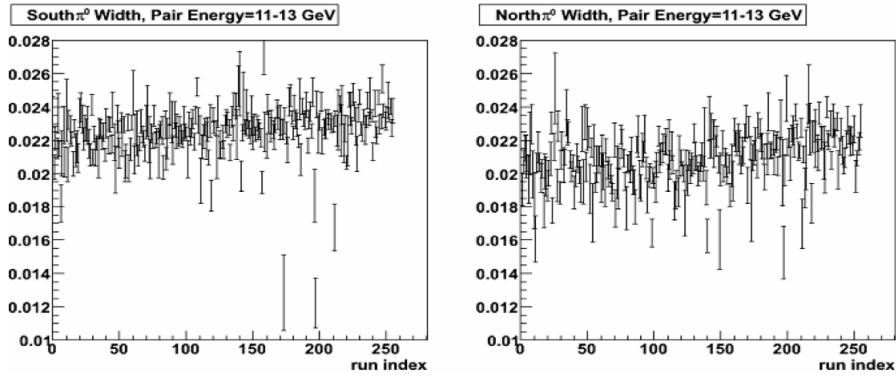


Figure 6.25: Width of  $\pi^0$  invariant mass peak from minimum bias events for MPC south(left) and north(right) for  $E_{pair} = 11 - 13 \text{ GeV}$ .

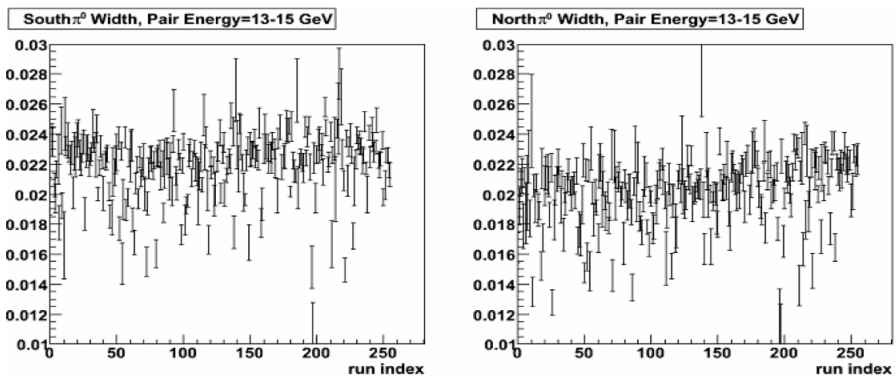


Figure 6.26: Width of  $\pi^0$  invariant mass peak from minimum bias events for MPC south(left) and north(right) for  $E_{pair} = 13 - 15 \text{ GeV}$ .

## 6.8 $\pi^0$ Eta Mass Reconstruction and Stability

An established way to check the overall energy scale of the MPC calibrations is to study the reconstructed  $\eta$  meson peak positions. The reconstructed  $\eta$  mass is expected to be less susceptible to upward drifting with pair energy due to the fact that the minimum reconstructable mass is well below the  $\eta$  mass of  $547\text{ MeV}$  (see Eq. 5.1). Assuming no energy asymmetry, a minimum separation of two crystal lengths, and a maximum separation of nine crystal lengths (beyond this it is geometrically difficult for both photons to shower in the MPC) we find that the minimum and maximum energies that an  $\eta$  meson can be reconstructed at are  $\approx 10\text{ GeV}$  and  $\approx 50\text{ GeV}$ , respectively. In practice, the background is too large at  $10\text{ GeV}$  to see the  $\eta$  in the MPC, but by  $E_{pair} \approx 15\text{ GeV}$  it can be discerned (e.g. Figs. 6.16 and 6.17). By increasing the energy binning further, the  $\eta$  peak becomes more and more prominent. In Figures 6.27 and 6.28 the  $\eta$  peak is shown for  $E_{pair} = 20 - 25\text{ GeV}$  in minimum bias and MPC triggered events. In Figures 6.29 and 6.30 the same is shown for  $E_{pair} = 25 - 30\text{ GeV}$ . Notice that in this and higher pair energy bins, the statistics from the MPC trigger start to dominate. The clusters found in these triggered events are becoming less due to random benefit clusters and more dominated by high energy clusters from the  $\eta$  decay photons that cause the trigger. Also of note is that already in this bin the efficiency to reconstruct a  $\pi^0$  has dropped to nearly zero. The mass spectrum has very few entries near the  $\pi^0$  mass. Figures 6.31 and 6.32 show the invariant mass spectra for the south and north MPC in minimum bias and MPC triggered events, respectively, for  $E_{pair} = 30 - 40\text{ GeV}$ . Figures 6.33 and 6.34 show the same thing when  $E_{pair} = 40 - 50\text{ GeV}$ . In this case, as the integrated statistics for the minimum bias trigger over the entire data taking period begin to be limited, the  $\eta$  peak is completely dominant. Additionally, the triggered spectra in Fig. 6.34 show an additional resonance above the background levels at  $757 \pm 8\text{ MeV}$  and  $771 \pm 11\text{ MeV}$  in the south and north MPC, respectively. Both the  $\rho$  and  $\omega$  mesons have a mass close to this at  $770\text{ MeV}$  and  $782\text{ MeV}$ , respectively. The  $\rho^0$  principally decays via  $\rho^0 \rightarrow \pi^+\pi^-$  ([93]), however, and charged pions do not create EM showers in the MPC and therefore would not be the source of this peak. The  $\rho^+$  decays principally via  $\rho^+ \rightarrow \pi^+\pi^0$ , which would result in only one merged cluster from the  $\pi^0$  decay. The  $\omega$  meson can, however, decay electromagnetically via  $\omega \rightarrow \pi^0\gamma$  with a branching fraction of about 8%. In this case the  $\pi^0$  creates a merged cluster which is then paired with the single  $\gamma$  cluster to create an invariant mass. Much of this resonance is not seen because the shower shape requirement imposed on clusters eliminates many of the merged  $\pi^0$  clusters. In Figure 6.35 we show a summary of all the  $\eta$  related information, including the mass, width and width/mass ratios versus energy for minimum bias and MPC triggered events in the south and north detectors separately. As expected, the reconstructed mass of the  $\eta$  is nearly independent of the cluster pair energy, varying by 1% at most.

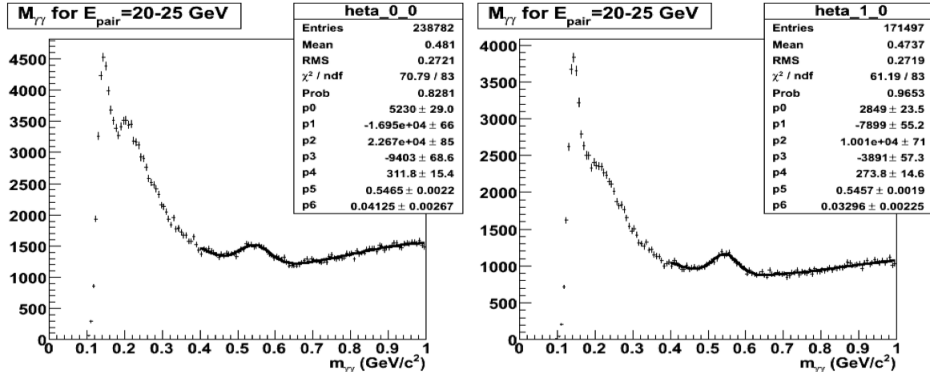


Figure 6.27:  $\eta$  invariant mass peak from minimum bias events for MPC south(left) and north(right) for  $E_{pair} = 20 - 25 \text{ GeV}$ .

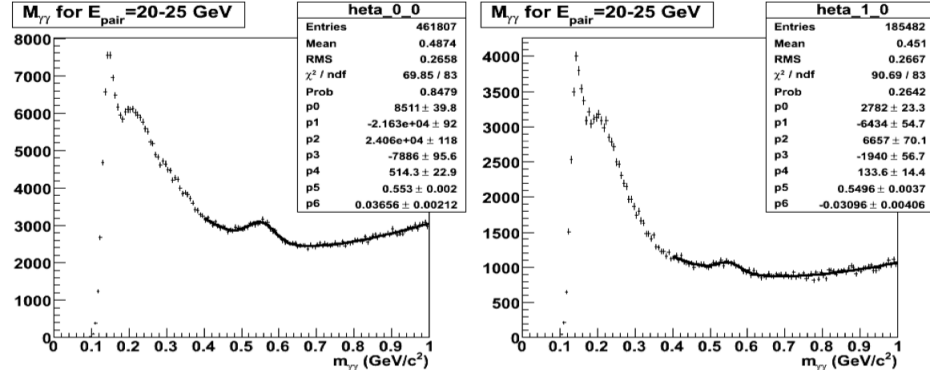


Figure 6.28:  $\eta$  invariant mass peak from MPC triggered events for MPC south(left) and north(right) for  $E_{pair} = 20 - 25 \text{ GeV}$ .

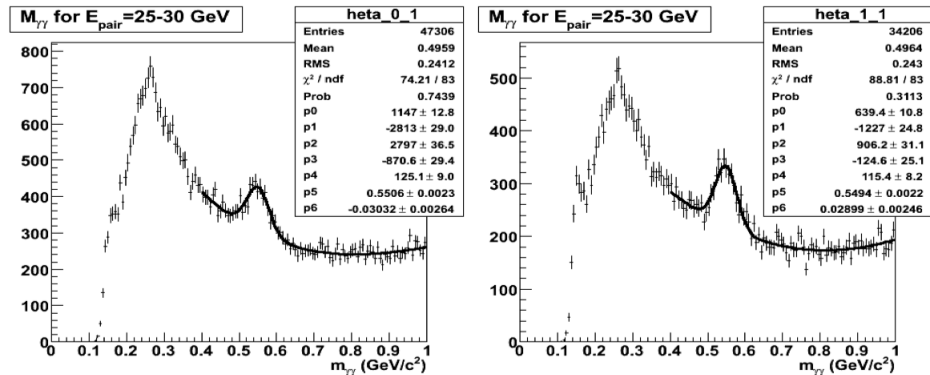


Figure 6.29:  $\eta$  invariant mass peak from minimum bias events for MPC south(left) and north(right) for  $E_{pair} = 25 - 30 \text{ GeV}$ .

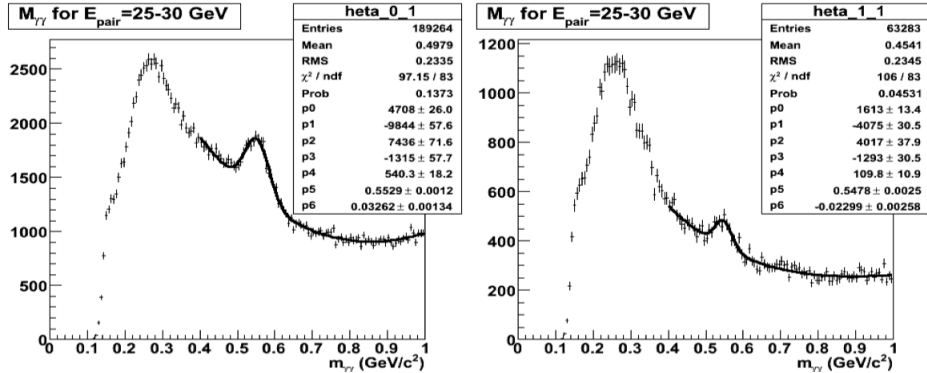


Figure 6.30:  $\eta$  invariant mass peak from MPC triggered events for MPC south(left) and north(right) for  $E_{pair} = 25 - 30 \text{ GeV}$ .

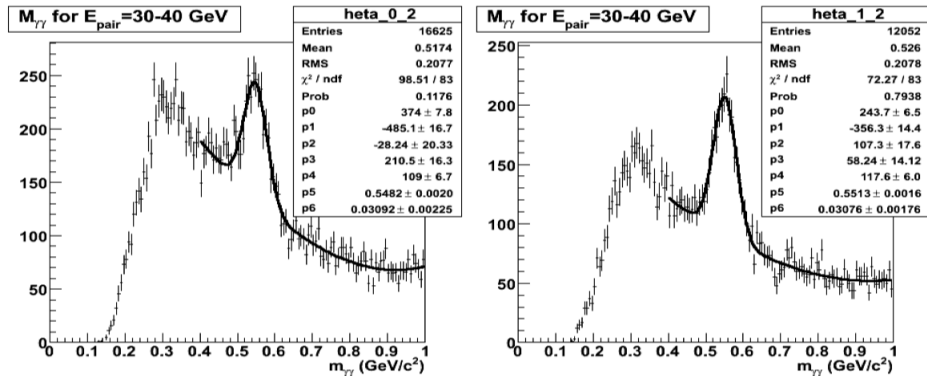


Figure 6.31:  $\eta$  invariant mass peak from minimum bias events for MPC south(left) and north(right) for  $E_{pair} = 30 - 40 \text{ GeV}$ .

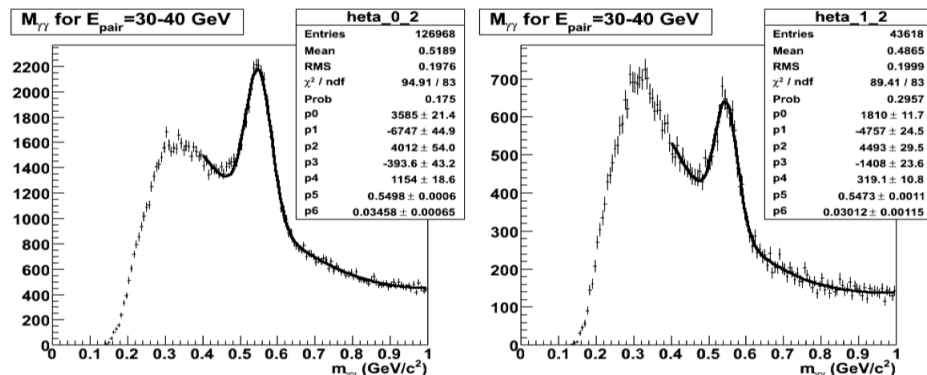


Figure 6.32:  $\eta$  invariant mass peak from MPC triggered events for MPC south(left) and north(right) for  $E_{pair} = 30 - 40 \text{ GeV}$ .

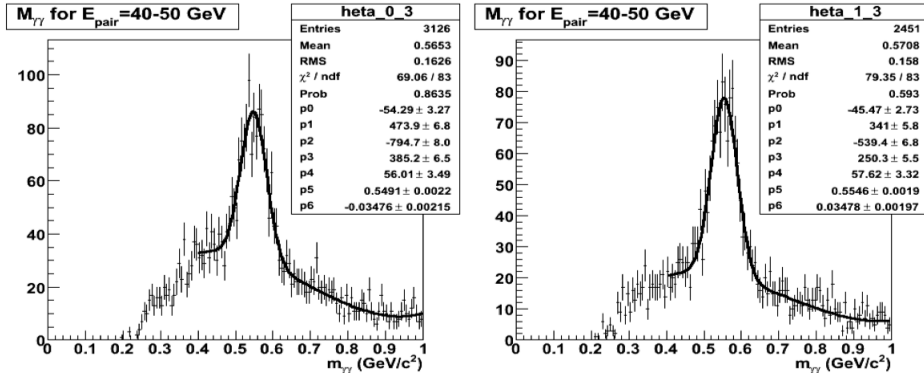


Figure 6.33:  $\eta$  invariant mass peak from minimum bias events for MPC south(left) and north(right) for  $E_{pair} = 40 - 50 \text{ GeV}$ .

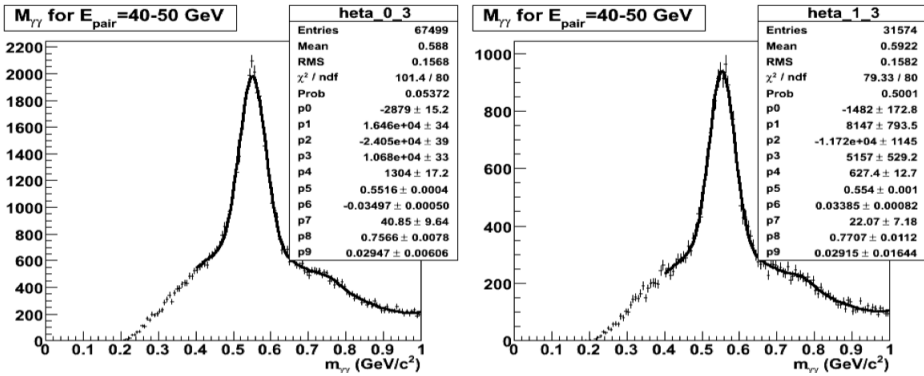


Figure 6.34:  $\eta$  invariant mass peak from MPC triggered events for MPC south(left) and north(right) for  $E_{pair} = 40 - 50 \text{ GeV}$ .

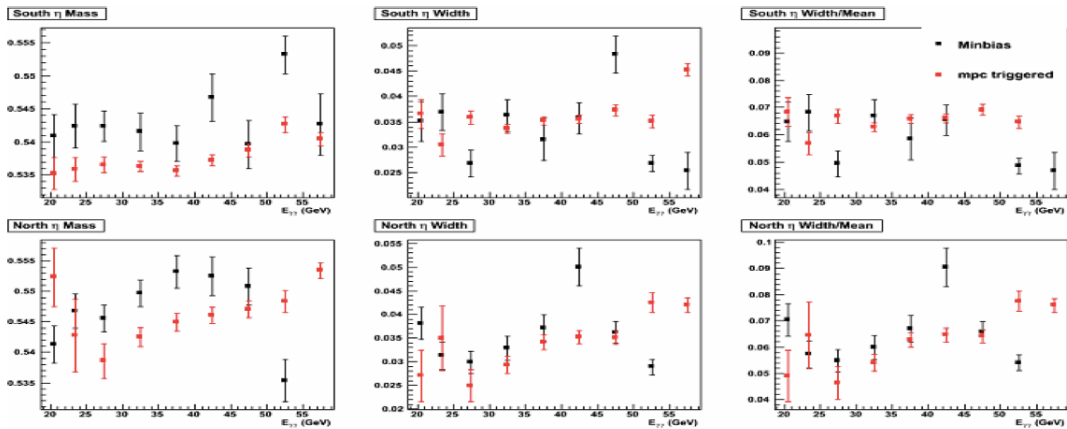


Figure 6.35: Summary of all  $\eta$  reconstruction information. The left, middle and right columns show the  $\eta$  mass,  $\eta$  width and  $\eta$  width/mass ratio as a function of pair energy. The top row shows the quantities for the south MPC while the bottom row shows the north. In each plot, the results from minimum bias (black) and MPC triggered (red) data are compared.

## 6.9 Quality Assurance

The quality assurance (QA) was done at several levels for this analysis. This included the MPC channel QA, MPC run-by-run QA, and spin and crossing information QA. The result is a list of excluded channels (the warnmap) a list of excluded crossings, and a list of excluded runs.

### 6.9.1 MPC QA

The MPC warnmap is the list of excluded channels. This list is fixed across the entire run for simplicity. It was determined during the energy calibrations by looking at the number of counts registered in various energy ranges as well as channels that could not be calibrated due to stuck ADC bits or other effects that adversely affected the shape of its ADC spectrum. The warnmap was shown in Fig. 6.6.

### 6.9.2 Run QA

A small number of runs were eliminated due to low number of  $\pi^0$ 's per MPC or minimum bias trigger. Additionally, runs were eliminated if the MPC high voltage (HV) did not get turned on by the shift crew or if the trigger delay was not properly set.

### 6.9.3 Spin and Bunch Crossing QA

For each run we plot the BBC luminosity scaler, MPC cluster yield and whether the crossing was filled or not together. An example of this is shown in Figure 6.36. It is important to confirm that crossing information from the MPC is properly aligned with the crossing data from the spin database, where spin and luminosity information is found. Otherwise, the asymmetry will be calculated incorrectly. The standard offset is five crossings and so the crossing reported by the MPC must be shifted according to  $crossing \rightarrow (crossing + 5) \% 120$ . This shift was confirmed to be correct in all but one run which is excluded. In addition, crossings in the abort gap, crossings with low scaler counts, and other unfilled bunches, as reported by the spin database, are excluded. Such checks are performed for every run. Additionally, the constancy of the spin pattern is checked for all runs within a given fill. Further, the run database is checked for comments from the shift crew that might indicate the data quality within a given run might be compromised for any specified reason.

### 6.9.4 Final List of Excluded Crossings and Runs

The full set of analyzable physics data includes 257 runs. 35 of these runs are excluded, for the stated reason:

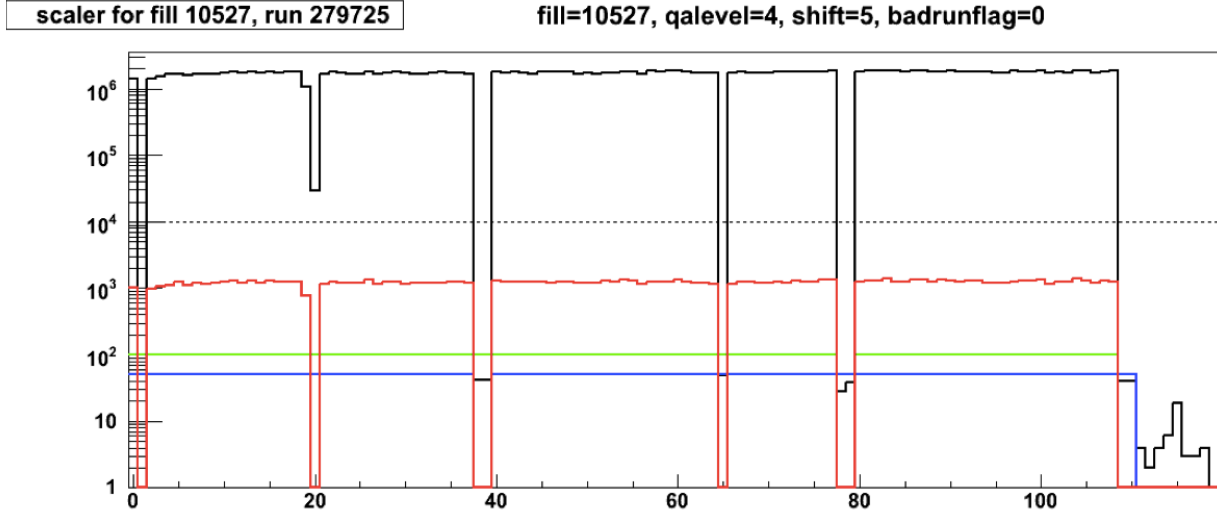


Figure 6.36: To ensure the bunch structure is aligned between the spin database and the MPC data, we plot cluster yields, spin helicities, and luminosity yields on a crossing by crossing basis for each run. One such example is shown here. The BBC luminosity counts are shown in black, the MPC cluster yield counts are in red. Green and blue have a set value if that crossing is filled for the yellow or blue beams, otherwise it is zero. Both must of course be filled in order to generate collisions. This figure shows that all crossings are properly lined up. If the crossing is filled both the MPC and BBC measure counts, otherwise they do not. The abort gap can be seen in the last 10 crossings. Crossings 1,20 and 65 are eliminated in this example. Crossing #1 cannot accept live triggers, crossing #20 is a steering bunch and crossing #65 is eliminated due to having no BBC or MPC counts.

- MPC trigger not timed in properly: 20 runs
- Corrupted GL1P scalers: 2 runs
- Crossing shift or spin helicity change recorded for different runs of the same fill: 2 runs
- Run not ended properly, scalers not reliable: 1 run
- Run has “badrunflag” set in database: 1 run
- MPC HV was not turned on: 1 run
- Low  $\pi^0$  counts per trigger: 5 runs
- No spin information in database: 3 runs

The complete list with more details can be found in Ref [92]. Having summarized the list of excluded MPC channels, the list of excluded runs, we complete the QA for this analysis by giving a list of all excluded crossings. Figure 6.37 shows this. The abort gap can be seen in the last  $\approx 10$  crossings. Additionally, crossings

**bad bunches per fill (no yield, no scaler values, or yell/blue spin==10)**

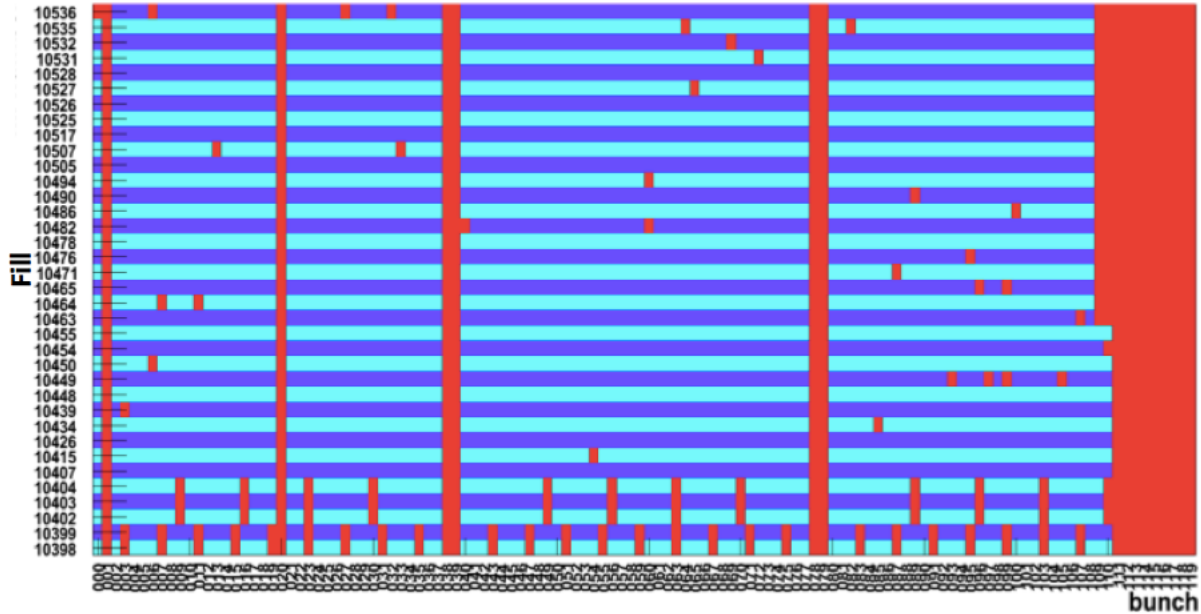


Figure 6.37: For each fill, we show the crossings that are excluded from analysis. These crossings are indicated in red. The fills are separated into blue and purple stripes for ease of visualization. Each row corresponds to a fill. Starting on the left for each fill is crossing 0 which ranges up to 119 as one goes to the right. The abort gap is clearly seen in each fill from bunches (109,110,111)-119. Other bunches are excluded if the GL1P scaler counts are much lower than other bunches, if the spin database says the blue or yellow bunch helicities are anything other than +1 or -1, or for any of the other reasons outlined in the text.

38,39,78, and 79 are always non-colliding crossings. During crossing 1, the GL1 is automatically set to busy and thus excluded, and crossing 20 is always excluded due beam steering. The first four fills have many excluded crossings because the beams are not completely filled. This is part of the beam commissioning. The MPC trigger was not properly timed for the first two fills and so would not be used regardless. A small number of additional crossings are excluded as well.

## 6.10 Cluster $A_{LL}$ and Bunch Shuffling Results

As in Chapter 5 where we described the  $A_{LL}^{cluster}$  analysis for the 2009 data taken at  $\sqrt{s} = 200\text{ GeV}$ , we use Eqs. 5.3, 5.4, and 5.5 to calculate, fill by fill, the values of  $A_{LL}^{cluster}$ , relative luminosity, and  $\delta A_{LL}^{stat}$ . As in the previous analysis, the official beam polarization values are obtained from Ref. [111]. For each fill this calculation is done separately for even and odd crossings in the south and north MPC. Because of the higher center of mass energy in this data set, the range of  $p_T^{clus}$  is now increased. The nine  $p_T$  bins used for this analysis are set at:  $[1.5 - 2.0]\text{ GeV}/c$ ,  $[2.0 - 2.5]\text{ GeV}/c$ ,  $[2.5 - 3.0]\text{ GeV}/c$ ,  $[3.0 - 4.0]\text{ GeV}/c$ ,  $[4.0 - 5.0]\text{ GeV}/c$ ,  $[5.0 - 6.0]\text{ GeV}/c$ ,  $[6.0 - 7.0]\text{ GeV}/c$ ,  $[7.0 - 8.0]\text{ GeV}/c$  and  $[8.0 - 12.0]\text{ GeV}/c$ . Each cluster from *MPC\_2x2(PT)* or *MPC\_4x4A* triggered events is subject to passing the following cuts:

- $|zvtx| < 120\text{ cm}$
- Single tower removal:  $partesum(1)/partesum(0) > 0.05$ . This means that the ratio of energy deposited in the second most energetic tower in the cluster and the most energetic tower must be greater than 5%.
- Single tower removal: cluster multiplicity  $> 2$ .
- Single tower removal: lateral dispersion in the  $x$  and  $y$  directions  $> 0.0001\text{ cm}^2$ .
- Cluster radius cut where  $r = \sqrt{x^2 + y^2}$ .  $11\text{ cm} < r < 19\text{ cm}$
- Warnmap veto on the center tower of each cluster.
- Lateral dispersion in the  $x$  and  $y$  directions  $< 4\text{ cm}^2$ .
- ADC overflow veto
- TDC overflow veto

In Figure 6.38 we show the fill by fill asymmetry results for the  $1.5 - 2.0\text{ GeV}/c$   $p_T$  bin. The calculation is separated by arm and by even versus odd crossings. In each case, the fill by fill results are fit to a constant value which is taken as the asymmetry for that bin, arm, and crossing subset. With the new electronics upgrade that will be discussed in the next chapter, the even/odd crossing separation will no longer be necessary. Recall that this separation is due to the trigger calculation occurring in alternating trigger cards. Therefore, it is conceivable that a systematic difference between the two might arise. The new electronics are much faster and compute a trigger calculation at six times the beam clock rate. Therefore, no such alternation between even and odd crossings is necessary and this potential source of systematic effects is

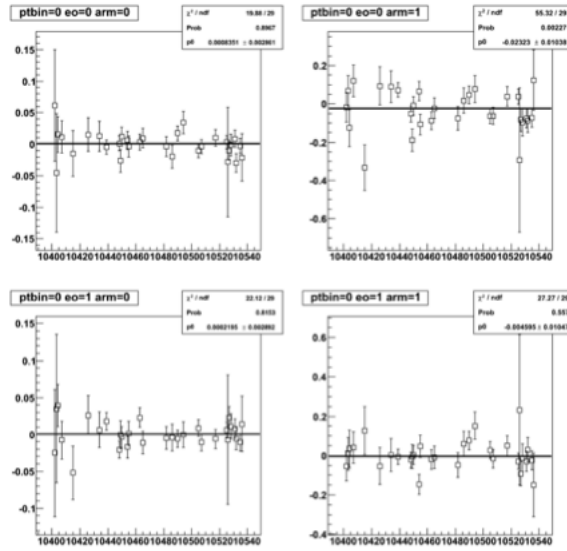


Figure 6.38:  $A_{LL}^{cluster}$  vs fill number is shown for the bin with  $1.5 \text{ GeV}/c < p_T^{clus} < 2.0 \text{ GeV}/c$ . Top Left (a): MPC south, even crossings. Top Right (b) : MPC north, even crossings. Bottom Left (a): MPC south, odd crossings. Bottom Right (b) : MPC north, odd crossings.

removed. Figure 6.39 shows the bunch shuffling results for even crossings in the south MPC in each  $p_T$  bin. The bunch shuffling technique is applied in the same way as described in Section 5.10. Here we perform 5000 spin randomizations. The bin by bin, asymmetries, statistical uncertainties, and fit goodness, along with the mean shuffled asymmetry and bunch shuffled width are summarized in Table 6.2.

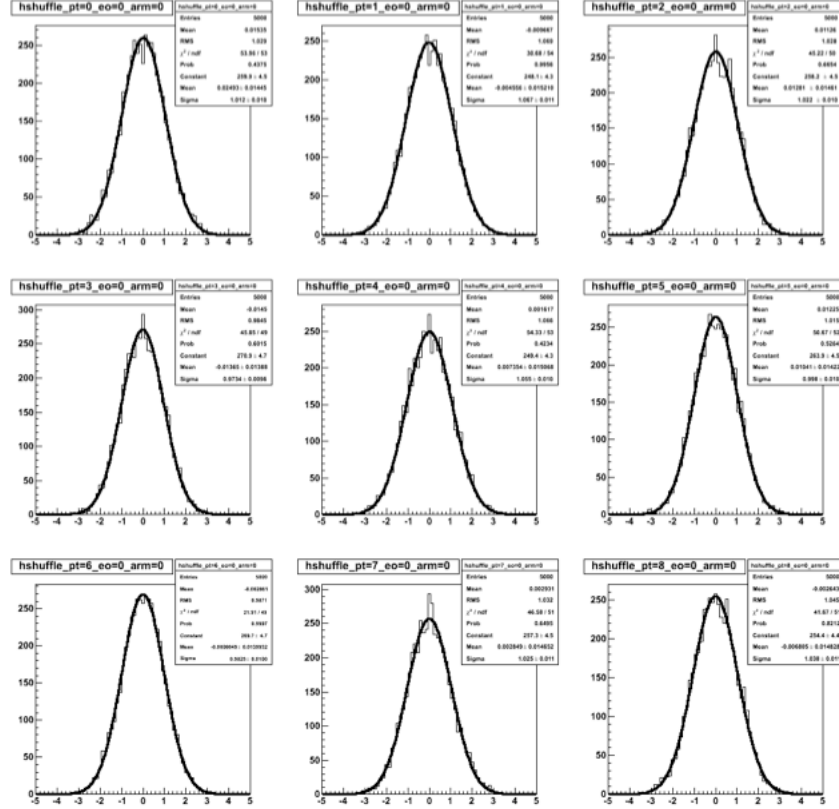


Figure 6.39: In each histogram the quantity  $\frac{A_{LL}^{shuf}}{\delta A_{LL}^{phys}}$  is plotted for every spin randomization. The top left histogram corresponds to the lowest  $p_T$  bin and each higher  $p_T$  goes across and down, like a book. This is for south MPC with even crossings only. Similar plots exist for the remaining combinations and the mean and width in each case is summarized in Table 6.2.

Table 6.2:  $A_{LL}$  results for electromagnetic clusters in the MPC at  $\sqrt{s} = 500$  GeV

$p_T^{min}$	$p_T^{max}$	Arm	Crossings	$A_{LL}$	$\delta A_{LL}$	$\chi^2/\text{NDF}$	$\langle A_{LL}^{shuf}/\delta A_{LL}^{phys} \rangle$	$\sigma_{A_{LL}^{shuf}/\delta A_{LL}^{phys}}$
1.5	2.0	south	even	0.0008351	0.002861	19.88/29	$0.024 \pm 0.014$	1.012
1.5	2.0	north	even	-0.02323	0.01038	55.32/29	$0.0142 \pm 0.015$	1.062
1.5	2.0	south	odd	0.0002195	0.002892	22.12/29	$0.0081 \pm 0.0149$	1.039
1.5	2.0	north	odd	-0.004595	0.01047	27.27/29	$0.0067 \pm 0.0147$	1.023
2.0	2.5	south	even	-0.0007937	0.003918	29.19/29	$-0.0046 \pm 0.015$	1.067
2.0	2.5	north	even	0.01058	0.0127	34.45/29	$-0.0283 \pm 0.0142$	0.9942
2.0	2.5	south	odd	-0.001757	0.003965	32.83/29	$0.0167 \pm 0.0140$	0.9800
2.0	2.5	north	odd	-0.004898	0.01284	17.36/29	$0.00253 \pm 0.0142$	1.0027
2.5	3.0	south	even	0.002529	0.005113	24.79/29	$0.0128 \pm 0.0146$	1.022
2.5	3.0	north	even	-0.01257	0.01172	18.56/29	$-0.0153 \pm 0.0146$	1.013
2.5	3.0	south	odd	-0.001469	0.005162	22.83/29	$0.01745 \pm 0.0143$	1.005
2.5	3.0	north	odd	-0.007842	0.01188	28.18/29	$0.00826 \pm 0.0142$	1.000
3.0	4.0	south	even	0.0001297	0.004868	35.11/29	$-0.0136 \pm 0.0139$	0.9734
3.0	4.0	north	even	0.002771	0.007148	33.53/29	$0.00331 \pm 0.0138$	0.9718
3.0	4.0	south	odd	0.002763	0.004905	32.76/29	$-0.00191 \pm 0.0137$	0.9626
3.0	4.0	north	odd	0.002639	0.007246	36.26/29	$0.01422 \pm 0.0147$	1.026
4.0	5.0	south	even	-0.00719	0.007941	23.13/29	$0.007354 \pm 0.0151$	1.055
4.0	5.0	north	even	0.005915	0.007599	49.46/29	$-0.0313 \pm 0.0142$	0.999
4.0	5.0	south	odd	0.00121	0.008013	26.81/29	$-0.0286 \pm 0.0147$	1.033
4.0	5.0	north	odd	-0.002349	0.007679	39.85/29	$-0.0244 \pm 0.0145$	1.011
5.0	6.0	south	even	0.08051	0.01386	23.24/29	$0.0104 \pm 0.0142$	0.998
5.0	6.0	north	even	-0.004539	0.01133	28.45/29	$0.02239 \pm 0.01503$	1.051
5.0	6.0	south	odd	0.02806	0.01399	18.86/29	$-0.0109 \pm 0.0141$	0.9847
5.0	6.0	north	odd	0.006826	0.01142	33.44/29	$-0.00868 \pm 0.0145$	1.018
6.0	7.0	south	even	-0.02282	0.02521	34.2/29	$-0.0020 \pm 0.0139$	0.9825
6.0	7.0	north	even	0.02531	0.02005	20.29/29	$0.00253 \pm 0.0149$	1.041
6.0	7.0	south	odd	0.003748	0.02547	36.53/29	$0.0035 \pm 0.0149$	1.034
6.0	7.0	north	odd	-0.02744	0.02028	37.21/29	$0.00297 \pm 0.0145$	1.016
7.0	8.0	south	even	-0.05182	0.04787	32.8/29	$0.002849 \pm 0.0146$	1.025
7.0	8.0	north	even	0.005077	0.03793	34.19/29	$0.0061 \pm 0.0137$	0.9634
7.0	8.0	south	odd	0.030001	0.04828	20.02/29	$0.00175 \pm 0.0145$	1.016
7.0	8.0	north	odd	0.02883	0.03804	31.52/29	$0.00523 \pm 0.01434$	1.003
8.0	12.0	south	even	-0.1338	0.07811	22.94/29	$-0.00681 \pm 0.0148$	1.038
8.0	12.0	north	even	0.01033	0.05983	39.58/29	$0.00256 \pm 0.0137$	0.9614
8.0	12.0	south	odd	0.0606	0.07941	23.61/29	$0.03565 \pm 0.0146$	1.021
8.0	12.0	north	odd	0.01739	0.06114	34.87/29	$0.01526 \pm 0.0147$	1.025

## 6.11 Final Result for $A_{LL}^{cluster}$

The trigger in the south becomes efficient at a lower  $p_T$  than for the north. Therefore in the first three bins the statistics from the south give it a much smaller uncertainty. The combined results are shown in Figure 6.40 and the numerical values are given in Table 6.3. For the dataset, a new method of understanding relative luminosity was developed and will be explained in Chapters 8 and 9. Based on that method a systematic uncertainty due to relative luminosity is assigned at  $1.3 \times 10^{-4}$  and is represented by the blue bar in Fig. 6.40. This relative luminosity method can also be applied to the analysis from the previous chapter to further reduce the systematic uncertainty in that case. In this case we account for the effects of multiple collisions on luminosity counting via coincidence counting in the BBC and ZDC. Using the standard relative luminosity procedure this important effect is neglected and substituted with the same width correction method as in the previous analysis, which has proven to yield the same systematic difference in luminosity monitoring as making no correction at all.

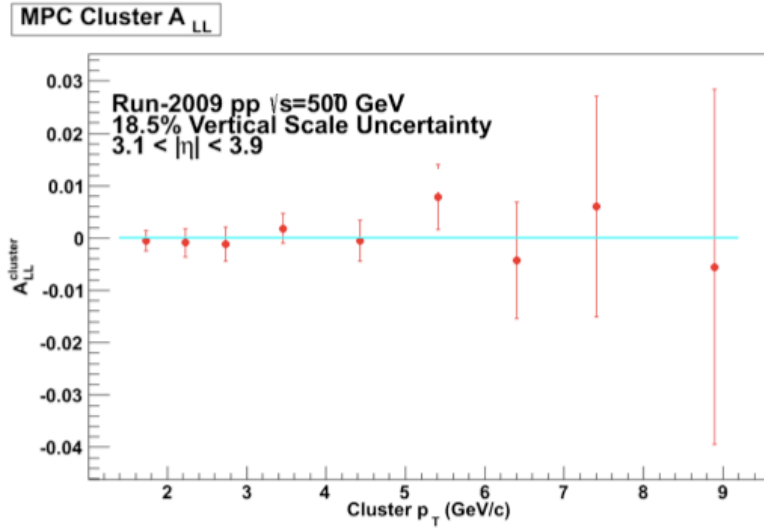


Figure 6.40: Final result for  $A_{LL}^{cluster}$  in the MPC for the 2009 data taken at  $\sqrt{s} = 500 \text{ GeV}$ .

Table 6.3:  $A_{LL}$  results for electromagnetic clusters in the MPC at  $\sqrt{s} = 500$  GeV

$p_T^{min}$	$p_T^{max}$	$\langle p_T \rangle$	$A_{LL}^{cluster}$	$\delta A_{LL}^{cluster,stat}$
1.5	2.0	1.72734	-0.000490758	0.00196068
2.0	2.5	2.23045	-0.000898714	0.00266293
2.5	3.0	2.738	-0.00116602	0.00333064
3.0	4.0	3.4531	0.00183924	0.00285858
4.0	5.0	4.43338	-0.000492818	0.00390111
5.0	6.0	5.41503	0.00785406	0.00622907
6.0	7.0	6.40502	-0.00422015	0.0111569
7.0	8.0	7.40237	0.00609267	0.0210751
8.0	12.0	8.88769	-0.00549181	0.0339161

## 6.12 Spin Pattern Separated $A_{LL}$ Check

The definition of the spin pattern definitions is given in Chapter 8. Spin patterns 0 and 3 follow the “OSSO” pattern while spin patterns 1 and 2 follow the “SOOS” spin pattern. In Figure 6.41 we show the asymmetries calculated separately for each spin pattern. To check the consistency between the various spin patterns we take the following approach. We find the t-test value between SP0 and SP3 and between SP1 and SP2. Then we combine SP0 and SP3 to get SP03, and similarly SP12. Then we calculate the t-test between SP03 and SP12. For each  $p_T$  bin we have three t-tests, and therefore 27 total. The results of these 27 independent

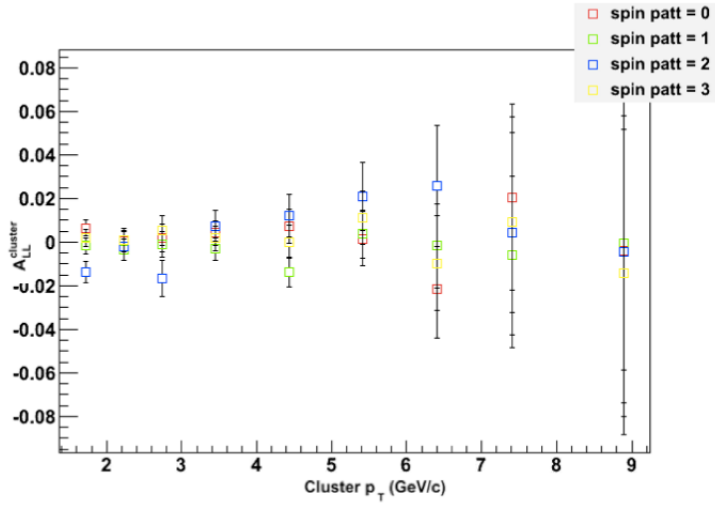


Figure 6.41:  $A_{LL}^{cluster}$  analysis separated by spin pattern.

comparisons are shown in Figure 6.42 and no irregularities are found. An in-depth look at these t-tests shows no clear indication that a systematic difference between spin patterns exists.

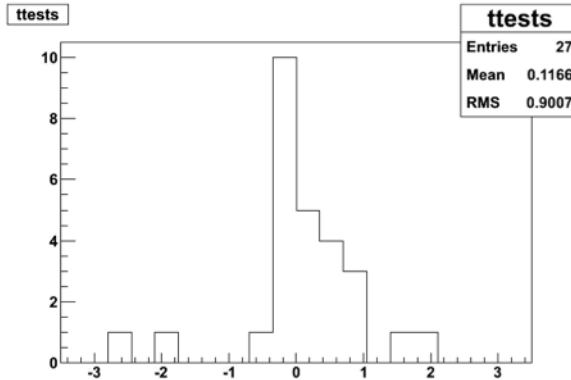


Figure 6.42: Histogram of the 27 possible independent t-tests between different spin pattern combinations.

## 6.13 Relative Luminosity

For this analysis we calculate the relative luminosity as described earlier but we have modified the raw luminosity scalers to account for multiple collision effects that we will discuss later at great length. Chapters 8 and 9 are devoted to fully explaining the methodology used in assigning the uncertainty we have stated for this set of data. Here, we briefly examine the results of reverting to the standard relative luminosity uncertainty analysis based on width corrections as outlined in Ref. [110]. In Figure 6.43 we show the final

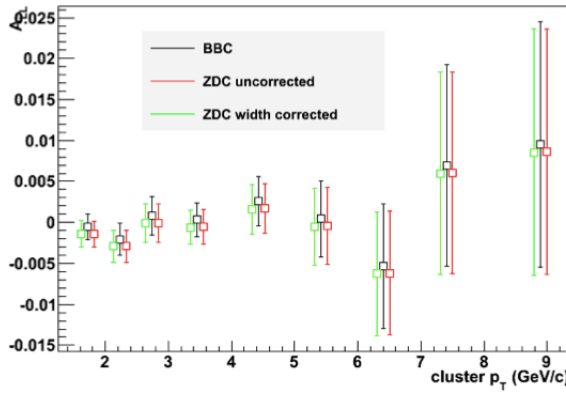


Figure 6.43: A comparison of the final  $A_{LL}^{cluster}$  is shown when three different choices of luminosity scalers are used. The black points show the BBC uncorrected scalers, the red points show the ZDC uncorrected scalers and the green shows the width corrected ZDC scalers. The BBC and ZDC uncorrected results can be seen to have a systematic offset. It is also seen that applying the width correction to the ZDC does little to resolve this difference. Applying this correction does not significantly modify the original uncorrected ZDC result.

result of the asymmetry calculation using the uncorrected raw BBC luminosity scalers, the uncorrected raw ZDC luminosity scalers and the width corrected ZDC luminosity scalers. The systematic offset of  $O(10^{-3})$  between the uncorrected scalers can be seen. However, modifying the ZDC scalers to account for width effects does not reduce the systematic offset. There is essentially no change from the uncorrected scalers. This indicates that a different effect is at play. This, in fact, turns out to be the case.

## 6.14 $A_L^{cluster}$ Results

As a further check we calculate the single spin asymmetry as in section 5.13. This asymmetry is expected to be 0 due to parity conservation of the QCD interaction. The single spin asymmetry is calculated for the blue and yellow beams in both their forward and backward directions. The results are summarized in

Figure 6.44.

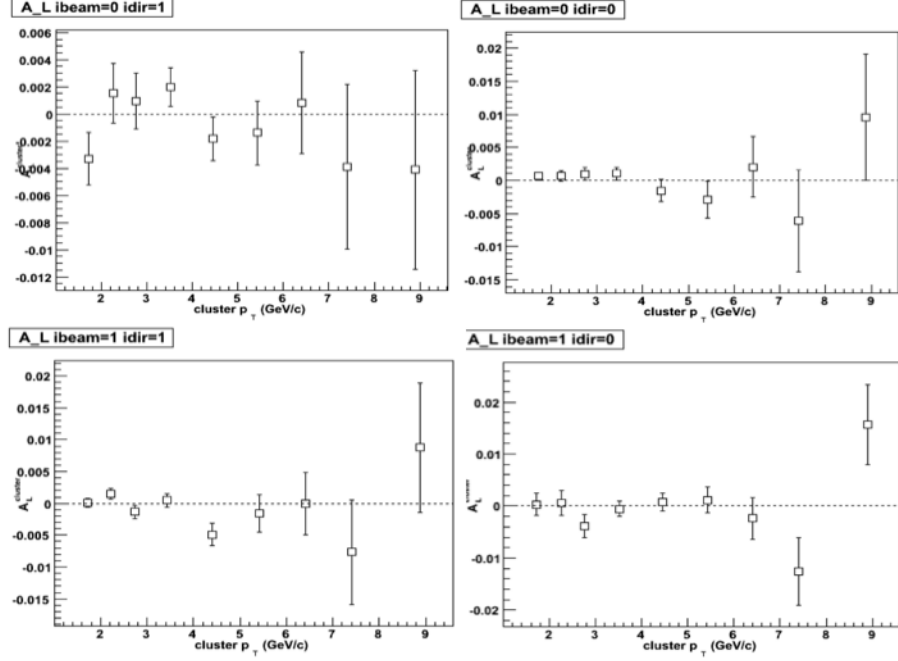


Figure 6.44: Top Left (a):  $A_L^{cluster}$  for the blue beam scattering off of an unpolarized yellow beam heading to the north MPC. Top Right (a):  $A_L^{cluster}$  for the blue beam scattering off of an unpolarized yellow beam heading to the south MPC. Bottom Left (a):  $A_L^{cluster}$  for the yellow beam scattering off of an unpolarized blue beam heading to the south MPC. Bottom Right (a):  $A_L^{cluster}$  for the yellow beam scattering off of an unpolarized blue beam heading to the north MPC.

## 6.15 Analysis of Ghost Clusters

The EMC and MPC electronics have the feature that when digitization occurs for readout in the FEM, a “pre”-adc and “post”-adc value are read out, and these digitizations are separated in time by 4 clock crossings. When an MPC trigger occurs, the triggering cluster is timed in to be in the correct crossing. However, if in one of the adjacent 3 crossings another cluster with a  $p_T$  in the same bin as the triggered cluster, as defined by the analyzer, also occurs, the “post”-adc will still contain information about this “ghost” cluster. The term random-benefit cluster is often used to refer to clusters occurring in an MPC triggered event, but not actually causing the trigger. In the case of a ghost cluster, there is a cluster from a previous crossing that gets read out due to a memory effect in the electronics. The hypothesis is that when taking into account that some crossings are same-sign helicity and others opposite sign helicity, these ghost clusters can cause a systematic effect on the measured  $A_{LL}$ . The goal is to analyze what this effect would be. In the case of the MPC cluster  $A_{LL}$  a TDC overflow cut is applied to the central tower of all clusters.

Since the dynamic range of the TDC's are about 2 beamclocks, any ghost effect would occur due to clusters occurring in just one adjacent crossing.

### 6.15.1 Definitions

We can divide up the cluster yield from all crossings in RHIC in a given  $p_T$  bin into six groups:

- $N_{SS}$  = the cluster yield from all crossings with same-sign helicity in the current crossing and same-sign helicity in the previous crossing.
- $N_{SO}$  = the cluster yield from all crossings with same-sign helicity in the current crossing and opposite-sign helicity in the previous crossing.
- $N_{SE}$  = the cluster yield from all crossings with same-sign helicity in the current crossing and unfilled in the previous crossing.
- $N_{OS}$  = the cluster yield from all crossings with opposite-sign helicity in the current crossing and same-sign helicity in the previous crossing.
- $N_{OO}$  = the cluster yield from all crossings with opposite-sign helicity in the current crossing and opposite-sign helicity in the previous crossing.
- $N_{OE}$  = the cluster yield from all crossings with opposite-sign helicity in the current crossing and unfilled in the previous crossing.

We will also make use of the additional subscript  $T$  to denote clusters that actually occurred in the current crossing. So for example,

- $N_{SO,T}$  = the cluster yield from all crossings with same-sign helicity in the current crossing and opposite-sign helicity in the previous crossing, only considering clusters that actually occurred in the same-sign crossing.

If we define  $P_g$  as the probability that a cluster observed in the current crossing is actually a ghost from the adjacent crossing, then we can write:

- $N_{SS,T} = (1 - P_g)N_{SS}$
- $N_{SO,T} = (1 - P_g)N_{SO}$
- $N_{SE,T} = N_{SE}$

- $N_{OS,T} = (1 - P_g)N_{OS}$
- $N_{OO,T} = (1 - P_g)N_{OO}$
- $N_{OE,T} = N_{OE}$

This includes the assumption that  $P_g$  is independent of spin pattern, which is true because this effect is electronics based and does not know about the spin pattern of the beam. Note that when the adjacent crossing in consideration is an empty crossing,  $P_g = 0$ , and so the ghost effect is absent for these crossings. The other simplification is that the bunch to bunch rate variation of  $O(10\%)$  is ignored. This can be safely done as long as the bunch rate is not correlated too strongly with the bunch helicity assignment, in which case the bunch to bunch fluctuations, due to rate, in ghost particles produced flow equally, on average, from same-sign crossings into opposite sign crossings and back an equal amount.

We also define  $P^2 = P_B P_Y$  for the beam polarizations and  $R$  as the relative luminosity. Also note that, by definition, the conventional values of  $N^{++}$  as the yield sum over all same-sign crossings and  $N^{+-}$  as the yield sum over all opposite sign crossings can be written as:

$$N^{++} = N_{SS} + N_{SO} + N_{SE}$$

and

$$N^{+-} = N_{OS} + N_{OO} + N_{OE}$$

### 6.15.2 The Effect of Ghost Clusters on $A_{LL}$

We now use these definitions to calculate how the asymmetry we actually measure,  $A_{LL}^{meas}$ , compares with the true asymmetry that we should measure, absent ghost clusters,  $A_{LL}^{true}$ . The asymmetry we actually measure can be written as:

$$P^2 A_{LL}^{meas} = \frac{(N_{SS} + N_{SO} + N_{SE}) - R(N_{OS} + N_{OO} + N_{OE})}{(N_{SS} + N_{SO} + N_{SE}) + R(N_{OS} + N_{OO} + N_{OE})} \quad (6.3)$$

While the asymmetry we should measure can be written as:

$$P^2 A_{LL}^{true} = \frac{(N_{SS} + N_{SO} + N_{SE})_T - R(N_{OS} + N_{OO} + N_{OE})_T}{(N_{SS} + N_{SO} + N_{SE})_T + R(N_{OS} + N_{OO} + N_{OE})_T} \quad (6.4)$$

We can rewrite the numerator of Eq. 6.4 as

$$(1 - P_g)(N_{SS} + N_{SO} + N_{SE}) + P_g N_{SE} - R(1 - P_g)(N_{OS} + N_{OO} + N_{OE}) - R P_g N_{OE} \quad (6.5)$$

And the denominator as

$$(1 - P_g)(N_{SS} + N_{SO} + N_{SE}) + P_g N_{SE} + R(1 - P_g)(N_{OS} + N_{OO} + N_{OE}) + R P_g N_{OE} \quad (6.6)$$

Dividing all terms in Eq.6.5 and Eq. 6.6 by the factor  $(1 - P_g)$  gives:

$$P^2 A_{LL}^{true} = \frac{N^{++} - RN^{+-} + \frac{P_g}{1-P_g}(N_{SE} - RN_{OE})}{N^{++} + RN^{+-} + \frac{P_g}{1-P_g}(N_{SE} + RN_{OE})} \quad (6.7)$$

Note that when  $P_g \rightarrow 0$ ,  $A_{LL}^{true} \rightarrow A_{LL}^{meas}$ . But if  $P_g > 0$  then the other way to eliminate the effect of ghost clusters is to force  $N_{SE}$  and  $N_{OE}$  to be 0. This is done by eliminating a crossing from the analysis if it is adjacent to an empty crossing. This derivation assumes that a triggered crossing can only be affected by ghost clusters from a specified adjacent crossing. This condition is true for the MPC when a TDC overflow cut is applied. In other circumstances where ghost clusters from more than one adjacent crossing need to be considered, more general considerations would have to be taken into account. When we rewrite Eq. 6.4, this amounts to subtracting the quantities  $P_g(N_{SS} + N_{SO})$  and  $P_g(N_{OS} + N_{OO})$  from the yields we would plug into  $N^{++}$  and  $N^{+-}$  for  $A_{LL}^{meas}$ , respectively. We might be tempted to say that  $P_g N_{SO}$  should switch from being counted in the  $N^{++}$  sum to the  $N^{+-}$  sum, and the  $P_g N_{OS}$  term should switch from being counted in the  $N^{+-}$  to the  $N^{++}$  sum. Whatever rate effects or real asymmetries might cause this swap to not completely wash out will be suppressed by the factor  $P_g$ . However, these terms represent clusters that occurred in a different crossing anyways, and therefore definitely did not cause a trigger in either the current or the ghost crossing.

### 6.15.3 Estimate of the Size of the Ghost Cluster Effect

The effect of removing such crossings on the overall statistics is very small. For spin pattern 1, which is an “OSSO” pattern, the final analysis uses 4717 bunches, a reduction of 3% from the initial 4858 bunches. Spin pattern 2, an “SOOS” pattern, now would use 4507 of 4642 bunches for a removal of 3%. Spin pattern 3, an “SOOS” pattern, now uses 4100 of 4251 bunches for a total removal of 3.6%. And lastly, spin pattern 4 uses 6703 of 6996 for a reduction of 4.2% of bunches.

It is instructive to estimate the value of  $P_g$  for the lowest  $p_T$  bins as well, starting with the  $1.5 < p_T < 2.0$  GeV/c bin. In minimum bias events the probability to observe a cluster with a  $p_T$  in this range is about 0.012. The minimum bias rate is about 10% of the clock rate (in run9) and also the minimum bias trigger

sees only about half of collisions. Therefore the collision rate is around 20% of the clock rate. This means the probability for a ghost cluster to appear in the previous crossing to an MPC trigger is  $0.012 \times 0.2 \sim 0.0024$ . In the  $2.0 < p_T < 2.5$  bin the probability of a minimum bias event giving such a cluster is 0.003, so the ghost probability is  $0.003 \times 0.2 \sim 0.0006$ . These numbers are overestimates of the true upper bound because many collisions that do not trigger the BBC are diffractive and therefore do not produce clusters in the MPC.

To now estimate how large the effect of ghost clusters is on the asymmetry we can use Eq. 6.9 which gives the true  $A_{LL}$  in terms of observed yields and the ghost cluster probability. We assume the largest possible effect, that all bunches following empty bunches are of same sign helicities. In a typical fill there are about 3 such bunches. So from the denominator we have:

$$N^{++} + RN^{+-} + \frac{P_g}{1 - P_g} (N_{SE} + RN_{OE}) \sim N^{++} + RN^{+-} \quad (6.8)$$

and the relative contribution of the last term, assuming 100 bunches in total, is  $\sim P_g \frac{N_{SE}}{N_{total}}$ . For the lowest  $p_T$  bin this evaluates to  $\sim 0.0024 * 0.03 = 7.2 \times 10^{-5}$ . So the denominator is essentially unchanged. This allows us to write the approximation:

$$P^2 \delta A_{LL}^{true-meas} \sim \frac{P_g N_{SE}}{N^{++} + RN^{+-}} \quad (6.9)$$

which for the lowest  $p_T$  bin, when accounting for the typical  $P^2 \sim 0.16$  gives an offset of  $4.3 \times 10^{-4}$ . This would cause a splitting of the observed  $A_{LL}^{meas} \sim 8.6 \times 10^{-4}$  which has been doubled to account for the fact that different signed bunches follow empty crossings in “SOOS” fills versus “OSSO” fills. This effect is strongly  $p_T$  dependent, however. For  $2.0 < p_T < 2.5$  the estimated splitting is  $\sim 2 \times 10^{-4}$ . In higher  $p_T$  bins, the effect drops below the  $1 \times 10^{-4}$  level.

# Chapter 7

# MPC Electronics and Trigger Upgrade

## 7.1 Motivation for an MPC Upgrade

At this point, we have seen an overview of the theoretical aspects involved in understanding the spin structure of the proton. We learned that the gluon polarized parton distribution function can be measured through scaling violations of the spin-dependent proton structure function,  $g_1$ , in SIDIS experiments. The existing data on  $g_1$ , however, is sparse and will require a polarized  $ep$  experiment with wider kinematic reach in both  $Q^2$  and  $x$ . This provided motivation to turn to polarized  $pp$ , where  $\Delta G$  can be measured directly through the difference in cross section between same sign helicity protons and opposite sign helicity protons. Over the last decade, RHIC has provided high quality polarized proton beams resulting in rich datasets for both the PHENIX and STAR experiments. This has, in turn, resulted in the best available constraints on the gluon spin by extending the kinematic range up to  $Q^2 \sim 10^3 \text{ GeV}^2$  (see Fig. 2.7). The challenge in this case has been the kinematic reach in the gluon momentum fraction,  $x_g$ , that we have been experimentally sensitive to. Before the MPC upgrade the sampled range was  $0.05 < x_g < 0.2$ . With the successful installation and operation of the MPC, the range of sensitivity is pushed down to  $\langle x_g \rangle \approx 0.01$  through our measurement of  $A_{LL}$  for single electromagnetic clusters at  $\sqrt{s} = 200 \text{ GeV}$  and  $\sqrt{s} = 500 \text{ GeV}$ .

From these two measurements, we have arrived at two essential conclusions. First, while the MPC measurements will provide the first constraints on  $\Delta g(x)$  for  $x < 0.05$ , it is important to gain sensitivity to gluons with yet lower momenta fractions. From Fig. 2.5 we saw that  $g(x)$  rises rapidly at low- $x$  which leaves open the potential for a large  $\Delta G$  in the absence of experimental constraints. As we showed in Chapter 4, if the MPC can trigger on di-hadrons, it can gain sensitivity to  $x \sim 0.001$ . Until 2012, this was not possible due to the electronics configuration of the MPC in which only one high energy cluster could be triggered on. However, an electronics and trigger upgrade to the MPC has now made it possible to trigger directly on two back-to-back clusters in the same arm, thereby allowing for a di-hadron measurement which will produce the first constraints on  $\Delta G$  in this range of  $x$ . In this chapter we will discuss the details of this successful upgrade.

The second essential conclusion that arises from the MPC measurements described in Chapters 5 and 6 is that the relative luminosity systematic uncertainty will become the limiting factor for the constraining power of high statistics  $A_{LL}$  measurements on  $\Delta G$ . It is a top priority to understand this issue deeply with the goal of reducing the systematic uncertainty from  $O(10^{-3})$  to  $O(10^{-4})$ . From runs 2012 and 2013, the expected level of the statistical uncertainties is  $O(10^{-4})$ , as are the expected size of the asymmetries at low  $p_T$  ([44],[45]). The following two chapters will be devoted to this topic.

## 7.2 Scope of Changes to the MPC Electronics

Figure 7.1 from Ref. [8] is slightly modified to illustrate where the changes to the old electronics configuration were made. In the old configuration, the driver board would send a differential signal to a receiver board

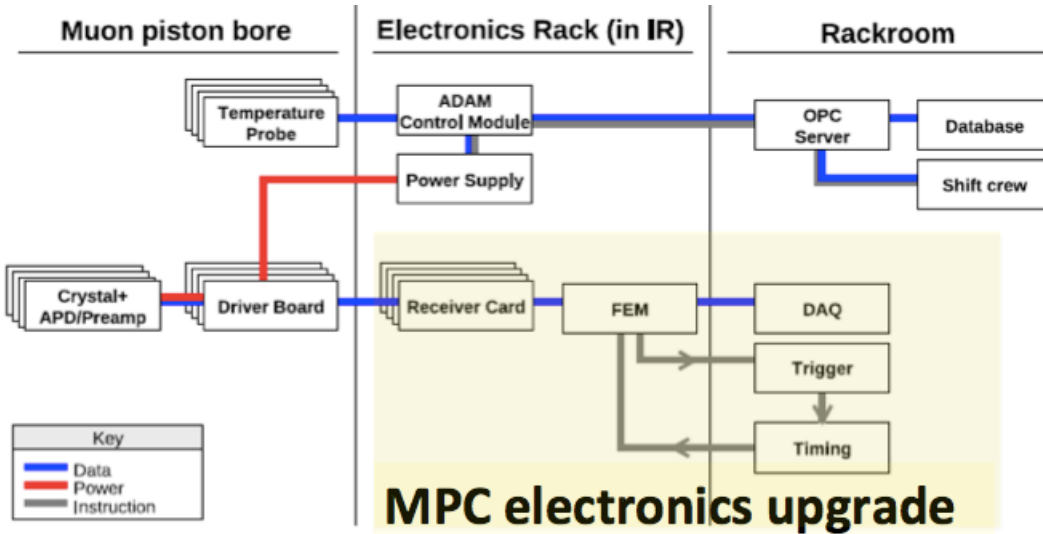


Figure 7.1: Diagram of MPC electronics flow. The original diagram is from Ref. [8]. The shaded yellow section is where the changes occur.

which would modify the pulse to the height expected by the Front End Electronics (FEE) board. The FEE boards, which combined are referred to as the Front End Module (FEM), were spare boards from the Central Arm Electromagnetic Calorimeter. More details on this are available in Ref. [94]. Within the FEM, the analog signal information is stored in 64 AMU cells for each channel. The FEM then sends this information to a separate trigger card (Ref. [95]) to perform an analog trigger calculation. The FEM only digitizes its signals before readout, due to the time lag incurred in the digitization process. In Figure 7.2

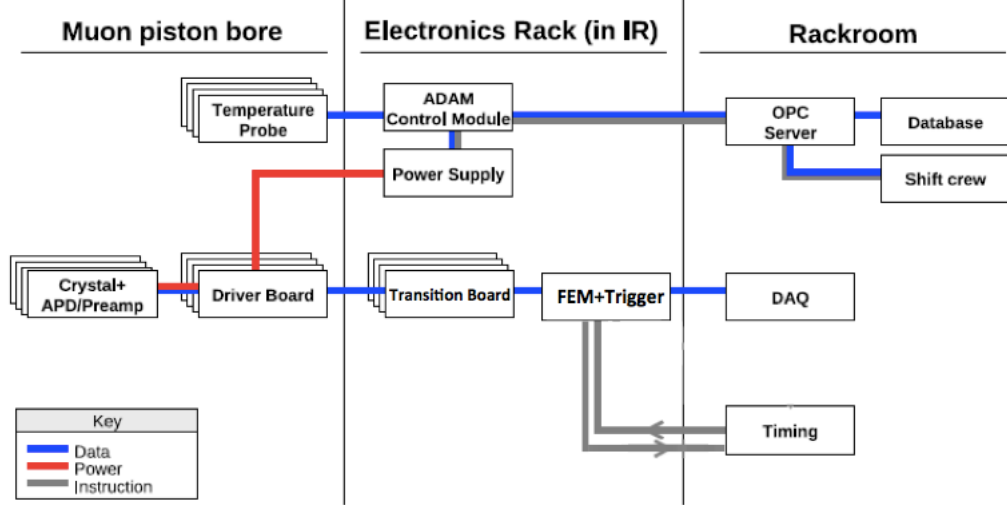


Figure 7.2: Diagram of the new MPC electronics information flow.

we show the resulting diagram. Note that the MPC crystal→APD→driver board signal chain in the MPC is preserved. No changes were made within the Muon Piston bore. The receiver card is now replaced by a passive transition board. This board has no power source and serves to shape the driver board signal to input to the FEM. The new Front End Module boards were taken from the decommissioned Hadron Blind Detector (HBD). The HBD FEMs perform both rapid digitalization as well as the trigger calculation. A separate trigger card is no longer needed.

### 7.3 Transition Board

The driver board sends a voltage proportional to the energy deposited in each crystal out of the piston hole, where it is converted to a 100-ohm impedance differential signal to reduce noise. While the receiver board was needed to convert this to a 93-ohm impedance single ended signal for input the EMCAL FEM, the new HBD FEM receives a 100-ohm differential signal, and therefore no impedance matching is necessary. The receiver boards can then be taken out and are replaced with passive transition, or interconnect, boards. Two modifications to the signal need to be made.

The first modification is to insert a gain factor of about  $\frac{1}{4}$  on the driver board signal amplitude. It was found that an input voltage of about 1V to the HBD FEM reached the dynamic limit of its ADCs<sup>1</sup>. By reducing the amplitude of the input, we set the corresponding energy at which the dynamic range will end

<sup>1</sup>Each ADC channel is 12-bit bipolar. Therefore, it effectively contains 11 bits of useful information since the sign of the signal is always the same.

to be around  $50\text{ GeV}$ . This can be estimated by knowing the signal amplitude corresponding to the MIP energy deposit.

The second modification is to reduce the length of the driver board signal from about  $400\text{ ns}$  to about  $100\text{ ns}$ , roughly the length of one bunch crossing. This will allow us to avoid seeing the tail of the waveform from the previous crossing in the current crossing. Figure 7.3 shows a diagram of the transition board, which

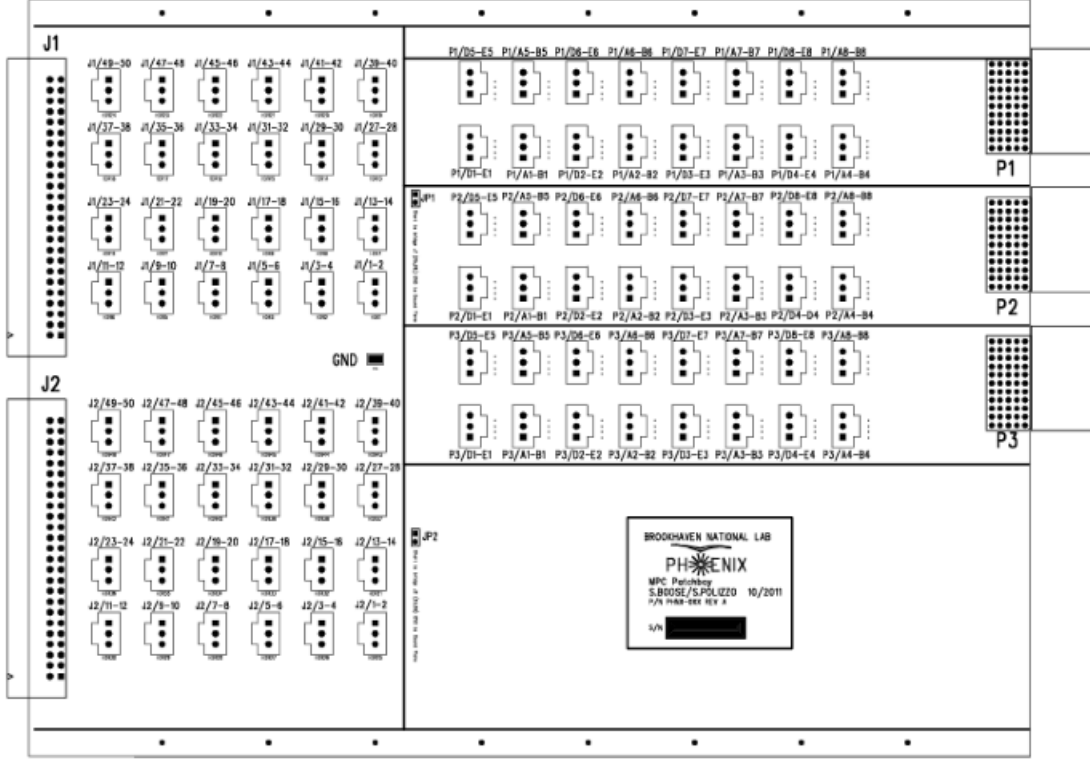


Figure 7.3: Schematic of the transition board design. The twisted pair cables coming up from the driver board feed into inputs J1 and J2, each with 24 available inputs, matching the driver board output. These channels can then be mapped in any desired fashion onto the P1/P2/P3 outputs which feed into the FEM. This mapping is chosen to be such that it matches the geometric locations of the physical crystals. The J1/J2 ports have two pins for each channel, the + and -, as the incoming signal is differential. The P1/P2/P3 ports have five pins to a row in the format +,-,G,+,-. Each row holds two channels with a ground in the middle.

was designed and produced by Steve Boos and Sal Polizzo. It is a passive board containing RC components that, in addition to modifying the signal as described, also allows the driver board signals to be mapped arbitrarily into the FEM channels. Figure 7.4 shows a PSPICE®([99]) simulation of the input signal (blue) and the output (green).

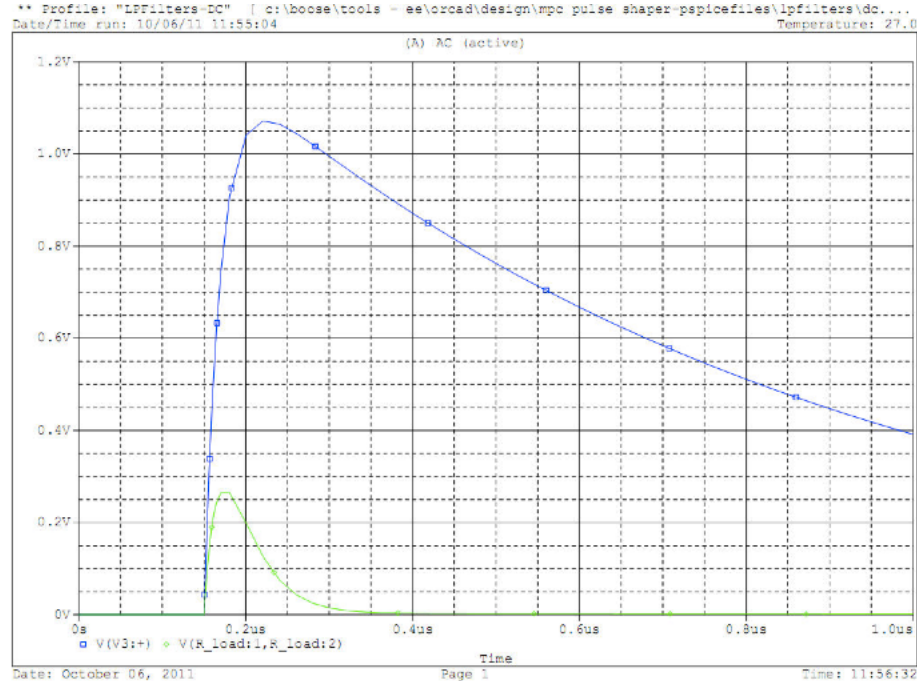


Figure 7.4: PSPICE®simulation of an incoming pulse shape from the driver board(blue) and the transition board response(green).

Once the transition board design was tested, a total of 15 were produced. Six boards are allocated to each arm and three spares were produced. Figure 7.5 shows the mapping from a given sector of the MPC to each transition board. As can be seen in the figure, the channels from one sector of the MPC within a given azimuthal range are mapped to one transition board. As each transition board feeds directly into a FEM, the signal processing chain, including the trigger calculation, preserves the azimuthal sectors. Therefore, we label these sectors as Top Left (TL), Top Right (TR), Middle Right (MR), Bottom Right (BR), Bottom Left (BL), and Middle Left (ML). In Figure 7.6 we show for both the south and north MPC the channel to driver board mapping designated by the color coding along with the channel to transition board mapping. In the south MPC all six transition boards receive input from precisely two driver boards while four driver board twisted pair cables must be split and recrimped at the connector for input into separate transition boards as they span two azimuthal sectors. In the north, it was not possible to always have only two driver board inputs for each transition board. For the four channels this affects, their signal was sent to the J1/J2 input of one transition board from which an external cable connecting to the P1/P2/P3 socket of the destination transition board. The specific mapping of driver board to transition board mapping is shown in Figure 7.7.

This new channel mapping also generates new channel numbers as shown in Fig. 7.6. Figure 7.8 illustrates an example of the wiring within a transition board. While the crystal to driver board channel mapping is not geometrically based, this is fixed by specifying the correct mapping between the J1/J2 inputs and the P1/P2/P3 outputs. A simple algorithm can be used to determine this mapping which is different in each transition board. The determination of this mapping occurs simultaneously with the driver board to transition board connection map of Fig. 7.7 . Since many twisted pair cables needed to be split, the exact mapping and placement of the transition boards within the electronics rack was determined with the constraint that transition boards with external cabling were placed adjacently to each other. Figure 7.8 also shows the empty versus occupied driver board channels as well as the empty versus occupied FEM input channels. Figure 7.9 shows the final product that is ready for installation into the electronic rack in the IR. Figure 7.10 shows the transition boards fully installed in the north MPC rack with twisted pair connections.

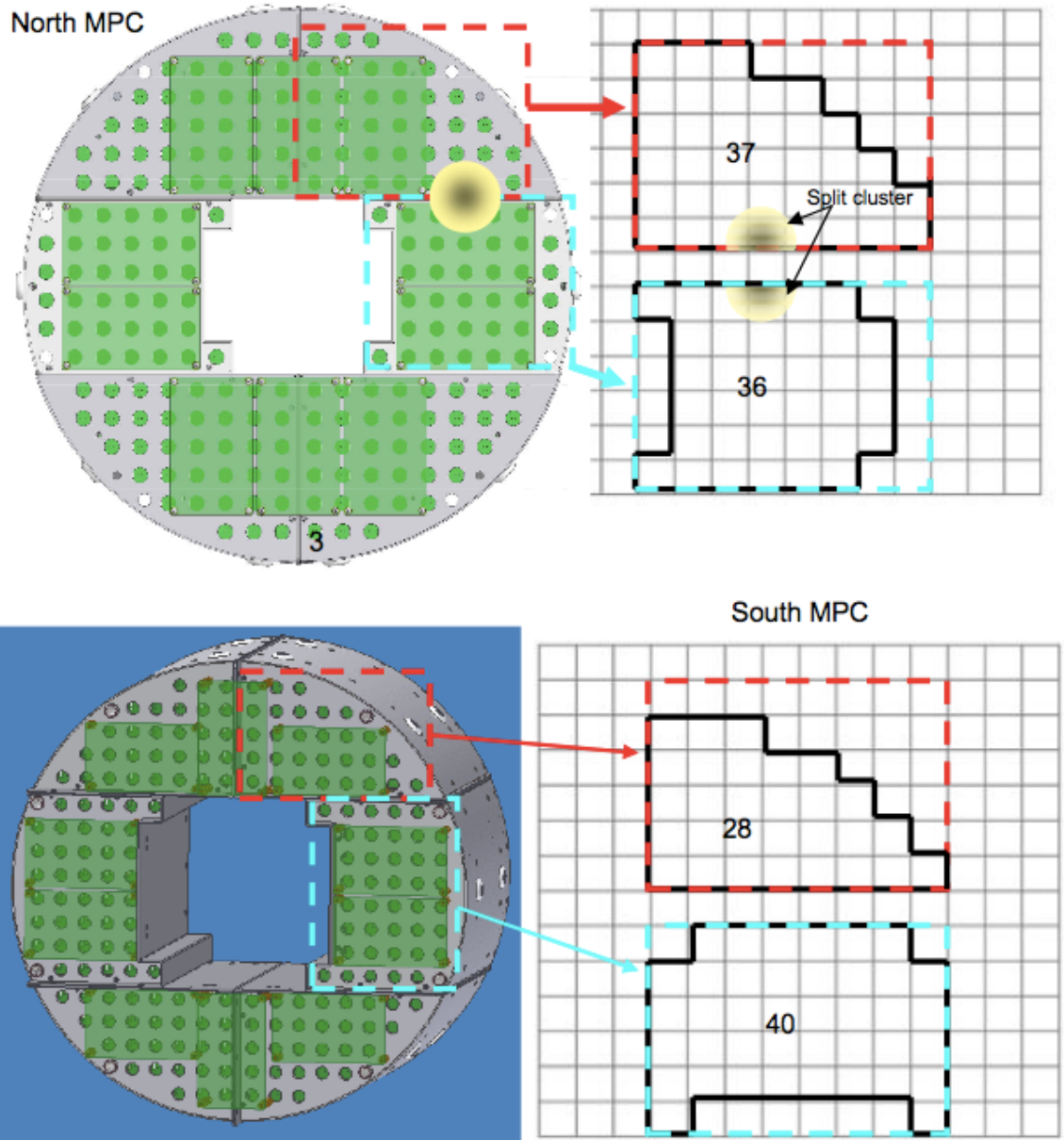


Figure 7.5: Illustration of the mapping from each MPC to the transition boards. Each board is designed to receive signal input from two driver boards which is typically the number of driver boards corresponding to a particular MPC azimuthal sector. Each transition board processes a maximum of 48 channels, but the maximum used channels is 40.

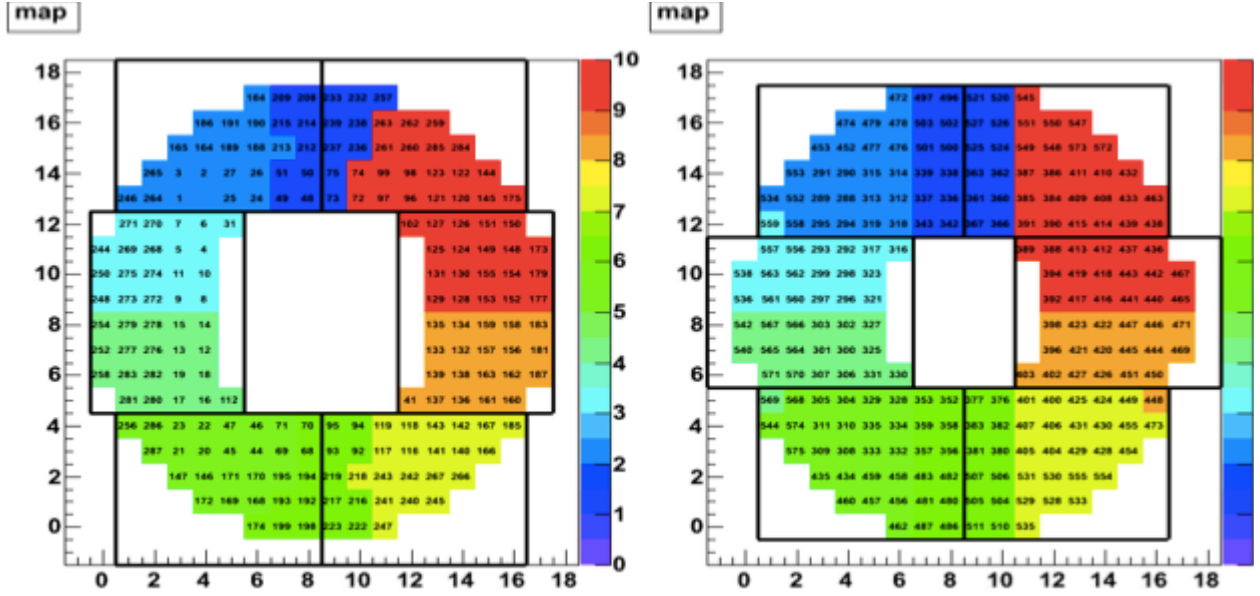


Figure 7.6: Illustration of the driver board (color coded) to transition board (black outlined) mapping. In the south MPC (left), a mapping was possible that always limits two driver boards to one transition board. In cases where the output from a single driver board needed to be split into two transition boards, the twisted pair cable was split in half and each half recrimped with a new terminating connector.

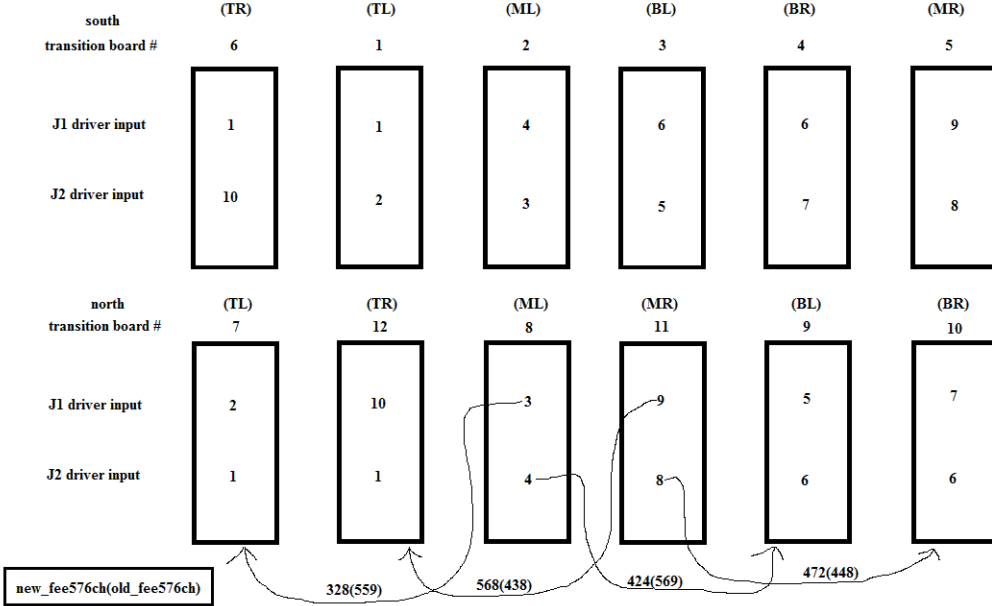


Figure 7.7: Each transition board is shown in the order it is placed on the electronics rack. The south transition boards are numbered 1-6 and in the north they are labeled 7-12. There are 10 driver boards from each arm labeled 1-10 in each case. For example, in the south, the J1 input to transition board 6 (MR) comes from driver board 1. This driver board cable is split and also feeds to the J1 input of board 1 (TL).

**transition\_board\_template**

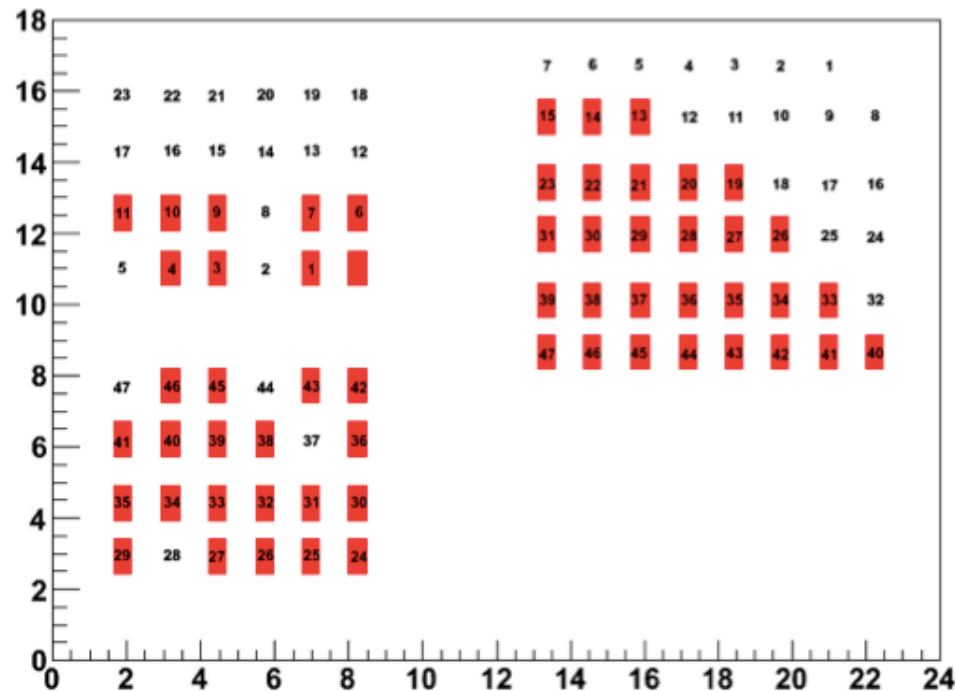


Figure 7.8: An illustration of the occupied driver board channel inputs to J1/J2 on the left side (top and bottom) are shown in red and the occupied FEM channel outputs on the right, also in red. The input and output signals are both differential.

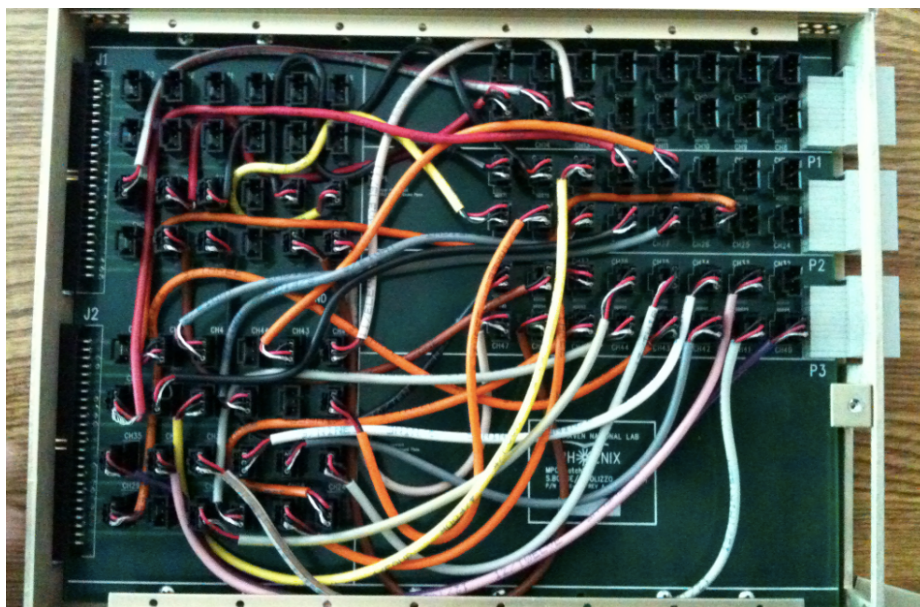


Figure 7.9: The implemented transition board cable mapping, ready for crate installation. The IDC input connectors are on the left and the Meritec output is on the right.

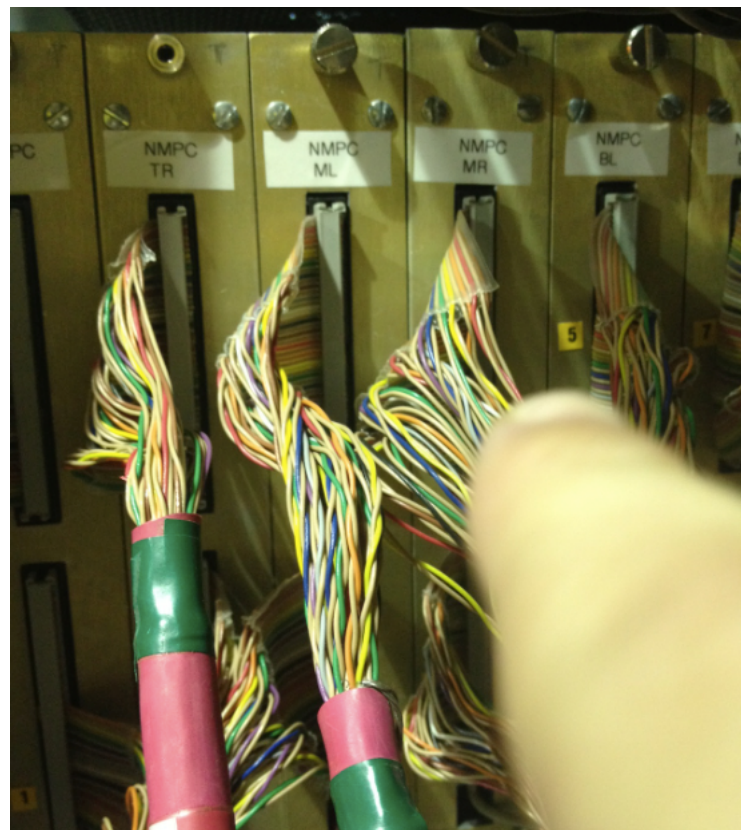


Figure 7.10: A view of the front of the installed transition boards and the twisted pair cable connections from the driver boards.

## 7.4 HBD Front End Module ADC Board

A schematic of the HBD ADC board is shown in Figure 7.11. The left side of the schematic faces outward when inserted into the crate and receives input from three eight-layered Meritec cables from the P1/P2/P3 output of the transition board. The schematic also shows the differential receiver for each channel individually. The data is then immediately digitized and passed to the FEM Field Programmable Gate Array (FPGA). The FPGA stores a buffer of data and was programmed to execute the trigger algorithm

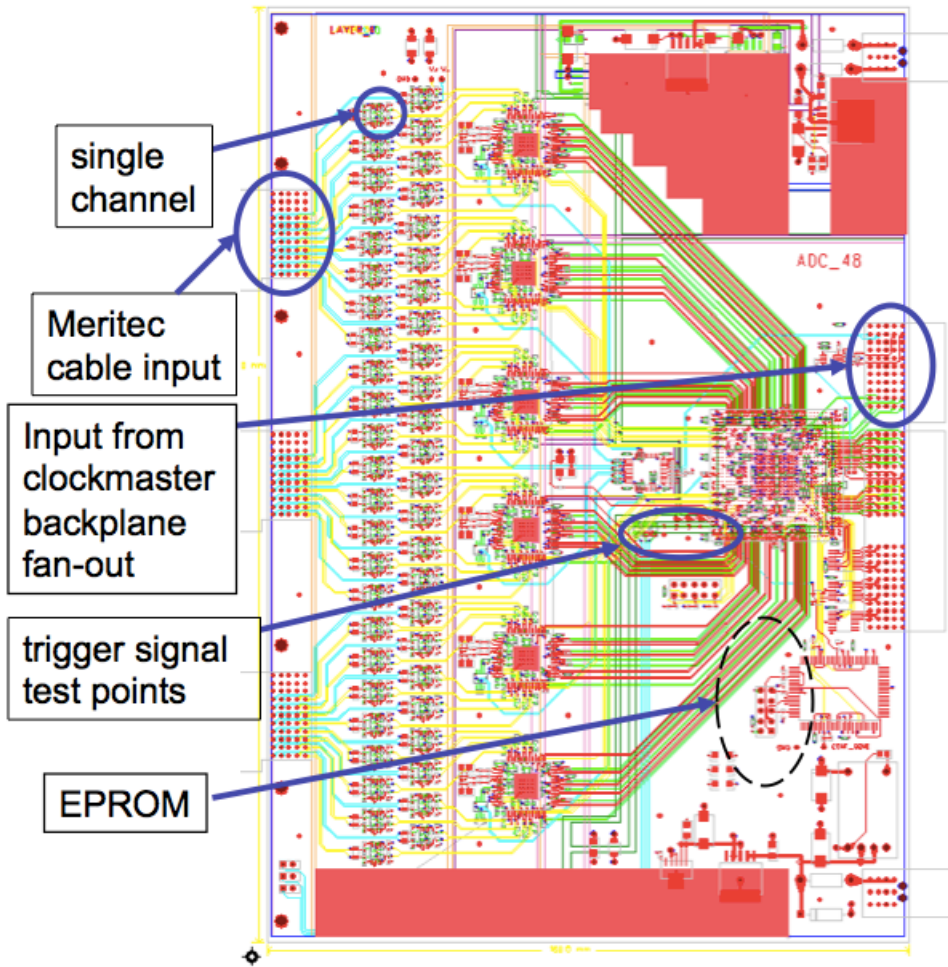


Figure 7.11: Schematic of the HBD Front End Module. Data flows in from the left and moves to the right. Power and clockmaster instructions are received from the backplane (right).

which we will discuss separately. Since the FEMs compute the trigger decisions internally, without a separate circuit, it was necessary to modify each board to physically include a trigger output. The trigger test points are shown and the front plane also includes one output for the trigger decision at each of the three programmable thresholds (not shown in this schematic). The FEM receives its low voltage power and

its timing instructions from the clockmaster fan-out (which gets its timing input from the MPC GTM) on the backplane. Figure 7.12 shows a detailed schematic of its functionality ([96]) and Figure 7.13 shows a

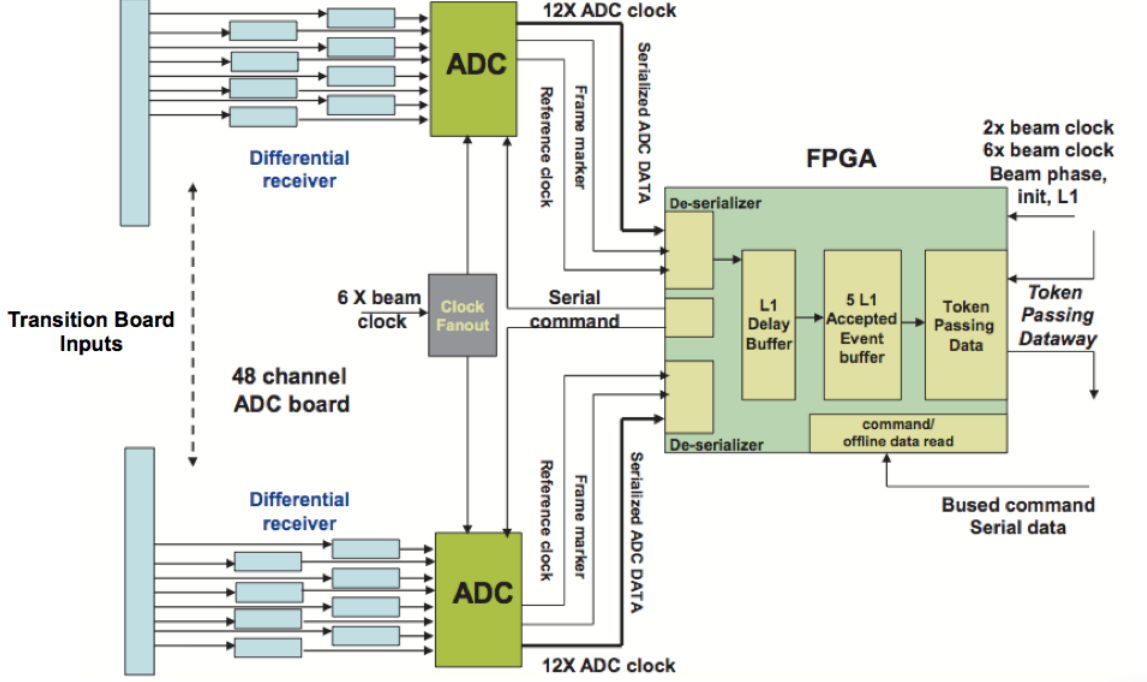


Figure 7.12: Diagram of the FEM board functionality. See ref. [96] for further details and discussion.

picture of the actual FEM board that is used. The ADCs receive a copy of the  $6 \times \text{BCLK} \approx 56.28 \text{ MHz}$  clock fan-out which provides the six ADC samples per bunch crossing. Figure 7.14 shows the backplane of the FEM rack. The clockmaster receives slow control instructions from a preset IP address. These instructions include the addresses of the FEMs on the crate, how many ADC samples to read out from each channel, and trigger configurations such as trigger thresholds, single tower thresholds and the minimum required number of channels above the single tower threshold. These instructions can be uploaded between PHENIX runs or during other downtime. The clockmaster also receives fast control input from a GTM optical fiber. This provides the signal for each FEM to send its data according to its configuration instructions. Figure 7.15 shows the Coldfire board that is used to boot the clockmaster. Finally, in Figure 7.16 the front of the FEM rack is shown. The transition boards send their output here for buffering and trigger computations in the FEM. The trigger outputs are shown and are sent into the rack room for Blue Logic processing and input to the RBIB before being sent to GL1. When commanded by the GTM, the FEMs will send data through

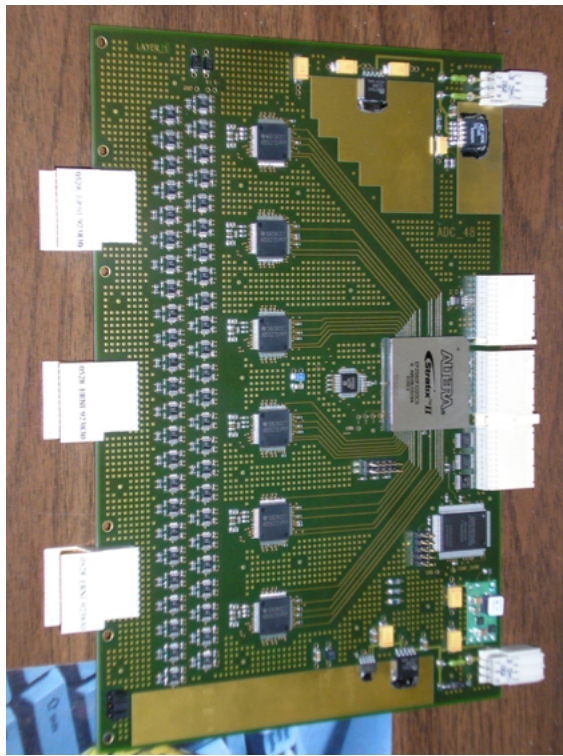


Figure 7.13: Picture of a Front End Module

the XMIT boards to the DCM.

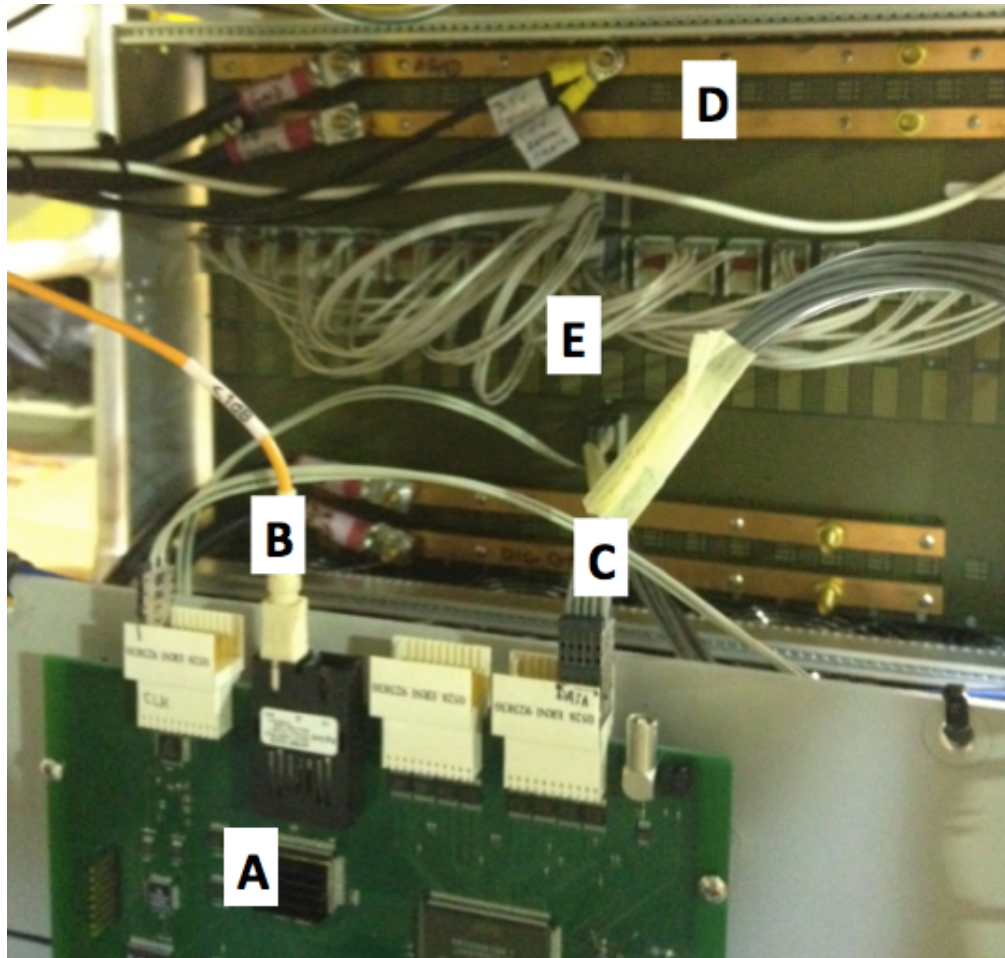


Figure 7.14: The backplane of the FEM crate. (a) The clockmaster receives slow control instructions via ethernet connection (not shown). These instructions include the number of ADC samples per channel to read out, phase offsets and trigger settings. It also receives fast timing instructions (beam clock signal, acquire data, etc.) from (b) the Granule Timing Module (GTM) optical fiber input. The GTM board is located in the PHENIX rack room. (c) The clockmaster provides a clock fan-out to each FEM through the backplane. (d) The common ground and required voltages of -3.5V, 4.0V, and 5.4V are provided to the FEMs via copper strips. (e) Clockmaster input to each FEM.

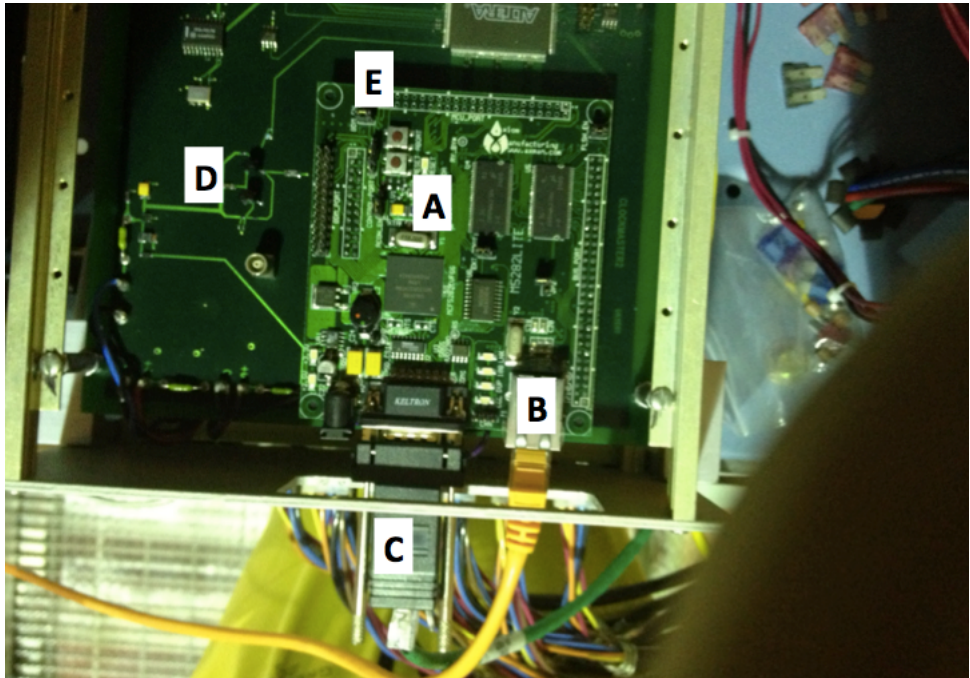


Figure 7.15: (a) Coldfire 5282 board. It is used to fetch a stripped down version of linux called UCLinux for the Clockmaster. (b) Ethernet communication port. (c) Serial communication port. This was used frequently during the testing phase, but is unused during operations. (d) Clockmaster board. (e) Jumper switch on the Coldfire board. If the jumper is open it executes the uboot image in its flash memory which then tells the clockmaster to load UCLinux from a specified IP address. The uboot then assigns the clockmaster its own IP address which allows it to communicate externally and receive configuration instructions. If the jumper is closed it goes to its own BIOS. Only the serial communication port is functional in this case.

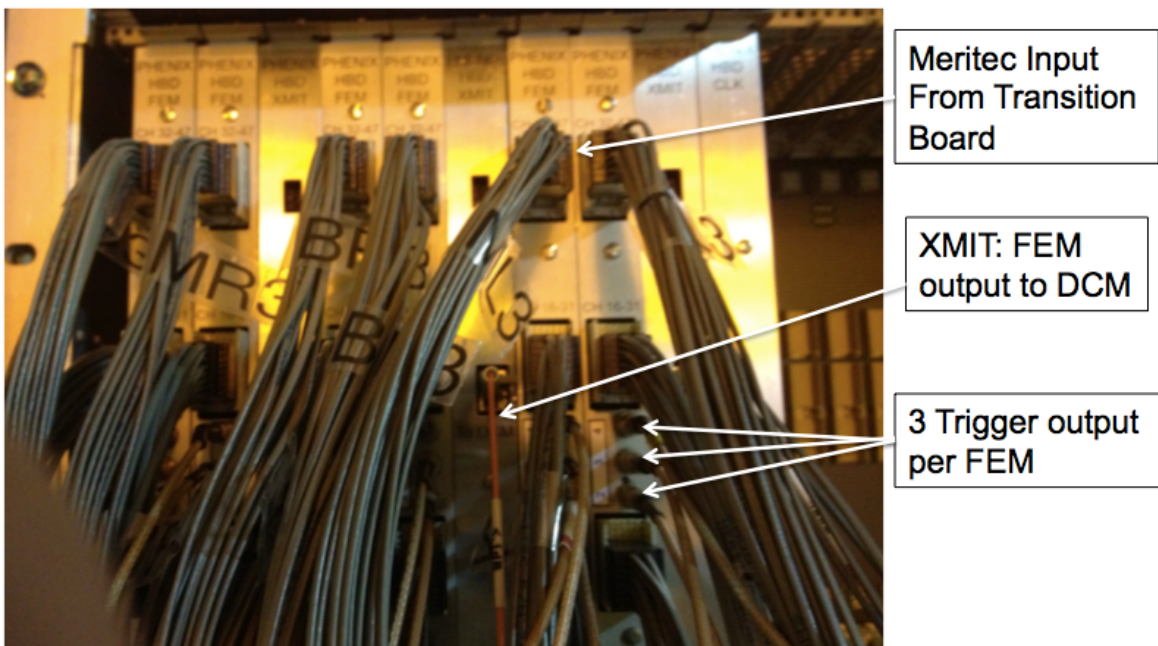


Figure 7.16: The front of the FEMs are shown. Each FEM receives three Meritec cable bundles. The data is read out from the FEM to the Data Collection Module (DCM) via an XMIT board. Each XMIT board sends data from a grouping of two FEMs in one packet. Additionally, each of the three trigger decisions is read out and sent via a 2 or 4 ns Lemo cable to an ECL-NIM level converter.

## 7.5 Test Stand Setup

Before installation in the PHENIX IR in Building 1008 all of the new hardware was integrated into the data acquisition chain, from MPC crystal to software analysis, in a cosmic ray test stand setup in Building 510 at BNL. A picture of the setup is shown in Figure 7.17. The wrapped MPC crystals are placed between two layers of scintillators. The crystals are further shielded from ambient light by an enclosing black box. A cosmic ray that causes a coincidence hit in the scintillators must have also passed through one of the crystals and so acts as a trigger. This trigger is sent to the clockmaster through a different input than the GTM. The reason for this is that it allows the clockmaster to use its own internal quartz oscillator for timing, which cannot be provided externally in this setup, while still allowing triggers to be initiated. The APD signal from the cosmic ray is passed through a sample transition board and then on to the FEM, which required significant debugging. The power supplies and a clockmaster, which also required significant debugging, are connected through the FEM backplane. The test stand was used initially to understand how to make each of the components communicate with each other as intended. Once data was successfully able to be read out, the digitized waveforms could be seen, indicating that the entire read out chain was working and the data was not getting corrupted at any point. Figure 7.18 shows an example of a pulse from the first bit of data taken after installation. One check when running with cosmic rays is to look for the MIP peak, expected to be at around 25 ADC units with the gains settings used. The ADC, or pulse height, of a given signal was taken as the difference of the maximum and minimum ADC samples. This is the simplest way to estimate the energy deposited in the crystal by the cosmic ray. For the real data, a thorough study is underway to correctly determine the energy deposition from the pulse shape.

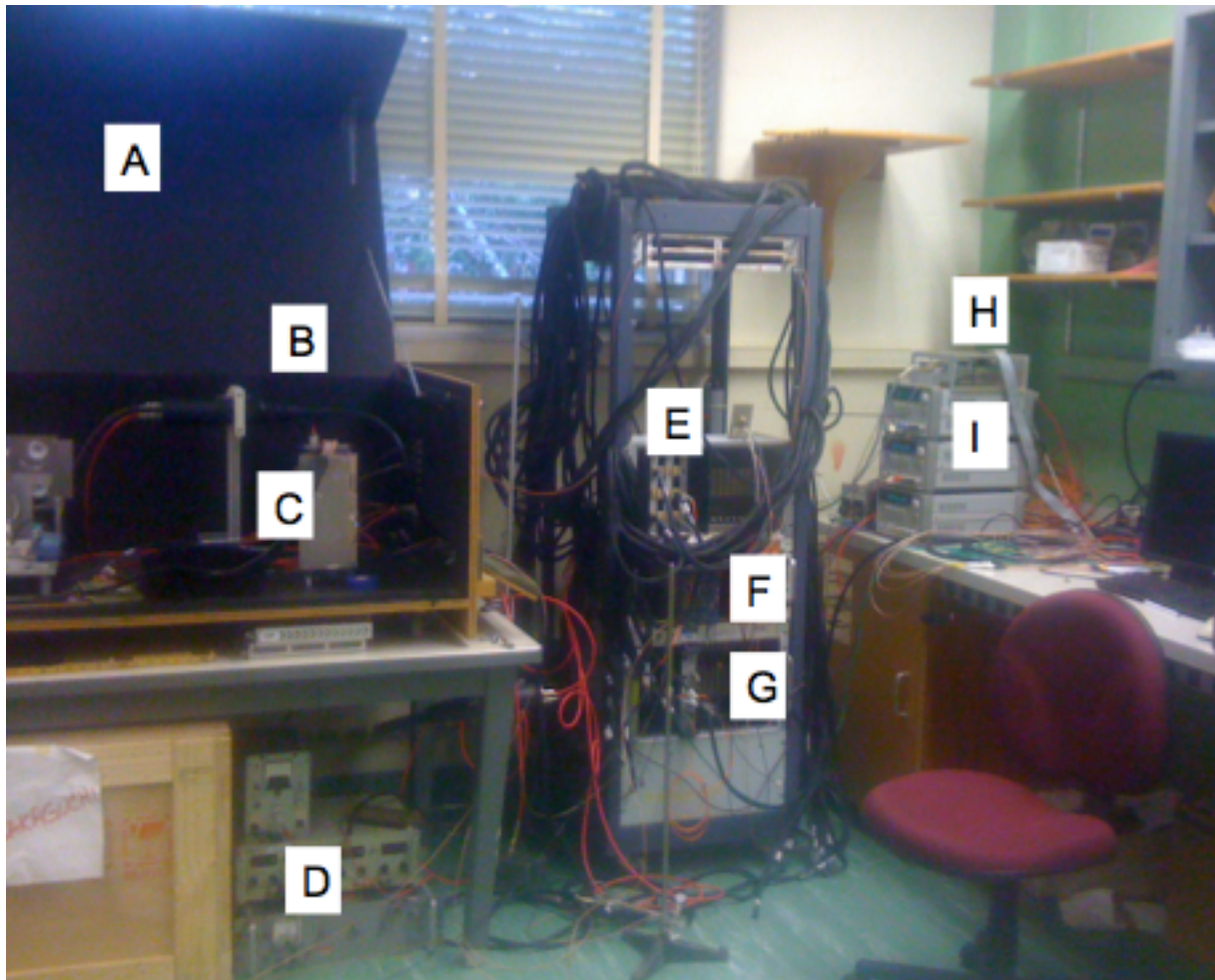


Figure 7.17: Diagram of test stand setup. (a) Cover to light tight box. It is important to minimize the amount of light entering the crystals and scintillators. (b) Scintillators are placed above and below the  $PbWO_4$  crystals to act as a trigger mechanism. They are also wrapped to be light tight. (c) A sample of 9 crystals with the APD readout setup are used to test the HBD electronics readout. (d) The power supplies for the scintillators. (e) Two HBD FEM boards used for testing. (f) Blue logic rack for triggering on cosmic rays and initiating readout. (g) Data acquisition panel. (h) Clockmaster board used for configuring and communicating with the FEM boards. (i) Low voltage power supplies provide three required voltage levels to the FEM backplane.

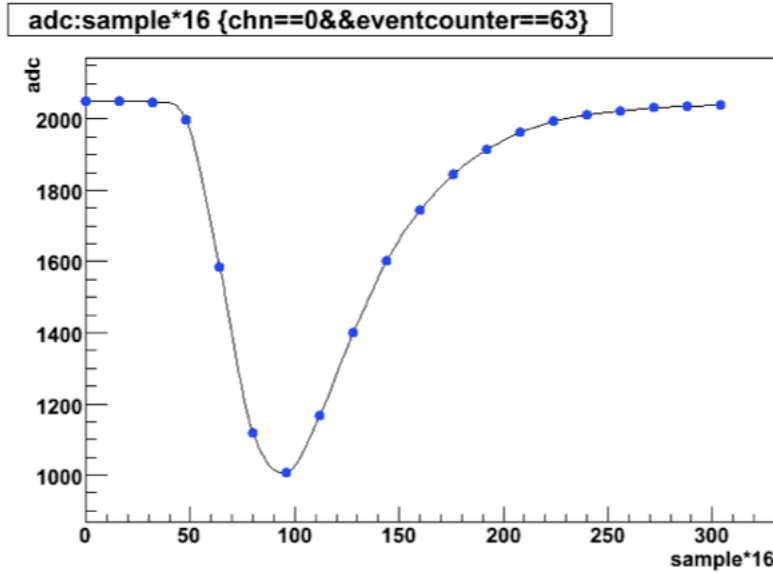


Figure 7.18: A sample pulse from the first collision data is shown. In this sample, 20 digitized readings are read out for each channel in the event. For physics data taking this was reduced to 12 samples. The shaping was optimized to produce a pulse of about 100 ns in length, roughly the RHIC clock period, to reduce the effect of overlapping pulses coming from events in adjacent crossings. The ADC readout is 12-bit bi-polar, meaning it has 11 bits of dynamic range. Noise was measured at 4-6 HBD ADC counts on the test stand, though it seems to be less than this in the IR crate setup.

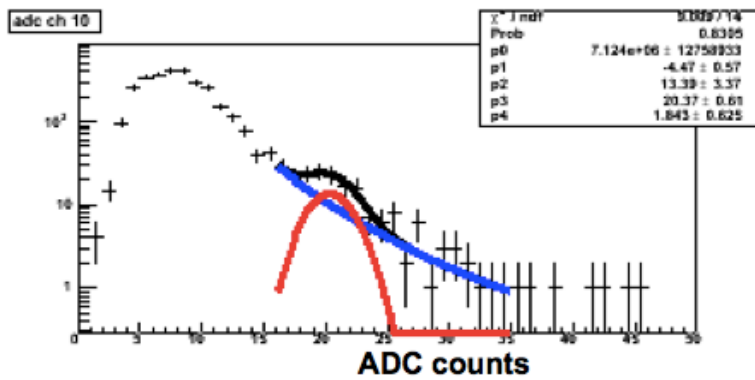


Figure 7.19: Using test stand data and the max-min sample method of determining the pulse amplitude the ADC spectrum of one crystal from cosmic ray running is shown. A MIP peak was able to be located as in the Run09  $\sqrt{s} = 200 \text{ GeV}$  data by fitting the spectrum to a Gaussian plus power law fit. The MIP peak is found at close to the expected value.

## 7.6 Trigger Algorithm

Recall from Figures 7.5 and 7.6 that because of the transition board mapping, the FEMs now have the MPC event information stored internally in a physically meaningful way. This allows the trigger to fire on a large energy deposit that occurred within a specified azimuthal range. The trigger algorithm is executed by the FPGA on its buffer of data at a frequency of  $6 \times \text{BCLK}$  (every 17.762 ns). The trigger calculation is given explicitly by the following algorithm <sup>2</sup>:

```

1   for (j=0; j<7; j++) {
2       for(k=0; k<6; k++) {
3           i=k+j*8;
4           adc_sub[i] = adc[i] - adc_delay[i];
5           if(adc_diff[i] < 0x7f8)    adc_diff[i] = adc_sub/8; //11 bits to 8 bits
6           else                      adc_diff[i] = 0xff;
7           if(adc_diff > thresh[i])  nhit[i] = 1;
8           else                      nhit[i] = 0;
9           adc_multi = adc_diff * scale;           // 8 bit x 8 bit multiplier
10          adc_sumin[i] = (adc_multi & 0x3fff) >> 6; //remove 2 top bits, bottom 6 bits
11          adc_sum[j] = adc_sum+adc_sumin[i]
12          nhit_sum[j] = nhit_sum+nhit;
13      }
14      if(adc_sum[j] >= 0xff )    adc_sum_red[j]= 0xff;
15      else                      adc_sum_red[j] = adc_sum[j] & 0xff;
16      tot_sum = tot_sum + adc_sum_red[j];
17      tot_nhhit_sum = tot_nhhit_sum+nhit_sum[j];
18  }
19  if(tot_sum >= 0xff )    tot_sum_red = 0xff;
20  else  tot_sum_red = tot_sum & 0xff;
21  if((tot_sum_red >= ph_thresh[0]) & (tot_nhhit_sum >= nhit_thresh[0]))  tp2 = 1;
22  else  tp2 = 0;
23  if((tot_sum_red >= ph_thresh[1]) & (tot_nhhit_sum >= nhit_thresh[1]))  tp3 = 1;
24  else  tp3 = 0;
25  if((tot_sum_red >= ph_thresh[2]) & (tot_nhhit_sum >= nhit_thresh[2]))  tp4 = 1;
```

---

<sup>2</sup>This is just pseudo-code, variables are effectively of type int or short

```
26     else  tp4 = 0;
```

This algorithm contains the essential information about how the trigger calculation manipulates the channel level information and how the trigger configurations affect the calculation. The double for loop in lines 1 and 2 identifies the channel number within the FEM in line 3. A full module sum over all 48 channels is calculated.  $2 \times 2$ ,  $3 \times 3$  and  $4 \times 4$  overlapping sums were considered but our simulations indicated there would be only minimally increased trigger performance by doing so, and this method was less error prone in the hardware. Line 4 indicates that amplitude for each channel is determined by taking the difference of the current ADC sample and a previous ADC sample. How many samples back “adc\\_delay” is taken from is a configurable parameter of the trigger. We set it to a 5 sample delay. Lines 5 and 6 remove the three least significant bits (LSB) and ensure that an 8-bit value remains. Lines 7 and 8 count the number of towers above a predetermined single tower threshold. This threshold is typically lower than the trigger threshold sum but has the purpose of prohibiting a trigger if the module ADC sum comes from just one channel. Line 9 allows for the introduction of an 8-bit channel dependent scale factor. Any channel that is empty automatically receives a scale of 0. For an energy based trigger, the scale factor can be the same for all occupied channels. For a  $p_T$  based trigger the scale factor can be set to a value proportional to  $\sin \theta$  where  $\theta$  is the angle of the crystal with respect to the nominal interaction point relative to the beam-line. Additionally, the scale factor can be tweaked to account for differences in gain between crystals if calibrations are available. In line 10, the resulting 16-bit value is reduced back to 8-bits by removing the six LSB and two MSB. In lines 11 and 12 the ADC row sum and channel count above the single tower threshold are incremented. Lines 14 and 15 then reduce the ADC sum to an 8-bit value and lines 16 computes the full module sum. Line 17 computes the total number of channels, from all rows, above the single tower threshold. Lines 19 and 20 reduce the module sum back to an 8-bit value. The trigger decision is now based on the 8-bit module sum and the number of channels above the single tower threshold. Lines 21-26 compare the module sum with each of three trigger thresholds. In each case, in order for the trigger to fire once the module sum condition is met, the single tower channel count must also be met. If it is not, the trigger does not fire regardless of the module sum.

This trigger algorithm includes all the desired features for an improvement over the old trigger calculation. It is digital, includes single tower rejection and allows for a  $p_T$  based trigger. The algorithm is identical in each FEM and the module sum is calculated simultaneously in each module. The trigger decisions from modules in opposing azimuth can then be directly combined to yield the desired di-hadron trigger.

## 7.7 MPC Trigger Emulation and Performance

The three trigger outputs from each module (Fig. 7.16) are discriminated and sent to ECL-NIM converters via Lemo cables. Figure 7.20 shows the trigger input from each module. Figure 7.21 shows the distribution

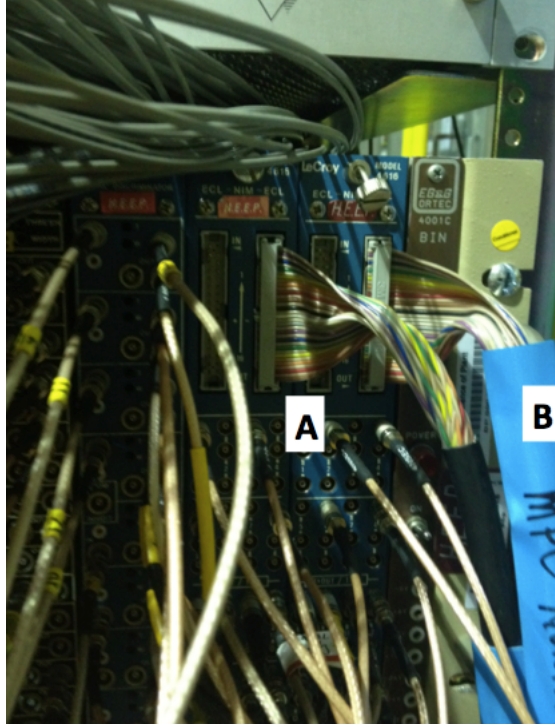


Figure 7.20: The trigger output from each module. (a) Trigger output of FEM is in ECL format. A LeCroy 4616 ECL-NIM converter ([100]) is used to convert to a NIM level signal in rack room. (b) LeCroy output of trigger signals to rack room.

of the module ADC sums for *MPC\_A* and *MPC\_B* triggered events. These triggers are set at module sum thresholds of 60 and 100 ADC trigger units, respectively. To test the performance of the trigger, we created and tested<sup>3</sup> a trigger emulator for the offline code based on the algorithm described above. There is a sharp turn-on at the threshold setting for each trigger and the emulator matches exactly what the real trigger is outputting, showing that the trigger has been implemented correctly.

Since the MPC triggered events only include those events which have passed the MPC trigger algorithm, one cannot check the efficiency of the trigger. A more robust check of the triggering system is given by analyzing events from a different and uncorrelated trigger, such as the BBC Minimum Bias (MB) trigger, and checking to see if the trigger decision from the electronics matches the one from the software emulator.

---

<sup>3</sup>Mickey Chiu, Emily Zarndt

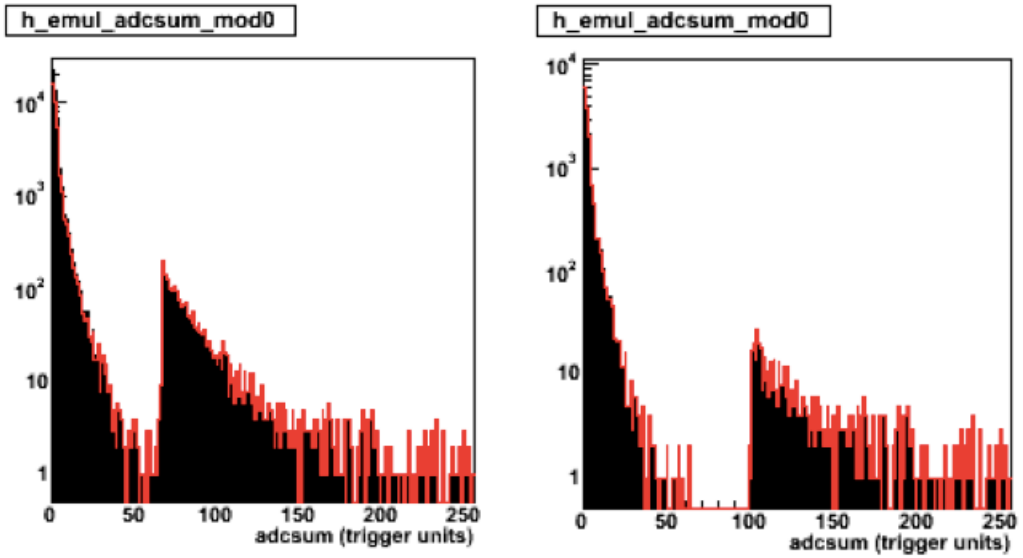


Figure 7.21: Trigger performance results, based on the trigger emulator for the *MPC\_A* (left) and *MPC\_B* (right) triggers. The black histogram shows the ADC sum distribution for the MPC triggered events, while the red histogram shows the distribution for when the software emulator says the trigger should have fired. Since they match exactly, it shows that the trigger was working.

In Figure 7.22 we show the ADC sum distributions in MB events for those events where the *MPC\_C* trigger fired and where the software emulator fired. One can see an inefficiency near the threshold, as well as a few events below the threshold which should not have fired but did. At high values of the ADC sum the trigger becomes fully efficient, so this inefficiency amounts to a small smearing near the trigger threshold only, with all of the more interesting higher energy events being triggered upon.

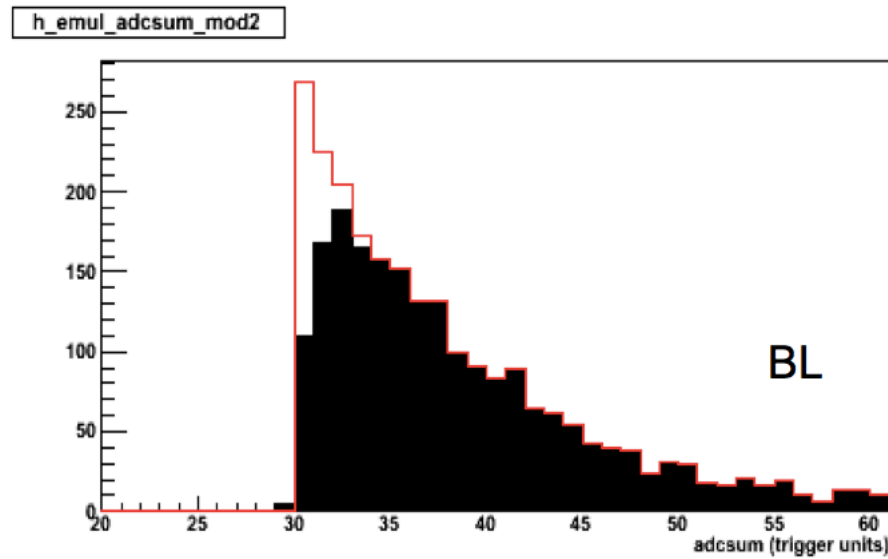


Figure 7.22: The trigger efficiency can be checked in Minimum Bias events. The trigger emulator evaluates these events to determine if a trigger should have fired, and this can be compared to whether the trigger actually did fire. The red spectrum shows the distribution of ADC module sums where the emulator trigger fired while the black spectrum shows the module sum when the MPC trigger actually did fire in the MB event. The trigger efficiency as a function of ADC module sum is just the ratio of the black and red histograms. Near the threshold a trigger inefficiency is seen.

## 7.8 MPC Trigger Configuration Details

The trigger algorithm can be configured through the following parameters: sample delay, single tower thresholds, single tower multiplicities, individual channel scales, output delay, and three trigger module sum thresholds. The command from the clockmaster module to the FEM is a 32 bit word which breaks into two 16 bits data words. The upper 16-bit word is address word. The lower 16-bit word is the data word. We document the valid configuration commands and their meanings in Tables 7.1, 7.2, 7.3, 7.4, 7.5, 7.6, 7.7, 7.8, 7.9, 7.10, and 7.11.

Table 7.1: 16 Bit Address Word

Bit Range	Instruction
3:0	OP code
4:4	write(0)/read(1)
10:5	channel number
15:11	module address

Table 7.2: 16 Bit Data Word if OP code=10: set channel multiplier factor. Allows for  $p_T$  based trigger sum.

Bit Range	Instruction
7:0	Scale factor
15:8	0

Table 7.3: 16 Bit Data Word if OP code=11, channel=0: set trigger 1 module sum threshold.

Bit Range	Instruction
7:0	trigger 1 pulse high SUM threshold
15:8	0

Table 7.4: 16 Bit Data Word if OP code=11, channel=1: set trigger 2 module sum threshold.

Bit Range	Instruction
7:0	trigger 2 pulse high SUM threshold
15:8	0

Table 7.5: 16 Bit Data Word if OP code=11, channel=2: set trigger 3 module sum threshold.

Bit Range	Instruction
7:0	trigger 3 pulse high SUM threshold
15:8	0

Table 7.6: 16 Bit Data Word if OP code=11, channel=3: set trigger 1 NHIT SUM threshold.

Bit Range	Instruction
6:0	trigger 1 NHIT SUM threshold
15:8	0

Table 7.7: 16 Bit Data Word if OP code=11, channel=4: set trigger 2 NHIT SUM threshold.

Bit Range	Instruction
6:0	trigger 2 NHIT SUM threshold
15:8	0

Table 7.8: 16 Bit Data Word if OP code=11, channel=5: set trigger 3 NHIT SUM threshold.

Bit Range	Instruction
6:0	trigger 3 NHIT SUM threshold
15:8	0

Table 7.9: 16 Bit Data Word if OP code=11, channel=6: delay parameter of post-pre subtraction.

Bit Range	Instruction
2:0	delay parameter of post-pre subtraction
15:8	0

Table 7.10: 16 Bit Data Word if OP code=11, channel=7: trigger output delay (2x BCLK frequency).

Bit Range	Instruction
3:0	trigger output delay
15:8	0

Table 7.11: 16 Bit Data Word if OP code=12: set channel discriminator threshold.

Bit Range	Instruction
7:0	threshold
15:8	0

## 7.9 DCM Readout Format

The Data Collection Modules (DCM) (Ref. [98]) are responsible for collecting raw event information from the Front End Modules (FEMs) when an event is to be read out. Each FEM consists of 48 channels of 12 bit ADC with  $\approx 60$  MHz sampling frequency. The number of ADC samples to be read out can be configured. The default is to read 12 samples, which covers approximately two crossings. For each module the format of the readout includes four header words and a last parity word in addition to the ADC samples. For every channel, an address word is sent along with a data word containing two ADC samples.

A zero-suppression can be implemented whereby if the samples in a given channel meet some condition it is not read out. This saves bandwidth when a lot of channels in an event get little to no energy deposits. The zero-suppression condition required for the DCM to pass a particular channel through is:

```
post_sample - pre_sample > threshold
```

Word Type	Flag bits				Empty (4 bits)	Block number	Channel number	Empty	12 bits raw data				
Header	1	1	1	1	0	0	3f	0	module number				
Header	1	1	0	0	0	0	3f	0	trigger number				
Header	1	1	0	0	0	0	3f	0	clock number				
Header	1	1	0	0	0	0	3f	0	physical address				
Address	1	1	1	0	channel address=0				don't care				
Data	ADC sample 1 ADC sample 0 (flag bits 0 1 X X)												
Data	repeat for all ADC samples in channel 0												
Address	1	1	1	0	channel address=1				don't care				
Data	repeat for all data in all channels in this module												
Header	1	1	1	1	0	1	3f	0	module number				
Data	repeat for all modules in the readout												
Last word	1	0	1	X	0	3	101111	0	parity				

Table 7.12: DCM readout format.

The threshold and timing difference between the pre- and post-samples considered for zero-suppression can be configured. In Table 7.12 the format of the data output from the DCM is shown. After the data is passed through event reconstruction where MPC packet level information is synchronized with packet level information from other detectors in the same event, the data can be accessed in a human-readable format via the library

```
<packet_hbd_fpgashort.h>
```

## 7.10 Modifications to MPC Offline Code and Node Structure

Due to the new HBD readout format of the DCM crates, the data is written to disk and a new software structure was implemented to handle the new format with the goal of making changes in this raw data format invisible to the end user, the analyzer. The node structure of the data files using the old and new readout format is shown in Figure 7.13.

Table 7.13: Node Structure. Going down represents additional layers of data processing.

Container Name	Old Electronics	New Electronics	Content
PRDF	used	used	raw DCM output
mpcSampleContainer	—	used	12 samples per channel
MpcRaw	used	—	ADC pre/post and high/low for each channel
MpcRaw2	—	used	1 ADC, 1 “TDC”/chan; adc sample analysis
mpcTowerContainer	used	used	calibrated energy/times for each channel
mpcClusterContainer	used	used	list of cluster information

## 7.11 MPC Di-Hadron Trigger

A color coded diagram of the MPC azimuthal sections in which the trigger sums are calculated is shown in Figure 7.23. In this figure a model scenario is shown for how the trigger reacts to a di-hadron (di-jet proxy)

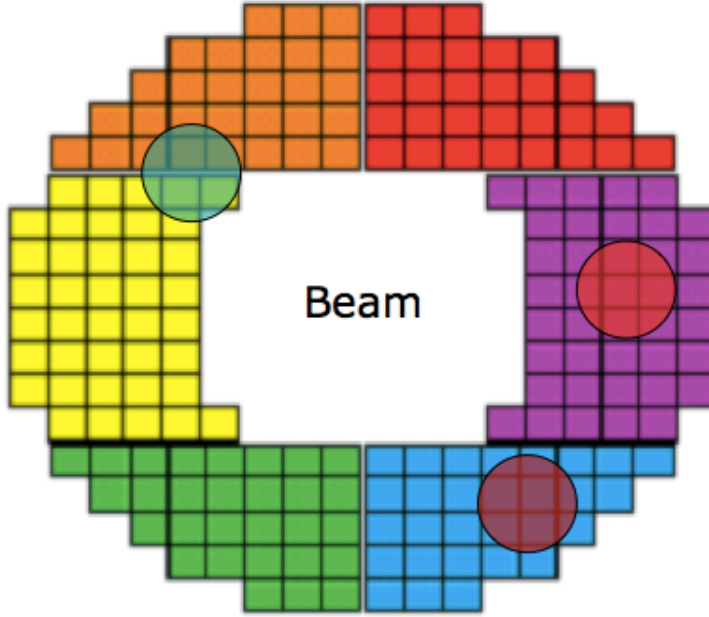


Figure 7.23: Each color represents one module sum. The calculations are done separately and simultaneously in each module. The  $18 = (6 \times 3)$  trigger outputs can then be combined as desired. A description of the di-hadron trigger is given in the text.

event in the MPC. The blue circle in this figure represents an ideal merged cluster from a  $\pi^0$  decay in one jet. The two red circles represent two photon EM clusters from the decay of a non-merged  $\pi^0$  in another jet. To trigger on this di-hadron event we want to require module TL (orange) to fire in coincidence with modules BL (green), BR (blue) or MR (purple). The trigger logic is created in this manner and the individual module thresholds used are lower than for the single hadron triggers because the intrinsic rejection power of requiring two modules to fire is much larger than just one. The single hadron triggers are typically defined by the *MPC\_A* trigger with a desired turn-on at  $p_T \approx 3 \text{ GeV}$  and the *MPC\_B* trigger set for a desired turn-on at  $p_T \approx 4 \text{ GeV}$ . For the di-hadron trigger, each *MPC\_C* threshold is desired to be at  $p_T \approx 1 \text{ GeV}$ . The di-hadron trigger is typically referred to as the *MPC\_C&MPC\_C* trigger or *C&C* for short. Note that a small inefficiency is expected in the trigger from clusters that span two modules. When this happens, each module may get an energy deposit that will not result in a module sum above threshold. On the other hand, had the cluster showered in crystals contained within a single trigger calculation, a trigger would have

occurred. This sort of effect is position dependent and expected to be largest near the boundaries of the modules. It affects triggers with any threshold. The old EMCAL electronics configuration was also subject to a similar effect.

## 7.12 New Electronics Rack Installation within PHENIX

The successful installation of the south electronics rack at the beginning of 2012 and the subsequent installation of the north rack before the Run12  $\sqrt{s} = 500\text{ GeV}$  run required the help of many talented technicians at BNL (Figure 7.24). After the uncabled rack was fully secured, the necessary cabling was prepared. Fig-



Figure 7.24: The BNL technicians used a crane to hoist the electronics rack for each arm from ground level to the top of the PHENIX IR.

ure 7.25 shows the full cabled rack including the driver board signal, Meritec cabling between the transition boards and FEMs, data readout and trigger processing. Figure 7.26 shows a side view of the entire PHENIX detector to give a reference for the location of the south and north electronics crates within the experimental hall. These are shown in Figures 7.27 and 7.28.

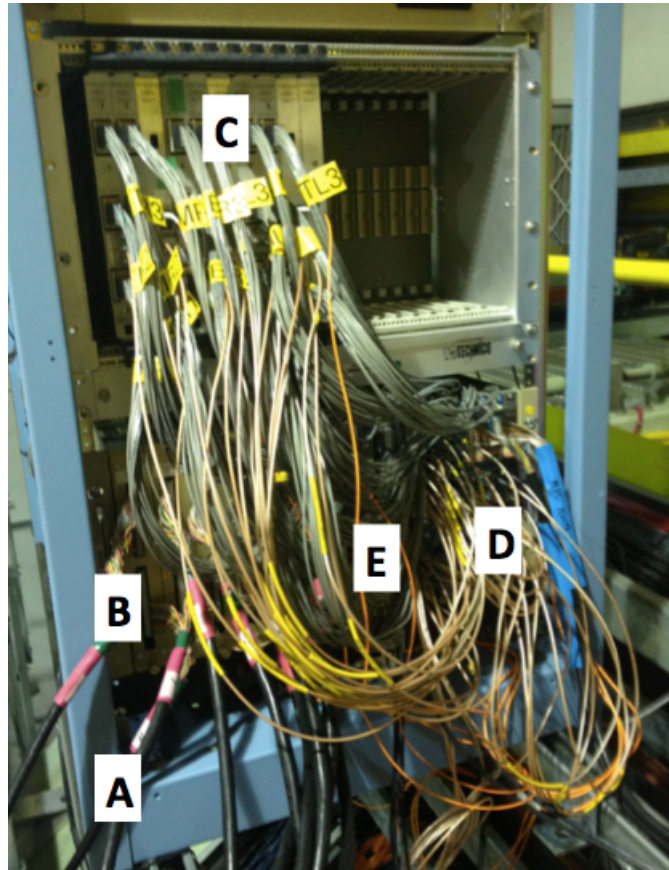


Figure 7.25: A view of the fully cabled rack ready for data taking. (a) and (b) Twisted pair cables from the driver boards. (c) Signal input from transition board to the FEMs after pulse shaping. (d) The trigger decisions are read out from the FEMs and sent to the rack room. (e) Fiber optic readout cable from the XMIT boards to the DCM.



Figure 7.26: Side View of PHENIX

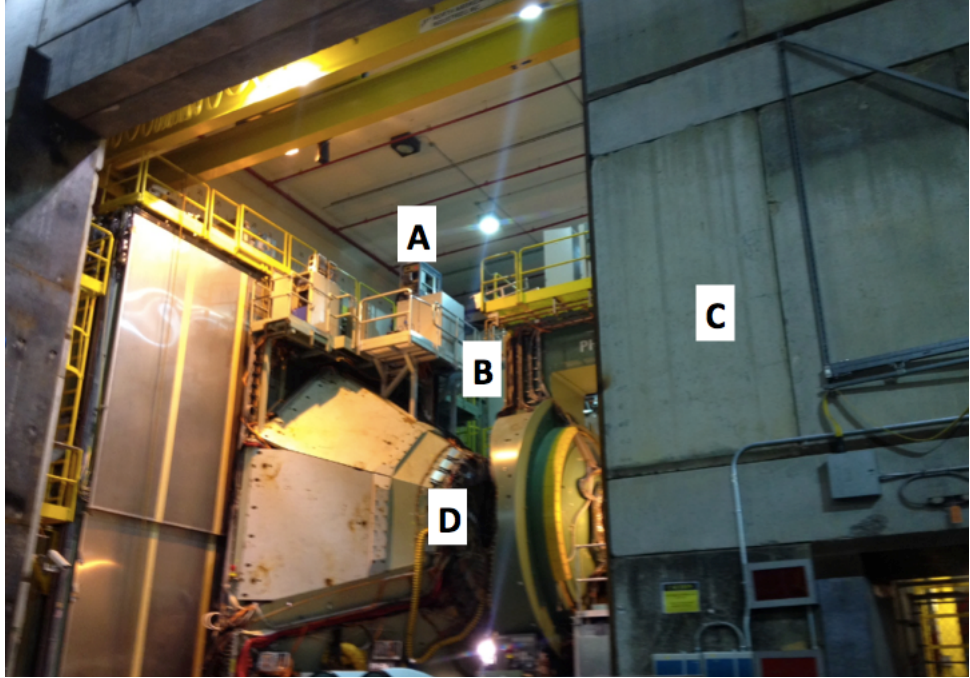


Figure 7.27: (a) South MPC electronics rack. (b) A typical example of a ladder this author has proven incapable of climbing. (c) Radiation shield wall. (d) Muon Piston bore where the south MPC crystals are located. The twisted pair cables from the driver boards at (d) run up along the lamp shade over the south muon arm up to (a).

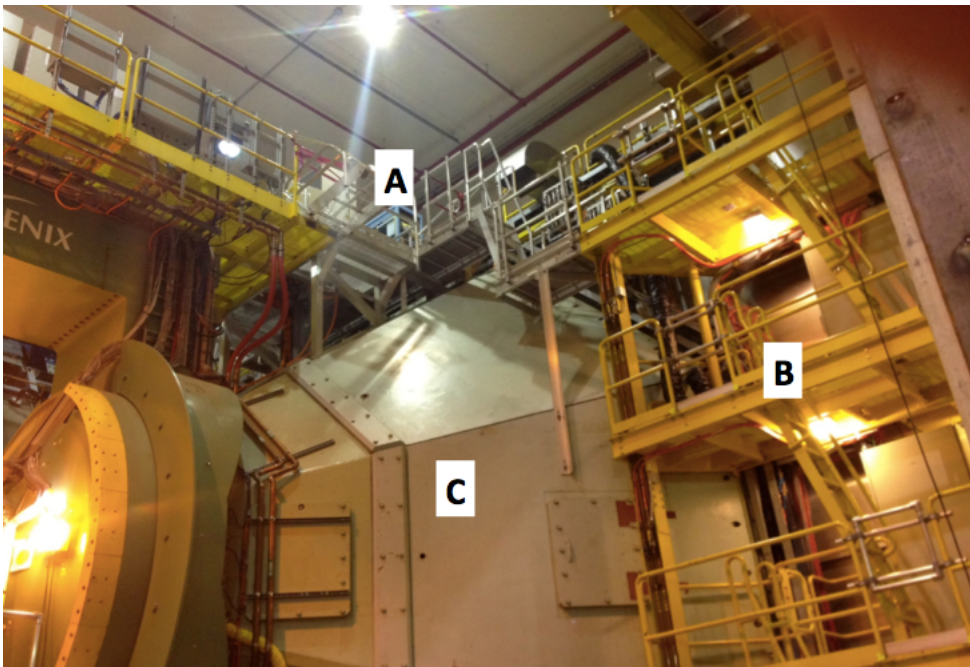


Figure 7.28: (a) North MPC electronics rack. (b) The only ladder more than 10 feet high that the author has been able to overcome his fear of heights to climb. (c) The north PHENIX muon arm lamp shade.

## 7.13 List of Advantages Of New Electronics

Having described in detail all of the changes involved in this upgrade, we now summarize the improvements to both the data read-out and the trigger calculation. In Table 7.14 we list several of the improvements to the MPC data. In Table 7.15 we list the improvements to the triggering ability of the MPC. The most important of all the improvements listed, however, is that the MPC is now a fully functional di-hadron trigger which pushes the sensitivity of  $\Delta G$  measurements at PHENIX down to  $x_g \approx 10^{-3}$ .

	EMCal electronics	HBD electronics
Raw data	ADC pre/post and high/low gain, TDC	12 samples over $\approx 2$ crossings
ADC overflow	yes	yes, but can extrapolate beyond dynamic range
Pedestals	not used, difficult to handle	stable, used for pulse shape fitting
Noise reduction	active receiver board	passive transition board
Ghost cluster/pileup	yes, pre and post are 4BCLK apart	no, waveform is sampled every 16ns

Table 7.14: Comparison of data between the old EMCal electronics and the new HBD electronics.

Trigger on di-hadrons	EMCal electronics <b>NO</b>	HBD electronics <b>YES</b>
Available triggers	2x2, 4x4A, 4x4B, 4x4C	Module A,B,C thresholds (18/arm)
RBIB inputs	5:(2x2), 4x4(A,C,B north, B south)	14:all 12 C, A(or), B(or)
Reject single tower background	no	yes
Turn-on curve	broad	sharp
$p_T$ trigger	not effective	possible
Geometric significance	no	yes
Can be emulated offline	no	yes

Table 7.15: Comparison of trigger between the old EMCal electronics and the new HBD electronics.

# Chapter 8

## Relative Luminosity

As we have seen, the relative luminosity is the dominant source of systematic uncertainty for the forward  $A_{LL}^{cluster}$  measurement in the MPC. This is the case for all high statistics measurements and, unfortunately, at low  $x$ , even a large gluon polarization is expected to produce small asymmetries,  $A_{LL} \sim O(10^{-4})$ . Thus, the relative luminosity systematic uncertainty must also be understood at this level in order to provide an effective probe of  $\Delta G$  at low- $x$ . With the integrated luminosity accumulated from 2009 at both  $\sqrt{s} = 200$  and 500 GeV, the statistical errors are still  $\delta A_{LL} \sim 10^{-3}$ . However, with  $\sim 20$  times more data available from 2011, 2012, and 2013 running, the measurement will quickly become systematics limited. In this chapter we outline a number of new ideas regarding relative luminosity along with a new take on some existing ideas. We start with a primer.

### 8.1 Bunch Helicities and Spin Patterns

The RHIC/AGS accelerator complex has the capability to inject up to 120 bunches of protons into the storage ring in a given fill. In order to dump the beam when the experiments and C-AD (Collider-Accelerator Department) agree the fill should end, an abort kicker ([104]) is used to steer the beam out of its orbit and into a concrete absorber. The abort kicker takes about 1  $\mu s$  to ramp up. The RF cavity has a frequency of 9.383 MHz so each bunch has an associated time (length) of 106.572ns (31.949m). Therefore, an abort gap of at least 9 bunches in each beam is left unfilled to allow time for the kicker to ramp up. There are therefore 111 maximum crossings with collisions for the PHENIX experiment to observe, though a given fill always has a few less than this. As each crossing passes through the PHENIX Interaction Region (IR) its polarization is rotated from its default transverse direction into the longitudinal direction, either in the same direction as its momentum, giving it positive helicity, or in the opposite direction of its momentum with negative helicity. Bunches with positive helicity are referred to as + bunches and bunches with negative helicity are referred to as - bunches. In Table 8.1 we show the four different types of spin patterns (SP) that RHIC was filled with in Run09. Note that for SP0, both the blue and yellow beam helicities are opposite of what is found in

Table 8.1: Spin Pattern Definitions in Run09.  $C_i$  refers to bunch crossing  $i$ , where crossing 0 is defined as the first crossing after the abort gap. The helicity of any proton bunch  $b$  is found from looking at crossing  $C_{b \bmod 8}$ .

Spin Pattern	Beam	$C_0$	$C_1$	$C_2$	$C_3$	$C_4$	$C_5$	$C_6$	$C_7$
0	blue	+	-	+	-	-	+	-	+
0	yellow	-	-	+	+	-	-	+	+
1	blue	-	+	-	+	+	-	+	-
1	yellow	-	-	+	+	-	-	+	+
2	blue	+	-	+	-	-	+	-	+
2	yellow	+	+	-	-	+	+	-	-
3	blue	-	+	-	+	+	-	+	-
3	yellow	+	+	-	-	+	+	-	-

SP3. SP1 is also completely flipped from SP2. The helicity state of an interaction between a proton from the blue beam and the yellow beam can be one of the four combinations:  $(b, y) = (+, +), (-, -), (+, -)$  or  $(-, +)$ . The first two cases are same sign and can be referred to as “S” while the second two have opposite signs and can be labelled “O”. Looking at the first four crossings of each spin pattern, we refer to SP0 and SP3 as “OSSO” and to SP1 and SP2 as “SOOS”. It should also be noted that each bunch has  $O(10^{11})$  protons. The helicity of a bunch indicates the direction of polarization, and should be differentiated from the spin orientation of any particular proton. In a + bunch, there are many protons with – helicity. This is what the polarization tells us. It is defined as

$$P \equiv \frac{N^+ - N^-}{N^+ + N^-} \quad (8.1)$$

where  $N^{+(-)}$  is the number of protons with positive(negative) helicity. Figure 8.1 shows the standard side view of PHENIX with the bunch helicities illustrated for both the blue and yellow (show in red) beams. We go into no detail here regarding the polarization determination, but the goal is for it to be as high as possible. The reader is referred to [111] for more information.

## 8.2 Definition of Relative Luminosity

Relative luminosity follows immediately from luminosity so we start with that. In its simplest form we seek to answer a very simple question: In bunch crossing X, how many  $pp$  collisions occurred over some length of time? Not knowing the answer to this question is essentially the source of the dominant systematic uncertainty to  $A_{LL}$  measurements which may ultimately be the limiting factor in the ability for PHENIX to provide powerful constraints on  $\Delta G$ , especially at low- $x$ . Recalling the physics-based definition of  $A_{LL}$

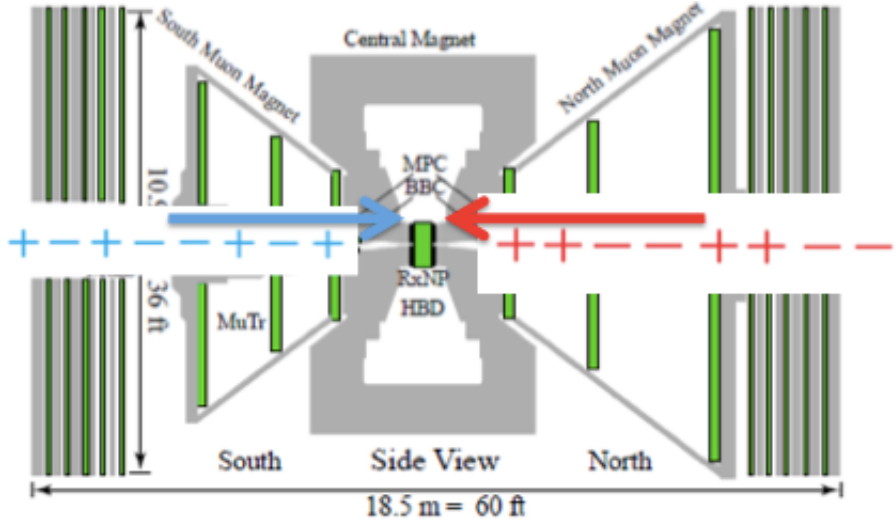


Figure 8.1: A snapshot of the bunch polarizations as they head to intersection in the PHENIX IR. The blue beam moves to the right (north) and the yellow beam moves to the left (south). The first crossing after the abort gap is  $(b, y) = (+, +)$ , the second is  $(b, y) = (-, +)$ , and so on. The specific example shown here corresponds to SP2 from Table 8.1.

from Eq. 2.30, we can rewrite the cross section as:

$$\sigma \propto \frac{N}{\epsilon L} \quad (8.2)$$

This is a simplified form of the overall cross section ([115]) but for our purposes it is sufficient.  $N$  refers to the observed yield of whatever final state is being considered.  $\epsilon$  refers to the acceptance factor, trigger efficiency and trigger bias and  $L$  refers to the integrated luminosity, which is the total number of collisions measured over some time. The instantaneous luminosity is defined as

$$\mathcal{L} \equiv \frac{\mathcal{R}}{\epsilon \sigma_{pp}} \quad (8.3)$$

where  $\sigma_{pp}$  is the total  $pp$  cross section. It could also be defined as just the inelastic part of the cross section  $\sigma_{pp,inel}$ , but it just changes the trigger efficiencies and ultimately makes little difference. We then have  $L = \int \mathcal{L} dt \propto \int \mathcal{R} dt$ .  $\mathcal{R}$  is the reaction rate. The standard unit of instantaneous luminosity is  $[\mathcal{L}] = cm^{-2}s^{-1}$ .  $\sigma_{pp}$  is typically determined from Vernier Scans (Refs.[112],[113],[114]). Measuring  $\mathcal{R}$  can be done via a detector hit rate. For example, one could count the BBC north hit rate or the ZDC south hit rate along with several other possibilities. The main problem with doing this is that the noise rates are much higher

when a hit on just a single detector is required. An example of this is shown in Fig. 8.2a where the noise level is seen to be at the  $O(10^{-3})$  level when singles sided hits are counted. In Fig. 8.2b, requiring a coincidence hit of both the north and south towers the noise level to the  $O(10^{-5})$  level. In the latter case we can be confident this is small enough to not affect the luminosity (and later, the relative luminosity) at the level required. In the former case this is not necessarily true. The cost of this noise reduction is roughly one order of magnitude in statistics. So there are three major factors that should be taken into account when deciding

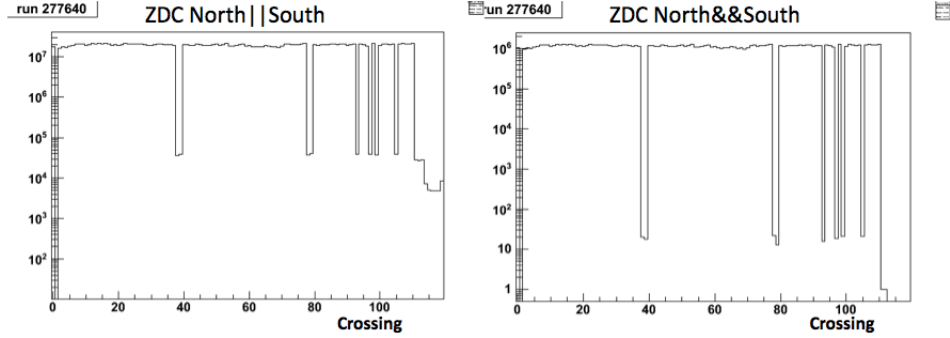


Figure 8.2: (a) Left: ZDC North||South (singles) trigger counts vs. crossing. (b) Right: ZDC North&&South (coincidence) triggers versus crossing. Empty bunch crossings including 38,39,78,79 and the abort gap can be clearly seen in both cases. In (a) the rate for empty bunch crossings is  $O(10^{-3})$  of the rate for filled bunch crossings. For ZDC coincidences the rate for empty crossings goes down to  $O(10^{-5})$ .

if a detector is good for luminosity monitoring:

- Low background from noise or beam gas events
- High statistics
- No spin dependence, i.e. should have a small  $A_{LL}$

Based on the first two criteria, the ZDC and BBC coincidence counts are the standard monitors of luminosity. The third requirement is very difficult to know in advance. It cannot be excluded that small double spin asymmetries for the ZDC and the BBC exist. However, the impact of a possible physics asymmetry in a relative luminosity monitor can be reduced by using a separate luminosity monitor based on a different detector with different acceptance. In an absolute sense, an  $A_{LL}$  for the ZDC and for the BBC can exist independently of one another. However, in a practical sense, asymmetries in one detector are always measured using luminosities in another. This can be seen by using Eq. 8.2 to rewrite Eq. 2.30 as

$$A_{LL} = \frac{1}{P_B P_Y} \frac{\frac{N^{++}}{L^{++}} - \frac{N^{+-}}{L^{+-}}}{\frac{N^{++}}{L^{++}} + \frac{N^{+-}}{L^{+-}}} \quad (8.4)$$

where  $N^{++,+-}$  is the yield in the detector we are measuring the asymmetry for and  $L^{++,+-}$  is the measured luminosity for same and opposite sign helicity crossings. All quantities are summed over all relevant bunches. For example,  $N^{++} = \sum_{i=(b,y)=(++,+-)} N^i$ . The beam polarizations,  $P_B$  and  $P_Y$ , must be taken into account as a scale factor as in Eq. 8.1. It is important to note here that the  $\epsilon$  factor is assumed to be the same between the two crossing types, that is,  $\epsilon^{++} = \epsilon^{+-}$ . The relative luminosity,  $R$ , is then defined as the ratio of luminosities between same and opposite sign helicity crossings:

$$R \equiv \frac{L^{++}}{L^{+-}} \quad (8.5)$$

To be clear, PHENIX typically uses coincidence counts from two-sided detectors (the BBC and ZDC) as a measure of luminosity, but there is nothing intrinsically necessary about this other than that it helps reduce noise and backgrounds as stated in the first condition above. All we really need is some counter that counts collisions at a rate proportional to the true number of collisions. For example, in  $p + p$  collisions at 500 GeV, a BBC coincidence will be counted in about 53% of collisions, while a BBC single sided counter will count about 68% of collisions. Under the assumption that these efficiencies are spin independent, they cancel in the ratio in Eq. 8.5.

### 8.3 Effect of an $A_{LL}$ in the Luminosity Monitor

The third condition above requires some care. We can recast Eq. 2.30 as

$$\frac{\sigma^{++}}{\sigma^{+-}} = \frac{1 + A_{LL}}{1 - A_{LL}} = \frac{\mathcal{R}^{++}}{\mathcal{R}^{+-}} \quad (8.6)$$

where the last equality comes from Eq. 8.3. This is to be interpreted as follows: for a given intrinsic beam luminosity,  $\mathcal{L}$ , an  $A_{LL}$  (assumed positive with no loss of generality) is identical to saying that  $\sigma_{pp}^{++} > \sigma_{pp}^{+-}$  and therefore the observed rates obey  $\mathcal{R}^{++} > \mathcal{R}^{+-}$ . In this way, a detector with an asymmetry will overestimate the true luminosity for “S” crossings and underestimate it for “O” crossings.

Obfuscating the situation further is that there are two detectors in play, one for the luminosity and one for the particle yield, and each can have their own asymmetry. In effect, we can really only measure the asymmetry seen in one detector with respect to another, and not the asymmetry in an absolute sense. Take, for example, the ZDC as the detector we want to measure  $A_{LL}$  for and the BBC as the luminosity monitor.

Then Eq. 8.4 reads as:

$$P_B P_Y A_{LL} = \frac{\frac{N_{ZDC}^{++}}{L_{BBC}^{++}} - \frac{N_{ZDC}^{+-}}{L_{BBC}^{+-}}}{\frac{N_{ZDC}^{++}}{L_{BBC}^{++}} + \frac{N_{ZDC}^{+-}}{L_{BBC}^{+-}}} \quad (8.7)$$

Playing devils advocate, let's assume that not only do the ZDC and BBC each have  $A_{LL} \neq 0$ , it is further the case that  $A_{LL,BBC} = A_{LL,ZDC} \equiv A$ . According to our line of reasoning, both  $N_{ZDC}^{++}$  and  $L_{BBC}^{++}$  are enhanced by the factor  $(1 + A)$  while  $N_{ZDC}^{+-}$  and  $L_{BBC}^{+-}$  are suppressed by the factor  $(1 - A)$ . But in each case the ratios cancel, leaving  $A_{LL}^{ZDC/BBC} = 0$  even though individually they have a nonzero asymmetry. If the asymmetries between the two detectors are different, then a net  $A_{LL}$  can be observed. In practice, while it is possible that the ZDC and/or the BBC can have an asymmetry, it is considered rather unlikely that they would be precisely the same. This is because the ZDC, located at very forward rapidity ( $|\eta| > 6$ ) and measuring mainly neutrons and some photons, samples mostly diffractive events. The BBC, on the other hand, measures charged particles (i.e.  $\pi^\pm$  and  $K^\pm$ ), primarily at low  $p_T$  and in the pseudo-rapidity range  $3.1 < |\eta| < 3.9$ . Nevertheless, the conventional wisdom is that a third detector is needed. Using the Forward Vertex (FVTX) detector ([101], [102], [103]) is a very promising possibility for this as it had a functional scaler readout during the 2013 running period<sup>1</sup>. This allows three asymmetries to be measured:  $A_{LL}^{ZDC/BBC}$ ,  $A_{LL}^{ZDC/FVTX}$ , and  $A_{LL}^{BBC/FVTX}$ . Without the FVTX, we can measure only the first of these and many questions inevitably remain. If  $A_{LL}^{ZDC/BBC} = 0$ , then all we really know is that  $A_{LL,BBC} = A_{LL,ZDC}$  but we don't know whether that common value is 0 or not. If  $A_{LL}^{ZDC/BBC} \neq 0$ , then we do not know if this is due to one or the other, or even both detectors having an asymmetry. But clarity can be provided by the FVTX. For example, if  $A_{LL}^{BBC/FVTX} = 0$  while  $A_{LL}^{ZDC/FVTX} \neq 0$  then we have increased confidence the real asymmetry is in the ZDC, and the BBC is the good measure of true luminosity. We now take an important digression into how the luminosity is counted.

## 8.4 GL1P Scalers and Live Triggers

To count detector coincidences and make a precise determination of the beam luminosity, it is insufficient to use data that has been written to disk because the number of events on disk is just a tiny fraction of all events that occurred and is far too small to provide a statistically precise determination of the luminosity. Instead, what is desired is a way to just count coincidence triggers without actually recording the entire event to disk. The GL1P accomplishes this task.

---

<sup>1</sup>A special thanks go to Mickey Chiu and Aaron Key for their tireless efforts to make this happen as well as Jin Huang and the Los Alamos team for successfully commissioning the FVTX.

The GL1P board is part of the GL1 (Global Level 1) hardware configuration that is dedicated to luminosity monitoring. It receives four inputs timed in with each bunch crossing (i.e. every 106.572 ns). Each input can be scaled for each of the 120 crossings (480 total scalers), therefore it goes without saying that this board must be properly timed in with the RHIC clock so that a count from one crossing does not show up during the time interval of a different crossing. Each of the four inputs is typically a live trigger, either the CLOCK, or from the BBC or ZDC. For the Run9 period (both at  $\sqrt{s} = 200$  GeV and  $\sqrt{s} = 500$  GeV) the GL1P inputs were as follows:

- BBCLL1 — Requires at least one PMT hit in both the south and north BBC. A timing cut is made on these hits.
- CLOCK — Every live bunch crossing is a clock count. This is used to determine the rate at which other triggers occur.
- ZDCLL1 — Requires both the south and north ZDC to register a hit above threshold. A timing cut is made on these hits.
- ZDCN|S — Requires either the south or north ZDC to register a trigger.

Each of these scalers count only live triggers as opposed to so-called raw triggers. We will illustrate the difference as well as the general idea by way of example using the BBCLL1. In a given crossing,  $i$ , of  $O(10^{11})$  protons in the blue beam and  $O(10^{11})$  protons in the yellow beam, assume that there is one  $pp$  interaction. Say this interaction produces a hit in the south BBC at  $t_S = 8\text{ ns}$  and a hit in the north BBC at  $t_N = 7\text{ ns}$ . There is a global degree of freedom in assigning where  $t = 0$ , but once this is locked in at a chosen phase relative to the RHIC RF pulse,  $t_{N,S}$  are well defined. Next, we use the approximation that all particles emerging from a collision travel at  $c$ . The degree to which this might not be perfectly true is far exceeded by a large number of other considerations and uncertainties. We also know that the BBC detectors are located symmetrically at  $z = \pm 144\text{ cm}$  from the center of PHENIX. So we know  $(t_S, z_S)$  and  $(t_N, z_N)$  which allows us to calculate both when,  $t_0$ , and where,  $z$  or  $zvt_x$ , the collision occurred via:

$$z = \frac{c}{2}(t_S - t_N) \quad (8.8)$$

$$t_0 = \frac{1}{2}(t_S + t_N) - \frac{L}{c} + t_{offset} \quad (8.9)$$

The BBCLL1 algorithm will be described later and an emulator will be shown to match precisely its trigger decision. In our example we would compute that  $z = \frac{1}{2}(30\frac{\text{cm}}{\text{ns}})(8\text{ ns} - 7\text{ ns}) = 15\text{ cm}$ . The timing cut made

in the BBCLL1 corresponds to  $|z| < 30\text{ cm}$ . Therefore, not only did the collision provide a hit in both detectors, the BBC detected hit times at both arms corresponding to a vertex cut passing the BBCLL1 condition, and so this trigger fires a “yes” pulse to the Global Level 1 (GL1). GL1 registers this as a raw trigger because the conditions for the trigger have been met at just the level of the BBC. The GL1 must be in a “live” state before it will attempt to write the event to disk. Every Granule Timing Module (GTM) that is considered by the GL1 has the ability to put the GL1 into a “busy” state or the GL1 can put itself in a busy state. For instance, if a detector is slow and needs some time to reset, its GTM will send a “busy” signal to GL1, preventing it from accepting any live trigger or writing any events to disk. Another example is during the time the GL1 is busy writing an event to disk. In this case, the GL1 will not promote any raw triggers to live triggers for about 15 crossings (or clock ticks, or BCLKs, etc.). However, if the state of GL1 is live during this crossing, then the GL1P board will receive a “yes” signal and increment the appropriate counters by 1. The distinction between raw and live scalers is important. When measuring an asymmetry, say in the MPC, we are running over data written to disk, so by definition the GL1 was live during all those crossings. The true luminosity that went into producing this data should therefore be counted only when there was a chance to get MPC data. If the BBC fires a raw trigger, but the GL1 is not live, then an MPC trigger would have no chance to be analyzed later. The reverse is also true. So the GL1 busy signal acts as a kind of global stop light that allows detector counts to accumulate from a strict subset of crossings that luminosity can be counted from.

The livetime of a trigger is defined as:

$$\text{livetime} = \frac{\# \text{ live triggers}}{\# \text{ raw triggers}} \quad (8.10)$$

In Run09 at  $\sqrt{s} = 500\text{ GeV}$ , the raw triggers were not scaled bunch by bunch, so in general the livetime cannot be determined. The one exception is with clock triggers, since we know the number of times a crossing occurred regardless of the state of GL1. For a run of length  $S$  seconds, and a revolution frequency  $F$ , the number of times crossing  $i$  occurs is  $S \times F$ . At RHIC,  $F \sim 78\text{ kHz}$  so for a typical run of length  $S = 3000\text{ s}$  there are about  $2.4 \times 10^8$  raw clock triggers for each bunch crossing. Figure 8.3 shows this for one typical run, and a clearly nonuniform behavior is seen crossing to crossing at the level of 1%. That the livetimes can vary bunch to bunch is cause for concern. It is also well documented that different triggers can have different livetimes. For a simple example of this, consider a malfunctioning trigger whose pulse length is two crossings long. It fires in the crossing it should along with the subsequent crossing. Assuming

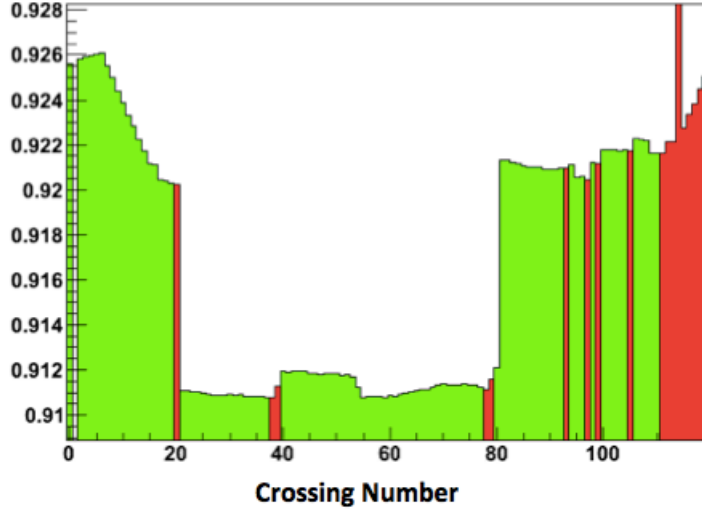


Figure 8.3: Livetime of the *CLOCK* trigger as a function of crossing number. Green crossings are those used for analysis while red crossings are excluded.

the GL1 is always live for the first crossing, it will begin the write process and be in a busy state the next crossing. So two raw triggers are received, but at most one of them is live. Thus the livetime is capped at 50%. A different trigger having a pulse with proper height and length is not subject to this and can have a 100% livetime. In reality, most triggers tend to have livetimes around 90%. As Fig. 8.3 shows, this livetime can also vary across different crossings. One of the most important quantities we will consider is the ratio of ZDC to BBC coincidence counts. It will become clear that this quantity, the ratio of counts in the two (as of 2009) standard luminosity detectors can provide deep insight into how well the luminosity really is being tracked. We made the argument that asymmetries in either the ZDC or BBC or both can affect the measured luminosity, if not accounted for. The same is true for trigger livetimes. Pretending for a moment we are dealing with unpolarized beams where each bunch has the same longitudinal profile (bunch intensity versus position), then from Eq. 8.2 we should measure a constant value of the ratio since the true luminosity is independent of the detector used to measure it. Since the ZDC and BBC cross sections are also fixed values this gives:

$$\frac{\sigma_{ZDC}}{\sigma_{BBC}} = \frac{N_{ZDC} \epsilon_{BBC}}{N_{BBC} \epsilon_{ZDC}} \quad (8.11)$$

Since the ratio of the efficiencies is also safely assumed to be constant, the ratio of the counts should be constant. But these are raw counts and so does not account for the state of GL1. From Eq. 8.10 we can rewrite the above as:

$$\frac{\sigma_{ZDC}}{\sigma_{BBC}} = \frac{N_{ZDC}^{live} \epsilon_{BBC} \text{livetime}_{BBC}}{N_{BBC}^{live} \epsilon_{ZDC} \text{livetime}_{ZDC}} \quad (8.12)$$

Table 8.2: Simple STAR scaler example.

Bit	Logic	Scaler
00(0)	$\text{BBCS} \& \& \text{BBCN}$	13
01(1)	$\text{BBCS} \& \& \text{BBCN}$	17
10(2)	$\text{BBCS} \& \& \text{BBCN}$	20
11(3)	$\text{BBCS} \& \& \text{BBCN}$	53

So as long as the trigger livetime is a constant ratio across bunch crossings then there is no problem. However, if the ratio changes, it will have an effect similar to what could be seen from asymmetries, but in this case the effect can be present without polarized beams. As mentioned before, we cannot really check this effect in Run09 because raw triggers were not scaled on a crossing by crossing basis. However in Run12, which had functional STAR scalers, the state of the GL1 is recorded, and so the livetime behavior can be checked in this way.

## 8.5 STAR Scalers

The STAR scaler board ([116]) has 24 bit inputs and performs the necessary logic to scale all possible  $2^{24}$  bit combinations. As a short example to illustrate the mechanics of this, consider the case of just two inputs from the south and north BBC:  $BBCS$  in bit 0 and  $BBCN$  in bit 1. Then we run 100 events and count 17  $BBCN$  only events, 20  $BBCS$  only events, 50  $BBCS \& \& BBCN$  events, and 13 events with no trigger. Table 8.2 shows what the STAR scaler output would look like. So, in this fabricated example, the number of times  $BBCS$  fired gets summed as  $20 + 53 = 73$ . Using bit-wise logic, the STAR scalers allow one to scale any trigger input or combinations of trigger inputs in coincidence. In reality, 7 bits are used to encode the crossing number ( $2^7 = 128$  covers the 120 crossings). Another bit records whether or not there is a “busy” signal, allowing differentiation between live triggers and not live triggers. Knowing the crossing number and the busy state is enough to be able to determine the crossing by crossing livetime for any trigger. The remaining bits are used for various physics triggers. The GL1P and STAR Scalers can be cross checked for consistency by comparing triggers that are scaled in both boards with each other. In Figure 8.4 we show the ratio of the livetimes of the  $ZDC$  and  $BBC$  triggers with the  $CLOCK$  trigger as a function of crossing number. Based on the statistics available from these scalers, taken from Run12, there is no clear evidence for a systematic crossing to crossing dependence of the ZDC or BBC trigger livetimes as a ratio of the CLOCK livetime. Further studies should look deeper into this, but based on the evidence from the Run12 period with working STAR scalers, we see no reason to apply a correction to the Run9 GL1P’s. While a livetime correction may be relevant for the true luminosity, since it acts as a constant scaling factor for all crossings,

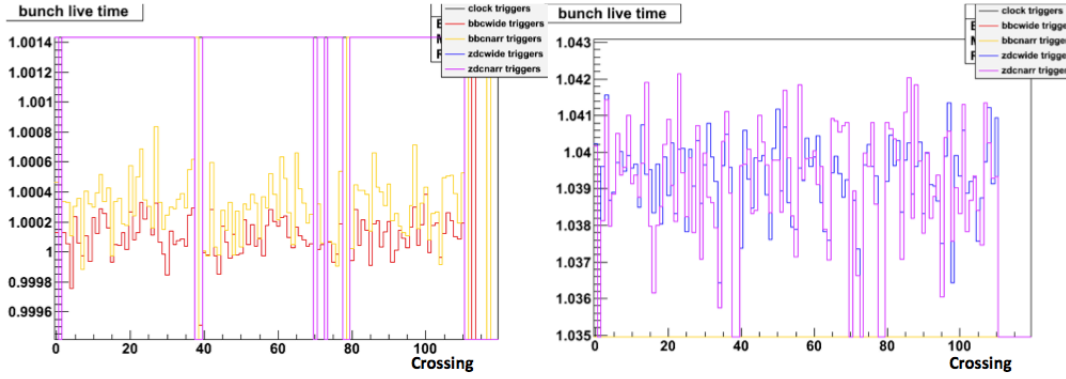


Figure 8.4: Bunch by bunch livetime ratios with the *CLOCK* trigger are shown. (a) Left: Shows the bunch by bunch livetimes for the *BBCwide* (coincidence with no vertex cut) and *BBCLL1*(coincidence with a 30 cm vertex cut) in red and yellow, respectively. (b) Right: The livetimes for *ZDCwide* and *ZDCLL1* in blue and purple, respectively. Note that in each case this is a ratio with the *CLOCK* livetime. So the same dip in crossings 20-80 seen in Fig. 8.3 appears in other triggers as well. This effect is known to come from an electronics reset from the Pad Chamber, a central arm detector.

the relative luminosity should not change when considering raw vs. live triggers.

## 8.6 Estimating the Relative Luminosity Uncertainty via Width Corrections

We have mentioned a number of practical issues that impact the luminosity monitoring. If these issues turn out to be significant they can manifest as a false asymmetry between the two luminosity detectors, the ZDC and BBC. Issues affecting the luminosity measurement, hence the relative luminosity, can be either spin related or non-spin related. Noise, beam gas, and livetime effects, all ostensibly non-spin related have not yet shown strong evidence of being significant factors. The hope is to isolate sources that can change the relative luminosity in a systematic way, understand how the systematic change is produced, and apply a correction. If these sources are understood, then calculating:

$$A_{LL}^{ZDC/BBC} = \frac{1}{P_B P_Y} \frac{\frac{N_{ZDC}^{++}}{N_{BBC}^{++}} - \frac{N_{ZDC}^{+-}}{N_{BBC}^{+-}}}{\frac{N_{ZDC}^{++}}{N_{BBC}^{++}} + \frac{N_{ZDC}^{+-}}{N_{BBC}^{+-}}} \quad (8.13)$$

where the  $L$ 's of Eq. 8.7 become  $N$ 's as we semi-intentionally lose the distinction between what we call the luminosity monitor and the detector yield, should yield a faithful measurement of the true physics asymmetry between the detectors. To the extent that it doesn't, it would be necessary to assign the asymmetry as

a systematic uncertainty on relative luminosity since it occurs as a result of unknown causes.

One such effect might come from the ZDC. It has a  $\sim 30\text{ cm}$  online and offline vertex resolution, not necessarily gaussian, as a result of its timing resolution. This is to be compared with  $\sim 5\text{ cm}$  online resolution for BBC vertex reconstruction and  $\sim 2\text{ cm}$  resolution offline in the BBC. When a coincidence occurs in either the ZDC or BBC, a vertex is reconstructed, and if it falls within the  $30\text{ cm}$  online trigger cut, the narrow trigger will fire. Due to this resolution however, a collision that truly occurs within  $30\text{ cm}$  can be reconstructed outside this range, and therefore not fire the trigger when it should. It can also happen that a collision occurs outside of  $30\text{ cm}$  but is reconstructed inside, thereby firing the trigger when it should not. In the first case, there is undercounting while in the second case there is over-counting. A typical vertex

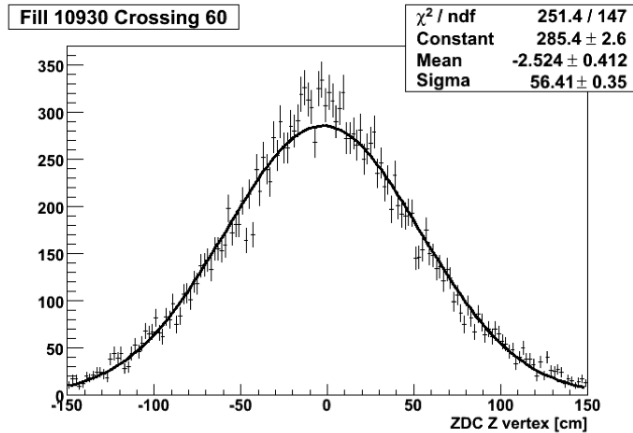


Figure 8.5: A typical example of the offline reconstructed vertex distribution from the ZDC. This distribution is a convolution of the intrinsic longitudinal (and transverse) beam profiles along with a  $30\text{ cm}$  detector resolution, which comes from its timing resolution. This plot comes from Ref. [110].

distribution is shown in Figure 8.5. The distribution is not exactly gaussian but has a width of  $\sigma_z \sim 56\text{ cm}$ . This comes from the  $30\text{ cm}$  timing resolution and the  $\sim 48\text{ cm}$  intrinsic width of the collision distribution. If the collision distribution were flat, i.e. had infinite width, the over-counting and undercounting would cancel out. However, since collisions are concentrated more within  $30\text{ cm}$  than outside, more counts are lost than gained. The narrower the distribution is, the more net counts are lost. For example, if the intrinsic collision distribution were a  $\delta$ -function, with all collisions occurring at  $z = 0$ , then the only effect is losing counts. For purposes of this width effect, currently PHENIX only considers this effect important for the ZDC, despite the fact that the BBC has finite resolution as well. This effect has been the standard method studied for estimating the relative luminosity uncertainty ([105], [106], [107], [108], [109], [110]). Future

efforts regarding the width correction would be served well by considering both. Nevertheless, this means that, assuming the BBC counts within  $30\text{ cm}$  are correct regardless of the intrinsic collision distribution, the ZDC should count less, relative to the BBC for crossings with a more narrow vertex distribution, and should count more relative to the BBC in crossings with a wider distribution. If the reconstructed vertex distribution were gaussian then  $\sigma_z$  would sufficiently quantify the width. However, it is not, so an imperfect width proxy is defined as:

$$\sigma_{proxy} = \frac{ZDCout}{ZDCin} \quad (8.14)$$

where  $ZDCout$  is the total counts where  $30\text{ cm} < |z| < 150\text{ cm}$  and  $ZDCin$  is the total counts with  $|z| < 30\text{ cm}$ . So for crossings where  $\sigma_{proxy}$  is relatively narrow, undercounting should dominate to a larger extent than when it is wider. Therefore the ratio  $\frac{ZDC}{BBC}$  should decrease for decreasing width. The conclusion is that the presence of a vertex cut in the trigger, combined with the reality that different crossings have different longitudinal profiles can cause Eq. 8.11 to not hold. Strictly speaking, the equation itself holds as well as the assumption that the efficiencies are spin independent. But we had also implicitly assumed that no other effects could cause bunch to bunch variations. While lifetimes effects can possibly cause this, bunch to bunch differences in longitudinal profiles can also result in this to a larger degree. This is what causes the assumption of constant crossing to crossing ratio to break down. For crossings with narrower intrinsic distributions, both  $\epsilon_{ZDC}$  and  $N_{ZDC}$  decrease while  $\epsilon_{BBC}$  and  $N_{BBC}$  are tentatively assumed to hold steady. This then comes into play when using Eq. 8.13 and has the potential to introduce a false asymmetry if there is some imbalance between vertex widths of “S” and “O” crossings. If this effect exists and is causing a false asymmetry, it should be eradicated by applying a width correction. Properly done, a width correction would account for the decreased trigger efficiency of the  $ZDCLL1$  trigger for narrower vertex distributions. Let us take a look to see both if this correlation is found in the data and what the correction should look like. Figure 8.6 shows an example fill from the 2009  $\sqrt{s} = 200\text{ GeV}$  running. Fig. 8.6a shows that indeed this fill sees the predicted correlation. The correlation fit is linear, and the assumption is that, to good enough approximation, this means the efficiency of the  $ZDCLL1$  trigger is changing linearly versus  $\sigma_{proxy}$ . Therefore, it is natural to assert that the ZDC scaler counts should be corrected as:

$$\left(\frac{ZDC}{BBC}\right)' = \left(\frac{ZDC}{BBC}\right) \frac{\langle \frac{ZDC}{BBC} \rangle}{a + b\sigma_{proxy}} \quad (8.15)$$

Of course this correction also implicitly assumes that no other factors impact the reconstructed vertex distribution width. This assumption turns out to be wrong as we will show later and means that the width correction may inadvertently be correcting for effects that should be left alone and/or corrected separately.

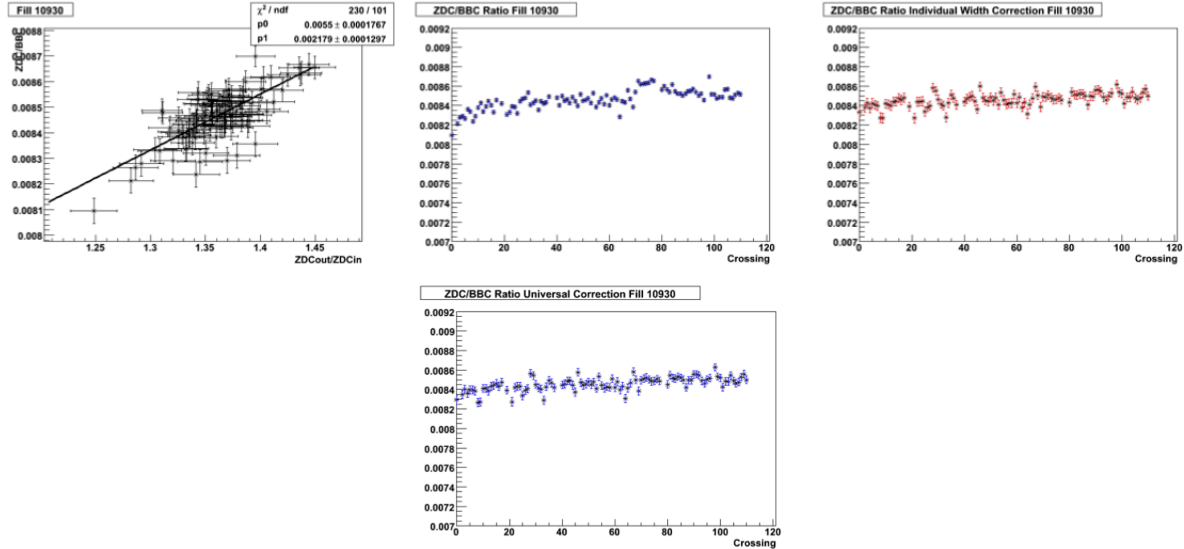


Figure 8.6: Top Left (a): The correlation plot between the scalar ratio  $\frac{ZDC}{BBC}$  and width proxy. Top Middle (b): The ratio  $\frac{ZDC}{BBC}$  vs. crossing with no corrections. Top Right (c): The ratio  $\frac{ZDC}{BBC}$  vs. crossing with a width correction applied. Middle Bottom (d): The ratio  $\frac{ZDC}{BBC}$  vs. crossing with a “universal” width correction applied. All plots shown are from Ref. [110].

As a result, what are ostensibly efficiency corrections due to width may have a different source. The check that the constancy of Eq. 8.11 is violated is shown in Fig. 8.6b. An inspection of the values shows a maximal variation of order 5% between crossings, far outside the statistical tolerance. A drop-off in the ratio is also seen in the first  $\sim 20$  crossings. Applying correction in Eq. 8.15 yields Fig. 8.6c. This drop-off and the sudden jump around crossing 70 seem to be fixed. However, looking at the remaining fluctuations indicates that systematic effects are still present and unaccounted for. Figure 8.7a shows the width correlation for a different fill. The data disagree with the hypothesis that the variation in  $\frac{ZDC}{BBC}$  is explained by the variation in vertex widths across crossings. The correlation is, at best, weak. The raw data is shown in Figure 8.7b and attempting to apply a width correction to this yields Figure 8.7c. A point by point comparison shows virtually no change and the systematic point to point variation is not accounted for. An additional trick is to try a “universal” width correction, obtained by averaging together the entire Run09  $\sqrt{s} = 200$  GeV data while ignoring the subset of data looking like Figure 8.7a. This results in Figs. 8.6d and 8.7d, which does not substantially change the results or the interpretation.

Figure 8.8a shows the raw asymmetry before the width correction and Figure 8.8b shows the raw asymmetry after the width correction has been applied to the ZDC. Notice that the central value of the asymmetry is not changed much:  $A_{LL}^{ZDC/BBC} = (1.116 \pm 0.064) \times 10^{-3}$  before and  $A_{LL}^{ZDC/BBC} = (1.118 \pm 0.136) \times 10^{-3}$ .

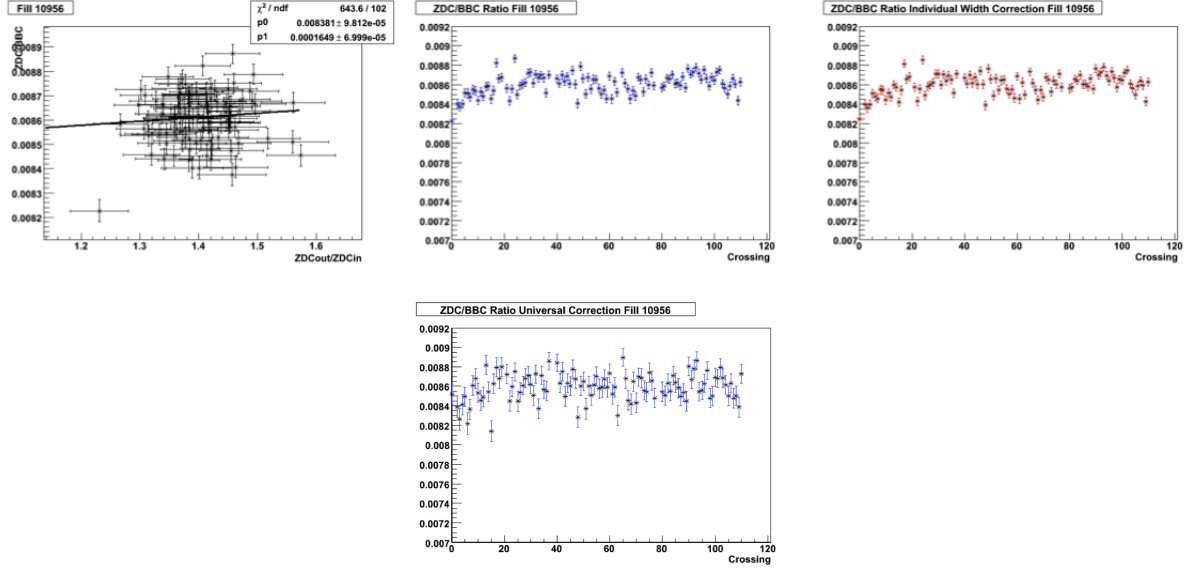


Figure 8.7: The same plots as Fig 8.6 shown for fill number 10956. In this fill, the width correlation is much more tenuous. Top Left (a): The width correlation. Top Middle (b): Uncorrected  $\frac{ZDC}{BBC}$ . Top Right (c): Width Corrected  $\frac{ZDC}{BBC}$ . Middle Bottom (d):  $\frac{ZDC}{BBC}$  with a “universal” width correction applied.

Table 8.3: Historical values of relative luminosity uncertainty error

Year	$\sqrt{s}$ (GeV)	$\sigma_{syst} (\times 10^{-4})$
2005	200	2.5
2006	200	7.5
2009	200	14
2009	500	??

So really all that happened was the error bars were blown up, which trivially is going to reduce the large  $\chi^2/NDF$ . This could be done without applying Eq. 8.15. It provides further evidence that the underlying systematic effect is not being accounted for. This asymmetry (with minor additions) forms the basis on which the systematic uncertainty is determined. We will discuss this at length in the next chapter, but the evidence strongly suggests that rate corrections, to be described shortly, are the proper correction on which to base the relative luminosity systematic determination. The Run06  $pp$  analysis for  $\sqrt{s} = 200$  GeV data (Ref. [109]) supports this conclusion. Here, a reduction in the  $\chi^2/NDF$  of the  $A_{LL}^{ZDC/BBC}$  fit by a factor 3.5 is achieved, even though the rate correction itself is not exactly correct. Nevertheless, the error bars in this case are not increased relative to the asymmetries before correction. Thus, the  $\chi^2$  improvement in this case can be attributed to the rate correction itself as opposed to trivially increasing the error bars.

Table 8.3 shows the systematic errors from three years of running at  $\sqrt{s} = 200$  GeV, each year with increased

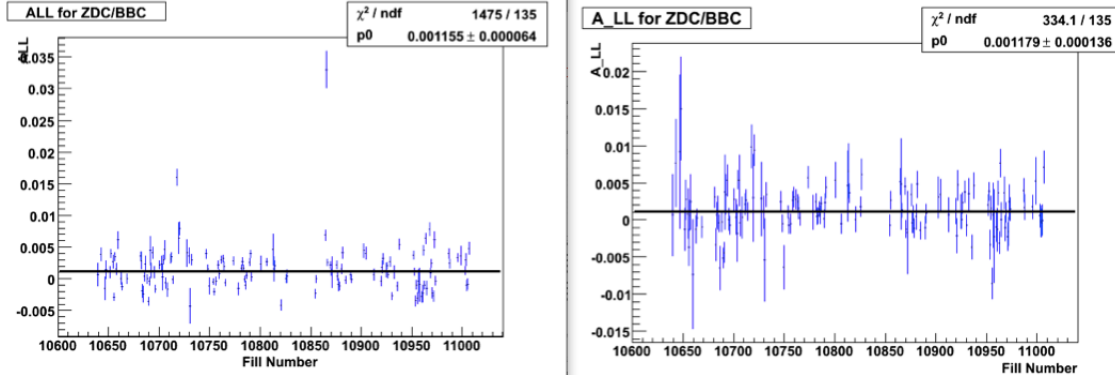


Figure 8.8: Left (a):  $A_{LL}^{ZDC/BBC}$  using raw scaler values. Right (b):  $A_{LL}^{ZDC/BBC}$  after applying a width correction to ZDC scalers.

rate from the previous. The salient feature, of course, is that in addition to the collision rate increasing, the systematic error in relative luminosity has also increased. At the  $O(10^{-3})$  level, this begins to have a crippling effect on the ability of PHENIX  $A_{LL}$  measurements to constrain  $\Delta G$  since asymmetries generated from expected gluon polarizations are expected to be  $O(10^{-4})$ , especially at forward rapidity.

The question mark in Table 8.3 next to the Run09  $\sqrt{s} = 500$  GeV is not an oversight. We investigate briefly what happens when one tries to apply a width correction to that data. An analogous set of plots to Figs. 8.6 and 8.7 is shown in Figure 8.9. That a width correlation exists can be seen from Figure 8.9a. In Figure 8.9b we show the raw  $\frac{ZDC}{BBC}$  vs crossing. Note just how large the dropoff in the first 20 bunches has become compared to at  $\sqrt{s} = 200$  GeV. It is  $O(10\%)$ . The errors bars are included in this plot, they just happen to be smaller than the plot marker size. The  $\chi^2/NDF$  for the fit to a constant ratio is extremely large, around 500. Figure 8.9c shows the result of applying the width correction and the results are abysmal. The low crossing dip is removed, but the  $O(10\%)$  variation persists. Meanwhile the  $\chi^2/NDF$  has increased since we have not chosen to increase the statistical error bars as a result of applying the correction as in Ref. [110]. It is clear that any sort of universal correction would perform no better, just as was the case before. Figure 8.10 shows another interesting effect seen in the  $\sqrt{s} = 500$  GeV data. It turns out the width correlation itself is spin combination dependent. ‘‘S’’ crossings have a steeper slope (and lower vertical offset) than ‘‘O’’ crossings in the width correlation. The meaning of this would need to be understood carefully in order to properly apply width corrections, if indeed it is appropriate at all to do so. Based on these observations, it seems clear the width correction does not correct the ZDC counts appropriately. In fact, one might even observe heuristically that the width correction seems less effective at higher collision rates, where collision pileup becomes non-negligible. Collision pileup is a totally separate effect which causes both

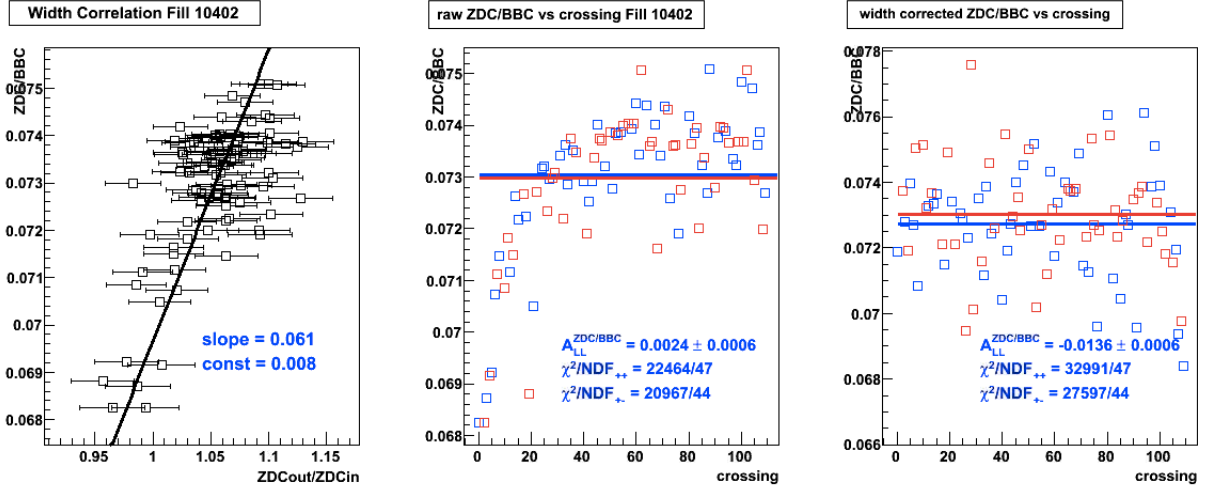


Figure 8.9: Attempt to apply a width correction at  $\sqrt{s} = 500$  GeV. Left (a): The width correlation is shown and seen to be present in this example. Middle (b): The raw  $\frac{ZDC}{BBC}$  vs crossing. The blue and red colors are shown to separate “S” crossings from “O” crossings. A constant is fit to the “S” and “O” crossings separately to obtain  $\langle \frac{ZDC}{BBC} \rangle^{++}$  and  $\langle \frac{ZDC}{BBC} \rangle^{+-}$ . Then  $P_B P_Y A_{LL}^{ZDC/BBC} = \frac{\langle \frac{ZDC}{BBC} \rangle^{++} - \langle \frac{ZDC}{BBC} \rangle^{+-}}{\langle \frac{ZDC}{BBC} \rangle^{++} + \langle \frac{ZDC}{BBC} \rangle^{+-}}$ .

the BBC and ZDC to incorrectly count coincidences. A clear understanding of this effect gets us closer to the path we want to be on to understand the large crossing to crossing variations in  $\frac{ZDC}{BBC}$ . After an in depth discussion of pileup corrections, we will briefly look back at width corrections again to see if there is improvement when applying a width correction to pileup corrected scalers.

## 8.7 Pileup Corrections

Collision pileup occurs when in a single crossing there is more than one  $pp$  collision. The true collision rate,  $\mu$ , is defined as the average number of  $pp$  collisions in a bunch crossing, so a higher rate corresponds to an increased likelihood of pileup. In a crossing with more than one collision, PHENIX will detect the remnants of both collisions superimposed on one another. Figure 8.11 shows a few of the simplest examples, in cartoon form, of what collision pileup looks like (from the perspective of the BBC or ZDC) in the case of two collisions. In the case three collisions occurs the permutations are even more numerous. Figure 8.11a shows the base case of just one collision. For this single collision, one of four things can happen with total probability one:

- $\epsilon_0$  = probability that, given a collision, a hit in neither the north or south detector is observed.

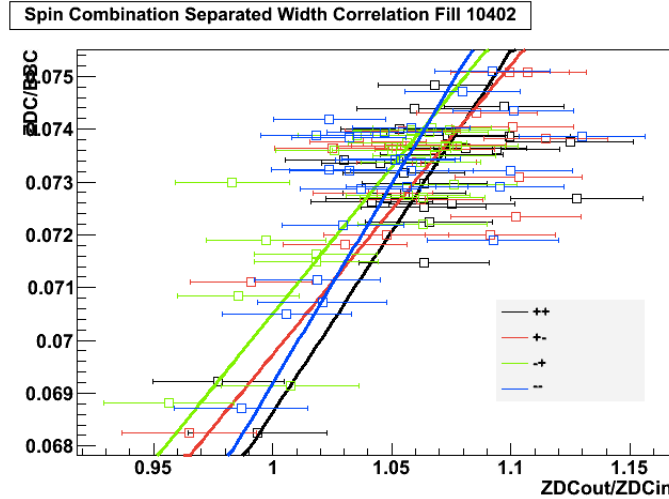


Figure 8.10: The width correlation for fill 10402 is shown separately for “S” crossings,  $(++)$  and  $(--)$ , and for “O” crossings,  $(+-)$  and  $(-+)$ , in black, blue, red and green, respectively.

- $\epsilon_S$  = probability that, given a collision, a hit in the south detector is observed and no hit in the north is observed.
- $\epsilon_N$  = probability that, given a collision, a hit in the north detector is observed and no hit in the south is observed.
- $\epsilon_{NS}$  = probability that, given a collision, a hit in the north and south detectors are observed.

These are the only four possibilities and

$$\epsilon_0 + \epsilon_N + \epsilon_S + \epsilon_{NS} = 1 \quad (8.16)$$

Segmenting collision types in this way is natural, as it is based on probabilities of observables. It is possible to segment collision types based on non-observables such as what a collision is “capable” of doing ([118]). For example, one can say a single diffractive event can only cause hits in a single sided detector. In the data it is not possible to distinguish between a single diffractive event and, say, a QCD event that just happened to produce remnants in only one detector. Segmenting collisions as we do here does mix events “capable” and “not capable” of producing hits in a given detector, but it is of no consequence, and correlations between different event types also cause no issue. Properly defining “capable” is difficult in and of itself and in neither the current method we are about to develop, nor alternative methods, has it been demonstrated that any form of noise, beam gas, or other spurious detector counts can be eliminated. Ultimately, all we have to go on are detector hits and, while we think the noise is very low in coincidence counting, we cannot currently

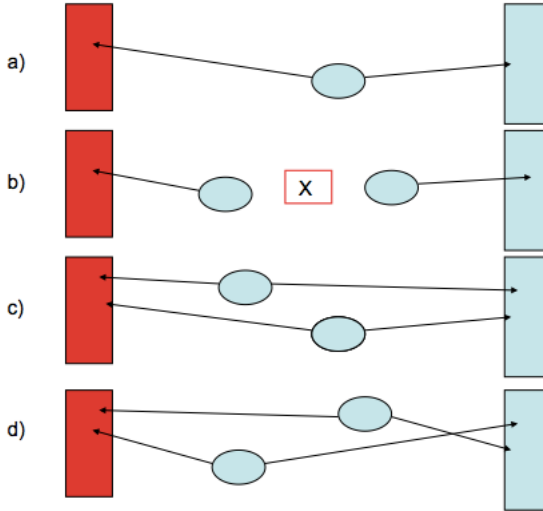


Figure 8.11: Cartoon diagram of how collision pileup appears in PHENIX. The red rectangle represents the south BBC or ZDC detector while the blue represents the north BBC or ZDC. (a) A single collision (no pileup) has some probability to produce hits in both detector arms. (b) A collision has some probability to hit only one arm. In the case of two collisions occurring in the same crossing, if one collision hits only one arm and the other collision hits the other, a false vertex,  $X$ , can be reconstructed that is not distinguishable from one collision causing a coincidence. (c) and (d) show a pileup scenario where both collisions produce a coincidence. Each arm in principle has two hit times, allowing for four possible reconstructed vertices, two real and two ghost.

Table 8.4: Examples of over and undercounting in the case of two collisions.

Collision 1	Collision 2	true coincidences	counted coincidences	Result
North	South	0	1	over-count
North&&South	North&&South	2	1	undercount

subtract it out analytically. Ultimately, however, the results from one derivation can be mapped onto the results of the other with appropriate redefinitions.

As we can see in Figure 8.11b-d, pileup effects can be a source of miscounting, both over-counting and undercounting. Table 8.4 summarizes two examples of how this can happen. In the case where there is no pileup, we would know for sure that an observed coincidence means that one collision occurred. Only a fraction of collisions produce a coincidence but we still have  $\mathcal{L} \propto \mathcal{R}_{collisions} \propto \mathcal{R}_{coincidences}$ . But Table 8.4 shows that pileup effects complicate the matter and  $\mathcal{L} \propto \mathcal{R}_{collisions} \propto \mathcal{R}_{real} + a\mathcal{R}_{under} - b\mathcal{R}_{over}$  where  $a$  and  $b$  are positive, rate dependent values and  $\mathcal{R}_{real}$ ,  $\mathcal{R}_{under}$  and  $\mathcal{R}_{over}$  are the rate of crossings where the number of coincidences is counted correctly, too low, and too high, respectively. Note that both the ZDC and BBC can only count 0 or 1 in each crossing. A setup where this restriction is lifted would require a separate analysis of pileup corrections.

We now have a clear understanding of the conceptual issues at play. Let us transition to a quantitative understanding by making two new definitions:

- $P_{kl}$  = the probability that in a given crossing, the north detector will see a hit from  $k$  different collisions and the south will see a hit from  $l$  different collisions.
- $P(kl|N)$  = the probability that in a given crossing where  $N$  collisions occur, the north detector will see a hit from  $k$  different collisions and the south will see a hit from  $l$  different collisions

Please note that  $P_{kl}$  does not necessarily mean the particular detector can or does actually resolve the different hit times if there is more than one. In fact, the ZDC cannot do this while in practice the BBC does not. The PMT's of the BBC can each register an independent hit time, but this turns out to be difficult to use offline. An interesting analysis of this was performed in Ref. [119] in the context of reconstructing multiple vertices. In the online trigger different hit times are simply averaged. More will be said about this later. Also, a subset of the results we obtain have been derived previously by others ([120]), but the method we use allows some additional insights. That being said, we start by calculating some of the  $P_{kl}$ 's. The simplest case is  $P_{00}$ , the probability that in a given crossing, both the north and south detectors do not observe any hits. Since the unknown is the true number of collisions, we can write  $P_{00}$  as a sum of conditional probabilities,  $P(00|N)$ , to observe no hits given all possible numbers of collisions.

$$P_{00} = \sum_{i=0}^{\infty} P(00|i)P(i, \mu) \quad (8.17)$$

Given  $i$  collisions, the probability that each of them independently results in no hit in either detector is  $P(00|i) = \epsilon_0^i$ . We also introduce the poisson probability distribution,  $P(i, \mu)$ , which describes the likelihood to have  $i$  rare and independent events occur, given an average rate  $\mu$ .  $pp$  collisions are “rare” in the sense that a crossing involves  $O(10^{11})$  protons passing through  $O(10^{11})$  protons, and we expect  $O(1)$  collisions. We have:

$$P(i, \mu) = \frac{e^{-\mu}\mu^i}{i!} \quad (8.18)$$

which gives:

$$P_{00} = \sum_{i=0}^{\infty} \epsilon_0^i \frac{e^{-\mu}\mu^i}{i!} = e^{-\mu} \sum_{i=0}^{\infty} \frac{(\mu\epsilon_0)^i}{i!} = e^{-\mu(1-\epsilon_0)} \quad (8.19)$$

We can build on this to determine the probability to observe  $k$  north hits and 0 south hits,  $P_{k0}$ . We need  $k$  north hit only collisions and  $i - k$  neither sided collisions, given  $i$  collisions. Of course, we have to start the sum at  $i = k$ , not  $i = 0$ , since we can not have less than  $k$  collisions if we are saying the north detector saw

$k$  hits. So:

$$P_{k0} = \sum_{i=k}^{\infty} \binom{i}{k} \epsilon_0^{i-k} \epsilon_N^k \frac{e^{-\mu} \mu^i}{i!} = e^{-\mu} \sum_{i=k}^{\infty} \frac{i!}{k!(i-k)!} \epsilon_0^{i-k} \epsilon_N^k \mu^k \frac{\mu^{i-k}}{i!} = e^{-\mu(1-\epsilon_0)} \frac{(\mu \epsilon_N^k)}{k!} \quad (8.20)$$

To find the total probability that the north sees any hits at all and the south sees no hits, we just need to sum this result from  $k = 1$  to  $k = \infty$ :

$$\sum_{k=1}^{\infty} e^{-\mu(1-\epsilon_0)} \frac{(\mu \epsilon_N^k)}{k!} = \sum_{k=0}^{\infty} e^{-\mu(1-\epsilon_0)} \frac{(\mu \epsilon_N^k)}{k!} - e^{-\mu(1-\epsilon_0)} = e^{-\mu(1-\epsilon_0)} (e^{\mu \epsilon_N} - 1) \quad (8.21)$$

So we find that

$$P(k > 0, 0) = e^{-\mu(1-\epsilon_0)} (e^{\mu \epsilon_N} - 1) \quad (8.22)$$

and by direct analogy

$$P(0, l > 0) = e^{-\mu(1-\epsilon_0)} (e^{\mu \epsilon_S} - 1) \quad (8.23)$$

If one is feeling particularly bored on a rainy overcast day, one could also extrapolate to find the arbitrary probability,  $P_{kl}$ . This is given explicitly via the formula:

$$P_{kl} = e^{-\mu(1-\epsilon_0)} \sum_{i=0}^{\min(k,l)} \frac{(\mu \epsilon_{NS})^i}{i!} \frac{(\mu \epsilon_N)^{k-i}}{(k-i)!} \frac{(\mu \epsilon_S)^{(l-i)}}{(l-i)!} \quad (8.24)$$

where the index  $i$  is essentially a summation index over the true number of double sided collisions. The other quantity we are interested in is the probability for the BBC or ZDC to be hit on each side at least one time, i.e.  $P(k > 0, l > 0)$ . This is the quantity describing the probability, hence the rate, of observing both sides of the detector to be hit regardless of the true number of collisions. This is the quantity that really encapsulates how a coincidence counter based on 0's and 1's counts. We could do some complicated sum based on Eq. 8.24 but an easier route is to say:

$$\begin{aligned} P(k > 0, l > 0) &= 1 - P_{00} - P(k > 0, 0) - P(0, l > 0) \\ &= 1 - e^{-\mu(1-\epsilon_0)} - e^{-\mu(1-\epsilon_0)} (e^{\mu \epsilon_N} - 1) - e^{-\mu(1-\epsilon_0)} (e^{\mu \epsilon_S} - 1) \\ &= 1 - e^{-\mu(\epsilon_S + \epsilon_{NS})} - e^{-\mu(\epsilon_N + \epsilon_{NS})} + e^{-\mu(\epsilon_S + \epsilon_N + \epsilon_{NS})} \end{aligned} \quad (8.25)$$

$$P(k > 0, l > 0) = 1 - e^{-\mu \epsilon_{NS}(1+k_S)} - e^{-\mu \epsilon_{NS}(1+k_N)} + e^{-\mu \epsilon_{NS}(1+k_S+k_N)}$$

Where we have made use of the definitions and Eq. 8.16. We have also made the definitions  $k_S = \frac{\epsilon_S}{\epsilon_{NS}}$  and  $k_N = \frac{\epsilon_N}{\epsilon_{NS}}$ . Note that from the very definitions of  $k_N$  and  $k_S$  it is clear this is a rate independent

number. It is the ratio of the probabilities for seeing a single sided collision to a double sided collision, and we typically refer to these quantities as the singles to doubles ratios. If the performance of the luminosity detectors were entirely stable over time, the values of  $k_{N,S}$  would be stable and would represent the ratio of the cross sections for single sided collisions to double sided collisions. But if the detector efficiency changes over time, this interpretation is not exactly correct. In this form Eq. 8.25 is to be used the following way:  $P(k > 0, l > 0) = \frac{BBCLL1}{CLOCK}$  is the observed collision counting rate and  $\mu\epsilon_{NS}$  is the true rate for collisions which produce coincidence hits. It is the actual scaler we want to use for determining the relative luminosity with pileup corrections correctly accounted for.  $k_{N,S}$  in this form can be determined from offline data using the maximally unbiased  $CLOCK$  triggers. We then solve for  $\mu\epsilon_{NS}$  numerically by plugging in the quantities  $P(k > 0, l > 0)$ ,  $k_N$  and  $k_S$ .

We could actually avoid the hassle of determining  $k_{N,S}$  if singles scalers had been recorded. In this case one can use Eqs. 8.19 - 8.25 to solve explicitly for the true collision rate in terms of observables as:

$$\mu\epsilon_{NS} = \ln P_{00} - \ln (P_{00} + P_{k0}) - \ln (P_{00} + P_{0l}) \quad (8.26)$$

In this form, however, we would have to use  $CLOCK$  triggered events, crossing by crossing, to determine the  $P_{kl}$ . Due to the  $\sim 500\text{ Hz}$  Data Acquisition (DAQ) bandwidth typically allocated to the  $CLOCK$  trigger, the statistical uncertainty that  $\mu\epsilon_{NS}$  would have is far too high. The other nice thing about the form with  $k_{N,S}$  is that it gives a nice way to think about rate corrections conceptually by imagining remnants of a  $pp$  collision and visualizing the relative likelihood for a single sided hit versus a double sided hit. In addition, this method can be used (improperly) with vertex cut scalers making it less susceptible to noise effects since only the coincidence scaler is used. The singles scalers, which are much more susceptible to noise, are not used.

An important caveat in this discussion is the issue of a vertex cut being a trigger requirement. In determining any of the aforementioned  $P_{kl}$ 's we assumed collisions at any vertex were valid. This assumption is embedded in the definition and usage of all the  $\epsilon$ 's. But in Run09  $pp$  at  $\sqrt{s} = 500\text{ GeV}$ , where the STAR Scalers were not functioning, only the  $BBCLL1$  trigger, which has a  $30\text{ cm}$  online vertex cut, was scaled. This adds an extra layer of difficulty in applying rate corrections because the arguments for when and how over-counting and undercounting occurs is now subject to the details of when and where the multiple collisions occur, i.e. Eqs. 8.8 and 8.9. For example, in Figure 8.11 we made no reference to the collision vertices.

Looking at the special case of Figure 8.11b, the ghost vertex that is reconstructed depends on  $(t_{0,a}, z_a)$  and  $(t_{0,b}, z_b)$  for collisions  $a$  and  $b$ . Assuming that collision  $a$  hits the south detector only and collision  $b$  hits the north detector only, we observe the quantities  $t_{S,a}$  and  $t_{N,b}$ . Eqs. 8.8 and 8.9 allow us to write these as:

$$\begin{aligned} t_{S,a} &= t_{0,a} - t_{offset} + \frac{z_a + L}{c} \\ t_{N,b} &= t_{0,b} - t_{offset} + \frac{L - z_b}{c} \end{aligned} \quad (8.27)$$

Therefore

$$z_{ghost} = \frac{c}{2}(t_{S,a} - t_{N,b}) = \frac{1}{2}[(ct_{0,a} + z_a) - (ct_{0,b} - z_b)] = \frac{c}{2}(t_{0,a} - t_{0,b}) + \frac{1}{2}(z_a + z_b) \quad (8.28)$$

The *BBCLL1* or *ZDCLL1* will only fire on this coincidence if the details of the experimental unknowns  $(t_{0,a}, z_a)$  and  $(t_{0,b}, z_b)$  happen to produce  $|z_{ghost}| < 30\text{ cm}$ . The four dimensional probability distribution  $P(t_{0,a}, z_a, t_{0,b}, z_b)$  is a complicated space but, more relevantly, depends on the details of the longitudinal bunch profiles. Therefore, a vertex cut makes it impractical to analytically understand and apply rate corrections. When two single sided collisions cause a ghost vertex outside of  $30\text{ cm}$ , there will no longer be an over-counting. One could say the trigger is “incorrectly correctly not over-counting”. That is, it should over-count, and the rate correction would account for this. But with a vertex cut, the rate correction is correcting for over-counting which did not actually happen if  $|z_{ghost}| > 30\text{ cm}$ . Additionally, many other scenarios with lower probability are possible that make the picture even more complicated. A full set of simulated multi-collision crossings is needed to study this properly and we detail our studies of this later.

## 8.8 Determining $k_N$ and $k_S$

We will now outline the procedure used to determine the singles to doubles ratios. Two things should be noted. First, once again these quantities can really only be determined from *CLOCK* triggered data with no vertex cut applied since, by definition, any crossing where only one side of the detector is hit has no reconstructed vertex. Hence no cut can be applied. Second, while the true ratio of singles to doubles is well defined, the observed singles to doubles ratio is expected to be rate dependent. At extremely low collision rates,  $\mu \rightarrow 0$ , multiple collisions in one crossing are completely negligible. Therefore, if a collision occurs, the south and north detectors give reliable information about whether that collision was single sided or double sided. Quite simply, only something like Fig. 8.11a is relevant.<sup>2</sup> Fig. 8.11b-d can be ignored.

---

<sup>2</sup>Unless the singles to double rates is extraordinarily large.

But as the rate increases, they cannot be. In the case of Fig. 8.11b, the north and south singles counts should increase from  $N_n \rightarrow N_n + 1$  and  $N_s \rightarrow N_s + 1$ , while the coincidence count,  $N_{ns}$  stays fixed. In other words,  $k_N = \frac{N_n}{N_{ns}} \rightarrow \frac{N_n+1}{N_{ns}}$ . But instead, because of the pileup creating a situation where another collision is superimposed and a fake coincidence is detected, we actually end up with counting looking like  $k_N = \frac{N_n}{N_{ns}} \rightarrow \frac{N_n}{N_{ns}+1}$ . Thus, the predicted effect is that both  $k_{N,S}$  decrease as a function of rate.

Figure 8.12 shows the raw counts versus crossing for single sided hits, coincidence hits, and no hits for both the ZDC and BBC. The salient feature is that for the BBC,  $k_{N,S} < 1$  while for the ZDC,  $k_{N,S} > 1$ .

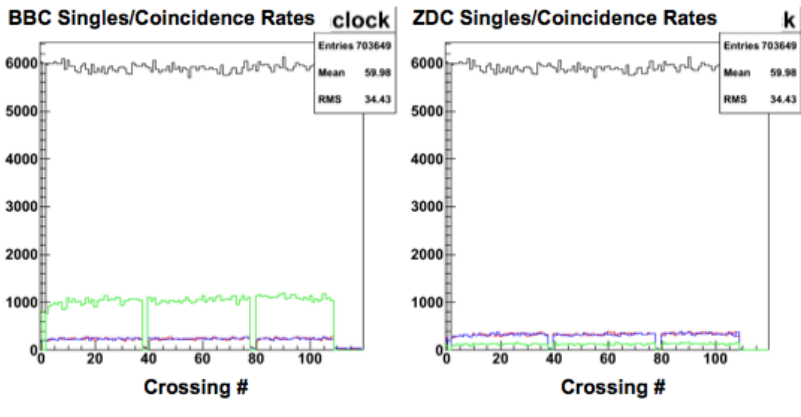


Figure 8.12: Left (a): Single sided and double sided (coincidence) counts for the BBC versus crossing. Right (b): Single sided and double sided counts for the ZDC. The black histogram shows the number of *CLOCK* triggers for each crossing. The green histogram is the number of crossings with a coincidence. The red and blue histograms show the north and south side singles hit counts, respectively.

In Figure 8.13 we perform an iteration procedure to determine the true values of  $k_{N,S}$  for both detectors. We do this by plotting the singles to doubles ratios from every crossing from every fill of Run09  $\sqrt{s} = 500$  GeV running, as in Fig. 8.12, versus the BBC rate for that crossing. In each iteration we use the same value of singles to doubles, which is plotted on the y-axis. However, the x-axis is the BBC or ZDC rate, which is what we ultimately want to correct. So for the first iteration, we use just the uncorrected scalar values from GL1P, i.e.  $R_{BBC} = \frac{BBCLL1}{CLOCK}$ . We do see the predicted decrease of observed singles to doubles with rate. The next step in the iteration is to fit this with plot with an  $N^{th}$  degree polynomial. Since at 0-rate, the observed singles to double ratio coincides with the true singles to doubles, we take the constant term of the polynomial fit as the value of  $k_{N,S}$  for the next iteration. To begin the next iteration, we use these values, along with  $R_{BBC}$  to solve Eq. 8.25 and obtain a corrected rate  $R_{BBC}^{cor}$ . We then remake the plot with  $R_{BBC}^{cor}$  replacing  $R_{BBC}$  on the x-axis. This procedure is repeated until a convergence is found in the  $k_{N,S}$ . The convergence happens in each case in four or less iterations. Table 8.5 shows the results of the iterative

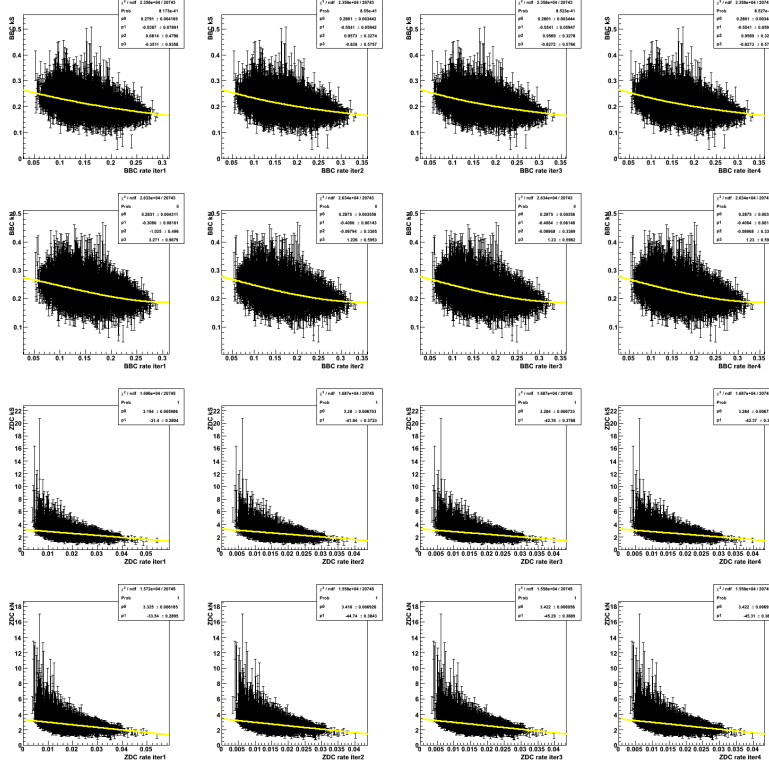


Figure 8.13: Iterative procedure, as described in the text, is shown. The top row shows four iterations (across) for BBC south. The second row shows the same for BBC north. The third row shows the same for ZDC south. The bottom row shows the same for ZDC north.

procedure using different order polynomials. For the BBC a cubic polynomial is used while for the ZDC a quadratic polynomial is used. The idea of using the iteration is that once the BBC or ZDC rate, along with the  $k_{N,S}$ , is correct the dependence of the observed singles to doubles ratio versus the true coincidence rate will be correctly reproduced and subsequent iterations will yield an unchanging result. If convergence has not yet happened, the constant term of the polynomial fit is used for the rate correction and a new iteration yields an updated value.

Based on this procedure we use the following values of singles to doubles ratios:  $k_{BBCS} = 0.280$ ,  $k_{BBCN} = 0.289$ ,  $k_{ZDCS} = 3.39$ ,  $k_{ZDCN} = 3.65$ . The uncertainties on these values are likely to be larger than the statistical uncertainties derived from the iterative fitting procedure. Later we will study what effects a 5% or even 10% correlated systematic uncertainty has on our results. Based on this study we can provide some very rough estimates on the probability of a collision causing a hit in neither side, one side or both. These estimates are summarized in Table 8.6. We use the a priori knowledge that the BBC has a  $\sim 53\%$  efficiency for a coincidence hit given a collision ([114]). So  $\epsilon_{BBC,NS} \sim 0.53$ . We use  $k_{N,S}$  to estimate  $\epsilon_{N,S}$  and take

Table 8.5: Results of iterative fitting to get singles to doubles ratio for the BBC and ZDC

Detector	Polynomial Order	$k_S$	$k_N$
BBC	1	0.260	0.275
BBC	2	0.276	0.295
BBC	3	0.280	0.289
BBC	4	Unreliable	Unreliable
ZDC	1	3.26	3.40
ZDC	2	3.39	3.65
ZDC	3	Unreliable	Unreliable

Table 8.6: Estimation of  $\epsilon_0, \epsilon_N, \epsilon_S$  and  $\epsilon_{NS}$

Detector	$\epsilon_0$	$\epsilon_N$	$\epsilon_S$	$\epsilon_{NS}$
BBC	0.17	0.15	0.15	0.53
ZDC	0.75	0.11	0.11	0.03

$\epsilon_0$  as the leftover. For the ZDC, we use Fig. 8.9 to estimate  $\frac{ZDC}{BBC} \sim 0.06$ . Therefore  $\epsilon_{ZDC, NS} \sim 0.03$ . Again using the singles to doubles ratios for the ZDC allows us to fill in the rest of the estimates.

## 8.9 Using the Pileup Corrections

It is an interesting exercise to study how the rate of accidental coincidences (leading to over-counting) and multiple double sided collisions (leading to undercounting) compare. This gives insight into whether a two sided detector has a net undercounting or net over-counting effect. One simplifying approximation we can make is to consider crossings with only zero, one, or two collisions. More collisions can and do, of course, occur according to Poisson statistics (Eq. 8.18). For the case of zero or one collision, the coincidence counting is correct. We can consider three distinct counting rates arising from the 20 ( $= 4 + 16$ ) possible combinations (each collision has four possible outcomes).  $R_{true}$  the rate at which one collision causing a coincidence occurs is given, in this approximation, by  $R_{true} \sim \mu\epsilon_{NS} + \mu\epsilon_{NS}[\mu(1 - \epsilon_{NS})]$ . The rate of accidental over-counting is given by  $R_{over} \sim (\mu\epsilon_N)(\mu\epsilon_N)$  and the rate of undercounting is given by  $R_{under} \sim \frac{1}{2}(\mu\epsilon_{NS})^2$ . Using Table 8.6 for approximate values along with a typical beam rate in Run09  $\sqrt{s} = 500$  GeV of  $\mu \sim 0.25$  shows that  $\frac{R_{under}}{R_{over}} \sim 6$  for the BBC and  $\frac{R_{over}}{R_{under}} \sim 27$  for the ZDC. This shows that the dominant effect in the BBC is undercounting and the dominant effect in the ZDC is over-counting. We can also estimate the absolute scale of miscounting. For the BBC this is estimated from  $\frac{R_{over} - R_{under}}{R_{true}} \sim -0.05$ . For the ZDC we have  $\frac{R_{over} - R_{under}}{R_{true}} \sim 0.10$ . This means the BBC undercounts the total coincidences by about 5% while the ZDC over-counts the total coincidences by around 10%. We can now improve upon the general diagram from Fig. 8.11 and be more specific with Fig. 8.14. Here we pictorially show the dominant effect in each detector. The example we just worked through was for just one value of  $\mu$ . Figure 8.15 shows the exact curve for

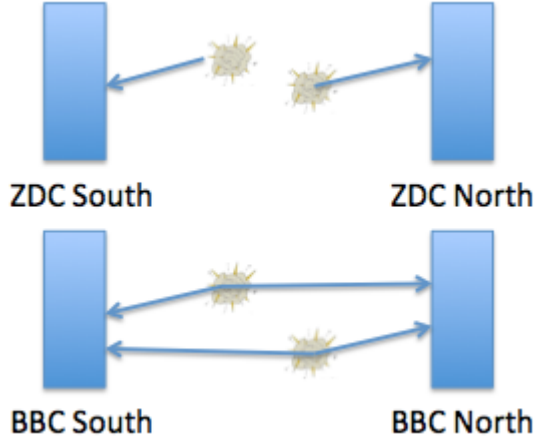


Figure 8.14: The main source of miscounting in the ZDC comes from an accidental coincidence leading to over-counting while the main source of miscounting in the BBC is due to multiple coincidences being undercounted as a single coincidence.

both the BBC and the ZDC. Here, the x-axis is not  $\mu$ , but rather  $\mu\epsilon_{NS}$ . For both the BBC and ZDC the miscounting gets more severe at higher rates, as one might expect.

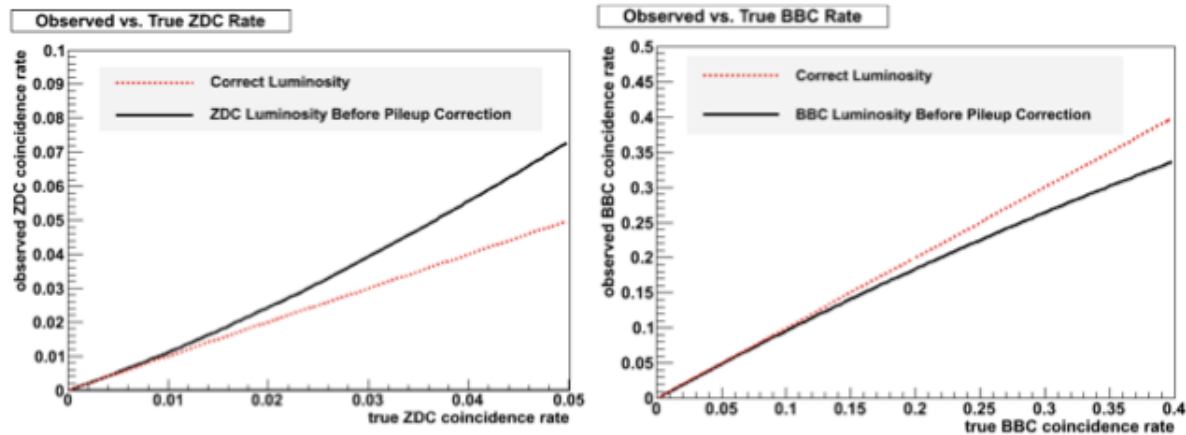


Figure 8.15: Left (a): The black curve shows the actual coincidence counting rate of the ZDC versus the true coincidence rate, shown in red. Right (b): The same comparison is shown for the BBC.

## 8.10 Combined Width and Pileup Corrections

Recall that our attempts to apply width corrections at the higher rates seen in  $\sqrt{s} = 500$  GeV, such as in Figure 8.9, failed to account for almost all the systematic bunch to bunch variation. There was also little evidence that it accounted for the somewhat smaller systematic variation in  $\frac{ZDC}{BBC}$  seen at lower rates in

$\sqrt{s} = 200$  GeV running. The same thing can be said at even lower rates yet, in the 2006  $\sqrt{s} = 200$  GeV run (pg. 10 of Ref. [109]). Now that we have developed the idea of pileup corrections, let us examine what, if any, improvement this gives. Figure 8.16 shows a comparison between the ratio of ZDC and BBC GL1P scalers without and with rate corrections applied. Before rate corrections are applied  $ZDC/BBC$  ranges from  $\sim 0.068$  to  $\sim 0.075$ . After rate corrections are applied the range is compressed and lowered to  $\sim 0.063$  to  $\sim 0.066$ . So a  $\sim 10\%$  variation is now a  $\sim 5\%$  variation. Before pileup corrections  $\chi^2/NDF \sim 193$  while after this is reduced to  $\chi^2/NDF \sim 46$ . At this point, we might wonder what, if any, effect the lack of vertex consideration when deriving the pileup corrections has when applying these corrections to scalers with a vertex cut imposed. Just as the presence of a vertex cut leads to the idea of luminosity miscounting via vertex width effects, so it might also lead to a residual miscounting due to rate effects. There is thus no a priori reason to expect the rate corrections to be correct. In fact, looking at Figure 8.17 ([121]) shows that,

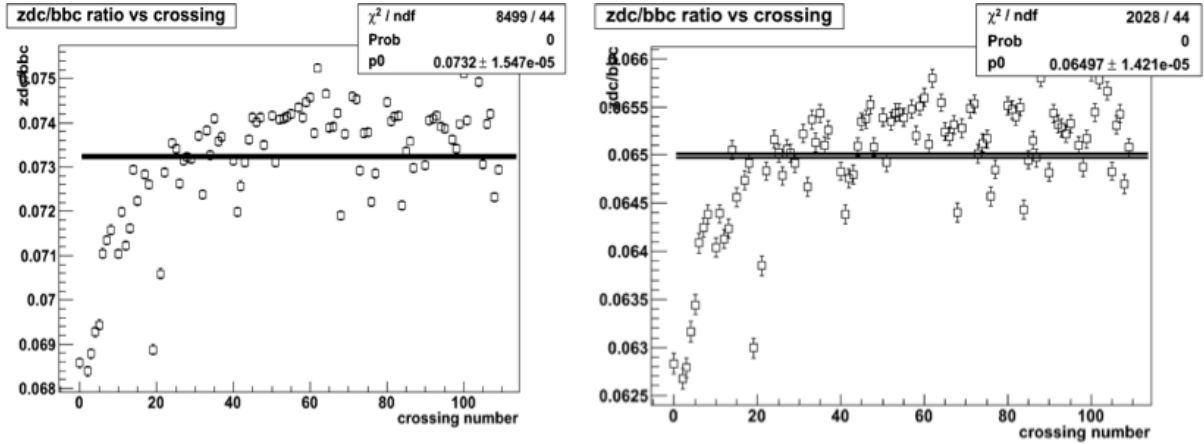


Figure 8.16: Left (a): The  $\frac{ZDC}{BBC}$  vs crossing plot using raw scalers. Right (b): A clear improvement is seen when applying rate corrections to both the raw ZDC and BBC scalers.

in fact, when we look at triggers with no vertex cut applied,  $ZDC_{wide}$  and  $BBC_{wide}$ , the pileup corrections work as expected. A  $\sim 5\%$  variation is seen in the uncorrected ratio of no-vertex triggers. When the rate correction is applied the ratio  $\frac{ZDC_{wide,cor}}{BBC_{wide,cor}}$  becomes remarkably flat. It is interesting to observe that for the no-vertex case the constant ratio of ZDC to BBC triggers is  $\sim 0.063$ . In the case of the  $30\text{cm}$ -vertex triggers, the constant ratio seems to be inching closer to this value as well based on Fig. 8.16, though we cannot say for sure due to the remaining systematic effect we cannot yet account for. Comparing these two plots leads one to the conclusion that we have isolated the problem of  $ZDC/BBC$  variation to the presence of the vertex requirement in the trigger. Exactly how the vertex interacts with the rate correction is still unknown but may be complicated. It should of course be observed that in Fig. 8.17 a small bunch to bunch variation exists

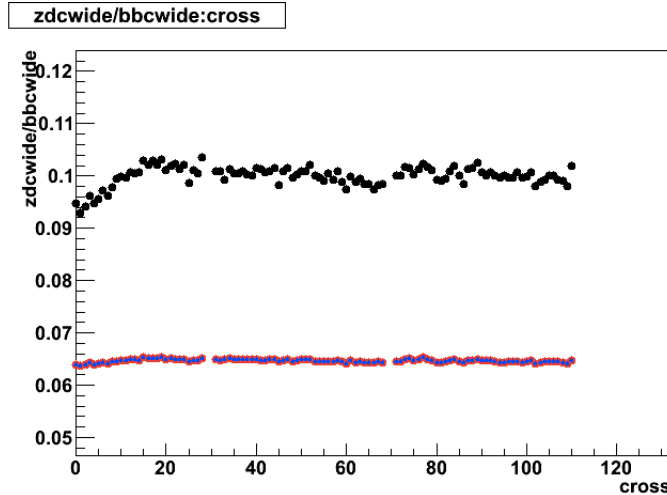


Figure 8.17: Using STAR Scaler data from Run13 data at  $\sqrt{s} = 510$  GeV, pileup corrections are applied to  $ZDCwide$  and  $BBCwide$  scalers. The uncorrected ratio  $\frac{ZDCwide}{BBCwide}$  is black while the corrected ratio is in blue.

including a small but discernible remaining drop-off in the first 20 bunches as seen in the uncorrected scalers.

Figure 8.18 shows the effect of the width correction before and after applying the pileup correction. The left column shows another example of a width correlation, the uncorrected  $ZDC/BBC$  ratio, and the width corrected ratio. The right column shows the same plots but a rate correction has been applied now. Applying a pileup correction does not make the width correction work any better. One could claim there is the possibility that because we know the rate corrections do not work properly for these scalers, we should not expect to see an improvement from the width corrections. The counter argument to this is that the premise of the width correction is built on a prediction about how scalers with a vertex cut should behave. But these are precisely the scalers that we now know are not properly rate corrected...yet. The width effect implicitly predicts that  $ZDC/BBC$ , with no vertex cut, should be constant versus crossing when it is manifestly not so. However, what is not predicted to be constant crossing to crossing is the collision rate itself.

In Figure 8.8 we showed the measurement of the asymmetry between the two luminosity monitors,  $A_{LL}^{ZDC/BBC}$ , before any corrections and after just a width correction. It seems clear that applying a rate correction in the  $\sqrt{s} = 200$  GeV is a promising avenue to reduce the false asymmetry and achieve an improved  $\chi^2/NDF$  without increasing the fill-by-fill uncertainties or using ad hoc universal corrections. In Figure 8.19 a clear improvement is seen in  $A_{LL}^{ZDC/BBC}$  when the pileup corrections are applied at  $\sqrt{s} = 500$  GeV. The results

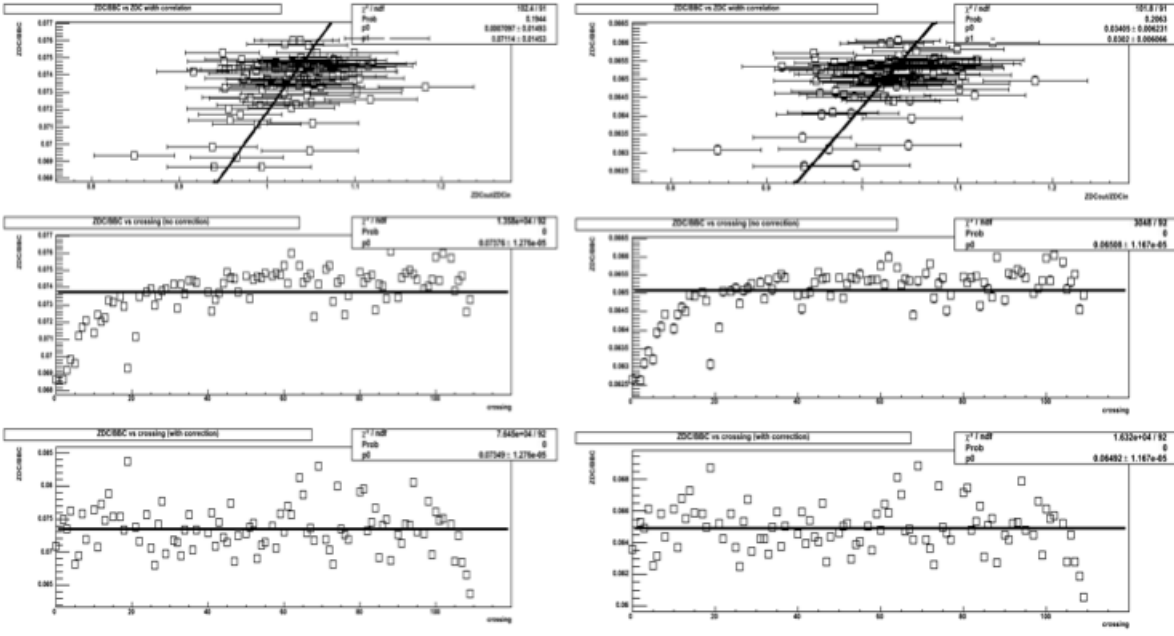


Figure 8.18: Left Column: Width correlation (top),  $\frac{ZDC}{BBC}$  uncorrected (middle), and  $\frac{ZDC}{BBC}$  corrected (bottom). Right Column: The same three plots but the width correlation and correction are now applied to pileup corrected rates.

Table 8.7: Results of  $A_{LL}^{ZDC/BBC}$  before and after pileup corrections.

Correction	$A_{LL}^{ZDC/BBC}$	$\chi^2/NDF$
None	$(8.96 \pm 0.50) \times 10^{-4}$	90
Pileup	$(2.92 \pm 0.52) \times 10^{-4}$	18

are summarized in Table 8.7. The run by run asymmetries here are taken from fits like the one in Fig. 8.18. When these run by run values are fit to a constant, we do not first scale up the individual asymmetry uncertainties by the  $\sqrt{\chi^2/NDF}$  value of the fit constant across crossings. The large  $\chi^2$  seen in the final result is largely due to this. We could trivially reduce the final  $\chi^2$  by increasing the statistical error bars, but then this would get confounded with the improvement due to just rate corrections.

## 8.11 Full BBC Simulations

We have demonstrated that applying pileup corrections does improve the situation. At the same time, we have demonstrated that luminosity miscounting in both detectors can and does lead to systematic errors in the relative luminosity. It is of course possible that the  $ZDC/BBC$  asymmetry seen after pileup corrections is a true physics asymmetry. However, we should be skeptical of this conclusion at this point because we

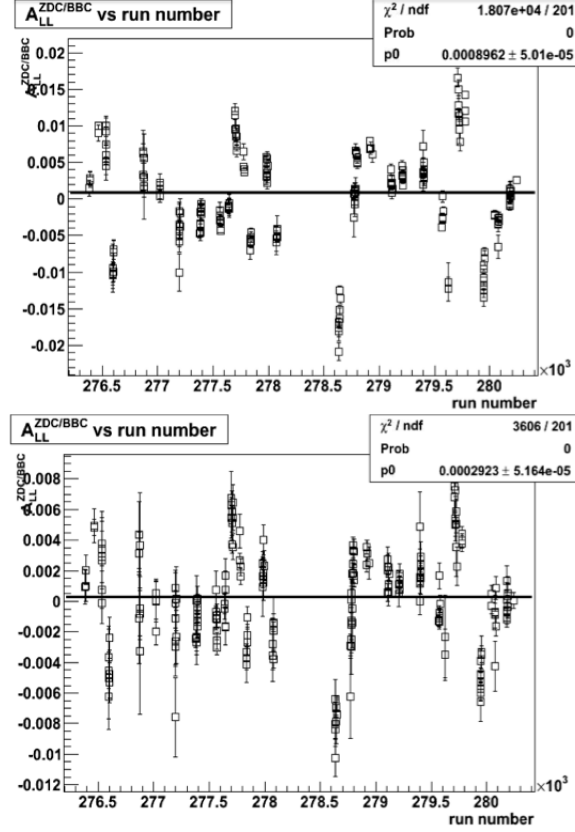


Figure 8.19: Top (a):  $A_{LL}^{ZDC/BBC}$  for the Run09  $\sqrt{s} = 500$  GeV data with no corrections applied to the scalers. Bottom (b): The same asymmetry for the Run09  $\sqrt{s} = 500$  GeV data with pileup corrections (and no width corrections) applied to the scalers.

know that applying pileup corrections to luminosity scalers with a vertex cut is not the correct thing to do, and therefore these scalers are still not precisely proportional to the true luminosity. Accounting for this analytically is not feasible at the moment, so we make a digression into the details of a full simulation of the BBC in hopes of understanding how the longitudinal and transverse beam profile, vertex width, detector resolution, trigger design, trigger vertex cut requirement, pileup effects, etc. interact with one another. This framework ultimately allows one to input a large number of known parameters and reproduce the observed crossing to crossing scatter in the  $ZDC/BBC$  ratio. In the context of simulations, this has the potential to allow a full study of exactly how badly the ZDC and BBC mismeasure the luminosity under very controlled circumstances.

### 8.11.1 Description of Simulations

The basic idea of the simulations is to consider the question: “Does the BBC coincidence trigger for this crossing?”. This is very similar to, but also quite different from the question we have essentially been asking up to now: “Should the BBC coincidence trigger fire for this collision?”. We are motivated to ask this first question by Eq. 8.28, where a complicated probability distribution requiring input from several sources is necessary. Under experimental conditions, we can truly only ever answer the first question and to do so requires several steps.

The first step is to generate  $N (= 10^6)$   $pp$  events at  $\sqrt{s} = 500$  GeV. We use the PYTHIAv6.4 event generator with Tune A ([122]). The configuration used is shown in Table 8.8.

Table 8.8: PYTHIA configuration details

Parameter	Value
roots	500
proj	p
targ	p
frame	cms
msel	2

We should note that due to technical issues with the ZDC reconstruction, along with the fact that diffractive physics is not reliably simulated we focus on the BBC. It is still possible to do less intricate ZDC simulations bootstrapping from real data and these BBC simulations. After each event is generated it is assigned a random  $(t_0, z)$  within the PHENIX coordinate system. The distribution of generated events is flat over the rectangle  $|z| < 100$  cm  $\times |t_0| < 10$  ns. The outgoing particles from these collisions are passed through GEANT ([123],[124]), a program that simulates the passage of particles through detector matter. The PHENIX Integrated Simulation Application (PISA) program is based on GEANT libraries and includes models specifically of the PHENIX detectors ([125]). The output of PISA is a list of detector hits. Typically the simulation procedure ends with outputting a simulated data file (*simDST*). However, we want to simulate crossings with multiple collisions. To do this, we imagine “crossings” instead of “collisions” and combine each of the  $N$  collisions into pairs. This yields the PHENIX, in particular the BBC, response to a crossing with two collisions, and we end up with  $\frac{N}{2}$  such crossings. In the same way we combine three collisions at a time to get a sample of  $\frac{N}{3}$  such crossings and four collisions at a time to get a sample of  $\frac{N}{4}$  such crossings. The collisions are combined into effective crossings with multiple collisions using code in the PHENIX CVS at `offline/analysis/nana/BbcJoinEvents`. This class stores  $k$  events and adds the ADC

above pedestal for each BBC PMT and takes the lowest TDC value. This way, when the PISA output is translated to the *simDST* the hit information from all collisions is included. In each of these samples of  $N$  crossings we are essentially sampling the probability space of  $\prod_{i=0}^k (t_{0,i}, z_i)$ . Calculating this space will be done shortly using Wall Current Monitor (WCM) data. In real data of course we do not know the true  $(t_{0,i}, z_i)$  but this is recorded in the *simDST* via the *OrigVtxT0Container* class. For purposes of the simulation we neglect crossings with more than four collisions based on Eq. 8.18. Crossings with five collisions occur at a relative rate to crossings with one collision of  $P(5, \mu)/P(1, \mu) = \mu^4/120$ . For even this highest collision rates achieved in Run09,  $\mu \sim 0.35$ , this translates into  $1.2 \times 10^{-4}$ . The fraction of all crossings in which five collisions occurs is  $3 \times 10^{-5}$ . Even in later years such as 2013, this is still a good approximation. If  $\mu \sim 1$ , this fraction is still  $3 \times 10^{-3}$ .

We now have a sample of crossings, which can be combined in specified ratios to correspond to a desired beam rate. However, all crossings with  $k$  collisions have not been created equally. The  $(t_0, z)$  pairs require that each crossing get an associated weighting based on the probability for  $(t_0, z)$  to occur in reality. It is not the flat probability distribution they have been generated based on. Second, we need to evaluate each crossing to determine whether the *BBCLL1* trigger is fired. This requires developing, testing, and using a trigger emulator.

### 8.11.2 Simulation Weighting

The paradigm of trying to understand the true rate of collisions causing a coincidence,  $\mu\epsilon_{NS}$ , has now changed.  $\epsilon_{NS}$  is something that we associate with a *collision*. It is the fraction (or efficiency in one prefers) of collisions to produce hits in both arms of the BBC. In the new paradigm *crossings* are the subject of our focus. Accordingly, we define the quantity  $f_i$  as the fraction of all crossings, in which  $i$  collisions occur, that result in a *BBCLL1* trigger. We now write down the following decomposition of the observed *BBCLL1* rate:

$$R_{BBCLL1}^{obs} = \frac{N_{BBCLL1}}{N_{CLOCK}} = \sum_{icoll=1}^4 \frac{N_{icoll,BBCLL1}}{N_{icoll}} \times \frac{N_{icoll}}{N_{CLOCK}} \quad (8.29)$$

There is nothing special about the *BBCLL1* trigger here and this decomposition could be done for any other trigger. The first term in the summation is precisely the definition of  $f_i$ . The second term is the probability to have  $icoll$  collisions in a crossing and can be read off from the poisson distribution. The poisson term of course depends only on the rate while the  $f_i$  depends on the details of the  $(t_0, z)$  distribution. This distribution can be most reliably obtained from the Wall Current Monitor data. Therefore, if we know the  $f_i$ 's reliably from our simulation, we can then plug in  $R_{BBCLL1}^{obs}$  from the GL1P scalers and numerically solve

for the true beam rate  $\mu$ . Writing Eq. 8.29 out explicitly, we have the main identity which we can use to solve for the true beam rate:

$$\frac{N_{BBCLL1}}{N_{CLOCK}} = f_1\mu e^{-\mu} + \frac{1}{2}f_2\mu^2 e^{-\mu} + \frac{1}{6}f_3\mu^3 e^{-\mu} + \frac{1}{24}f_4\mu^4 e^{-\mu} \quad (8.30)$$

Now the goal is to use the simulations to determine  $f_i$ . We also mention that the issue of livetime can crop up again on the left hand side. As mentioned before, the GL1P scaler counts come from live triggers only. So if the livetime of the BBC and CLOCK triggers differ, the incorrect ratio will propagate through to an incorrectly determined rate. This applies also to Eq. 8.25, so it always has to be considered. In Run09 this is not possible but, as before, based on studies such as in Fig. 8.4 this effect does not seem to be systematically present based on studies of later runs.

### 8.11.3 Wall Current Monitor Data

The Wall Current Monitor (WCM) system ([126]) is a system of detectors located at various points around the RHIC ring and throughout other parts of the injection and acceleration phases. Its purpose is to monitor the beam intensity and serves quite a few functions. The function we are most interested in is being able to know the longitudinal profile of each bunch in both beams. Every  $\sim 5$  minutes a  $\sim 120\mu\text{s}$  sampling of the RHIC ring is taken. This corresponds to the time a proton takes to make one full revolution around the ring. During this sampling time, the beam intensity is recorded every 0.05 ns and a longitudinal profile of the beam intensity vs. position is obtained. An example of this is shown in Figure 8.20. This figure represents a snapshot in time of the longitudinal profiles of the beams right as they approach each other in PHENIX. The blue beam is moving to the right and the yellow beam is moving to the left. As this data is not collision based, it gives us a very unbiased picture of the bunch structure. By passing the beams through each other in steps of  $dt = 0.025$  ns, and assuming that the number of  $pp$  interactions at each corresponding  $(t_0, z)$  point is proportional to the product of the intensities of the two beams at the intersecting points, we can build up a predicted probability distribution,  $P(t_0, z)$ , for collisions. For instance, if we define  $t = 0$  when the bunches are as seen in Fig. 8.20 right before they begin to pass through each other, then the  $i$ -th sampling of the yellow bunch has initial position  $z_y(t = 0) = icdt$  cm and in general the  $z$  position of the  $i$ -th sampling in the yellow beam as a function of time is given by  $z_{i,y}(t) = icdt - ct$ . For the blue bunch, the  $z$  position of the  $j$ -th sampling is given by  $z_{j,b}(t) = -jcdt + ct$ . Then using Eqs. 8.8 and 8.9 we find that when the  $i$ -th sample of the yellow beam passes through the  $j$ -th sample of the blue beam, this corresponds

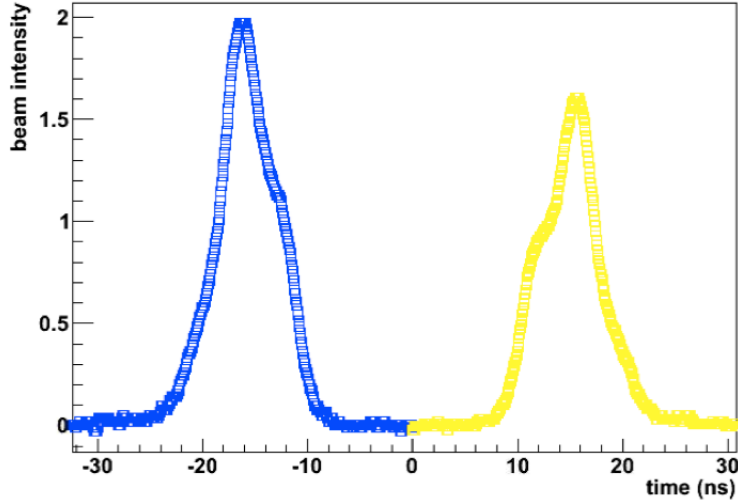


Figure 8.20: The WCM measurement of the longitudinal beam profile for the blue and yellow beams are shown. The x-axis has units of ns and the typical length of a bunch can be seen to be  $\sim 3$ m. The profiles have a similar shape but the blue beam bunch can be seen to have  $\sim 30\%$  more protons, based on its amplitude, than the yellow beam bunch. The units of the y-axis are essentially arbitrary.

to:

$$t_0 = \frac{1}{2}(i + j)dt, z = \frac{c}{2}(i - j)dt \quad (8.31)$$

$t_0 = \text{const}$  lines have negative slope while  $z = \text{const}$  lines have positive slope. Combined, they give the characteristic diamond shape for the boundaries of the  $t_0, z$  phase space within which collisions can occur. Within this diamond,  $P(t_0, z)$  is determined by the details of the bunch structure. Two additional considerations are the transverse size of the beam as a function of  $z$  ([114]) and beam-beam coulomb interactions ([117]). The latter occurs due to electromagnetic repulsion of the ions within a bunch or of a bunch in the opposite beam as they pass through each other, causing the beam to have a larger transverse size and lower transverse number density. These effects are assumed to be small and in our approximation we do not account for this. The former is called the hourglass effect which describes the transverse size of a bunch as a function of  $z$  due to focusing of the magnets. As the protons pass through the center of PHENIX at  $z = 0$  they are squeezed to a minimal transverse size. At large  $|z|$  the transverse size expands. A “tubular” beam

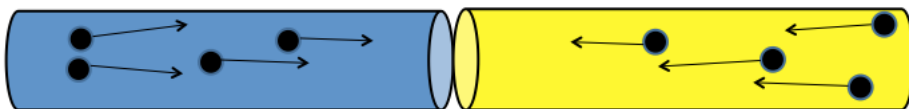


Figure 8.21: A side view sketch of the blue and yellow beams heading towards each other if their cross sectional areas were independent of  $z$ .

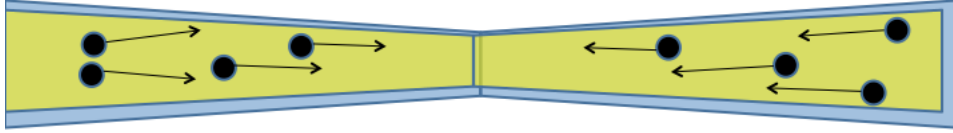


Figure 8.22: A semi-realistic side view sketch of the blue and yellow beams intersecting showing how they are each squeezed near  $z = 0$  and expand in the transverse direction as they leave the PHENIX IR.

with no hourglass shape is shown in Figure 8.21. In this case we could take the collision probability as

$$P(t_0, z) \propto I_{i,y} I_{j,b} \quad (8.32)$$

$I_{i,y}$  is the intensity of the yellow bunch at sample  $i$  and  $I_{j,b}$  is the intensity of the blue bunch at sample  $j$ . Figure 8.22 shows approximately what the beams look like with the hourglass effect present. With no hourglass,  $\frac{dI}{dz} = 0$  and with the hourglass  $\frac{dI}{d|z|} < 0$ . This has the qualitative effect of enhancing the probability of collisions near  $z = 0$  with respect to collisions at large  $z$ . The additional weight applied comes from using the approximation that the width of the beam along the  $x$ -axis, as a function of  $z$  is given by:

$$\sigma_x^*(z) = \sigma_x(z = 0) \sqrt{1 + \left(\frac{z}{\beta_x^*}\right)^2} \quad (8.33)$$

$\beta^*$  is the parameter that describes how “non-tubular” or, equivalently, how “squeezed” the beams are and  $\sigma_x(z = 0)$  is the width of the beam in the  $x$  direction at  $z = 0$ . A smaller value of  $\beta^*$  corresponds to more squeezing and is typically what the PHENIX and STAR experiments request of the accelerator operators to maximize the recorded luminosity within a narrow range of  $z$ . But we digress. Eq. 8.33 is applicable to both the  $x$  and  $y$  transverse directions of both the blue and yellow beams. Accordingly, we modify Eq. 8.32 to:

$$P(t_0, z) \propto \frac{I_{i,y} I_{j,b}}{\sqrt{1 + \left(\frac{z}{\beta_{y,x}^*}\right)^2} \sqrt{1 + \left(\frac{z}{\beta_{y,y}^*}\right)^2} \sqrt{1 + \left(\frac{z}{\beta_{b,x}^*}\right)^2} \sqrt{1 + \left(\frac{z}{\beta_{b,y}^*}\right)^2}} \quad (8.34)$$

Based on Ref. [114] we take  $\beta_{y,x}^* = \beta_{y,y}^* = \beta_{b,x}^* = \beta_{b,y}^* = \beta^* = 70\text{ cm}$ , even though we find better agreement assuming  $\beta^* \sim 95\text{ cm}$ . We assume the discrepancy comes from the fact that the beam has a more complicated shape than is encapsulated in this approximation. So the weight we use to determine the unbiased distribution of collisions is:

$$P(t_0, z) \propto \frac{I_{i,y} I_{j,b}}{\left[1 + \left(\frac{z}{\beta^*}\right)^2\right]^2} \quad (8.35)$$

Figure 8.23 shows the comparison of  $P_{data}(t_0, z)$  as generated from the WCM as we have described,  $P_{sim}(t_0, z)$ .

Based on this, every simulated collision must have a weight applied to it of:

$$w_{sim}(t_0, z) = \frac{P_{data}(t_0, z)}{P_{sim}(t_0, z)} \quad (8.36)$$

A check of the weighting scheme can be done by comparing the predicted  $t_0$  and  $z$  distributions based on

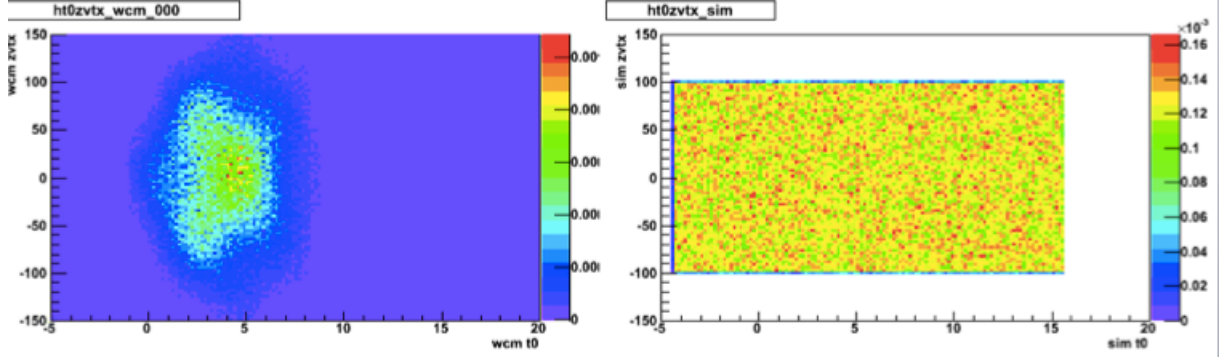


Figure 8.23: Left (a): The unbiased collision probability distribution  $P_{data}(t_0, z)$  is generated based on WCM data. Right (b): A flat distribution,  $P_{sim}(t_0, z)$ , is used to generate the simulations.

using the WCM weights applied to the simulation with the distributions actually found from data. These two distributions are independent of one another. The comparison is shown in Figure 8.24. In order to

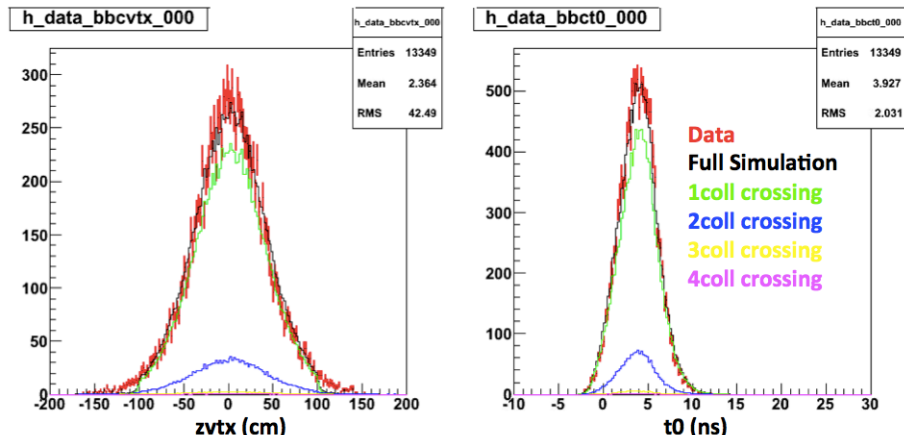


Figure 8.24: Left (a): Comparison of predicted  $z$  from the WCM data (black) and the realized  $z$  distribution from *CLOCK* data. A beam rate of  $\mu = 0.2$  is assumed which is approximately correct. The green, blue, yellow and magenta plots show the decomposition of the full simulated  $z$  spectrum into crossings where one, two, three and four collisions, respectively, occurred. Right (b): The comparison of the  $t_0$  spectra are shown with a similar decomposition.

weight each collision appropriately three things must be considered:

- The relative number of crossings simulated for each number of collisions per crossing, call them  $N_1$ ,  $N_2$ ,  $N_3$  and  $N_4$ .
- For each collision generated, regardless of the other collisions in a crossing, the weight from Eq. 8.36 is applied.
- According to the beam rate, all crossings containing a specified number of collisions get a poisson weighting.

Based on these considerations, the proper crossing weightings that should be applied are:

$$\begin{aligned} w_{crossing}(1) &= w_{sim}(t_0, z) \\ w_{crossing}(2) &= \frac{1}{2} \mu \frac{N_1}{N_2} w_{sim}(t_{0a}, z_a) w_{sim}(t_{0b}, z_b) \\ w_{crossing}(3) &= \frac{1}{6} \mu^2 \frac{N_1}{N_3} w_{sim}(t_{0a}, z_a) w_{sim}(t_{0b}, z_b) w_{sim}(t_{0c}, z_c) \\ w_{crossing}(4) &= \frac{1}{24} \mu^3 \frac{N_1}{N_4} w_{sim}(t_{0a}, z_a) w_{sim}(t_{0b}, z_b) w_{sim}(t_{0c}, z_c) w_{sim}(t_{0d}, z_d) \end{aligned} \quad (8.37)$$

With the appropriate crossing weightings, we can now use the simulations to properly determine the  $f_i$ . To do this, we define *isBBC* which takes a value of either 0 or 1 if a crossing results in the *BBCLL1* trigger not firing or firing, respectively. The  $f_i$  are then given by the following weighted averages:

$$\begin{aligned} f_1 &= \frac{\sum_{1\,coll} w_A(isBBC)}{\sum_{1\,coll} w_A} \\ f_2 &= \frac{\sum_{2\,coll} w_A w_B(isBBC)}{\sum_{2\,coll} w_A w_B} \\ f_3 &= \frac{\sum_{3\,coll} w_A w_B w_C(isBBC)}{\sum_{3\,coll} w_A w_B w_C} \\ f_4 &= \frac{\sum_{4\,coll} w_A w_B w_C w_D(isBBC)}{\sum_{4\,coll} w_A w_B w_C w_D} \end{aligned} \quad (8.38)$$

The sum for  $f_i$  is taken over crossings with  $i$  collisions, and *isBBC* is weighted by the product of the individual collision weights where  $w_{sim}(t_{0a}, z_a)$  is shortened to  $w_A$ , etc. The remaining ingredient to determine the  $f_i$ 's is to determine *isBBC*.

#### 8.11.4 BBC and ZDC Trigger Emulation

To determine *isBBC* we need a way to determine if a simulated crossing fires the *BBCLL1* trigger or not. This requires making a trigger emulator that faithfully replicates the output of the online trigger hardware.

Fortunately, the *BBCLL1* (and *ZDCLL1*) triggers are digitally based and use just their respective TDC values as inputs. So we use the following steps:

- Understand the online trigger algorithm.
- Emulate the algorithm in offline code.
- Test the emulator on events from real data where the online trigger decision is known to confirm agreement.
- Apply the emulator to simulated data to get the simulated trigger decision output *isBBC*.

The *BBCLL1* trigger algorithm operates on the TDC values<sup>3</sup> of each of the 128 PMT's and goes as follows (it is a very simple operation):

- For the 64 TDC values in the south(north) arm, remove the least significant bit (LSB). The 12 bit input is now 11 bits and ranges from 0 – 2047. This is called the Lookup Table Address (LUTaddr).
- A lookup table provides a mapping:  $(PMT, LUTaddr) \xrightarrow{LUTmap} LUT$ . The Lookup Table Map (LUTmap) is a map from all possible  $128 \times 2048$  TDC1 values to a predetermined 8 bit value 0 – 255 which we call LUT. The LUTmap is determined based on rapid PMT calibrations at the beginning of the running period and sometimes periodically thereafter. This value is set to 0 if the TDC is an underflow or overflow value indicating the PMT was not hit. Hot channels are also masked out.
- For the south arm PMT's, all non-zero LUT values are averaged to get  $t_{S,LL1}$ . The same is done in the north to get  $t_{N,LL1}$ .
- Apply a hard cut to the difference  $z_{LL1} = t_{S,LL1} - t_{N,LL1}$ . For a novertex trigger, no cut is applied and the only requirement is that the LL1 finds at least one non-zero LUT value in each arm.

To check that we have implemented the algorithm exactly right in offline code we try it out on real data where we can get the true *BBCLL1* trigger decision from the trigger bit in the *TrigLvl1* data node. Figure 8.25 shows the result of this check. The idea is to run over a large sample of minbias events and compute  $z_{LL1}$  for each event. Then take the subset of these events for which the *BBCLL1* triggered and plot these values separately. For the events where *BBCLL1* fired, we should find a hard cutoff on  $|z_{LL1}|$ . We do in fact see this cutoff and confirm that for  $|z_{LL1}| < 25$  the trigger fires while otherwise it does not.

---

<sup>3</sup>The PMT output for each BBC channel is split three ways: one for the ADC calculation, and two TDC determinations, TDC0 and TDC1. The trigger receives input from the TDC1. For the emulator testing on real data we use TDC1 value, but the TDC1 in the simulated BBC reconstruction module was not quite right. Instead the TDC0 was used. The difference between using TDC0 vs TDC1 produces a negligible impact on the *isBBC* decision.

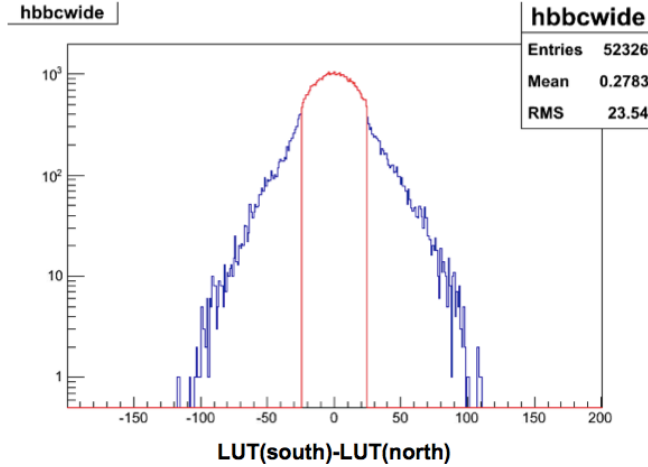


Figure 8.25: Confirmation of the fidelity of the *BBCLL1* trigger emulator is demonstrated. The blue histogram shows the distribution of  $z_{LL1}$  for a minimum bias sampling of events. In red, we take the subset of these events where the *BBCLL1* trigger fired. The hard cutoff seen proves that we can now use this emulator to make a faithful trigger decision on simulated events.

All of the discussion we have had in this section can also apply to the ZDC trigger as well. We can repeat these same steps for the ZDC to confirm we understand the *ZDCLL1* operation. The algorithm is actually even easier since the trigger input is just a single TDC. The same signal splitting as in the BBC is used here meaning we process TDC1 values. The three ZDC modules each output their own signal but for input to the trigger, the fan-out (essentially the sum) of these signals is used. This 12 bit value is stripped of its LSB to get an 11 bit value. A ZDC Lookup Table (now essentially just a  $2 \times 2048$  table) maps both values to an 8 bit LUT value and, once again,  $z_{LL1}$  is computed. As seen in Figure 8.26 the trigger algorithm is confirmed and the hard cutoff is  $|z_{LL1}| < 10$ .

### 8.11.5 Method of ZDC Simulation

We take a quick aside to discuss a proposed method of simulating ZDC events by bootstrapping off of the BBC simulations we have. As mentioned before, the diffractive physics sampled by the ZDC is not modeled well by simulations so the PYTHIA→PISA →simDST method to generate BBC events cannot be applied here. Instead, we use the procedure outlined in Fig. 8.27. The proposed procedure starts by generating collisions according to the probability distribution  $P(t_0, z)$  derived from the WCM data. To generate a crossing with  $N$  collisions we simply pick  $N$  such pairs. From this, we can determine what the travel time to the ZDC is and smear it by the known ZDC timing resolution. The ZDC calibrations turn raw TDC counts into times (Ref.[127] or the calibration code in PHENIX CVS at `offline/packages/zdc`, for example).

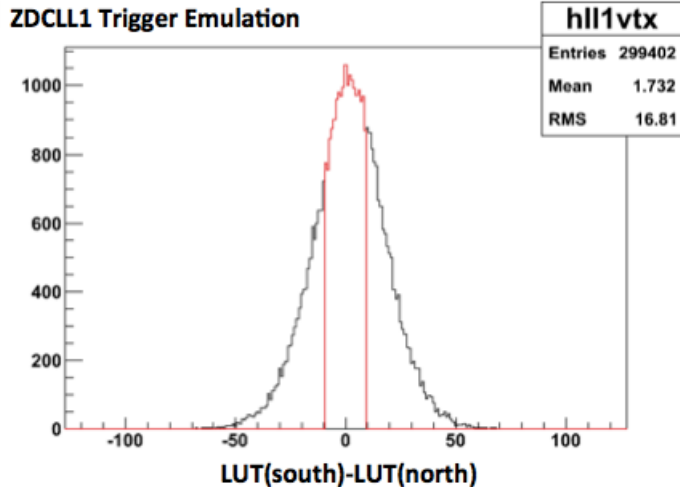


Figure 8.26: Confirmation of the *ZDCLL1* trigger algorithm is done the same way as for the BBC. The black plot shows the  $z_{LL1}$  distribution for minimum bias events while the red plot shows the  $z_{LL1}$  distribution only for events where the online *ZDCLL1* trigger fired.

Therefore, if we have the expected ZDC hit time we can pull the required ZDC calibration constants from the required databases and apply the calibrations in reverse, starting with a time and ending with a TDC1 value. These TDC1 values can then be fed into the *ZDCLL1* trigger emulator to make a trigger decision.

The main issue that must be taken into account is whether the ZDC actually sees a hit or not. If both ZDC arms see a hit then the trigger decision holds. However, we need to know the probabilities for a collision to produce a single sided hit, coincidence hit or no hit. If the collision does not produce a coincidence, then the trigger decision is automatically false. Because the ZDC is very far away from the vertex ( $\sim 18\text{m}$ ) and has such a small acceptance we assume the probabilities are independent of  $z$  and Table 8.6 is handy to use. However, as we see in Figure 8.28,  $k_{N,S}$  for the BBC is vertex dependent. Because the ADC pedestal in the ZDC happens to also be very close to the trigger threshold, we must rely on the ZDC TDC0 to determine whether the ZDC was hit.<sup>4</sup> Based on knowledge of  $P(0) = \epsilon_0$ ,  $P(n) = \epsilon_N$ ,  $P(s) = \epsilon_S$ , and  $P(ns) = \epsilon_{NS}$ , determined from the TDC0 in *CLOCK* data, we can then randomly assign one of these possibilities to each collision and consider the trigger emulator decision only in the case of a coincidence. In a crossing with more than one collision, a random outcome is picked for each collision and a coincidence could come from two single sided events. If one arm sees a hit from two or more collisions, the collision producing the earliest TDC

<sup>4</sup> This works because the ADC integration gate is only opened by the TDC. If the TDC did not open the gate, we know the ADC value is a pedestal. If the gate did open we know we are looking at the integrated signal amplitude and not a pedestal. Thus, the TDC must be used to discern a ZDC hit from no hit.

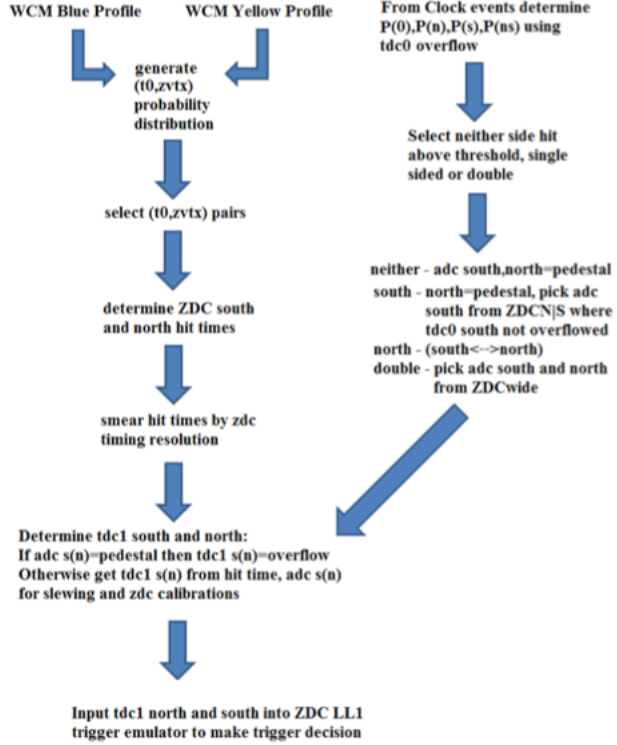


Figure 8.27: A summary of the proposed outline to simulate the ZDC response to multiple collision crossings.

count is used as input to the  $ZDCLL1$  emulator.<sup>5</sup> The concern that one comes back to is why the  $\frac{ZDC}{BBC}$  ratio is not constant across different bunches. This would give every bunch different probabilities of  $\epsilon_0$ ,  $\epsilon_N$ ,  $\epsilon_S$ , and  $\epsilon_{NS}$ . There are bunch to bunch fluctuations in the longitudinal profiles, as seen in Figure 8.29 where the longitudinal profile from the WCM for four bunches are overlaid. These fluctuations might combine with the  $z$  dependent BBC efficiencies to produce slightly different  $z$  averaged values for the detection efficiencies. However, the sheer size,  $\sim 10\%$  in  $\sqrt{s} = 500$  GeV, of the variations is far too big for this to be the cause.<sup>6</sup>

### 8.11.6 Comparison of Data and Simulation

While the ZDC simulations based on PYTHIA would not be reliable, we would like to show that the BBC simulations are reliable. We do so by comparing the charge spectrum seen by the BBC in simulations with data. This is shown in Figure 8.24 and uses the full crossing weightings from Eq. 8.37. In addition to comparing the full simulation with the data, it is also interesting to look at the contributions to this spectrum

<sup>5</sup>Note this difference between the ZDC and BBC triggers: the ZDC uses the earliest hit time approach while the BBC uses the average hit time approach.

<sup>6</sup>In a moment of candor, the author would like to note that a thought very similar to this is what prompted further direct studies of what the real source of the  $\frac{ZDC}{BBC}$  variation was. This caused much hesitation in implementing this ZDC simulation procedure because the changing detector efficiencies had to be known far more precisely for this method to work than had been possible.

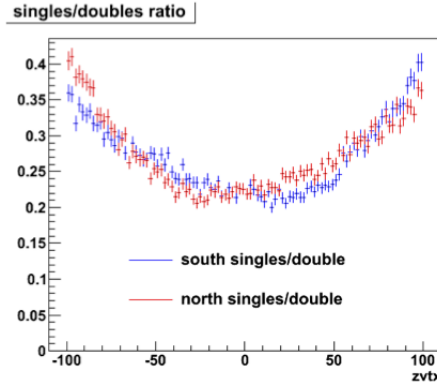


Figure 8.28: From the full BBC simulations we show the BBC  $k_{N,S}$ , which have a clear dependence on  $z$ . This is due to the changing acceptance of the BBC as seen from collisions at different  $z$ . The ZDC acceptance is largely independent of where the collision occurs.

from crossings with one, two, three, and four collisions separately. Note that the effect of multiple collisions on this spectrum is demonstrated. If no crossings had more than one collision the red spectrum from data would fall off slightly faster and match the green spectrum from single collision crossings. Instead, the data points lie above this and match the black spectrum better. The contribution of two collision crossings is necessary.

### 8.11.7 Vertex Width Dependence on Beam Rate

The BBC vertex distribution is also known to be a function of the beam rate. With these simulations segmented into crossings with different numbers of collisions, we can produce the vertex distribution for each segment separately, as was done in Fig. 8.24. Then we apply a poisson weight,  $P(i,\mu)$ , to the vertex distribution for  $i$  collisions and sum. In Figure 8.31 we show the result of doing this. In this plot  $BBCout$  is defined as the number of counts with  $30\text{ cm} < |z_{BBC}| < 150\text{ cm}$  and  $BBCin$  is the number of counts with  $|z_{BBC}| < 30\text{ cm}$ . This shows that rate and width are not independent and enhances the idea that the pileup corrections, due to rate, really need to be scaled with no vertex cut to be done properly.

Another interesting consequence of this is what it means for the applicability of the width corrections. We showed that although a width correction can frequently be found in the data, at the beam rates in Run06 and Run09 at  $\sqrt{s} = 200\text{ GeV}$  and Run09 at  $\sqrt{s} = 500\text{ GeV}$  (more severely in the latter) this correlation fails to account for the  $\frac{ZDC}{BBC}$  variation or the clearly false, and very large, asymmetry that is present. From Eq. 8.6, we expect a splitting in the true observed rate in the presence of a real asymmetry,  $A$ . In fact, the expected counting rate for an ‘‘S’’ crossing is  $\mathcal{R}_{++} = \mathcal{R}_{true}(1 + A)$  and for an ‘‘O’’ crossing it

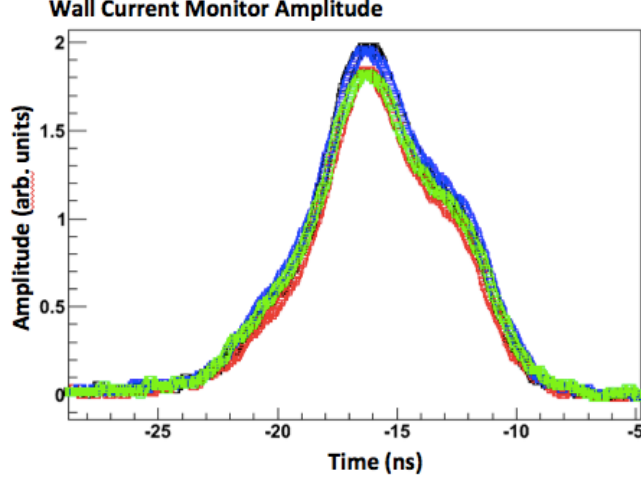


Figure 8.29: WCM bunch profiles for four different bunches. The shapes are similar, but not identical, to one another.

is  $\mathcal{R}_{+-} = \mathcal{R}_{true}(1 - A)$ . This increased(decreased) rate causes an increased(decreased) vertex distribution width. Therefore the width proxies  $ZDCout/ZDCin$  and  $BBCout/BBCin$  are affected by the presence of a true  $A_{LL}^{ZDC/BBC}$ . Also, of course, the premise of the width correction is that  $\frac{ZDC}{BBC}$  is affected by the width, but it is also affected by a possible asymmetry. Even though the longitudinal profiles can explain a good amount of the width variation, it is not the only factor involved. Thus, both axes of the width correlation,  $\frac{ZDC}{BBC}$  and  $\frac{ZDCout}{ZDCin}$ , are affected by an  $A_{LL}$ . Therefore, even if one still believes the width correction is actually improving the systematic variation, there is still the risk that a true asymmetry gets masked out. At the very least, the width correction is interacting with an  $A_{LL}$  in a way that is not understood. This could of course be studied using the simulation framework we have set up.

### 8.11.8 Determining the True Beam Rate

We have gleaned substantial insight up to now from the width correction, the rate correction and the simulations. We now know that the rate and width corrections are in fact not independent. In fact, this realization, along with the known issue of applying pileup corrections to coincidence scalers with a vertex cut, formed much of the impetus to look to simulations for an answer. The last topic we will mention, before moving to greener pastures, is the determination of the  $f_i$  and the extraction of  $\mu$ . Knowing  $\mu$ , independent of detection efficiencies, for each crossing immediately allows one to determine the (relative) luminosity since

$$L_i = \mu_i N_{CLOCK,i} \quad (8.39)$$

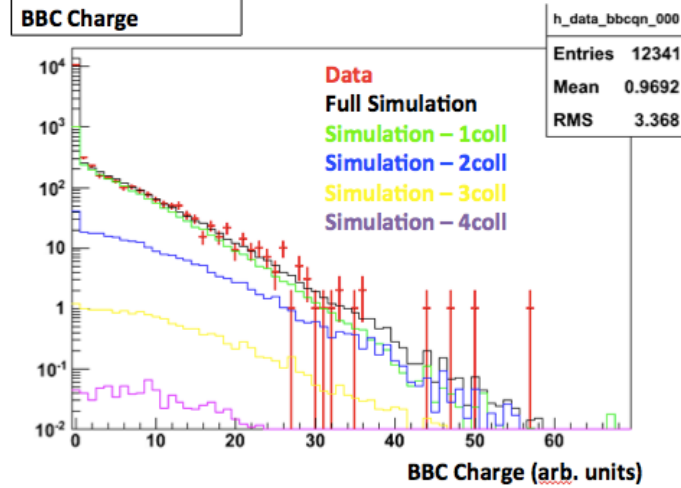


Figure 8.30: Comparison of the BBC North Chargesum from data and simulations. Good agreement is demonstrated and the effect of multiple collisions can be seen in the spectrum. The spectrum from data agrees better with simulations when multiple collisions are considered than when just one collision is possible.

$L_i$  is the total number of collisions occurring in crossing  $i$ ,  $\mu_i$  is the mean collision rate for the crossing and  $N_{CLOCK,i}$  is the number of live  $CLOCK$  cycles. The GL1P scaler gives  $N_{CLOCK,i}$ . We then put all the pieces of the simulation framework together, Eqs. 8.29-8.38, to solve for  $\mu_i$ . As mentioned before there is some uncertainty in the appropriate value of  $\beta^*$  to use. There is perhaps a 10% experimental uncertainty in its measurement and there is also some tension between the measured value,  $\beta^* = 70\text{ cm}$ , and the value that gives the best agreement between the simulations and the data of  $\beta^* = 95\text{ cm}$ . Since this simulation was never intended to be a competing measurement of  $\beta^*$ , we defer to the officially quoted value. Therefore, in Figure 8.32 we show the simulation result for one bunch as a function of this  $\beta^*$  from 60cm to 80 cm. Using these values for  $f_i$  and the GL1P scalers as input, we calculate the value of  $\mu_i$  for a particular crossing versus  $\beta^*$ . These values are obtained numerically from Eq. 8.30 and shown in Figure 8.33. The  $f_i$  in general can be seen to decrease with  $\beta^*$ . Qualitatively, this can be understood because this is equivalent to spreading out the collision distribution. In the case of one collision crossings, for example, this simply means that less collisions are occurring within  $|z| < 30\text{ cm}$  so a smaller fraction of crossings/collisions will cause a trigger.  $f_1$  is also close to the expected value. We know that  $\sim 53\%$  of collisions cause a coincidence, and roughly 60% of those are within 30 cm, so we expect  $f_1 \sim 0.53 \times 0.6 \sim 0.32$ . The simulations confirm this. For increasing  $i$  the simulations show that  $f_i$  increases. The increasing ‘squiggliness’ of the  $f_i$  is due to increasing systematic uncertainty in their determination. This is essentially due to the fact that several samplings of the  $(t_0, z)$  distribution are taken. For  $f_1$  the sampling space is just  $(t_0, z)$ . But for  $f_2$  the sampling space is  $(t_0, z) \times (t_0, z)$ , etc. This increase in dimensionality of the phase space, combined with using just  $2.5 \times 10^5$

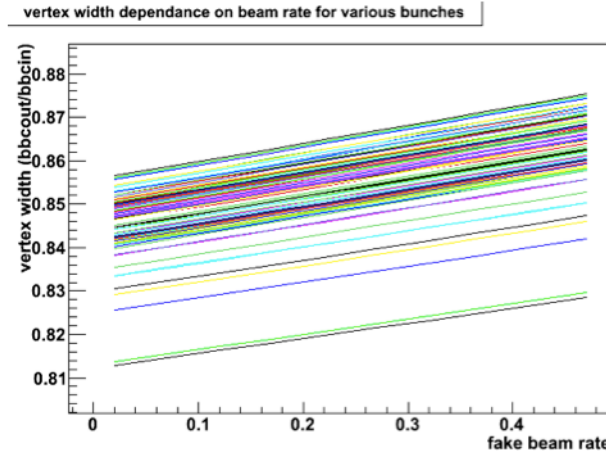


Figure 8.31: The BBC vertex width as a function of a fake beam rate,  $\mu$ , is shown for a number of different bunches. Due to the slightly different WCM profiles, each crossing has a slightly different 0-rate width, but all crossings show the same increasing behavior of width versus vertex.

simulated crossings for  $f_4$ , means we have a very sparse sampling of the full parameter space, especially compared with the sampling done in  $f_1$ . However, it can be shown pretty easily that crossings with four collisions at most any rate available in PHENIX play a nearly insignificant role. Here, it does not affect the determination of  $\mu$ . While more simulated events would make this more precise, it is not necessary. Extracting the beam rates in this way has given agreement in the relative luminosity determination at the  $O(10^{-4})$  level with the GL1P.

## 8.12 Concluding Remarks on Relative Luminosity Status

The relative luminosity uncertainties are quantified by measuring  $A_{LL}^{ZDC/BBC}$  over the course of a running period. The asymmetries, and hence the quoted systematic uncertainties in the relative luminosity, have grown consistently year over year, something a true asymmetry would not cause (See Table 8.3). Historically, there have been two methods employed, officially or unofficially, to correct for luminosity mismeasurements purported to occur in one or both of the standard luminosity detectors. These are width corrections and rate corrections.

In Run06 at  $\sqrt{s} = 200$  GeV, and Run09 at  $\sqrt{s} = 500$  GeV, applying pileup corrections reduced the measured  $A_{LL}^{ZDC/BBC}$  by factors of 1.7 and 3.0 respectively. So a large component of the fake  $A_{LL}$  is reduced. Additionally, the  $\chi^2/NDF$  of the fits improved. On a fill by fill basis, where one fits  $\frac{ZDC}{BBC}$  to a constant, improvement is clear. The fit of  $A_{LL}^{ZDC/BBC}$  vs. *fill* shows marked improvement as well. In Run06 the

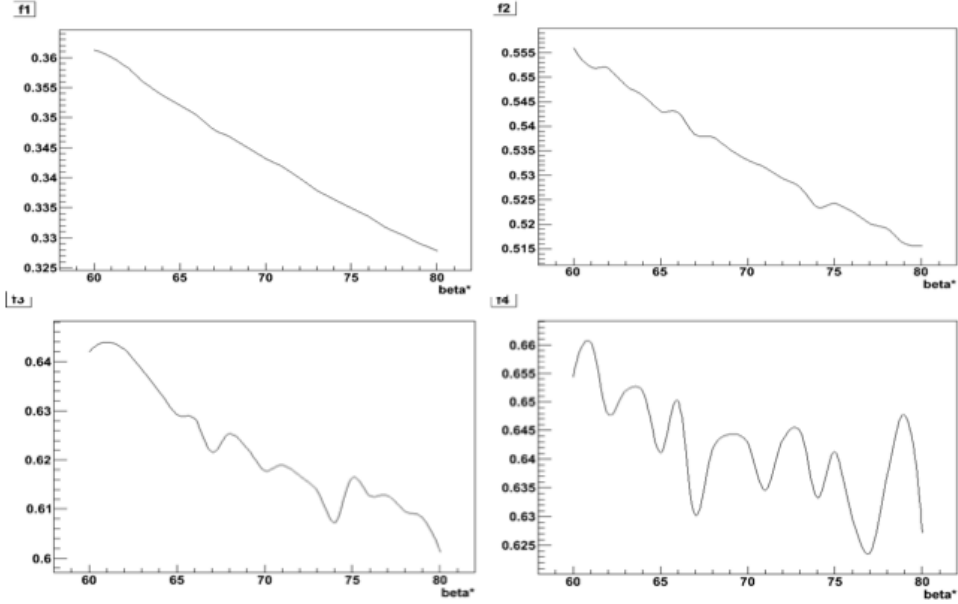


Figure 8.32: The behavior of  $f_1$  (top left),  $f_2$  (top right),  $f_3$  (bottom left), and  $f_4$  (bottom right) as a function of  $\beta^*$ .

improvement is by a factor of 3.5 while in Run09 the improvement is a factor of 5.0.

The performance of the width corrections, even in low (instantaneous and integrated) luminosity runs is questionable. In Run06,  $A_{LL}^{ZDC/BBC} = (6.85 \pm 0.56) \times 10^{-4}$  before the width correction and  $A_{LL}^{ZDC/BBC} = (6.47 \pm 0.64) \times 10^{-4}$  after the width correction. These numbers are completely statistically consistent, indicating that no systematic improvement can be attributed to applying the width correction. In Run09  $A_{LL}^{ZDC/BBC} = (11.55 \pm 0.64) \times 10^{-4}$  before the width correction while  $A_{LL}^{ZDC/BBC} = (11.79 \pm 1.36) \times 10^{-4}$ . Again, these asymmetries are statistically consistent and also consistent with the notion that the applying a width correction at any rate is unable to remove a fake asymmetry.

The apparent success of the width correction is that, even though the systematic asymmetry is not touched, at least the  $\chi^2$  is reduced. While true, this turns out to not be due to the effectiveness of the width correction, but rather its ineffectiveness. This is because when determining the width correlation parameters, the uncertainties in these parameters are propagated into the statistical uncertainties of the fill by fill  $A_{LL}^{ZDC/BBC}$  results. This is seen by comparing the uncertainty in the asymmetry determination before and after a width correction is applied. In Run06  $\delta A_{LL}$  increases by a factor of 1.14 and in Run09  $\delta A_{LL}$  increases by a factor of 2.13. Just due to this, the  $\chi^2$  in Run06 is expected to decrease by a factor of  $1.14^2 \sim 1.3$  and by  $2.13^2 \sim 4.53$

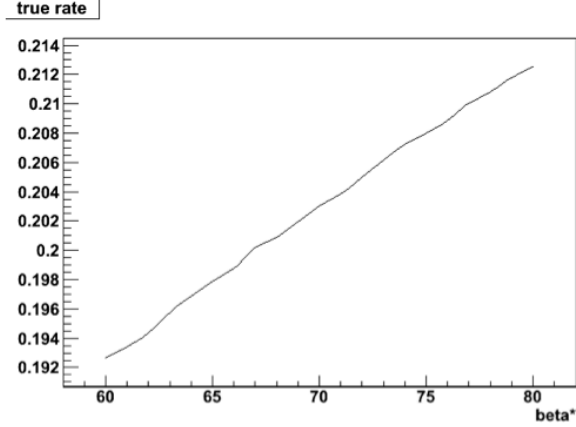


Figure 8.33: True beam rate,  $\mu$ , vs,  $\beta^*$  for one bunch crossing.

in Run09. Yet in Run06,  $\chi^2$  drops from 389 to 326, a factor of just 1.19. In Run09,  $\chi^2$  drops from 1475 to 334, a factor of 4.41. In neither case is this improvement even as good as just blindly increasing the statistical error bars and doing nothing else.

An attempt to use width corrections on the  $\sqrt{s} = 500$  GeV data was performed and found to make matters worse.

The nature of the width correction is also poorly understood and a number of questions remain. While theoretically it is clear that a width correlation should always exist, the data does not always show it. In some fills it is seen while in other fills a very weak correlation, if any at all, is seen. Due to this fact, a “universal” correction was used whereby fills with a weak correlation are explicitly ignored. But it is not understood why this is done. Further, even when the correlation is strong, the slope of the correlation varies by a factor of three. This is not understood. We showed an example where, within a single fill, the width correlation parameters depend on the helicity state of the two protons bunches. This is not understood, has not been studied and has not been replicated in simulations. Further, it is clear that both the ZDC and the BBC have a smearing, or resolution, associated with their vertex determination. Yet a width correction is only applied to the ZDC. While the BBC resolution is smaller by a factor of six, it is merely asserted that a BBC width correction is not necessary. A simulation study would be necessary to show how large the BBC correction factor should be. Another outstanding question is the behavior of  $A_{LL}^{ZDC/BBC}$  versus spin pattern. As we will show in the next chapter from the Run09  $\sqrt{s} = 500$  GeV data, a large difference is found. In Run06 and Run09  $\sqrt{s} = 200$  GeV this has not been checked, and the spin pattern dependence of

the effect of the width correction on  $A_{LL}$  is not understood.

In the next chapter we discuss the idea of the Residual Rate Correlation and its associated correction. The driving motivation for this is the need to precisely understand  $\frac{ZDC}{BBC}$ . It is based primarily on the observation that the pileup corrections seem to work to some extent but fail due to the vertex cut. A method to translate scalers with a vertex cut into a number that scales proportionally to the luminosity is needed. Width effects will be shown to enter into this new framework but it is not a central feature, conceptually or quantitatively.

# Chapter 9

## Residual Rate Correlation

The pileup correction formalism of Eq. 8.25 is analytic. If the BBC and ZDC coincidence triggers have no vertex cut, the formalism works well on the data as illustrated in Fig. 8.17. But in Fig. 8.18 we also see the formalism does not work when a vertex cut is present. Let's see if we can understand this quantitatively.

### 9.1 Derivation of a Residual Rate Correlation in the Two Collision Approximation

Eq. 8.25 can be approximated using a Taylor expansion in each term to order  $(\mu\epsilon_{NS})^2$ , which means we are working in the approximation that each crossing has either zero, one, or two collisions. This is the two collision approximation. For the BBC  $(\mu\epsilon_{NS})(1+k_N+k_S) \sim 0.15$  and for the ZDC  $(\mu\epsilon_{NS})(1+k_N+k_S) \sim 0.06$  so a second order Taylor expansion is appropriate in each case. In this approximation, the coincidence rate comes from the standard  $\mu\epsilon_{NS}$  when one collision occurs and various combinations of two collisions, which we describe now. A third collision contributes at the level of  $P(3,\mu)/P(2,\mu) = \mu/3$ . So at the highest collision rates in Run09  $\sqrt{s} = 500$  GeV of  $\mu \sim 0.35$ , we would expect deviations from this approximation to occur at the level of  $\sim 10\%$ . In Table 9.1 we write out all possibilities when two collisions occur. The value in the table indicates the number of coincidences that should be counted. In Table 9.2 we show the number of coincidences that actually are counted when two collisions occur. Comparing the two tables we see that over-counting occurs at a rate  $\propto \frac{\mu^2}{2}(2\epsilon_N\epsilon_S)$  while undercounting occurs at a rate  $\propto \frac{\mu^2}{2}\epsilon_{NS}^2$ . We thus arrive

Table 9.1: Number of coincidences that should be counted from two collisions.

	$\epsilon_0$	$\epsilon_N$	$\epsilon_S$	$\epsilon_{NS}$
$\epsilon_0$	0	0	0	1
$\epsilon_N$	0	0	0	1
$\epsilon_S$	0	0	0	1
$\epsilon_{NS}$	1	1	1	2

Table 9.2: Number of coincidences that are counted from two collisions.

	$\epsilon_0$	$\epsilon_N$	$\epsilon_S$	$\epsilon_{NS}$
$\epsilon_0$	0	0	0	1
$\epsilon_N$	0	0	1	1
$\epsilon_S$	0	1	0	1
$\epsilon_{NS}$	1	1	1	1

at the interesting conclusion, in this approximation, that over-counting and undercounting cancel when

$$K \equiv k_N k_S - \frac{1}{2} = 0 \quad (9.1)$$

If  $K > 0$  over-counting dominates while undercounting dominates when  $K < 0$ . For the BBC,  $K_{BBC} = -0.419$  while for the ZDC  $K_{ZDC} = 11.87$ . In the approximation where  $k_N = k_S = k$  the break-even point occurs when  $k = \frac{1}{\sqrt{2}}$ .

The Taylor expansion of Eq. 8.25 is

$$\begin{aligned} R_{obs} = 1 &- \left[ 1 - R_{true}(1 + k_N) + \frac{1}{2}R_{true}^2(1 + k_N)^2 \right] \\ &- \left[ 1 - R_{true}(1 + k_S) + \frac{1}{2}R_{true}^2(1 + k_S)^2 \right] \\ &+ \left[ 1 - R_{true}(1 + k_N + k_S) + \frac{1}{2}R_{true}^2(1 + k_N + k_S)^2 \right] \end{aligned} \quad (9.2)$$

Where  $R_{obs}$  is the observed coincidence counting rate, the same as  $P(k > 0, l > 0)$  from last chapter, and  $R_{true} = \mu\epsilon_{NS}$ . This simplifies to:

$$R_{obs} = R_{true} + KR_{true}^2 \quad (9.3)$$

We can then solve for  $R_{true}$  using the quadratic equation and picking the + sign to ensure that  $R_{true} = 0 \longleftrightarrow R_{obs} = 0$ . This gives:

$$R_{true} = -\frac{1}{2K} \left[ 1 - \sqrt{1 + 4KR_{obs}} \right] \quad (9.4)$$

For the BBC,  $4KR_{obs} \sim 0.16$  and for the ZDC  $4KR_{obs} \sim 0.33$ , when the beam rate is  $\mu = 0.2$ . Using a square root Taylor expansion to second order, we get:

$$R_{true} = R_{obs} - KR_{obs}^2 \quad (9.5)$$

Now we make the definition:

- $f$  = the fraction of crossings where a coincidence is found, real or accidental, such that the vertex is reconstructed within the 30 cm vertex cut.

$f_{ZDC}$  and  $f_{BBC}$  are the relevant quantities for the ZDC and the BBC. Up to now in this section we have assumed no vertex cut. We can now insert that cut, which means that instead of the observed coincidence rate being  $R_{obs}$  it is now  $fR_{obs}$ . When the standard pileup correction is applied to this value we substitute:

$$R_{obs} \rightarrow fR_{obs} \quad (9.6)$$

into Eq. 9.5 and get

$$R_{true,vtx} = fR_{obs} - Kf^2R_{obs}^2 \quad (9.7)$$

$R_{true,vtx}$  is the quantity of interest. It is the pileup corrected rate obtained by correcting an observed rate with a vertex cut in a framework where no vertex cut is assumed. So it is a wrong number because it is based on a correction that is incorrectly applied. The number is wrong, however, only in the sense that it does not scale the true luminosity. This expression of  $R_{true,vtx}$ , however, is correct in this approximation. Now we can calculate the ratio of the 30 cm corrected rate and the no vertex corrected rate as:

$$\frac{R_{true,vtx}}{R_{true}} = \frac{f(1 - KfR_{obs})}{1 - KR_{obs}} \approx f [1 + (1 - f)KR_{obs}] \quad (9.8)$$

This can be rearranged to get:

$$R_{true} = R_{true,vtx} \times \frac{1 - KR_{obs}}{f(1 - KfR_{obs})} \quad (9.9)$$

But the scaled value is not  $R_{obs}$ , the no vertex uncorrected scaler, rather  $R_{obs,vtx} = fR_{obs}$ . In terms of this we get:

$$R_{true} = R_{true,vtx} \times \frac{1 - \frac{K}{f}R_{obs,vtx}}{f(1 - KR_{obs,vtx})} \quad (9.10)$$

We define the residual correction factor by:

$$C_{res} \equiv \frac{1 - \frac{K}{f}R_{obs,vtx}}{(1 - KR_{obs,vtx})} \quad (9.11)$$

We leave out the scaling factor of  $f$ . The result is shown independently for the BBC and the ZDC in Figure 9.1a and 9.1b. Note that  $f$  itself has a small dependence on the coincidence rate. However, if both the no vertex and 30 cm vertex trigger are scaled, it can be measured directly in data at the same time as

the rate itself. If they are not scaled then the WCM data can be tuned to precisely fit the collision data and extract  $f$  as well. Fig 9.1 has a satisfying qualitative interpretation as well. For the ZDC, when a vertex

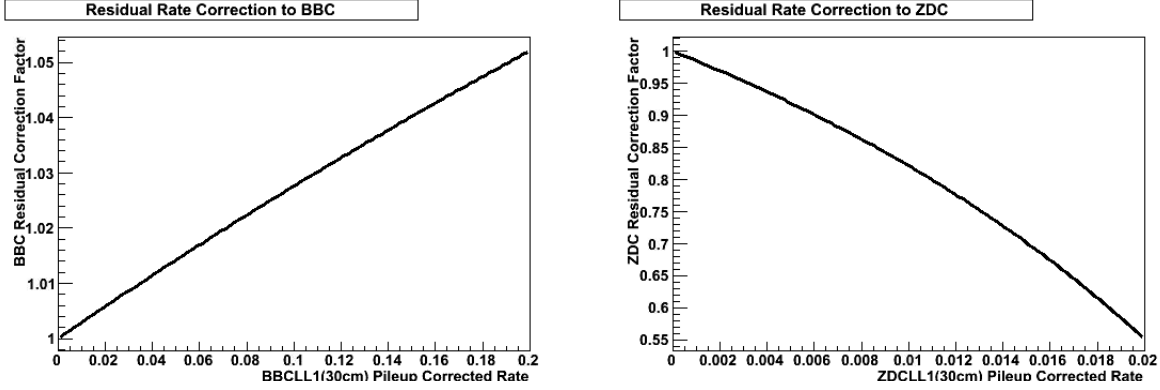


Figure 9.1: Left (a) BBC, Right (b) ZDC. The residual correction factor,  $C_{res}$ , is shown for the BBC and ZDC in the two collision approximation. At the typical rates of Run09 at  $\sqrt{s} = 500$  GeV with  $R_{true,vtx,BBC} \sim 0.1$  and  $R_{true,vtx,ZDC} \sim 0.007$ , we find a correction of 2.5% to the BBC luminosity and -10% to the ZDC luminosity.

cut is used in the trigger, some of the accidental coincidences that should occur do not. So the raw scalers do not count as fast as they should. In other words, looking back to Fig. 8.15, we are not as high up on the black curve as we should be, therefore the downward correction is not as severe as it should be. The downward residual correction to the ZDC makes up the difference. A similar line of reasoning applies to the BBC in the opposite direction.

Now let's write down the residual ZDC to BBC ratio:

$$\frac{R_{true,vtx,ZDC}}{R_{true,vtx,BBC}} \approx \frac{R_{true,ZDC}}{R_{true,BBC}} \frac{f_{ZDC} [1 + (1 - f_{ZDC}) K_{ZDC} R_{obs,ZDC}]}{f_{BBC} [1 + (1 - f_{BBC}) K_{BBC} R_{obs,BBC}]} \quad (9.12)$$

From Fig. 8.17 (from 2013 running where the no vertex triggers were scaled) we know that  $\frac{R_{true,ZDC}}{R_{true,BBC}} \approx 0.063$ . This comes from applying the standard rate corrections and it normalizes the ratio to a nearly constant value crossing to crossing. By the definition of  $f$  it is very easy to just read off these scalers (although it is averaged over all crossings and so loses sensitivity to the slightly different details of the bunch structure between bunches). We get  $f_{ZDC} \approx 0.446$  and  $f_{BBC} \approx 0.588$ . We can also read off that the uncorrected, no vertex, ratio of ZDC to BBC is  $\frac{R_{obs,ZDC}}{R_{obs,BBC}} \approx 0.095$  (a similar number is found by looking at Fig. 8.17).

Plugging in all these values, and again using  $\frac{1}{1-x} \approx 1+x$  yields the residual rate correlation:

$$\frac{R_{true,vtx,ZDC}}{R_{true,vtx,BBC}} \approx 0.048 + 0.40R_{obs,ZDC} \quad (9.13)$$

But again, we have only 30 cm scaler values to look at and the correlation we want to study ultimately is

$$\frac{R_{true,vtx,ZDC}}{R_{true,vtx,BBC}} \text{ vs. } R_{true,vtx,ZDC} \quad (9.14)$$

So it is necessary to transform  $R_{obs,ZDC}$ , the non-rate corrected ZDC scaler with no vertex cut, into the rate corrected ZDC scaler with a vertex cut. Applying Eq. 9.7 to the ZDC and plugging in the known values gives  $R_{true,vtx,ZDC} = 0.446R_{obs,ZDC}(1 - 5.29R_{obs,ZDC})$ . To within 10% error in the slope of the residual correlation, we can discard the rate correcting term and make the approximation  $R_{obs,ZDC} \approx \frac{R_{true,vtx,ZDC}}{0.446}$  giving:

$$\frac{R_{true,vtx,ZDC}}{R_{true,vtx,BBC}} \approx 0.05 + 0.90R_{true,vtx,ZDC} \quad (9.15)$$

Let's take stock of what we have done. Eq. 9.12 really encompasses the idea that the pileup corrected ZDC and BBC scalers, with a vertex cut, do depend on the vertex widths via the  $f_{ZDC}$  and  $f_{BBC}$ . But this is not just a width effect, the singles to doubles ratio comes in via  $K_{ZDC}$  and  $K_{BBC}$ . The  $f$  factors encompass both the intrinsic collision distribution width along with the detector resolution. This equation basically says:

*The residual rate correlation is a complicated effect arising, even in this approximation scheme, from multiple factors. The fraction of coincidences reconstructed within 30 cm is one factor. This has a bunch profile component as well as a detector resolution component. Additionally, the detector acceptances, efficiencies, and cross sections enter through the K factor, which is seen to directly couple with f and the observed coincidence rates. No single parameter can explain the effect by itself. Rather, it arises from a coupling of many experimental details that is induced as the result of a vertex cut being imposed on the coincidence trigger.*

The width correlation and correction is far too simplistic. It does not take into account the complicated interplay between all the relevant details. This is most likely the explanation for why the width effect has no impact on the data. The pileup correction, even though incorrectly used, does yield improvement. The central arm measurements require a coincidence detection in the BBC. This coincidence also has a vertex requirement of 30 cm in order to match the central arm acceptance. However, at the same time it causes the

pileup correction formalism to fail. And yet, the pileup corrections to scalers with a vertex cut do show more improvement than the width correction. This is a sign this is where to start gaining a deeper understanding. We have now gained this deeper understanding by starting from pileup corrections and eventually folding width effects in. However, nothing we are doing should be construed as a “better” width correction because a residual correlation exists even when a width correction would not be necessary. In every single case except when  $f_{ZDC} \equiv f_{BBC} \equiv 1$ , the factor of  $K$  still comes into play, and this couples to the observed coincidence rate. Further, this single exception case is completely unrealizable. It requires every collision to happen within  $|z_{true}| < 30\text{ cm}$  and perfect detector resolution. Moreover, a relative timing requirement between collisions, when more than one occurs, would also exist. The only realistic way to ensure  $f_{ZDC} \equiv f_{BBC} \equiv 1$  is by removing the vertex cut. By this method alone, the “ $fKR$ ” coupling term is removed.

The limitation of this model, and the results that come from it, is the assumption of two collisions only. This is equivalent to a small rate approximation. For example, in Eq. 9.11, when  $KR_{obs,vtx} \rightarrow 1$  the approximation becomes singular. Therefore, the domain of applicability of this approximation is  $|KR_{obs,vtx}| \ll 1$ . In Run09 at  $\sqrt{s} = 500\text{ GeV}$ , the maximum observed rates put an upper bound of  $|K_{BBC}R_{obs,vtx,BBC}| \leq 0.06$  and  $|K_{ZDC}R_{obs,vtx,ZDC}| \leq 0.30$ . But the residual correlation can still be computed when this approximation completely breaks down by adding more terms in the Taylor expansion of Eq.9.2. This equation very quickly stops being able to be solved analytically, and at higher rates where the higher order terms require consideration, a numerical solution would be needed. But the concept does not change. The pileup corrections to the  $30\text{ cm}$  vertex cut triggers fail in a well defined way and can be corrected without interfering with the effect of a possible asymmetry. Also, we have shown that while the residual correlation is predicted in terms of the ratio between two detectors,  $ZDC/BBC$ , the correction for the ZDC need not be based on the BBC. Each detector has been shown to be able to be corrected using only measured constants for that detector. The reason we will ultimately compute the residual correlation from the detector ratio is that this is what is available to compare with in the real data. From the scaler ratio alone, the fact it is not constant only definitively tells us that one or the other or both detectors are measuring the luminosity incorrectly. Based on this model, we know that both detectors suffer a problem but that the ZDC luminosity error is large compared with the BBC.

## 9.2 Observation of a Residual Rate Correlation in the Data

We would not have gone to the trouble to explain this theoretical prediction if the data did not convincingly bear it out. But, like so many other ideas first seen and later predicted, we take the same approach here. In Figure 9.2 we show the residual correlation, as observed in real data. We show two correlations between  $\frac{ZDC}{BBC}$  and  $ZDC$ . The red points show the correlation between raw scalers with a  $30\text{ cm}$  vertex cut that have not been pileup corrected. The blue points show the correlation after a pileup correction has been done to the same scalers. The prediction from our model corresponds to the blue points and in this particular run it is found that:

$$\frac{R_{true,vtx,ZDC}}{R_{true,vtx,BBC}} \approx 0.058 + 1.00 R_{true,vtx,ZDC} \quad (9.16)$$

Comparing this with Eq. 9.15 shows a remarkable quantitative agreement with even the simple model we worked from. The constant term agrees to within 20% of the model while the slope agrees to within 10%. Given the approximations made along the way, the contributions from three and higher collision crossings, and expected bunch to bunch variations in the values of  $f$ , this level of agreement is appropriate. The values

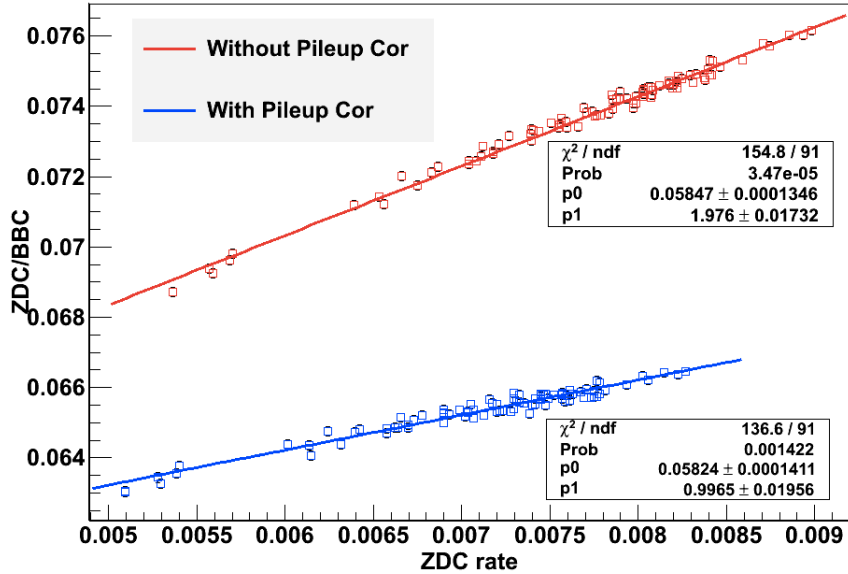


Figure 9.2: In red the quantities plotted are  $\frac{R_{obs,vtx,ZDC}}{R_{obs,vtx,BBC}}$  vs  $R_{obs,vtx,BBC}$ . This means we are using the observed rates, with a  $30\text{ cm}$  vertex cut, for the ZDC and BBC. No pileup corrections are done. In blue the quantities plotted are  $\frac{R_{true,vtx,ZDC}}{R_{true,vtx,BBC}}$  vs  $R_{true,vtx,BBC}$ . These values are obtained by applying pileup corrections to the points in red. Each point plotted comes from one bunch crossing.

of the parameters are very interesting. First let's look at the slope -  $p1$  from Fig. 9.2. If the luminosity monitors are monitoring the luminosity correctly, the slope is expected to be zero. The pileup correction

reduces the value of the correlation slope, indicating that the pileup corrections are having an improving effect, but do not provide a fully complete correction by themselves. A correlation is clearly expected in the uncorrected values because we know they miscount the luminosity, even without a vertex cut. The fact that the slope is decreased, but not eliminated, is precisely why this idea is called a Residual Rate Correlation. If the slope were eliminated, this would indicate that the ZDC and BBC scalers were linearly proportional to each other, i.e.  $ZDC = k * BBC$ . It is exceedingly unlikely, given the very different nature of the ZDC and BBC, that they could truly count luminosity proportionally to each other, but still both be wrong in exactly the same way. If we do find  $ZDC = k * BBC$  then the most favored explanation is that the luminosity detectors are both scaling the true luminosity correctly, and we would expect a high precision determination of the relative luminosity.

That the residual correlation is positive can also be explained qualitatively, in addition to the quantitative calculation showing so. It comes from the vertex cut having two separate effects. The first is that it causes the ZDC to not over-count as much as it should. The second is that due to the ZDC resolution, more counts inside the vertex cut are lost than counts outside are gained (the same logic leading one to want to apply width corrections). Since the rate correction gets larger with rate itself and the ZDC is not corrected downward enough the effect is more pronounced at higher rates. The BBC, on the other hand, needs a comparatively small correction upward due to its undercounting. However, its resolution is better and the magnitude of the rate correction is smaller. In this case, the BBC is corrected up, but not by enough. When the rate correction fails, the magnitude of the failure is smaller than in the ZDC. The dominating effect is that ZDC is a larger number than it should be which causes  $\frac{ZDC}{BBC}$  to be larger than it should be. But the BBC is also smaller than it should be, so it, too, contributes to the systematically too large value of  $\frac{ZDC}{BBC}$ . The higher the ZDC rate, the higher the pileup corrected ZDC scaler (pileup corrected, with a vertex cut) is relative to what it should be.

The constant term -  $p0$  - from Fig. 9.2 also has a physical meaning. The salient feature is how remarkably close these parameters are in the fit to both the corrected and uncorrected scalers. This is not surprising. It is essentially saying that in the limit of 0-rate, the uncorrected and corrected ratios should be identical. But the only difference between the two is a pileup correction and in this same limit, the uncorrected values are not modified. So in this limit the blue points should coincide with the red points. A systematic difference between the two values of 0.4% does exist, however. We do not purport to understand quantitatively the origin of this small difference, but it is likely due to differing longitudinal bunch profiles which cause

slightly different collision probability distributions,  $P(t_0, z)$ , which in turn slightly changes how many accidental coincidences are reconstructed by the ZDC outside versus inside of its vertex cut. The value itself,  $\frac{ZDC}{BBC} \approx 0.058$ , is also lower than the value found when applying pileup corrections to the no vertex cut scalers. Eq. 9.12 encodes this expectation from the model. In the 0-rate limit, it reduces to

$$\frac{R_{true,vtx,ZDC}}{R_{true,vtx,BBC}} \approx \frac{R_{true,ZDC}}{R_{true,BBC}} \frac{f_{ZDC}}{f_{BBC}} \quad (9.17)$$

It is hard to know exactly what  $f_{ZDC}$  is in this 0-rate limit. As we said before,  $f$  has some rate dependence, and a simulation of the ZDC vertex reconstruction would be necessary before making further predictions regarding its value in this case. We do expect  $\frac{f_{ZDC}}{f_{BBC}} < 1$ , however, just based on the much larger ZDC resolution. As before  $\frac{R_{true,ZDC}}{R_{true,BBC}} \approx 0.063$ , so the value found in the data of  $\approx 0.058$  is very consistent with what one might expect.

We should also take a minute to note just how precise this correlation is found to be in the data. In a typical run of say, 45 minutes, a given pair of bunches pass through each other  $\approx 2 \times 10^8$  times. A BBC coincidence is found in  $\approx 10\%$  of the crossings while a ZDC coincidence if found in  $\approx 1\%$  of these crossings. So the typical number of BBC and ZDC triggers found in one crossing is  $\approx 2 \times 10^7$  and  $2 \times 10^6$ , respectively. With these statistics, the typical value with an estimated statistical uncertainty is  $\frac{ZDC}{BBC} = (6500 \pm 4) \times 10^{-5}$ . With this level of statistical precision, the residual rate correlation fit, a simple first order polynomial, still manages to have a  $\chi^2/NDF \approx 1.5$  as seen in Figure 9.2.

Despite the weight of the evidence showing the residual rate correlation exists, let us say that maybe the pile up corrections actually do work on the scalers with a vertex cut. In this case we expect to find  $ZDC = k * BBC$ . In Figure 9.3 we completely decouple the detectors by plotting  $ZDC$  versus  $BBC$  and fit it to a line. We expect the  $y$ -intercept of the line to be consistent with 0. If the BBC is not counting then surely neither should the ZDC. Interestingly enough, the fit does produce a favorable  $\chi^2$ , but the parameters do not make physical sense. The  $y$ -intercept actually turns out to have a negative value, implying one detector is capable of counting at a negative rate. Also the slope is predicted to be 0.0717, which is larger than the ratio in the no vertex case. This is untenable. In Figure 9.4 we show the blue, pileup corrected points from Fig. 9.2 but again with the axis decoupled. The fit to these points is:

$$ZDC = \frac{p0 * BBC}{1 - p1 * BBC} \quad (9.18)$$

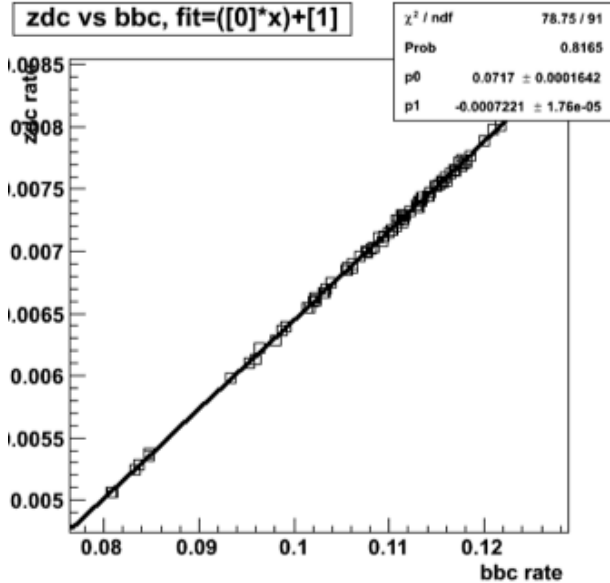


Figure 9.3: The ZDC pileup corrected rate with a vertex cut vs BBC pileup corrected rate with a vertex cut is shown. This is fit to a line. This produces a good  $\chi^2/NDF$  but cannot represent the correct fit to the data on physical grounds based on the results of the fit parameters.

which is just rearranging the terms from Fig. 9.2. The red comparison line is  $ZDC = k * BBC$  and again shows how the deviation of the ZDC from the BBC increases with rate. We have now concluded the main thrust of our arguments regarding the existence of a residual rate correlation. It is not a simple effect by any means, but rather arises from a combination of considerations. The one sweeping assertion that can be made, however, is that the Residual Rate Correlation is caused by the presence of a vertex cut in the luminosity triggers. With a vertex cut the correlation exists. Without a vertex cut it does not. We have also provided explanations at each possible juncture to show that the assertions being made are consistent quantitatively and qualitatively with what the data shows. Therefore, we now accept the existence of the Residual Rate Correlation and proceed to study its properties in further detail and then see how it impacts the relative luminosity uncertainty (Spoiler alert<sup>1</sup>).

## 9.3 Time Dependence of the Residual Rate Correlation Parameters

Figure 9.5 shows the residual correlation fit parameters as a function of runnumber. Recall that the physical interpretation of this number is the 0-rate limit of the ratio of the ZDC to BBC rate within the 30 cm vertex

---

<sup>1</sup>It works.

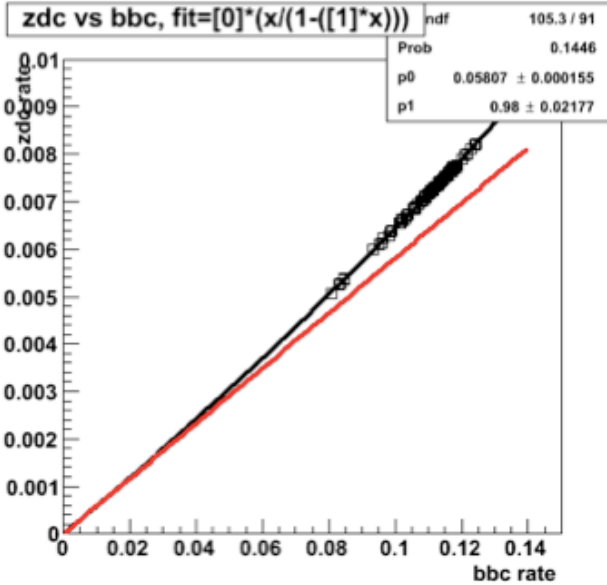


Figure 9.4: ZDC vs. BBC rates corrected scalers are shown. This correlation is compared with, and seen to deviate significantly from, a linear correlation. It provides further evidence that one or both detectors still do not scale correctly with the true luminosity.

cut. In this limit, by definition, the  $f$ 's do not have a rate component. This means ghost vertices from multiple collisions are negligible and that  $f$  can be interpreted as the fraction of collisions (which is limited to either zero or one per crossing) that are reconstructed within the vertex cut. This interpretation is not exactly correct at finite rates. If we make the fair assumption that the detector resolutions do not change over time, then the observed time dependence, both within a fill and between fills, can be attributed to the time dependent spreading of the longitudinal bunch profiles. At finite  $\beta^*$  this also results in a decreased rate (caused also by beam decay), but of course in the 0-rate limit we refer to, this is not important. This can be seen by looking at the very close correspondence between the BBC width proxy,  $\frac{BBC_{out}}{BBC_{in}}$ , versus runnumber as shown in Figure 9.6. The width proxy in the ZDC is more sensitive to bunch structure changes than the BBC because of its resolution. So an increase in the BBC width proxy corresponds to a larger increase in the ZDC width proxy. Therefore, the ratio of the two is expected to go up. The data supports this claim. Figure 9.5b shows the time dependence of the residual correlation slope. The slope is influenced by the factors we just considered and also by the rate. This means  $f$  has a less clean interpretation, and the singles to doubles ratio of each detector plays a role.

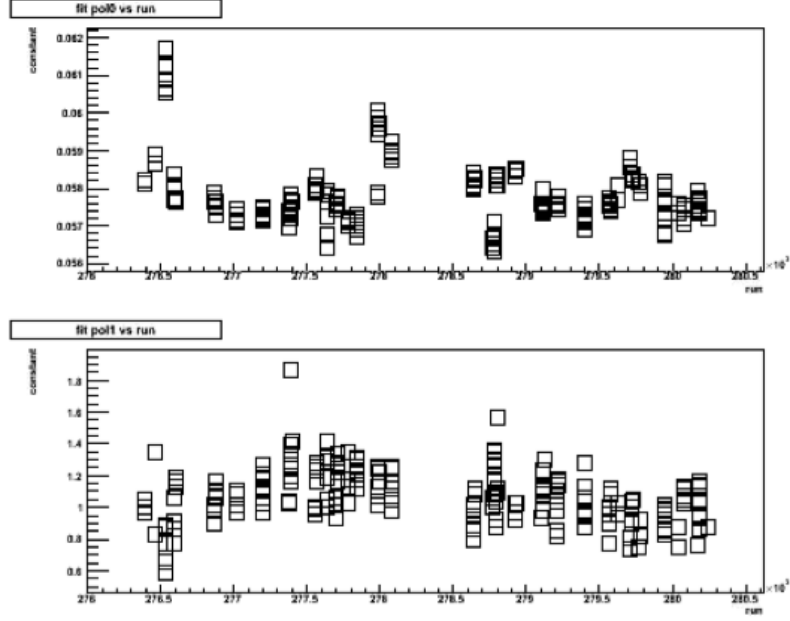


Figure 9.5: Top (a):  $y$ -intercept of the residual correlation fit versus runnumber is shown. Bottom (b): The slope of the residual correlation fit versus runnumber is shown. The clusters of points are single runs within a fill. The slightly different properties of the bunches in each fill causes the clumps to jump around.

## 9.4 Residual Rate Correction to the ZDC Luminosity

As a first attempt at a proper residual rate correction, we take the same approach used in the width correction that the mismeasurement in the ZDC is much more severe than in the BBC. In the case of the width corrections the true value of  $\frac{ZDC}{BBC}$  requires a correction to both, but a correction to the ZDC only is used as a sufficient approximation. That correction is ([110])

$$\left(\frac{ZDC}{BBC}\right)' = \left(\frac{ZDC}{BBC}\right) \frac{\langle \frac{ZDC}{BBC} \rangle}{a + b \frac{ZDC_{out}}{ZDC_{in}}} \quad (9.19)$$

It is not the case here that the ZDC is being corrected to the BBC, because the only information used in the correction is the ZDC width proxy,  $\frac{ZDC_{out}}{ZDC_{in}}$ . The same can be said if we define the residual rate correction by:

$$\left(\frac{ZDC}{BBC}\right)' = \left(\frac{ZDC}{BBC}\right) \frac{a}{a + b * ZDC} \quad (9.20)$$

where  $a$  and  $b$  are the residual correlation fit parameters and  $ZDC$  and  $BBC$  are the  $30\text{ cm}$  pileup corrected rates. Just as in the width correction, the BBC rate only appears in this equation to keep the ratio visually present. It is the same value on both the left and right sides of this equation and could be canceled out.

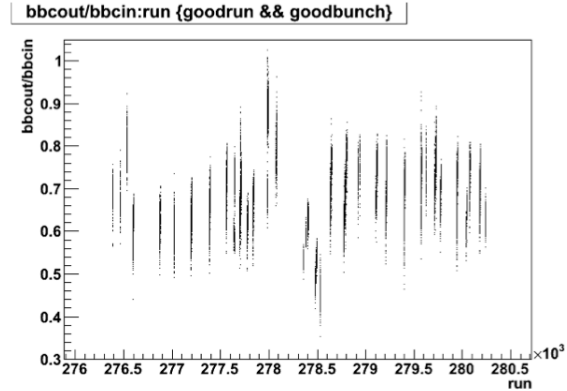


Figure 9.6: The BBC width proxy,  $\frac{BBCout}{BBCin}$ , versus runnumber is shown for every bunch in every fill. Within a fill there is a clear spread between bunches but this is modulated by fill to fill differences as well. A clear correspondence with the residual 0-rate parameter of the residual correlation in Figure 9.5 can be seen.

Due to the very strong residual correlation observed over any (human) time scale, we find it advantageous to apply the correction on the shortest time scale possible. This is one run with a typical length of  $O(1 \text{ hour})$ . Because of the time dependence observed in the fit parameters, this is more precise than making some average correction over a longer time scale. The width correction is forced to use a long time scale,  $O(2 \text{ months})$  or  $O(10^3 \text{ hours})$ , because the correlation does not always exist on short time scales. Figure 9.7a shows a standard example of the residual correlation. Figure 9.7b shows the pileup corrected result for  $\frac{ZDC}{BBC}$  versus crossing. Figure 9.7c shows how effectively the residual correlation accounts for the systematic fluctuations in the ratio. The constant value is, by construction, normalized to the average 0-rate, 30 cm vertex cut ratio of  $\frac{ZDC}{BBC}$  across all bunches, as it should be when correcting the luminosity monitor to a rate independent value. The  $\chi^2/NDF$  is observed to be larger than unity. The example run we have shown produces slightly better than average  $\chi^2/NDF$  than seen when applying to correction to all runs. Figure 9.8 shows the  $\chi^2/NDF$  distribution of the fits done to all runs. The typical  $\chi^2/NDF \approx 50$  with pileup corrections has been reduced to  $\langle \chi^2/NDF \rangle \approx 3.2$  after the residual rate correction is applied to the ZDC. In Figure 9.9, which adds onto Fig. 9.2, the  $\frac{ZDC}{BBC}$  vs.  $ZDC$  correction is shown after no corrections, the pileup correction, and a residual correction.

In addition to showing the expected constancy of  $\frac{ZDC}{BBC}$  after the residual correction, we also note that the ZDC rate itself is quite substantially modified in each case. This can be explained by working through an example starting with Eq. 9.5. The maximum ZDC uncorrected rate with a vertex cut is  $R_{obs,vtx} \approx 0.009$ . Using  $f \approx 0.45$ , the ZDC uncorrected rate with no vertex cut is  $R_{obs} \approx 0.02$ . We now look at the size of the

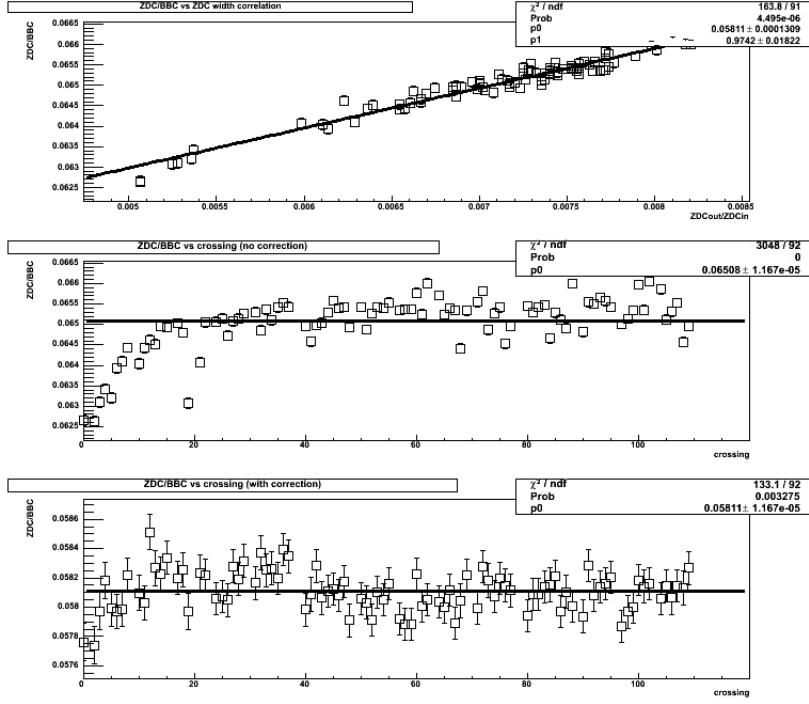


Figure 9.7: Top (a): The residual correlation. Middle (b):  $\frac{ZDC}{BBC}$  vs crossing with pileup corrections. Bottom (c): Result of applying the residual correction from Eq. 9.20. Before the residual correction, the constant fit has  $\chi^2/NDF \approx 33$ . After the residual correction the constant fit has  $\chi^2/NDF \approx 1.45$ .

pileup correction. We have:

$$\frac{R_{true}}{R_{obs}} = 1 - KR_{obs} \quad (9.21)$$

When this is applied to vertex cut scalers we get

$$\frac{R_{true,vtx}}{R_{obs,vtx}} = 1 - 11.87(0.009) \approx 0.89 \quad (9.22)$$

corresponding to an 11% downward correction. But when this is applied to scalers without a vertex cut we get:

$$\frac{R_{true}}{R_{obs}} = 1 - 11.87(0.02) \approx 0.76 \quad (9.23)$$

corresponding to a 24% downward correction. So we have two things: a) the vertex cut causes the observed rate to be lower than it should be and b) the magnitude of the pileup correction gets larger at larger rate. Therefore, when a pileup correction is applied, it is not applied strongly enough. The observed rate is too low, therefore the downward correction is too small, therefore the resulting ZDC pileup corrected rate is too high. This effect is more severe at higher rates, hence the positive residual slope. This is, at its core, the

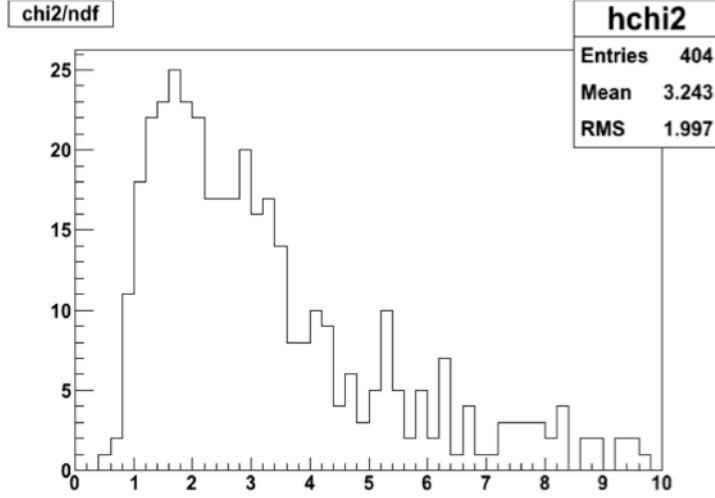


Figure 9.8:  $\chi^2/NDF$  distribution from the fit in Fig 9.7c is shown for all runs in Run09  $\sqrt{s} = 500$  GeV. The mean of 3.2 in this plot shows a drastic improvement over the typical  $\chi^2/NDF \approx 200$  with no pileup corrections and  $\chi^2/NDF \approx 50$  with pileup corrections only.

point of the Residual Rate Correction. If it is understood how much of the observed rate is cut out by the vertex cut, then it can be understood by how much the pileup correction over or underestimates the true effect of pileup. Doing the same exercise for the BBC shows that its vertex cut causes the pileup correction to correct upwards by about 3% too little.

The remaining amount of systematic fluctuation likely stems from not applying a residual rate correction to the BBC, bunch to bunch differences in longitudinal profiles, beam offsets or angles or boosts, detector noise, beam gas, and trigger livetime effects. Once all of these effects can be controlled for, it would be plausible to claim that a statistically significant  $A_{LL}^{ZDC/BBC}$  might indicate the observation of a true, physics based asymmetry. On that note, let's see what the asymmetries look like.

## 9.5 Impact of Residual Rate Correction on $A_{LL}^{ZDC/BBC}$

Figure 9.10a shows the measurement of  $A_{LL}^{ZDC/BBC}$  based on raw scalers, with no corrections of any kind. This result was shown previously in Fig. 8.19a and we show it again here for comparison. Figure 9.10b shows the bunch spin shuffled asymmetries. To obtain this plot, we randomize the spins of all bunches and rerun the same code used to produce Fig. 9.10a. We do this a fixed number of times, chosen to be 1000. Doing so confirms that the asymmetry seen is consistent with the spread of asymmetries obtained with randomized spins. Figure 9.11a shows the measurement of  $A_{LL}^{ZDC/BBC}$  with pileup corrections applied to the 30 cm

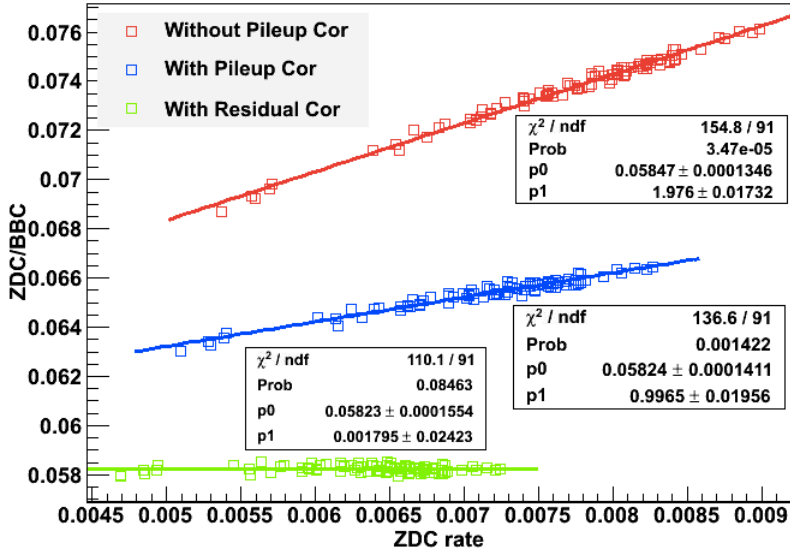


Figure 9.9: Direct comparison of  $\frac{ZDC}{BBC}$  vs.  $ZDC$  for the three indicated cases.

vertex cut scalers. This result was also shown previously in Fig. 8.19b. In Figure 9.11b we show the bunch shuffled result. Again, as expected, the asymmetry obtained from real data is consistent with the width of the bunch shuffled distribution. Figure 9.12 shows the improvement that results from applying a residual rate correction to the ZDC. Figure 9.13 shows the bunch shuffled result. Table 8.7 can now be expanded to include this new information. This is shown Table 9.3. Applying a residual correction to just the ZDC (which

Table 9.3: Results of  $A_{LL}^{ZDC/BBC}$  with no corrections, with a pileup correction, and with a residual rate correction in addition to the pileup correction.

Correction	$A_{LL}^{ZDC/BBC}$	$\chi^2/NDF$	$\sigma_{A_{LL,shuf}} (\times 10^{-4})$
None	$(8.96 \pm 0.50) \times 10^{-4}$	90	9.1
Pileup	$(2.92 \pm 0.52) \times 10^{-4}$	18	4.3
Residual Rate	$(-1.36 \pm 0.54) \times 10^{-4}$	2.61	1.3

is not correcting the ZDC to the BBC) shows that the Residual Rate Correction is capable of accounting for a large amount of what was previously considered systematic effects. It reduces the  $A_{LL}^{ZDC/BBC}$  by a factor of 6.59 from the case of no corrections and by a factor of 2.15 from just applying pileup corrections. The  $\chi^2/NDF$  is reduced by a factor of 34.5 from the case of no corrections and by a factor of 6.90 from the case of applying pileup corrections. The width of the bunch shuffled asymmetry plot is reduced by a factor of 7.0 from the case of no correction and by a factor of 3.31 from the case of a pileup correction. The BBC does need a correction as well which would likely improve the results further. The magnitude of this correction would be several times smaller than for the ZDC. But with a first attempt (keeping in mind that

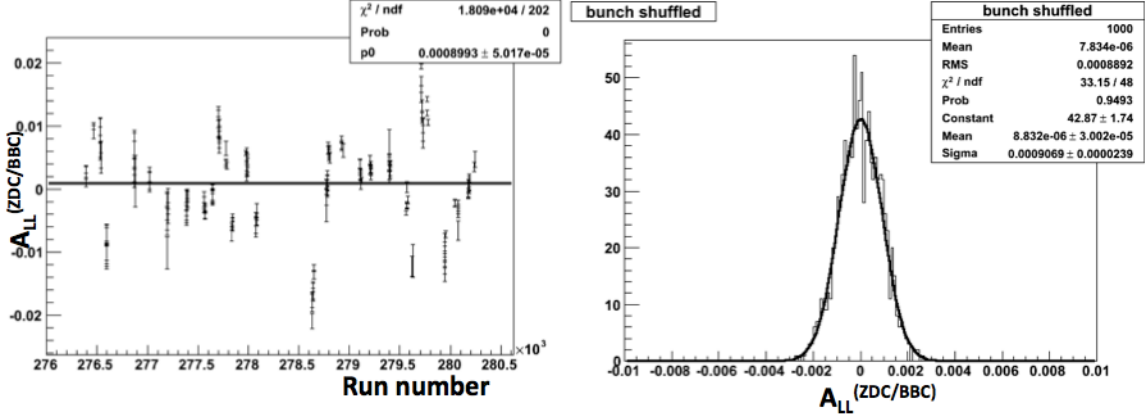


Figure 9.10: Left (a):  $A_{LL}^{ZDC/BBC}$  result shown for Run09  $\sqrt{s} = 500$  GeV data when raw, uncorrected scalers are used. Right (b):  $A_{LL,\text{shuf}}^{ZDC/BBC}$  showing the expected width of the distribution at  $9.1 \times 10^{-4}$ , similar to the value realized in the real data.

the no vertex scalers are not available in this period and only one run of WCM data was available) there is already a large impact. The systematic uncertainty in Run09, as quantified by  $A_{LL}^{ZDC/BBC}$  can be reduced by an order of magnitude from  $O(10^{-3})$  to  $O(10^{-4})$ . The accepted method ([110]) to quantify the relative luminosity uncertainty is from the asymmetry plus its uncertainty, scaled by  $\sqrt{\chi^2/NDF}$ . This would yield

$$\delta R^{ZDC/BBC} = (1.36 + 0.87(\text{stat})) \times 10^{-4} = 2.23 \times 10^{-4} \quad (9.24)$$

We will revise this number slightly after a study of the systematic effects involved. Nevertheless, this is the level of systematic uncertainty that needs to be maintained in the 2012 and 2013 runs with very high integrated luminosity in order to be sensitive to the expected  $10^{-4}$  level asymmetries that would arise from the DSSV model prediction for  $\Delta G$ , especially at low-x. These runs also had very high instantaneous luminosities, so pileup effects are expected to play a prominent role. The Residual Rate Correction is built precisely to handle a high rate environment and so offers a promising path to achieve this goal.

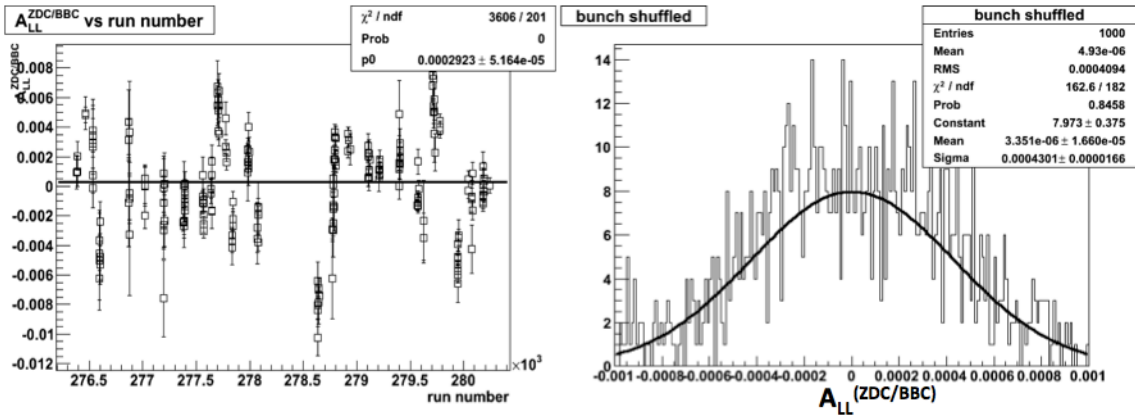


Figure 9.11: Left (a):  $A_{LL}^{ZDC/BBC}$  result shown for Run09  $\sqrt{s} = 500$  GeV data when pileup corrected scalers are used. Right (b):  $A_{LL,\text{shuf}}$  showing the expected width of the distribution at  $4.3 \times 10^{-4}$ , similar to the value realized in the real data.

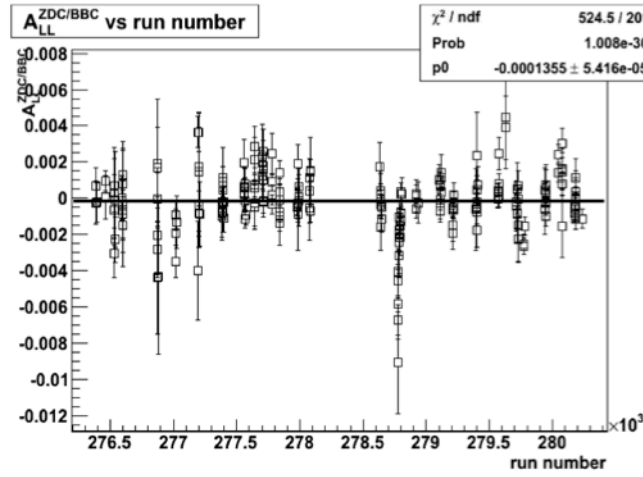


Figure 9.12:  $A_{LL}^{ZDC/BBC}$  result shown for Run09  $\sqrt{s} = 500$  GeV data when pileup and residual rate corrected scalers are used.

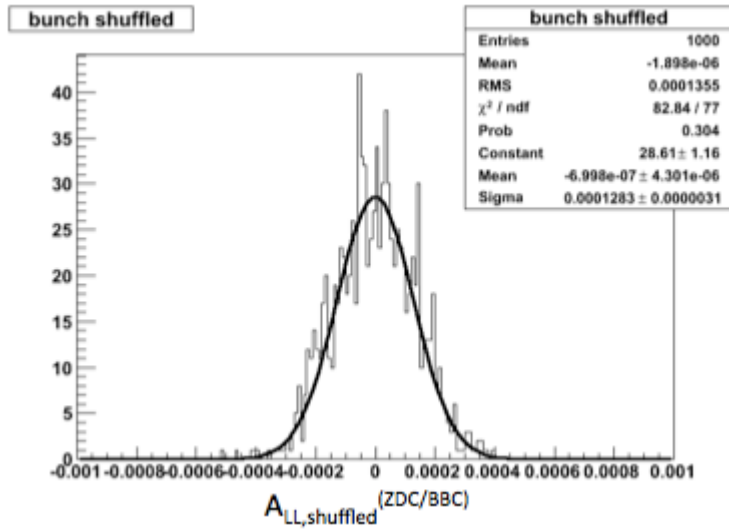


Figure 9.13:  $A_{LL,shuf}^{ZDC/BBC}$  showing the width of the asymmetry distribution at  $1.3 \times 10^{-4}$  when a ZDC residual rate correction is applied. This width is no longer very large compared with the statistical uncertainty of  $0.54 \times 10^{-4}$ .

## 9.6 The Spin Pattern Problem

We now start the first of four ancillary sections to address various aspects of the Residual Rate Correlation and Correction in further detail. One of the unresolved mysteries we discussed regarding the width correction technique was what effect this correction did or did not have in a spin pattern dependent way. As a reminder, in Run09 there were four different spin patterns that CA-D injected into RHIC. These were defined in Table 8.1. In Figure 9.14a we show the same plot as in Fig. 9.11a but color coded by spin pattern. A clear

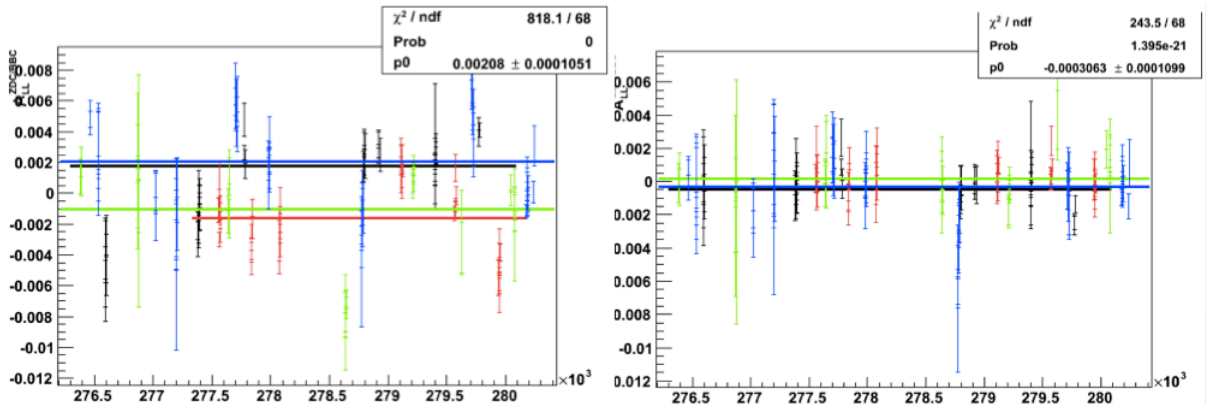


Figure 9.14: Left (a):  $A_{LL}^{ZDC/BBC}$  versus run is shown for each spin pattern separately with pileup corrections applied. Spin Patterns 1,2,3 and 4 are colored black, red, green and blue, respectively. Right (b):  $A_{LL}^{ZDC/BBC}$  versus run is shown for each spin pattern separately with the residual rate correction applied. The color scheme is the same.

separation is seen between “OSSO” spin patterns 1 and 4, which seem to be systematically shifted positive and “SOOS” spin patterns 2 and 3 which are systematically shifted negatively. This is concerning because even though the combined asymmetry from Fig. 9.11a yielded an asymmetry of  $A_{LL}^{ZDC/BBC} = 2.92 \times 10^{-4}$  this actually arises from the four systematically different asymmetries whose values are shown in Table 9.4. Recalling that the residual rate correlation and correction is manifestly blind to any spin related effects, we note that applying a residual correction dramatically reduces the observed discrepancy between spin patterns. So somewhere the residual rate correlation has “learned” about the existence of spin. Table 9.4 shows this. Note that the sign of the asymmetry is flipped after applying the residual correlation for each spin pattern. If in fact the residual correction knows about spin then one reason for this could be that our simplified residual correction is actually slightly overcorrecting the ZDC. We know this to be true and we also know that our simplified correction does not correct the BBC, even though a fully accurate residual rate correction would correct the BBC by  $O(3\%)$ . The residual correlation is actually due to a combination of luminosity mismeasurements from the BBC and the ZDC. By attributing all of the correlation to just the

Table 9.4: Spin Pattern Separated  $A_{LL}^{ZDC/BBC}$  results no rate corrections and with residual rate corrections. All asymmetries and their uncertainties are in units of ( $\times 10^{-4}$ ).

Spin Pattern	$A_{LL,without}^{ZDC/BBC}$	$\delta A_{LL,without}^{ZDC/BBC}$	$A_{LL,with}^{ZDC/BBC}$	$\delta A_{LL,with}^{ZDC/BBC}$
1	17.922	1.000	-4.510	1.047
2	-16.153	0.939	1.543	0.984
3	-10.060	1.194	1.467	1.255
4	20.080	1.051	-3.063	1.098

ZDC the net residual correlation may be too severe. It is likely that a future in-depth study can determine precisely, crossing by crossing, how much of the residual correlation is due to the ZDC and how much to the BBC, much in the way we showed in the Two-Collision Approximation. We are careful here not to bias ourselves by assuming that the true asymmetry is 0. Instead, we are merely speculating about the possible connection between the sign flip of the asymmetries after applying the residual correction and the fact that some of the residual correction to the ZDC (a downward correction) should have been applied to the BBC instead (an upward correction). If a true asymmetry exists, it would be independent of spin pattern, yet a systematic difference still exists. However, with our imperfect residual rate correction, it exists at the  $\approx 4\sigma$  level, compared with the  $\approx 18\sigma$  level without the correction.

Now let us turn that speculation into something concrete. Even though the residual correction to the ZDC only has largely, though, not fully, eradicated this spin pattern problem, it is still unclear where the observed splitting should come from. The residual rate correlation tells us that after pileup corrections we are left with

$$\frac{ZDC}{BBC} = a + b * ZDC \quad (9.25)$$

where  $a \approx 0.058$  and  $b \approx 0.95$  (though both values do change slightly within a fill and between fills as discussed). The definition of  $A_{LL}^{ZDC/BBC}$  is:

$$A_{LL}^{ZDC/BBC} = \frac{1}{P_B P_Y} \frac{\left(\frac{ZDC}{BBC}\right)^{++} - \left(\frac{ZDC}{BBC}\right)^{+-}}{\left(\frac{ZDC}{BBC}\right)^{++} + \left(\frac{ZDC}{BBC}\right)^{+-}} \quad (9.26)$$

Inserting Eq. 9.25 into this yields

$$A_{LL}^{ZDC/BBC} \approx \frac{1}{P_B P_Y} \frac{\frac{b}{2} \Delta ZDC}{a + b \langle ZDC \rangle} \quad (9.27)$$

where  $\Delta ZDC = \langle ZDC^{++} \rangle - \langle ZDC^{+-} \rangle$ . Therefore, if the average ZDC rate is found to be larger in same sign helicity crossings than opposite sign crossings a positive  $A_{LL}$  is expected. A negative  $A_{LL}$  is expected

when the opposite is true. Table 9.5 shows, for each helicity state in each spin pattern, the average ZDC

Table 9.5: Average pileup corrected ZDC rate for each helicity combination and spin pattern. The key point to note is that for SP1 and SP4 the mean ZDC rate is higher in “S” crossings than in “O” crossings. The opposite is true in SP2 and SP3 where the mean ZDC rate is higher in “O” crossings than “S” crossings.

Spin Pattern	Helicity combination ( $b, y$ )	$\langle P_B P_Y \rangle$	$\langle ZDC \rangle$
1	(+, +)	0.164	0.005023
	(+, -)	0.164	0.004975
	(-, +)	0.164	0.004986
	(-, -)	0.164	0.005043
2	(+, +)	0.168	0.005623
	(+, -)	0.168	0.005706
	(-, +)	0.168	0.005671
	(-, -)	0.168	0.005633
3	(+, +)	0.131	0.005921
	(+, -)	0.132	0.005950
	(-, +)	0.131	0.005984
	(-, -)	0.132	0.005911
4	(+, +)	0.138	0.005300
	(+, -)	0.137	0.005234
	(-, +)	0.138	0.005230
	(-, -)	0.138	0.005260

pileup corrected rate, along with the average polarization. These average rates are straight averages with no polarization or integrated luminosity weightings applied. However, these values can be used to make a rough prediction of the expected asymmetry. This prediction, along with the actual asymmetry, on a spin

Table 9.6: Predicted false asymmetry generated by residual rate correlation combined with systematic spin dependent rate splitting.

Spin Pattern	Avg rate comparison	Residual correlation $A_{LL}$ prediction	Observed $A_{LL}$
1	$\Delta ZDC > 0$	0.0024	0.0018
2	$\Delta ZDC < 0$	-0.0026	-0.0016
3	$\Delta ZDC < 0$	-0.0028	-0.0010
4	$\Delta ZDC > 0$	0.0025	0.0020

pattern separated basis, is shown in Table 9.6. It is not clear (at least to the author) why a given spin pattern might have a higher average rate for one helicity combination than another, and moreover, why this effect should flip for a different spin pattern. But this is what the data shows. The WCM data also confirms that one helicity state has a higher average number of protons per bunch than the opposite helicity state. This indicates the systematic issue may arise with how polarized protons are bunched and then injected into RHIC. Given this observation, the residual correlation directly predicts a splitting of the asymmetries and gets the magnitude to within a factor of 2 in three of the four spin patterns.

## 9.7 Replicating the Residual Rate Correlation in Simulations

The residual correlation arises in even the simplest of simulation settings. It can be predicted theoretically, it is seen in the data, so a simulation is the only place left to look. A full simulation is still in progress but we describe the procedure for a quick simulation that generates the residual correlations. This procedure is very short, and goes as follows:

- Use a gaussian distribution to describe both the blue and yellow longitudinal profiles. This is not exactly the shape of the bunches in reality, but it is a reasonable approximation.
- Input the desired values of  $k_S$  and  $k_N$ . For the ZDC and BBC these have of course been measured from data, but one can simulate other values.
- (Optional) Introduce a  $\beta^*$  parameter for the beam focusing.
- Input a known collision rate that generates a Poisson collision distribution.
- Begin a loop of bunch crossings, essentially *CLOCK* triggers. Perform the following steps for each crossing:
  - Choose the number of collisions to occur from the Poisson distribution.
  - Pick a random value from each collision distribution that defines the true  $(t_0, z)$  of the event.
  - Pick randomly, according to the respective detector  $k_{N,S}$ , whether neither side was hit, one side was hit, or a coincidence hit occurred.
  - For each detector side, pick either the earliest hit time (ZDC) or average hit time (BBC) and assign the detector hit time accordingly.
  - If both detector sides are hit, reconstruct the associated vertex.
  - Smear any reconstructed vertices by the respective detector resolutions.
  - Determine if the resulting vertex falls within the required vertex cut.
- In this way, a simulated GL1P scaler, with a vertex cut, can be determined. Thus the observed rate, corresponding to a known input rate, can also be determined.
- Apply a pileup correction to this value.
- Rerun the simulation at any desired input rate to generate a residual rate correlation.

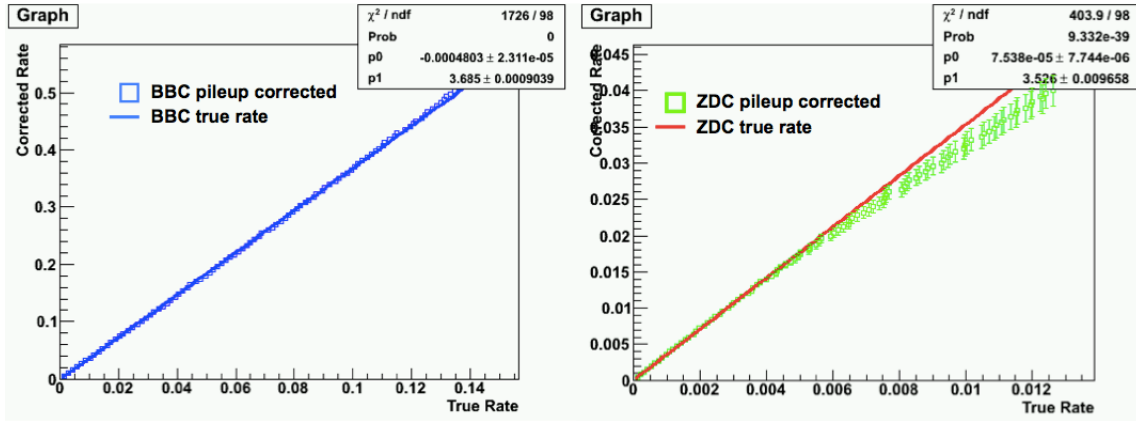


Figure 9.15: Left (a): BBC Simulation results showing the true input rate and the vertex cut scaler with a pileup correction applied. Right (b): The same comparison is shown for the ZDC. The simulation confirms that the luminosity mismeasurement is significantly more severe in the ZDC than the BBC.

Figure 9.15 shows the results obtained from implementing this procedure for both the BBC and ZDC. It shows that the residual rate correction that should be applied to the BBC is very small compared to that needed for the ZDC. This simulation demonstrates the principle that a residual correction can be determined for each detector individually<sup>2</sup>. When the residual correction is made to just one detector, to get from the pileup corrected rate to the true rate, an underlying asymmetry is preserved. The residual correction does not, and cannot, know about a true asymmetry (unlike the case of the fake asymmetries we saw in the previous section). It is just a recipe to get from the pileup corrected scalers to the true rate. This true rate will happen to be slightly higher or lower if an asymmetry exists, but the residual correction only corrects back to this rate. It does not magically know that an asymmetry exists and somehow corrects back to the “true” rate that should have been generated in the absence of an asymmetry. Figure 9.16 shows the comparison of  $\frac{ZDC}{BBC}$  vs  $ZDC$  for the case when there is a 30 cm vertex cut (green) and when the scalers do not have a vertex cut (blue). When there is no vertex cut, the slope is consistent with 0. The 30 cm vertex cut generates a slope of  $\approx 1.21$ , which is within 20% of what the real data shows. Further, this indicates a clear causal relationship between having a vertex cut in the trigger and the generation of a residual correlation.

A full simulation can provide several improvements over the procedure described here. Some of these improvements are:

- Use the WCM data in place of the Gaussian distributions to generate the collision distributions.

<sup>2</sup>We have also shown this to be the case theoretically.

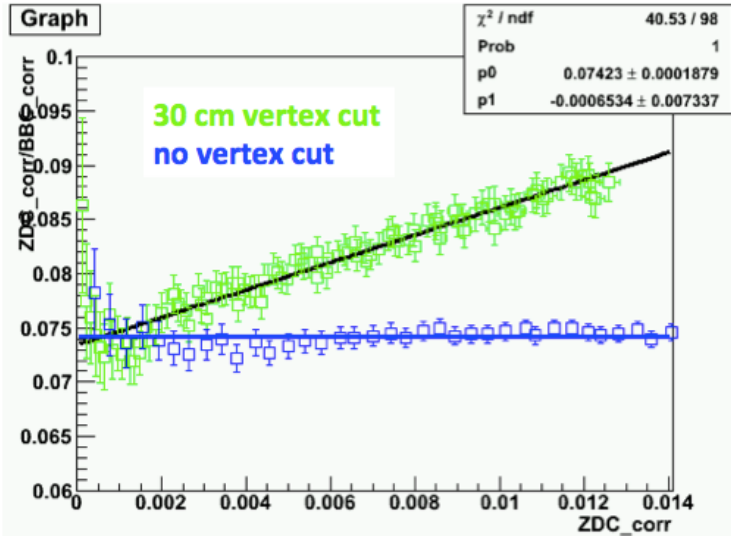


Figure 9.16: Fast simulation showing that just a few realistic experimental inputs (those mentioned above) reproduce the residual correlation. The green points show the ratio of the ZDC to BBC 30 cm pileup corrected scalers.

- Use the fully simulated set of crossings, with appropriate weightings based on the WCM, instead of inputting  $k_{N,S}$  and randomly generating hit results. This will also fold in the  $z$  dependence of the singles to doubles ratios for the BBC.
- Use the TDC values for the BBC as input to the *BBCLL1* trigger emulator to make a trigger decision.
- From the associated hit times at the ZDC, generated by the WCM, use the ZDC calibration constants to work back from hit time to TDC. Use the TDC values as input to the *ZDCLL1* trigger emulator to make a trigger decision.
- Implement the true smearing function for each detector instead of assuming a normal distribution.

## 9.8 Effect of a Systematic Error of $k_{N,S}$ on the Residual Correlation

The value of  $k_{S,N}$  determine the exact shape of the pileup correction. Therefore, a systematic error in these values propagates to a systematic error in the slope of the residual correlation that is generated. Because the 0-rate value is equivalent to having no beam rate, and hence no pileup correction, we expect it to be strongly insensitive to systematic changes in  $k_{N,S}$ . However, the slope of the correlation, which does couple

to  $K$ , should be affected. We assume that a systematic error would be correlated for both the north and south singles to double ratios and thus vary them together. The result is shown in Table 9.7. The residual correlation parameters for one run are determined as a scan through  $\frac{\Delta k}{k} = 0, \pm 5\%, \pm 10\%$  is performed for the BBC and ZDC independently. As expected, the 0-rate ratio is very nearly unaffected while the slope does change, especially when varying the the ZDC  $k_{N,S}$

The next step is to look at how the final asymmetry is affected by a systematic error in  $k_{N,S}$ . We perform the same scan over variations of  $\frac{\Delta k}{k}$  as before. Table 9.8 shows the result of the scan when pileup corrections alone are used. Table 9.9 shows the results of the scan when a residual correction is done to the BBC. Table 9.10 shows the results of doing the residual correction to the ZDC. It is admittedly difficult to precisely estimate the systematic error in  $k_{N,S}$  and therefore propagate it through to the asymmetry. The statistical error in its determination is quite small, but the true value may fluctuate systematically over time due to changing detector performance (efficiency). One way to check this would be to determine  $k_{N,S}$  on shorter time scales than what was done in Fig. 8.13. This could be done using STAR scalers instead of *CLOCK* triggered data. In Run09  $\sqrt{s} = 500$  GeV we can only use the available data. We take, as a very conservative estimate, a 10% correlated systematic uncertainty in  $k_N$  and  $k_S$ , separately for the BBC and ZDC. Further, we assume a flat probability distribution over the scanning range, as opposed to a normal distribution. Therefore, we give the same weight to values lying further from the central value than a normal distribution would. Doing this, we find the resulting r.m.s. variation of the asymmetry is  $\delta A_{LL} = 0.15 \times 10^{-4}$ . A more thorough study would likely show the true effect to be smaller. As a result, we modify the final estimate for the relative luminosity systematic uncertainty from Eq. 9.24 to

$$\delta R^{ZDC/BBC} = (1.36 + 0.87(stat.) + 0.15(syst.)) \times 10^{-4} = 2.38 \times 10^{-4} \quad (9.28)$$

The final value is a linear sum as before, not a sum in quadrature. Taking the quadrature sum would yield  $\delta R^{ZDC/BBC} = 1.62 \times 10^{-4}$ .

Table 9.7: Effect of Systematic Error of  $k_{N,S}$  on 0-rate value of  $\frac{ZDC}{BBC}$  and residual correlation slope for one run.

BBC $\frac{\Delta k_{N,S}}{k_{N,S}}$	ZDC $\frac{\Delta k_{N,S}}{k_{N,S}}$	Fit Constant for 0-rate value	Fit Constant for Slope
-10%	-10%	0.05834	1.043
	-5%	0.05821	1.004
	0%	0.05817	0.9512
	5%	0.05807	0.9046
	10%	0.05803	0.8498
-5%	-10%	0.05833	1.051
	-5%	0.05820	1.012
	0%	0.05817	0.9589
	5%	0.05807	0.9123
	10%	0.05802	0.8575
0%	-10%	0.05834	1.057
	-5%	0.05821	1.019
	0%	0.05817	0.9655
	5%	0.05807	0.9190
	10%	0.05803	0.8641
5%	-10%	0.05834	1.064
	-5%	0.05821	1.026
	0%	0.05817	0.9728
	5%	0.05808	0.9262
	10%	0.05803	0.8714
10%	-10%	0.05836	1.070
	-5%	0.05823	1.031
	0%	0.05820	0.9870
	5%	0.05810	0.9314
	10%	0.05805	0.8766

Table 9.8: Effect of Systematic Error of  $k_{N,S}$  on  $A_{LL}^{ZDC/BBC}$  and the fitting  $\chi^2$  with pileup corrections but no residual rate corrections. The number of degrees of freedom of the fit is  $NDF = 202$  in each case.

BBC $\frac{\Delta k_{N,S}}{k_{N,S}}$	ZDC $\frac{\Delta k_{N,S}}{k_{N,S}}$	$A_{LL}^{ZDC/BBC} (\times 10^{-4})$	$\chi^2$ of fit to constant
-10%	-10%	3.398	4754
	-5%	3.294	4034
	0%	2.875	3549
	5%	2.445	3252
	10%	2.623	2982
-5%	-10%	3.483	4803
	-5%	3.378	4085
	0%	2.960	3591
	5%	2.529	3291
	10%	2.708	3022
0%	-10%	3.553	4869
	-5%	3.449	4141
	0%	3.030	3645
	5%	2.599	3344
	10%	2.777	3074
5%	-10%	3.539	4930
	-5%	3.434	4197
	0%	3.015	3699
	5%	2.584	3394
	10%	2.762	3113
10%	-10%	3.613	4992
	-5%	3.508	4256
	0%	3.089	3750
	5%	2.658	3445
	10%	2.836	3164

Table 9.9: Effect of Systematic Error of  $k_{N,S}$  on  $A_{LL}^{ZDC/BBC}$  and the fitting  $\chi^2$  with pileup corrections and a residual rate correction applied to the BBC only. The number of degrees of freedom of the fit is  $NDF = 201$  in each case.

BBC $\frac{\Delta k_{N,S}}{k_{N,S}}$	ZDC $\frac{\Delta k_{N,S}}{k_{N,S}}$	$A_{LL}^{ZDC/BBC} (\times 10^{-4})$	$\chi^2$ of fit to constant
-10%	-10%	-0.3428	1324
	-5%	-0.6236	960
	0%	-1.275	906
	5%	-2.019	985
	10%	-2.183	1093
-5%	-10%	-0.2242	1344
	-5%	-0.523	975
	0%	-1.1151	903
	5%	-1.890	970
	10%	-2.048	1068
0%	-10%	-0.1145	1379
	-5%	-0.3899	993
	0%	-1.035	910
	5%	-1.769	966
	10%	-1.921	1050
5%	-10%	-0.0946	1403
	-5%	-0.3678	1005
	0%	-1.010	911
	5%	-1.739	952
	10%	-1.886	1013
10%	-10%	0.0197	1439
	-5%	-0.2503	1031
	0%	-0.8885	919
	5%	-1.612	950
	10%	-1.753	1000

Table 9.10: Effect of Systematic Error of  $k_{N,S}$  on  $A_{LL}^{ZDC/BBC}$  and the fitting  $\chi^2$  with pileup corrections and a residual rate correction applied to the ZDC only. The number of degrees of freedom of the fit is  $NDF = 201$  in each case.

BBC $\frac{\Delta k_{N,S}}{k_{N,S}}$	ZDC $\frac{\Delta k_{N,S}}{k_{N,S}}$	$A_{LL}^{ZDC/BBC} (\times 10^{-4})$	$\chi^2$ of fit to constant
-10%	-10%	-1.296	626
	-5%	-1.190	505
	0%	-1.304	520
	5%	-1.428	549
	10%	-0.9542	558
-5%	-10%	-1.238	620
	-5%	-1.113	505
	0%	-1.246	515
	5%	-1.369	544
	10%	-0.8961	557
0%	-10%	-1.203	627
	-5%	-1.097	507
	0%	-1.211	520
	5%	-1.334	550
	10%	-0.8614	564
5%	-10%	-1.250	620
	-5%	-1.145	500
	0%	-1.259	514
	5%	-1.382	545
	10%	-0.9098	551
10%	-10%	-1.207	622
	-5%	-1.102	503
	0%	-1.216	514
	5%	-1.339	548
	10%	-0.8664	557

## 9.9 Residual Rate Correlation in the Run09 $\sqrt{s} = 200$ GeV Data and Elsewhere

The residual correlation is a very general consequence of a vertex cut being imposed on a coincidence trigger. Therefore, as ubiquitous as it has been in the 2009 dataset at  $\sqrt{s} = 500$  GeV, we look for it as well in other datasets. Table 9.11 shows a summary of where this effect has been seen. The same ubiquity is found elsewhere.

Case	Year	$\sqrt{s}(GeV)$	Res. Rate Corr. seen?
2-coll approx	—	—	yes
simulation	—	—	yes
GL1P data	2009	500	yes
GL1P data	2009	200	yes
STAR scaler data	2012	510	yes
STAR scaler data	2013	510	yes

Table 9.11: Summary of all instances where a residual correlation has been predicted or found to exist. No examples have been found where a residual rate correlation does not exist or is predicted to not exist.

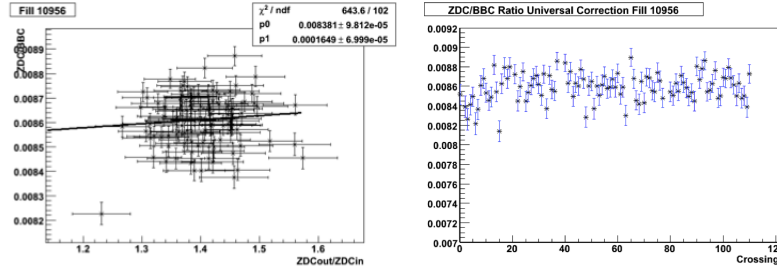


Figure 9.17: The width correction plots shown for fill 10956 taken during Run09  $\sqrt{s} = 200$  GeV. Left (a): The width correlation. Right (b): The resulting  $\frac{ZDC}{BBC}$  vs. crossing is shown with artificially increased error bars due to the determination of the width correlation itself.

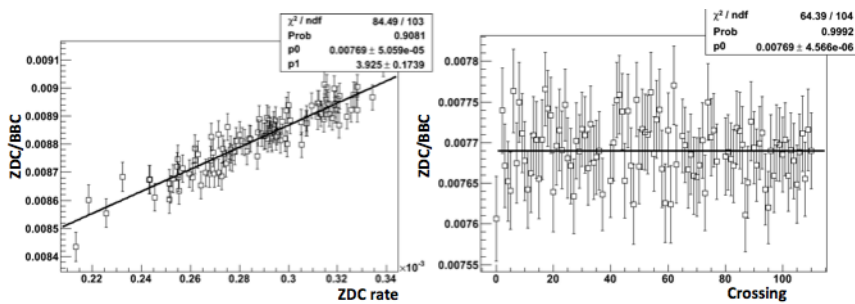


Figure 9.18: Left (a): A sample residual correlation is shown at  $\sqrt{s} = 200$  GeV. Right (b): The result of a residual correction to the ZDC. These plots use the same data as shown in Fig. 9.17.

In Figure 9.17a we show an example from the last chapter where the width correlation is tenuous. Figure 9.17b shows the result after applying the universal width correction. Note that the error bars in this plot have been increased which makes the fluctuation appear more statistical than it truly is. To show the potency of the residual correlation and correction, we compare to the same data from the same fill using the same scalers. The resulting residual rate correlation is shown in Figure 9.18a. In Figure 9.18b, we show the result of a ZDC residual rate correction. Note that the slope of the residual correlation here is much different. This is due, surprisingly, to very different  $k_{N,S}$  for the ZDC. While at  $\sqrt{s} = 500$  GeV we found a value of around 3.5, at  $\sqrt{s} = 200$  GeV we find a very large value of  $\approx 18$ . Note also that a comparison of the width correction and the residual correction yield a different absolute level of the ratio. The width correction assumes the uncorrected absolute ratio is rate independent, and therefore should not be modified. Of course, applying a standard set of pileup corrections shows that the baseline changes significantly. The residual correction modifies the baseline value to the true 0-rate value, found to be  $\approx 0.00769$  at this center of mass energy. The error bars, as always in the residual rate correction, are not artificially increased. It seems that a treatment of the systematic errors in this dataset where rate effects are considered is essential. Pileup corrections are not currently considered. A large improvement in the precision of this dataset can be realized by doing so, and a further improvement is likely to be seen by considering the residual rate correlation, which is demonstrated to exist.

## 9.10 Concluding Remarks on the Residual Rate Correlation and Correction

$A_{LL}$  measurements at PHENIX, with the intent to provide strong constraints on the size and shape of  $\Delta G = \int_0^1 \Delta g(x)dx$ , are quickly turning out to be systematics limited. As the collision rates have historically gone up, the systematic uncertainties have also gone up while the statistical error bars have gone down. With the accumulated data through Run13, the statistical error bars will decrease further. In this chapter we have outlined a new idea, the Residual Rate Correlation. We have shown that even a cursory attempt at a Residual Rate Correction to the luminosity provides a substantial improvement to our understanding by any measurable standard. As this idea is new, the most immediate improvement towards an enhanced Residual Rate Correction would be determining the exact form of the correction for both the ZDC and the BBC as a function of their respective rates. The BBC requires a correction that is very roughly 25% as large as the ZDC at the rates seen in the data we studied.

The Residual Rate Correlation can be predicted using a simple approximation scheme, it is replicated in simulations and it is seen in the data. There is no doubt about whether this correlation exists and a Residual Rate Correction is very much needed. A fully proper correction to both the BBC and the ZDC can be determined from a simulation study and most likely more can be learned from the data itself. The limited simulation we outlined showed the principle that a correction to each detector can be determined independently of the other. Yet, even in the approximation that only the ZDC is subject to a residual correlation we have seen a reduction in the systematic uncertainty by one order of magnitude to the  $O(10^{-4})$  level. This is the predicted size of  $A_{LL}$  at low- $p_T$  due to a gluon polarization and also the approximate size of the expected statistical error bars from the combination of statistics in 2009, 2011, 2012 and 2013. Therefore, the Residual Rate Correlation may make sensitivity to  $\Delta G$  at low- $x$  an achievable goal.

# Chapter 10

## Conclusion

The proton spin arises from a combination of quark polarization, gluon polarization, and quark and gluon orbital angular momentum. The quark polarizations have been measured and well constrained in Deep Inelastic Scattering (DIS) experiments. It is found that this accounts for  $\approx 30\%$  of the total proton spin. The next step to understand the proton spin is to constrain the gluon polarization,  $\Delta G$ . This can be done in polarized  $ep$  scattering by measuring scaling violations of  $g_1^p$ , but the kinematic range of the available data does not allow for a precise constraint on  $\Delta G$  to be imposed. Even extreme scenarios of gluon polarization, such as  $|\Delta G| \gtrsim \frac{1}{2}\hbar$ , are not excluded by the polarized DIS data.

The motivation to study the gluon polarization at a  $pp$  collider is that the gluons of one proton interact directly, at leading order, with the quarks and gluons of the other proton.  $A_{LL}$ , the cross section asymmetry between collisions of protons of like and unlike sign helicities, has significant contributions from gluon-gluon scattering,  $\propto \Delta g(x_1)\Delta g(x_2)$ , quark-gluon scattering,  $\propto \Delta q(x_1)\Delta g(x_2)$ , and quark-quark scattering,  $\propto \Delta q(x_1)\Delta q(x_2)$  at high  $p_T$ . The relative weighting of these contributions depends on the details of the final state that is measured, such as the selected particles,  $p_T$ , rapidity, etc. At PHENIX, one of two experiments at RHIC - the only polarized  $pp$  collider in the world - extreme scenarios of gluon polarization have been excluded by measuring  $A_{LL}$  at mid-rapidity. However,  $pp$  interactions where jets or hadrons at mid-rapidity are observed do not effectively sample gluons with Bjorken- $x < 0.05$ . This leaves the experimenter blind with respect to a potentially substantial gluon polarization in this region. This means that once more, the inability of experiments to access a broad enough kinematic range has resulted in a serious limitation on the constraining power for  $\Delta G$ .

This serves as motivation to build a forward electromagnetic calorimeter that can trigger on single hadrons. A measurement of  $A_{LL}$  for a final state in which a forward hadron is triggered has significant sensitivity to collisions in which a gluon with  $x \sim 0.01$  interacts with a quark in the valence region. This means that the value of  $\Delta g(x \approx 0.01)$  will play a substantial role in the observed  $A_{LL}$ . In Chapters 5 and 6 we discussed

the first two such measurements using data taken at  $\sqrt{s} = 200 \text{ GeV}$  and  $\sqrt{s} = 500 \text{ GeV}$ .

To extend the sensitivity of the  $A_{LL}$  measurement to even lower  $x$  with the goal of extending the constraint to  $\Delta g(x \approx 0.001)$ , it was shown that the final state at forward rapidity had to be modified from a single hadron to a di-hadron. To realize this, an upgrade to the MPC electronics including an overhaul of the trigger was required. This upgrade was successfully completed as part of this thesis in time to record  $180 \text{ pb}^{-1}$  of data within a  $30 \text{ cm}$  vertex cut which amounts to about 85% of the total longitudinal  $pp$  data recorded at  $\sqrt{s} = 500 \text{ GeV}$  and  $\sqrt{s} = 510 \text{ GeV}$ . This data will provide the strongest constraint on  $\Delta G$  for the next decade before the construction and commissioning of an EIC is complete. It should be noted just how incredibly cost-efficient the MPC is in providing these new abilities. The cost to construct PHENIX was  $O(\$10^8)$ . The cost to operate the RHIC accelerator for 24 hours is  $O(\$10^6)$ . Meanwhile, the additional cost to construct the MPC was  $\approx \$4 \times 10^4$  and the cost of the electronics upgrade was  $\approx 1 \times 10^4$ . In other words, the total cost associated with the MPC represents 0.05% of the total cost of PHENIX and the equivalent of roughly 1 hour of RHIC operations.

The last major hurdle to making the entire  $\Delta G$  program feasible is the reduction of the systematic uncertainty in relative luminosity. The expected  $A_{LL}$  of  $\pi^0$ 's with moderate  $p_T$  at mid-rapidity, as well as at forward rapidity, is  $O(10^{-4})$ . However, the size of this systematic uncertainty, until recently, has been  $O(10^{-3})$  which is at the level of the statistical uncertainty prior to the high luminosity data samples from 2012 and 2013. PHENIX, in its mid-rapidity  $A_{LL}$  measurements, has proven unable to control this uncertainty and unable to understand its origins. This makes the relative luminosity uncertainty the bottleneck of the measurement and renders further statistics irrelevant in the case of the mid-rapidity  $\pi^0$ . The same bottleneck applies to the high statistics single hadron  $A_{LL}$  at forward rapidity. Because of its fundamental importance, an extensive effort was undertaken in this thesis to control this systematic uncertainty and to prevent it from remaining the bottleneck in the constraint of  $\Delta G$ . Chapters 8 and 9 were dedicated to explaining my work in this very important aspect of the  $\Delta G$  measurement. As a result of the new insights provided, this systematic can now be controlled, and the very rich sets of data accumulated over the past two years can now be utilized to their full potential.

Figure 10.1 shows a summary of the progress in  $A_{LL}$  that results directly from my thesis work. The best sensitivity to low- $x$  gluons occurs in the lower  $p_T$  bins and at high  $\sqrt{s} (= 500 \text{ GeV})$  which is the data shown. The measured result for single hadrons at this collision energy from the 2009 data is shown in blue.

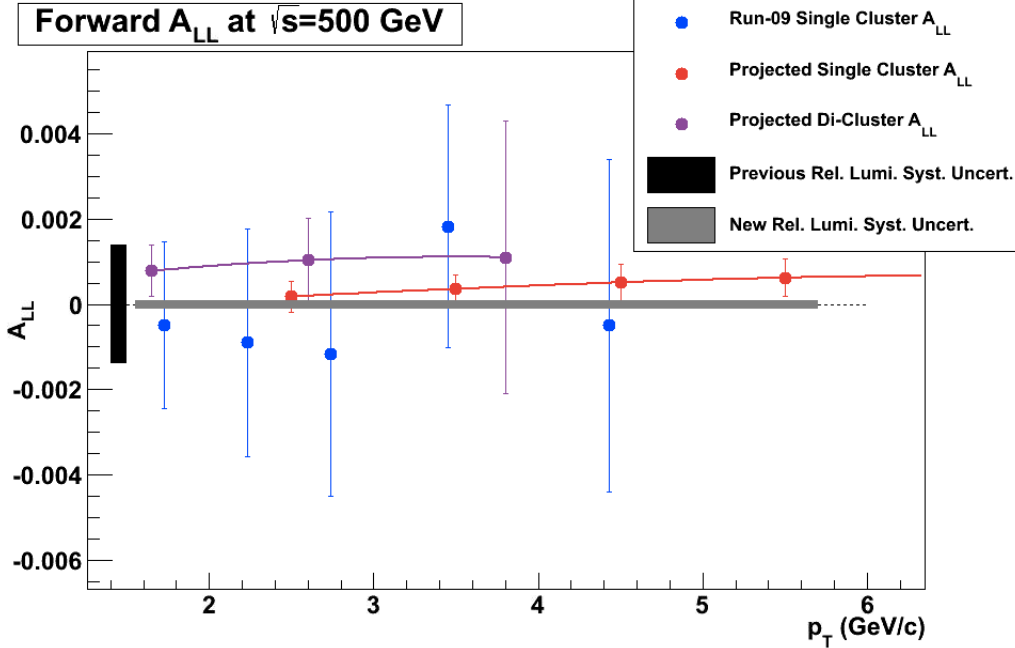


Figure 10.1: A final summary plot of the current and projected status of the forward single and di-hadron measurements. The error bars on the projected asymmetries use an assumed integrated luminosity of  $200 \text{ pb}^{-1}$  within a  $30 \text{ cm}$  vertex cut which represents the available longitudinal data. A full description of the information contained in this figure is given in the text.

In red, the projected  $A_{LL}$  is shown with the error bars scaled to the total figure of merit <sup>1</sup> accumulated at PHENIX at this energy. The magenta points represent the projected  $A_{LL}$  from di-hadrons as a function of the leading hadron  $p_T$ . In both of these projections it is clear that the figure of merit of the data taken, considered alone, will allow a strong constraint to be placed on  $\Delta G$  at low- $x$ . Even a small value of the asymmetry can imply a substantial gluon polarization due to large gluon number density at low- $x$ . It is for this reason that the  $\Delta G$  measurement at low- $x$  is crucial to understanding the spin structure of the proton. Even though the measurements require high precision, the range of possible gluon polarizations that can be extracted from a global QCD analysis is quite large.

Finally, the black bar in this figure shows the relative luminosity uncertainty that has been achieved in the mid-rapidity  $A_{LL}$  results and would, by default, be applied to the forward  $A_{LL}$  results. If applied to the data, this uncertainty would single-handedly erase the increased statistical precision resulting from the large amount of data now accumulated for both the mid- and forward rapidity measurements. The accomplishment I am most proud of is the new level of understanding achieved in the relative luminosity determination

<sup>1</sup>The figure of merit is defined at  $P^4 L$  where  $P$  is the average beam polarization and  $L$  is the integrated luminosity.

as shown in the grey bar. This significant reduction in the relative luminosity uncertainty achieved in this thesis will make it possible to take full advantage of the large statistics data samples acquired in 2012 and 2013 at RHIC.

# References

- [1] <http://matt.might.net/articles/phd-school-in-pictures>
- [2] Thomson, J.J. (1904) 'XXIV. On the Structure of the Atom: An Investigation of the Stability and Periods of Oscillation of a Number of Corpuscles Arranged at Equal Intervals Around the Circumference of a Circle; with Application of the Results to the Theory of Atomic Structure', Philosophical Magazine Series 6, 7, 39: 237-265
- [3] Rutherford, E. (1911) 'LXXIX. The Scattering of  $\alpha$  and  $\beta$  Particles By Matter and the Structure of the Atom', Philosophical Magazine Series 6, 21: 125, 669-688
- [4] Precision Measurement of Charged Pion and Kaon Multiplicities in  $e^+e^-$  Annihilation at  $Q = 10.5\text{ GeV}$ , Thesis Dissertation, Martin Leitgab (University of Illinois at Urbana-Champaign, 2013). Publication Pending.
- [5] High-Energy Inelastic  $e p$  Scattering at 6-Degrees and 10-Degrees, E. Bloom, et. al., Phys. Rev. Lett. 23 930 (1969)
- [6] Observed Behavior of Highly Inelastic Electron-Proton Scattering, M. Breidenbach et al., Phys. Rev. Lett. 23, 935 (1969)
- [7] Asymptotic Sum Rules at Infinite Momentum, J.D. Bjorken, Phys. Rev. 179, 1547 (1969)
- [8] Measurement of Transverse Spin Asymmetries in Polarized Proton-Proton Collisions, and the Realization of New Electromagnetic Calorimeters for Forward Physics. Thesis Dissertation, John Koster (University of Illinois at Urbana-Champaign, 2010)
- [9] Alekseev, I., et al. Polarized Proton Collider at RHIC. Nucl. Instrum. Methods A 499 (2003), 392414
- [10] R.P. Feynman, Photon-hadron interactions (Benjamin, New York, 1972)
- [11] J. Kogut and L. Susskind, Phys. Reports 8 (1973) 76
- [12] Prospects for Spin Physics, Ann.Rev.Nucl.Part.Sci.50:525-575, 2000
- [13] Parton distributions for the LHC, Eur.Phys.J.C63:189-285,2009
- [14] C. Adloff, et. al., Measurement and QCD Analysis of Neutral and Charged Current Cross Sections at HERA. Eur. Phys. J. C30 (2003) 1-32.
- [15] C. Adloff, et. al., Deep-Inelastic Inclusive  $e p$  Scattering at low  $x$  and a Determination of  $\alpha_S$ . Eur. Phys. J. C21 (2001) 33-61.
- [16] S. Chekanov, et. al., Measurement of the Neutral Current Cross Section and F2 Structure Function for Deep Inelastic  $e + p$  Scattering at HERA. Eur. Phys. J. C21 (2001) 443471
- [17] F. D. Aaron, et. al., Combined Measurement and QCD Analysis of the Inclusive  $e p$  Scattering Cross Sections at HERA. JHEP 01 (2010) 109

- [18] M. Arneodo, et. al., Measurement of the Proton and the Deuteron Structure Functions, F2(p) and F2(d). Phys. Lett. B364 (1995) 107115
- [19] A. C. Benvenuti, et. al., Test of QCD and a Measurement of Lambda from Scaling Violations in the Proton Structure Functions F(2)(x, Q\*\*2) at High Q\*\*2. Phys. Lett. B223 (1989) 490
- [20] Asymptotic Freedom in Parton Language, G. Altarelli, G. Parisi. Nucl. Phys. B126:298 (1977); Calculation of the Structure Functions for Deep Inelastic Scattering and  $e^+e^-$  Annihilation by Perturbation Theory in Quantum Chromodynamics, Yu. L. Dokshitzer. Sov. Phys. JETP, 46:641 (1977)
- [21] Polarized Electroproduction in Asymptotically Free Gauge Theories, Sasaki K 1975 Prog. Theor. Phys. 54 1816
- [22] Polarized lepton-hadron scattering in asymptotically free gauge theories, M.A. Ahmed and G.G. Ross, Nucl. Phys. B 111 441 (1976)
- [23] The Calculation of the Two-Loop Spin Splitting Functions  $P_{ij}^{(1)}(x)$ , R. Mertig and W.L. van Neerven, Z.Phys. C 70 (1996) 637-654
- [24] Rederivation of the Spin-Dependent Next-to-Leading Order Splitting Functions, W. Vogelsang, Phys. Rev. D 54 2023 (1996); The Spin-Dependent Two-Loop Splitting Functions, W. Vogelsang, Nucl. Phys. B 475 47 (1996)
- [25] Halzen, Martin. Quarks and Leptons: An Introductory Course in Particle Physics (1984)
- [26] The Spin Structure of the Nucleon, Phil. Trans. R. Soc. Lond. A 2001 359, 379-389
- [27] Where Does the Proton Really Get Its Spin?, Robert Jaffe, Physics Today, 1995
- [28] The  $g_1$  Problem: Deep Inelastic Scattering and the Spin of the Proton, R.L. Jaffe and A. Manohar, Nucl. Phys. B 337, 509 (1990)
- [29] Gauge-Invariant Decomposition of Nucleon Spin, X. Ji, Phys. Rev. Lett. 78, 610 (1997)
- [30] Spin and Orbital Angular Momentum of the Proton, A.W. Thomas, Int.J.Mod.Phys.E18:1116-1134,2009
- [31] Precise Determination of the Spin Structure Function  $g_1$  of the Proton, Deuteron and Neutron. A. Airapetian et al, Phys. Rev. D 75 (2007) 012007
- [32] Deep Inelastic Scattering of Polarized Electrons by Polarized Protons, M.J. Alguard et. al., Phys. Rev. Lett. 37, 1261 (1976)
- [33] Deep-Inelastic e-p Asymmetry Measurements and Comparison with the Bjorken Sum Rule of Proton Spin Structure, M.J. Alguard et. al., Phys. Rev. Lett. 41, 70 (1978)
- [34] New Measurement of Deep-Inelastic e-p Asymmetries, G. Buam, et. al., Phys. Rev. Lett. 51, 1135 (1983)
- [35] Determination of Polarized Parton Distribution Functions and Their Uncertainties, M. Hirai, S. Kumano and N. Saito (AAC), Phys. Rev. D69 054021 (2004)
- [36] QCD Analysis of Polarized Deep-Inelastic Scattering Data and Parton Distributions, J. Blümlein, H. Böttcher (BB), Nucl. Phys. B 636 225 (2002)
- [37] Models for the Polarized Parton Distributions of the Nucleon, M. Glück, E. Reya, M. Stratmann, W. Vogelsang (GRSV), Phys. Rev. D 63 094005 (2001)
- [38] An Investigation of the Spin Structure of the Proton in Deep Inelastic Scattering of Polarised Muons on Polarised Protons, EMC, CERN-EP/89-73, 8 June 1989
- [39] Electron Ion Collider: The Next QCD Frontier - Understanding the Glue that Binds Us All. A. Accardi, et. al., BNL-98815-2012-JA; JLAB-PHY-12-1652. arXiv:1212.1701 [nucl-ex]

- [40] Chiral Substructure of the Nucleon, R.D. Carlitz, J. Kaur: Phys. Rev. Lett. 38 (1977) 673
- [41] Chiral Substructure of the Nucleon, R.D. Carlitz, J. Kaur: Phys. Rev. Lett. 38 (1977) 1102
- [42] Spin Distributions in the Quark Parton Model, J Kaur, Nucl. Phys. B128 (1977) 219
- [43] J. Ellis and R.L. Jaffe, Phys. Rev. D9 (1974) 1444; D10 (1974) 1669
- [44] Global Analysis of Helicity Parton Densities and Their Uncertainties, D. de Florian, R. Sassot, M. Stratmann, and W. Vogelsang, Phys. Rev. Lett. 101:072001,2008
- [45] Extraction of Spin-Dependent Parton Densities and Their Uncertainties, D. de Florian, R. Sassot, M. Stratmann, and W. Vogelsang, Phys. Rev. D80:034030,2009
- [46] Private Communications with M. Chiu, M. Stratmann
- [47] Lectures on Perturbative QCD, July 25-28 2005, PHENIX SpinFest, RIKEN, Wako, Japan
- [48] Inclusive Cross Section and Double Helicity Asymmetry for  $\pi^0$  Production in  $p+p$  collisions at  $\sqrt{s} = 200$  GeV: Implications for the Polarized Gluon Distribution in the Proton, Phys. Rev. D 76, 051106 (2007)
- [49] Cross Section and Double Helicity Asymmetry for Eta Mesons and Their Comparison to Neutral Pion Production in Proton-Proton Collisions at  $\sqrt{s} = 200$  GeV, Phys. Rev. D 83, 032001 (2011)
- [50] Cross Sections and Double Helicity Asymmetries of Mid-Rapidity Inclusive Charged Hadrons in  $p + p$  at  $\sqrt{s} = 62.4$  GeV, Phys. Rev. D 86, 092006 (2012)
- [51] Double-Spin Asymmetry of Electrons From Heavy-Flavor Decays in  $p + p$  Collisions at  $\sqrt{s} = 200$  GeV, Phys. Rev. D 87, 012011 (2012)
- [52] Unbiased Determination of Polarized Parton Distributions and Their Uncertainties, R. Ball, et. al, CERN-PH-TH/2012-036, IFUM-987-FT, Edinburgh 2013/04
- [53] The RHIC Spin Program, 2012 Tribble Committee Document, [www.bnl.gov/npp/docs/RHIC-Spin-WriteUp-121105.pdf](http://www.bnl.gov/npp/docs/RHIC-Spin-WriteUp-121105.pdf)
- [54] A. Zelenski, et al., The RHIC Optically-Pumped Polarized H- Ion Source. AIP Conf. Proc., Vol. 980, 22123 (2008)
- [55] A. Kponou, et al., Sona Transition Studies in the RHIC OPPIS. AIP Conf. Proc., Vol. 980, 241247 (2008)
- [56] H. Hahn, et al., The RHIC Design Overview. NIM A499 245-263 (2003)
- [57] T. Roser, et al., Accelerating and Colliding Polarized Protons in RHIC with Siberian Snakes. Proceedings of EPAC 2002, Paris, France
- [58] A. Zelenski et al., Absolute Polarized H-jet Polarimeter Development for RHIC. NIM A536, 248254 (2005)
- [59] H. Huang et al., Commissioning of RHIC p-Carbon CNI Polarimeter. NIM A721, 356359 (2003)
- [60] T. Roser, et al., Spin Rotators and Split Siberian Snakes. NIM A342, 343-347 (1990)
- [61] S. H. Aronson et al., PHENIX Magnet System. NIM A499, 480488 (2003)
- [62] D.S. Barton, et al., RHIC Control System. NIM A499 356-371 (2003)
- [63] M. Bai, et al., RHIC Beam Instrumentation. NIM A499 372-387 (2003)
- [64] PHENIX Detector Overview. K. Adcox et al., NIM A499 469-479 (2003)

- [65] K. Adcox, et al., PHENIX Central Arm Tracking Detectors. NIM A499, 489507 (2003)
- [66] M. Aizawa, et al., PHENIX Central Arm Particle ID Detectors. NIM A499, 508520 (2003)
- [67] L. Aphecetche, et al., The PHENIX Calorimeter, NIM A499, 521536 (2003)
- [68] H. Akikawa, et al., PHENIX Muon Arms. NIM A499, 537548 (2003)
- [69] Conceptual Design Report for a Fast Muon Trigger. [https://www.phenix.bnl.gov/WWW/trigger/muonupgrade/CDR/CDR\\_final.pdf](https://www.phenix.bnl.gov/WWW/trigger/muonupgrade/CDR/CDR_final.pdf)
- [70] S. Butsyk, The Forward Vertex Upgrade Detector for PHENIX. Eur. Phys. J. C (2009) 62: 21-24
- [71] PHENIX Inner Detectors. M. Allen et. al., NIM A499 549-559 (2003)
- [72] C. Adler, et al. The RHIC Zero Degree Calorimeters. NIM A470 488499 (2001)
- [73] The RHIC Zero-Degree Calorimeters. C. Adler, et al., NIM A499 433-436 (2003)
- [74] PHENIX On-line Systems. S.S. Adler et al., NIM A499 560-592 (2003)
- [75] Double Helicity Asymmetry in Inclusive Mid-Rapidity Neutral Pion Production for Polarized  $p + p$  Collisions at  $\sqrt{s} = 200 \text{ GeV}$ . S. Adler, et. al., Phys. Rev. Lett. 93:202002,2004
- [76] Improved Measurement of Double Helicity Asymmetry in Inclusive Midrapidity  $\pi^0$  Production for Polarized  $p + p$  Collisions at  $\sqrt{s} = 200 \text{ GeV}$ . S. Adler, et. al., Phys. Rev. D73:091102,2006
- [77] Inclusive Cross Section and Double Helicity Asymmetry for  $\pi^0$  Production in  $p + p$  Collisions at  $\sqrt{s} = 200 \text{ GeV}$ : Implications for the Polarized Gluon Distribution in the Proton. A. Adare, et. al., Phys. Rev. D76:051106,2007
- [78] The Gluon Spin Contribution to the Proton Spin from the Double Helicity Asymmetry in Inclusive  $\pi^0$  Production in Polarized  $p + p$  Collisions at  $\sqrt{s} = 200 \text{ GeV}$ . A. Adare, et. al., Phys. Rev. Lett. 103:012003,2009
- [79] Cross sections and Double-Helicity Asymmetries of Midrapidity Inclusive Charged Hadrons in  $p + p$  Collisions at  $\sqrt{s} = 62.4 \text{ GeV}$ . A. Adare, et. al, arXiv:1202.4020 [hep-ex]
- [80] Double Spin Asymmetry of Electrons from Heavy Flavor Decays in  $p + p$  Collisions at  $\sqrt{s} = 200 \text{ GeV}$ . A. Adare, et. al, arXiv:1209.3278 [hep-ex]
- [81] Constraining  $\Delta G$  at Low x with Double Longitudinal Spin Asymmetries for Forward  $pi^0$ 's. C. McKinney, et. al., PHENIX Analysis Note 1005
- [82] MPC Calibration, M. Chiu, et. al., PHENIX Analysis Note 927.
- [83] MPC Cluster  $A_{LL}$  in Run-09  $p + p$  200 GeV, S. Wolin, et. al., PHENIX Analysis Note 944
- [84] MPC Clustering: Description, Performance, and Comparison of Run8  $p + p$  Data and Simulation, B. Meredith, PHENIX Analysis Note 949
- [85] MPC Cluster Decomposition Estimates at  $\sqrt{s} = 200 \text{ GeV}$ . A. Vossen, et. al, Phenix Analysis Note 895
- [86] Muon Piston Calorimeter offline code in the PHENIX CVS Repository `offline/packages/mpc`
- [87] Stopping of Energetic Light Ions in Elemental Matter, J. F. Ziegler, Applied Physics Reviews/J. Applied Physics, 85, 1249-1272 (1999)
- [88] Muon Piston Calorimeter Letter of Intent, T. Awes, et al., PHENIX Technical Note 429
- [89] Presentation on MPC Beam Test Results, (2006) <https://www.phenix.bnl.gov/WWW/p/draft/chiu/talks/mpc/20061101>

- [90] Beam Test Results, Andrey Kazantsev, <http://www.phenix.bnl.gov/~stkav/MPC/BT.html>
- [91] Muon Piston Calorimeter Homepage, <https://www.phenix.bnl.gov/WWW/p/upgrades/mpc/index.html>
- [92] Run9 500 GeV Cluster  $A_{LL}$  in the MPC, S. Wolin, et. al, PHENIX Analysis Note 1023.
- [93] J. Beringer, et al. (Particle Data Group), PRD 86, 010001 (2012) <http://pdg.lbl.gov>
- [94] L. Aphecetche et al., The PHENIX Calorimeter. Nucl. Instr. and Meth., Vol. A499, pp. 521536 (2003)
- [95] S.S. Frank, C.L. Britton, A. L. Wintenberg, G. R. Young, Trigger Circuits for the PHENIX Electromagnetic Calorimeter. Nuclear Science Symposium, IEEE, Vol. 1, 9-15, pp.680,684 (Nov 1997)
- [96] W. Anderson, et al., Nucl. Instr. and Meth. A (2011)
- [97] B. Azmoun, et. al., Conceptual Design Report on a HBD Upgrade for the PHENIX Detector. March 2005. [http://www.phenix.bnl.gov/WWW/TPCHBD/HBD\\_CDR.pdf](http://www.phenix.bnl.gov/WWW/TPCHBD/HBD_CDR.pdf)
- [98] C. -Y Chi, B. Cole, J. Nagle, W. Sippach, W.A. Zajc, Data Collection Modules for the PHENIX Experiment. Nuclear Science, IEEE Transactions, Vol 45, No.4, (1913,1916) (Aug 1998)
- [99] Cadence PSpice A/D and Advanced Analysis. [http://www.cadence.com/products/orcad/pspice\\_simulation/Pages/default.aspx](http://www.cadence.com/products/orcad/pspice_simulation/Pages/default.aspx)
- [100] <http://www.fnal.gov/projects/ckm/jlab/4616-spec.htm>
- [101] Forward Vertex Detector Homepage, <https://www.phenix.bnl.gov/WWW/fvtx>
- [102] PHENIX Focus Seminar: Forward Vertex Detector (FVTX)–Physics, Melynda Brooks, 2007
- [103] PHENIX Focus Seminar: FVTX-Detector, Sergey Butsyk, 2007
- [104] The RHIC Beam Abort Kicker System, H. Hahn, et. al, Proceedings of the 1999 Particle Accelerator Conference, New York (1999)
- [105] Relative Luminosity in Run3  $pp$ , K. Tanida, PHENIX Analysis Note 222
- [106] Relative Luminosity Analysis in Run4  $pp$ , Y. Fukao, PHENIX Analysis Note 446
- [107] Analysis Note on Relative Luminosity in  $pp$  Collisions at 62.4GeV in Run6  $pp$ , K. Aoki, PHENIX Analysis Note 548
- [108] Analysis Note on Relative Luminosity in  $pp$  Collisions at  $\sqrt{s} = 62.4\text{GeV}$  in Run6  $pp$  - Update, K. Aoki, PHENIX Analysis Note 686
- [109] Final Relative Luminosity in Run6 Longitudinally Polarized  $p + p$  at  $\sqrt{s} = 200 \text{ GeV}$ , PHENIX Analysis Note 720
- [110] Relative Luminosity in Run9 Polarized  $p + p$  Collisions at  $\sqrt{s} = 200 \text{ GeV}$ , P. Kline, PHENIX Analysis Note 881
- [111] Run-09 pC Polarimeter Analysis, I. Alekseev, et. al [http://www4.rcf.bnl.gov/~cnipol/pubdocs/Run09offline/pC\\_2009.pdf](http://www4.rcf.bnl.gov/~cnipol/pubdocs/Run09offline/pC_2009.pdf)
- [112] Absolute Luminosity Determination Using the Vernier Scan Technique: Run4 – 6 Analysis and Preliminary Results at  $\sqrt{s} = 62.4 \text{ GeV}$ , A. Bazilevsky, et. al., PHENIX Analysis Note 597
- [113] Absolute Luminosity Determination Using the Vernier Scan Technique: Run5 – 6 Analysis and Final Results at  $\sqrt{s} = 62.4 \text{ GeV}$ , R. Bennet, et. al., PHENIX Analysis Note 688

- [114] BBC Cross Section Using Vernier Scans for 500 GeV  $pp$  Data in Run09, A. Datta, D. Kawall, PHENIX Analysis Note 888
- [115] Private Communications, Notes, Presentations with and from Sasha Bazilevsky.
- [116] The STAR Scaler Board, A 10 MHz 24-bit VME Memory Module, H.J. Crawford, et. al., 2004
- [117] PHENIX SpinFest Presentations by Mei Bai (2012).
- [118] Method For Determining Relative Luminosity From Detection Probabilities (Run9 200 GeV), PHENIX Analysis Note 953.
- [119] Run 11  $W \rightarrow \mu$  Cross Section and Asymmetry Analysis, Seidl et. al, PHENIX Analysis Note 1024.
- [120] Central Arm  $W$  Analysis, K. Okada, M. Chiu, et. al., PHENIX Analysis Note 923.
- [121] Private Communications with Mickey Chiu based on Run13 Star Scaler Analysis.
- [122] PYTHIA 6.4 Physics and Manual. T. Sjöstrand, S. Mrenna, P. Skands., <http://home.thep.lu.se/~torbjorn/pythia/1utp0613man2.pdf>
- [123] GEANT Homepage, <http://wwwasd.web.cern.ch/wwwasd/geant>
- [124] GEANT Documentation, <http://wwwasdoc.web.cern.ch/wwwasdoc/geant/geantall.html>
- [125] PISA Homepage, <http://phenix.vanderbilt.edu/simulation>
- [126] <http://accelconf.web.cern.ch/accelconf/p99/PAPERS/WEA116.PDF>
- [127] PHENIX Focus Seminar: Zero Degree Calorimeter, Mickey Chiu, 2003. <http://www.phenix.bnl.gov/WWW/run/03/focus/index.html>